



HAL
open science

Lattice coherence and local non-local duality in f -electron materials

Bishal Poudel

► **To cite this version:**

Bishal Poudel. Lattice coherence and local non-local duality in f -electron materials. Condensed Matter [cond-mat]. Université de Bordeaux, 2022. English. NNT: . tel-03688895v2

HAL Id: tel-03688895

<https://hal.science/tel-03688895v2>

Submitted on 28 Oct 2022

HAL is a multi-disciplinary open access archive for the deposit and dissemination of scientific research documents, whether they are published or not. The documents may come from teaching and research institutions in France or abroad, or from public or private research centers.

L'archive ouverte pluridisciplinaire **HAL**, est destinée au dépôt et à la diffusion de documents scientifiques de niveau recherche, publiés ou non, émanant des établissements d'enseignement et de recherche français ou étrangers, des laboratoires publics ou privés.

THÈSE PRÉSENTÉE
POUR OBTENIR LE GRADE DE
DOCTEUR
DE L'UNIVERSITÉ DE BORDEAUX
ECOLE DOCTORALE SCIENCES PHYSIQUES DE
L'INGÉNIEUR

LASERS, MATIÈRE ET NANOSCIENCES

Par **Bishal POUDEL**

Lattice coherence and local non-local duality in f -electron
materials

Sous la direction de : **Sébastien BURDIN**

Co-directrice : **Gertrud ZWICKNAGL**

Soutenue le 2 mars 2022

Membres du jury :

M. Alexandre BOUZDINE	Professeur	Université de Bordeaux	Président
M. Frank LECHERMANN	Professeur	Universität Hamburg	Rapporteur
M. Marcelo ROZENBERG	Directeur de recherches	LPS	Rapporteur
M ^{me} Catherine PEPIN	Directrice de recherches	IPHT CEA Saclay	Examinatrice
M ^{me} Sophie TENCE	Chargée de recherches	ICMCB-CNRS	Invitée
M ^{me} Claudine LACROIX	Directrice de recherches	Institut Néel	Invitée
M. Sébastien BURDIN	Maître de conférences	Université de Bordeaux	Directeur de thèse
M ^{me} Gertrud ZWICKNAGL	Professeure	TU Braunschweig	Co-directrice de thèse

असतो मा सद्गमय ।
तमसो मा ज्योतिर्गमय ।
मृत्योर्माऽमृतं गमय ॥
ॐ शान्तिः शान्तिः शान्तिः ॥

From falsehood lead me to truth,
From darkness lead me to light,
From death lead me to immortality.
Om shanti shanti shanti.

मेरो मुआ र आमालाई समर्पित ।

Cohérence du réseau et local non-local dualité dans les matériaux à électrons f

Résumé : Dans cette thèse, nous étudierons les systèmes d'électrons f sous deux aspects différents : d'une part la formation et la brisure de cohérence du réseau, et d'autre part la nature des électrons f qui peuvent être localisés, itinérants ou duals. Dans la première partie, nous aborderons le sujet de la cohérence du réseau dans les systèmes $4f$ sous l'angle de la substitution atomique des atomes magnétiques par des atomes non-magnétiques. Nous traiterons du désordre généré par la substitution par la théorie de champ moyen dynamique. Nous commençons par généraliser le diagramme de phase de type Doniach avec la substitution en considérant les phases : ferromagnétique, antiferromagnétique et paramagnétique Kondo. Nous étudions également la pertinence de nos diagrammes de phases vis-à-vis des données expérimentales des alliages à la base de cérium. Par la suite, nous nous concentrerons sur la phase paramagnétique Kondo avec un réseau carré afin d'étudier les signatures de la brisure de cohérence du réseau en diluant les impuretés magnétiques. Pour cela, on analyse les signaux de photoémission, les masses effectives, le local potential scattering, et l'ordre de charges. Nous confirmerons les précédentes prédictions de transition type Lifshitz entre les systèmes dilués et denses. De plus, nous détecterons une nouvelle concentration critique pour une instabilité au liquide de Fermi. Ce dernier est caractérisé par une annulation de la masse effective. La deuxième partie de cette thèse traite le caractère dual apparent des électrons $5f$ dans les fermions lourds à la base d'actinides, où les degrés de liberté $5f$ itinérants et localisés semblent coexister. Nous utiliserons la méthode des bosons esclaves invariants par rotation pour étudier l'influence de corrélations intra-atomiques, i. e., de type de règle de Hund. Nos résultats confirmeront la conjecture selon laquelle les corrélations intra-atomiques peuvent renforcer les anisotropies dans l'intégrale de saut effectif $5f$ - $5f$, et conduisent à une localisation partielle sélective en orbitale. Enfin, nous analysons les différentes phases partiellement localisées en fonction de la masse de quasi-particules, l'occupation, d'aimantation et la configuration de valence dépendantes en orbitale.

Mots-clés : matériaux fortement corrélés, matériaux quantiques, transition de phases quantiques, fermion lourd, théorie de champ moyen dynamique, bosons esclaves invariants par rotation, l'alliages Kondo désordonnés, brisure de cohérence, photoémission résolue en angle, transition de Lifshitz, topology de surface de Fermi, dualité, localisation partielle sélective en orbitale

Lattice coherence and local non-local duality in f -electron materials

Abstract: In this thesis, we will study f -electron systems under two different aspects: the formation and the breakdown of lattice coherence, and the nature of f -electrons, which can be either localized, itinerant, or dual. In the first part, we study lattice coherence in $4f$ systems with the atomic substitution of magnetic atoms by non-magnetic atoms. We will deal with the substitutional disorder by using the dynamic mean-field theory. We start by generalizing the Doniach type phase diagram with substitution by considering the phases: ferromagnetic, antiferromagnetic, and paramagnetic Kondo. We also study the relevance of our phase diagrams by comparing the experimental data of various cerium-based Kondo alloys. Next, we will focus on the Kondo paramagnetic phase on a square lattice in order to study the signatures of lattice coherence breakdown with the dilution of magnetic impurities. To do this, we analyze the photoemission signals, the effective masses, the local potential scattering, and the charge order. We confirmed previous predictions of a Lifshitz-type transition between dilute and dense impurity systems. In addition, we detect a new critical concentration for a Fermi liquid instability. The latter is highlighted by a vanishing effective mass. The second part of this thesis deals with the apparent dual character of $5f$ electrons in actinide-based heavy-fermion compounds where itinerant and localized $5f$ -degrees of freedom seem to coexist. We adopt the rotationally invariant slave-boson method to study the influence of intra-atomic, i. e., Hund's rule type correlations. Our results confirm the conjecture that intra-atomic correlations may enhance anisotropies in the effective $5f$ - $5f$ hopping and thus eventually lead to orbital-selective partial localization. Finally, we analyze the different partially localized phases in terms of orbital-dependent quasiparticle mass and occupation, magnetization, and valency configurations.

Keywords: strongly correlated systems, quantum matter, quantum phase transitions, heavy-fermion, dynamical mean-field theory, rotationally invariant slave-bosons, disordered Kondo alloys, coherence breakdown, angle-resolved photoemission spectroscopy, Lifshitz transition, Fermi surface topology, duality, orbital-selective partial localization

Contents

Remerciements	i
Acknowledgments	v
Foreword	vii
1 General introduction	1
1.1 Strongly correlated electron systems	2
1.1.1 Large diversity of families of systems with remarkable macroscopic emergent phenomena	2
1.1.2 Various microscopic mechanisms and interactions	3
1.1.3 Appropriate theoretical methods	3
1.2 Motivations	5
1.2.1 Strongly correlated f -electron systems	5
1.2.2 Lattice coherence and local-itinerant duality	7
I Kondo alloys	9
2 An overview of Kondo systems	11
2.1 Introduction to Kondo physics	11
2.1.1 Kondo effect as a scattering process	11
2.1.2 From single-impurity to Kondo lattice	14
2.1.2.1 Magnetism versus Kondo: Doniach's argument	14
2.1.2.2 Effect of electronic filling: Nozières's exhaustion problem and coherence formation	15
2.2 Kondo substitution in Kondo alloys	17
2.2.1 Strong coupling picture	18
2.2.2 Weak coupling limit	18
2.2.3 Experimental realization of lattice coherence breakdown	19
2.3 Motivations and objectives	20

3	Model, method and approximations	21
3.1	The Kondo alloy model	21
3.2	Treatment of disorder due to Kondo impurity substitution	22
3.2.1	An overview of methods	22
3.2.2	A brief introduction to dynamical mean-field theory (DMFT)	22
3.2.3	Matrix DMFT/CPA	23
3.2.3.1	Paramagnetic Kondo phase	23
3.2.3.2	Dynamical local bath	28
3.2.3.3	Antiferromagnetic phase	29
3.2.3.4	Local Green's function	30
3.3	Treatment of local Kondo interaction	33
3.3.1	An overview of methods	33
3.3.2	Magnetically ordered phases: Weiss mean-field approximation	33
3.3.3	Paramagnetic Kondo phases: "large N" slave-bosons mean-field approximation	34
3.4	Numerical approach and algorithm scheme	36
4	Magnetic phase diagrams of Kondo alloys	39
4.1	A state of the art	39
4.1.1	Experimental phase diagrams	39
4.1.1.1	Mechanical pressure as tuning parameter	40
4.1.1.2	Substitution as tuning parameter	40
4.1.2	Phase diagrams through various theoretical approaches	42
4.2	Symmetries considerations for numerical calculations	43
4.3	Results: ground-state phase diagram	43
4.3.1	Tuning of n_c and T_K for periodic Kondo lattice	44
4.3.2	Tuning of x and T_K at fixed n_c for Kondo alloys	46
4.4	Discussion: comparison with experimental data	46
5	Photo-emission properties of Kondo alloys	51
5.1	A state of the art	51
5.2	Theoretical approach for disordered systems	52
5.2.1	Disorder averaged one-body Green's function	53
5.2.2	Spectral function and Fermi surface	54
5.2.3	Local density of states	55
5.2.4	Local self-energy and effective mass	55
5.3	Results: Spectral function and electronic density of states	55
5.3.1	Evidence for a Lifshitz-like transition in the Kondo phase at large T_K	56
5.3.2	Evidence for a new critical concentration at low T_K	57
5.4	Results: Fermi surface	58
5.4.1	Fermi surface in the Kondo phases: coherence breakdown	59

5.4.2	Fermi surface in the magnetically ordered phases	61
5.5	Results: emergence of two transitions in the paramagnetic Kondo phases	62
5.6	Discussion	67
6	Local potential scattering and charge inhomogeneity in Kondo alloys	69
6.1	Introduction	69
6.1.1	Local potential scattering	69
6.1.2	Charge inhomogeneity	70
6.2	Results: Local Potential scattering	71
6.2.1	Large T_K case	71
6.2.2	Low T_K case	72
6.3	Results: Charge inhomogeneity	73
6.4	Discussion	75
7	Conclusion and Perspectives	77
II	5f electrons in Uranium alloys	81
8	Introduction	83
8.1	Nature of 5f electrons in uranium based compounds	84
8.1.1	Hill criterion	84
8.1.2	Heavy fermions	84
8.2	Microscopic mechanism: dualism of f-electron	85
8.3	Phenomenological modeling of duality	86
8.3.1	Model Hamiltonian	87
8.3.2	Approaches	88
8.4	An outline to slave-bosons approaches	89
8.4.1	Barnes' representation	89
8.4.2	Kotliar and Ruckenstein's representation	90
8.4.3	Li, Wölfel and Hirschfeld's representation	92
8.4.4	Other variations of slave-bosons techniques	93
8.5	Motivations and objectives	94
9	Model and rotationally-invariant slave bosons	97
9.1	Model Hamiltonian	97
9.2	Method: rotationally-invariant slave-bosons	98
9.2.1	Expanded Hilbert space and basis set	98
9.2.2	Local constraints	99
9.2.3	Representation of physical electron operators and RISB Hamiltonian	100
9.2.4	Basis transformations	100
9.3	Approximations	101

9.3.1	Mean-field approximations for auxiliary fields	101
9.3.2	Constant density of states	103
9.4	Self-consistent equations system and parameters	103
10	Numerical approach: algorithm and technical challenges	105
10.1	Reduction of Hilbert space and slave-bosons	105
10.2	Minimization of Energy	106
10.2.1	Choice of optimization algorithms	107
10.2.2	Global and local optimizations	107
10.3	Numerical error tolerance on constraints	108
11	Results	111
11.1	Non-localized paramagnetic phase in isotropic hopping case	112
11.1.1	Non-interacting limit	112
11.1.2	Atomic limit	112
11.1.3	From atomic limit to non-interacting limit: the appearance of three distinct regions	114
11.2	Ground-state phase diagram	116
11.2.1	One-electron localized phases	118
11.2.2	Two-electrons localized phases	120
11.3	Physical signatures and manifestations of duality	121
11.3.1	Quasiparticle weight	121
11.3.2	Occupations and magnetization	123
11.3.3	Fermi surfaces	125
11.3.4	f -electron valency configurations	128
12	Conclusions and perspectives	131
III	Appendices	135
	Appendices	137
A	Evaluation of energies and ground state phase diagrams	139
A.1	Expressions of energies	139
A.2	Evaluation of ground state phase diagram	139
B	Matrix DMFT/CPA for Néel ordered antiferromagnetic phase	141
B.1	Diagrammatic development of Green function	141
B.2	Green's function matrix in reduced Brillouin zone	142
B.3	Some relations using Pauli matrices	144
B.4	Local Green's function matrix	145
B.5	Dynamical local bath	147

C	Results on Bethe lattice	151
C.1	Equations for local Green's functions	151
C.2	Phase diagram	152
C.3	Local potential scattering	153
C.3.1	Large Kondo coupling	153
C.3.2	Low Kondo coupling	153
D	Toy model for negative mass	155
D.1	Two reservoirs model	155
D.2	Application to $\Sigma_{alloy}(\omega)$	156
E	Slave-bosons mappings	157

Remerciements

Ce doctorat n'est pas simplement le fruit de travail de quatre ans, mais un enchaînement d'événements qui se sont produits de tout long de ma vie depuis mon arrivée en France. Toutefois, tout cela n'aurait pas été possible sans l'éducation transmise par mes parents et ma famille dès mon premier âge, et je suis très reconnaissant à eux. De mes débuts en tant que serveur ou livreur, ignorant complètement que j'allais faire de ma vie, à ce moment d'achèvement de ma thèse, je mesure le chemin parcouru. L'environnement façonné par chacune des personnes rencontrées durant toutes ces années m'a permis d'achever ce long travail.

Tout d'abord, je tiens à remercier Sébastien Burdin et Gerturd Zwicknagl pour leur encadrement avec pédagogie et avec patience. Leur présence constante m'a permis d'avoir un bon élan dès le début de ma thèse jusqu'à la fin malgré les difficultés. Je vous remercie également d'être présent au niveau personnel à plusieurs reprises.

Je tiens aussi à remercier Claudine Lacroix pour sa présence durant tout le long de ma thèse. Merci à Christophe Geibel, Sophie Tencé, Véronique Brouet et Yvan Sidis pour m'avoir apporté une vision d'expérimentateur sur mes travaux de thèse. Je suis très reconnaissant à Rémi et Fabio d'avoir prêté leur serveur de calcul, ce qui m'a permis de gagner un temps considérable. Je remercie tous nos collaborateurs de Fermi-NESSt pour toutes les discussions stimulantes et enrichissantes. Je remercie également Quantum Matter Bordeaux, qui m'a donné plusieurs occasions d'exposer mes travaux et de les partager lors de discussions animées avec d'autres chercheurs.

Je remercie Frank Lechermann et Marcelo Rozenberg d'avoir accepté d'être les rapporteurs de cette thèse et également à Alexandre Bouzdine, Catherine Pépin, Sophie Tencé, Claudine Lacroix d'avoir accepté de faire partie du jury de cette thèse. Je remercie à Daniel Malterre d'avoir accepté de lire mon manuscrit même si les circonstances l'ont empêché de participer à ce jury de thèse.

Je remercie l'Agence National de Recherche (ANR) et Deutsche Forschungsgemeinschaft (DFG) d'avoir financé cette thèse. Merci au Pays basque et à l'école doctorale d'avoir financé une partie de mes déplacements durant cette thèse.

Mes années à LOMA étaient très agréables. Pour cela, je souhaite remercier Jonathan, Julie, Jeremy, et Vadim qui ont été parfaits partenaires de bureaux. Merci à Jérémy pour tous nos échanges scientifiques qui ont été une grande aide pour ma thèse. Je souhaite également remercier Benjamin et Léo pour tous nos échanges lors

de repas à la cantine et dans les couloirs du LOMA. Je souhaite de plus remercier Alain, David et Éric pour leurs conseils et les services informatique qui ont été très utiles durant les confinements pour la poursuite du travail à distance. Merci à Josiane, Suzanne, Sophie et Marie-Andrée du service de gestion pour leur gentillesse.

Je souhaite également remercier l'Université de Grenoble Alpes, l'Université de Toulouse III – Paul Sabatier et l'Université de Bordeaux qui m'ont accueilli à différents instants de ma vie depuis la licence à la thèse. Merci à tous les enseignants qui ont suscité en moi l'intérêt pour la recherche fondamentale. Je souhaite remercier Théo, Fernand et Cyril pour leur encadrement durant mes stages d'études.

Je remercie tout particulièrement Tara et Ananta Upadhaya. Sans vous, je me serai probablement perdu dès mon premier jour en France. Merci à Lauren, et également à Damien et Jacqueline Bernard d'avoir cru en moi. Je remercie les Grenoblois : Charlotte, Manon, Bertrand, Vincent, Elie et Pierre-Louis, pour toutes les attentions que vous m'avez apportées. Mes souvenirs de Toulouse vont vers Nicolas Canavera (M. Météo) et ses soirées couchsurfing inoubliables, je te remercie. Cihan, je pense encore à nos révisions la veille des partiels. Merci à Sophie, Etienne, Maëlys, Eloïse, Oliver, Zoé et Nico, mes amis toulousains (ou ex-toulousains maintenant) favoris. Je remercie particulièrement Amandine de m'avoir accompagnée une partie de ma vie.

Mon séjour à Braunschweig dans le cadre de cette thèse a été très réjouissant et enrichissant. Pour cela, je souhaite remercier TU Braunschweig. Et merci à Evrard, Kevin, Niklas, Lena, Alexandros, Benjamin et Cornelia, de m'avoir accueilli chaleureusement.

Je remercie Dominique, toujours là pour me dépanner. Merci à Ludo et Boris, les meilleurs voisins que je n'ai jamais eus. Merci à tous les Bordelais qui ont été proches de moi : Alexandre, Antoine, Audrey, Brice, Camille, Florent, Joséphine, Julie, Kévin, Laurent, Mady, Maëlis, Mikael, Natacha, Nousk, Pauline et Thomas.

Je remercie Wolfgang et Claire-Lise Herdrich. Je remercie Chloé de m'avoir écouté, soutenu et calmé mes angoisses durant ma dernière année de thèse. Sans toi, cette thèse n'aurait été probablement pas pareille. Merci à tes très précieux encouragements qui m'ont permis d'avancer dans ma thèse tout comme dans ma vie.

Acknowledgments

This doctorate is not simply the fruit of four years' work but a result of a chain of events that have occurred throughout my life since my arrival in France. However, all this would not have been possible without the education transmitted by my parents and my family from an early age, and I am very grateful to them. In the beginning, as a waiter or a delivery man, I was completely unaware of what I was going to do with my life. At this moment, with the completion of the thesis, I measure the path traveled. The environment shaped by each of the people that I met during all these years allowed me to complete this long work.

First of all, I would like to thank Sébastien Burdin and Gerturd Zwicknagl for their pedagogical and patient supervision. Their constant presence allowed me to advance at a good pace from the beginning of my thesis until the end despite the difficulties. I would also like to thank you for being present on a personal level on several occasions.

I would also like to thank Claudine Lacroix for her presence and help throughout my thesis. Thanks to Christophe Geibel, Sophie Tencé, Véronique Brouet and Yvan Sidis for providing me an experimental perspective over my thesis work. I am very grateful to Rémi and Fabio for lending me their calculation server, which permitted me to save a considerable amount of time. I thank all our Fermi-NESSt collaborators for all the stimulating and enriching discussions. I also thank Quantum Matter Bordeaux, which gave me several opportunities to present my work and share it during lively discussions with other researchers.

I would thank Frank Lechermann and Marcelo Rozenberg for accepting to be the reporters of this thesis and also to Alexandre Bouzdine, Catherine Pépin, Sophie Tencé, Claudine Lacroix accepting to be part of the jury of this thesis. I would thank Daniel Malterre for agreeing to read my manuscript even if circumstances prevented him from participating in this thesis jury.

I would like to thank the National Research Agency (ANR) and Deutsche Forschungsgemeinschaft (DFG) for the grant to conduct this thesis. Thank you to the Basque Country and to the doctoral school for their financial support during this thesis.

My years at LOMA were very enjoyable. For this, I would like to thank Jonathan, Julie, Jeremy, and Vadim, who were perfect office partners. Special thanks to Jérémy for all our scientific exchanges, which were a great help to my thesis. I would also like to thank Benjamin and Léo for all our discussions during meals in the canteen and

in the corridors of LOMA. I would also like to thank Alain, David, and Éric for their advice and their IT services which were very useful during the lockdowns to conduct the work from home. Thanks to Josiane, Suzanne, Sophie, and Marie-Andrée from the management department for their kindness.

I would also like to thank the University of Grenoble Alpes, the University of Toulouse III – Paul Sabatier, and the University of Bordeaux, where I have conducted my bachelor's degree to the thesis at the different instant of my life. Thank you to all the teachers who have ignited my interest in fundamental research on me. I would like to thank Théo, Fernand, and Cyril for their support during my study internships.

Special thanks to Tara and Ananta Upadhaya. Without you, I would probably have been lost on my first day in France. Thanks to Lauren and also to Damien and Jacqueline Bernard for believing in me. I would like to thank the Grenoblois: Charlotte, Manon, Bertrand, Vincent, Elie, and Pierre-Louis, for all the attention you have given me. Thank you to Nicolas Canavera (Mr. Weather) for all the unforgettable moments in Toulouse. Cihan, I'm still thinking about our revisions the day before finals exams. Thanks to Sophie, Etienne, Maëlys, Eloïse, Oliver, Zoé and Nico, my favorite friends from Toulouse (or ex-Toulouse now perhaps). I particularly thank Amandine for accompanying me for part of my life.

My stay in Braunschweig within the framework of this thesis was very pleasant and enriching. For that, I would like to thank TU Braunschweig. And also, special thanks to Evrard, Kevin, Niklas, Lena, Alexandros, Benjamin, and Cornelia, for welcoming me warmly.

I thank Dominique, who was always there to help me out. Thanks to Ludo and Boris, the best neighbors that I've ever had. Thank you to all the Bordelais who have been close to me: Alexandre, Antoine, Audrey, Brice, Camille, Florent, Joséphine, Julie, Kévin, Laurent, Mady, Maëlis, Mikael, Natacha, Nousk, Pauline and Thomas.

I thank Wolfgang and Claire-Lise Herdrich. I would like to thank Chloé for listening to me, supporting me, and calming my anxieties during my last year of the thesis. Without you, this thesis would probably not have been the same. Thank you for your very precious encouragements which allowed me to move forward in my thesis as well as in my life.

Foreword

The investigation of the electronic properties of a material is one of the key elements to understanding the state of matter. The electronic properties in a solid get defined either by the delocalization of the electrons by forming coherent Bloch states through the overlapping of their wave functions of neighboring sites or by its localization due to strong Coulomb repulsion. A usual way to study them is to use the band theory, which captures the physical properties defined by freely moving electrons in the periodic potential of a lattice. This picture of free electrons is supported by Landau's Fermi liquid theory [1], which adiabatically connects low-energy excitations to the non-interacting one with one-to-one correspondence. These low-energy excitations are also called quasiparticles, and they are characterized by the renormalized mass with a finite lifetime. Even though this Fermi liquid theory correctly defines the various macroscopic properties like resistivity of varieties of metals, it tends to fail to capture the underlying physics of complex systems with strong electron-electron interactions [2]. For these systems, one might do band-structure calculations using theories based on density functional theory (DFT) [3, 4]. Again, DFT fails to capture the low-energy excitations when the electron-electron interactions become strong. This gave rise to alternative methods like dynamical mean-field theory (DMFT) [5, 6] to study the strongly correlated systems. The study of these strongly correlated systems is the core subject of this thesis.

Research in strongly correlated electronic systems presents a challenge on both experimental and theoretical sides. Experimental studies of these systems are not straightforward and might require extreme experimental conditions [7] such as very low temperature, high pressure, and/or high magnetic field. Therefore, a forward theoretical understanding of the correlation effect is useful. But, the theoretical treatment of the correlations can be tedious and can require particular theoretical [8] and numerical [9] techniques. In the simplest scenario, we can define models embedded with the terms defining the interactions between electrons. However, the exact resolution of these models remains a difficult task and is possible only under certain contexts such as low dimensionality. In order to have qualitative results on the thermodynamic limit, we often use methods with some approximations on electronic interactions or on the dimensionality of the system.

In this thesis, we focus on two distinct systems in this thesis: rare-earth-based compounds and uranium-based compounds, where both have strong electron-electron

correlations with partially filled f -shell. Even though our research into these two systems is separate, they provide a complementary view of the physics that may emerge from the nature of f -electrons, which can be localized, itinerant, or both (dual) [10].

This thesis contains two independent parts for $4f$ and $5f$ systems. Every part contains an introduction, methods and approximations, results, and conclusions. Below, we present a summary of each chapter:

Chapter 1 is a common opening chapter for the two halves, in which we place our subject in the context of several strongly correlated electron systems. We give an overview of a variety of strongly correlated systems, including their notable features and possible microscopic origins. We also go over various choices of theoretical methods available. Finally, we will discuss the motivations that led to this thesis and our goals.

Part I: Kondo alloys

Chapter 2 is the introductory chapter of the first part of this thesis. In this part, we present an introduction to Kondo physics by tracing its historical developments. The Kondo effect occurs when a localized magnetic impurity immersed in a metal host interacts with the conduction electrons. In lattice systems with many impurities, this effect could lead to a coherent macroscopic manifestation. One of the experimental indicators of this lattice coherence is the enlargement of the Fermi surface vis-à-vis the single impurity system. This lattice coherence and its breakdown as a function of the concentration of magnetic impurities is the core problem of this part. Here, We present experimental evidence and theoretical treatment of lattice coherence and its breakdown on various Kondo systems, and finally, we express our motivation for this study.

Chapter 3 is dedicated to the theoretical aspects of this part related to the treatment of disorder and Kondo interaction decoupling. The dynamical mean-field theory is used extensively in strongly correlated systems, and it becomes exact at the limit of infinite coordination. Here, we start by detailing our model Hamiltonian, and then we introduce matrix dynamical mean-field theory (DMFT) for the paramagnetic phase. Thereafter, we extend former DMFT formalism for the antiferromagnetic phase. The Kondo interaction is decoupled through mean-field approximations. At last, we present the system of self-consistent equations and our method of their numerical resolution.

Chapter 4 discusses our findings from DMFT on the phase diagrams of Kondo alloys. To put our study in context, we present an overview of the pressure and the atomic substitution as tuning factors for Kondo alloys. Then we show our results on a lattice with one magnetic impurity per site, followed by phase diagrams with magnetic impurity dilution. Finally, we explore the relevance of our findings by comparing them to experimental data.

Chapter 5 is devoted to our findings on lattice coherence upon the magnetic impurity dilution in the paramagnetic Kondo phase. Through photoemission signals, we show and analyze the hallmarks of lattice coherence breakdown in Fermi surfaces, the density of states, and electronic band structure. The influence of disorder on the effective mass and quasiparticle lifetime is also investigated. Finally, we extend the phase diagram obtained in the previous chapter.

Chapter 6 continues the study of the paramagnetic Kondo phase. Here, to characterize further the coherence breakdown in Kondo alloys, we look at local potential scattering and charge order.

Chapter 7 summarizes the important findings of our study of Kondo alloys and discusses future directions for both experimental and theoretical research.

Part II: 5f electrons in Uranium alloys

Chapter 8 is the introductory chapter of the second part. The f -electron can acquire both itinerant and localized nature in this chapter. This paradigm was motivated by the direct evidence of this dual nature of f -electron was observed in UPd_2Al_3 through photoemission. However, other direct or indirect experimental evidence pointing towards the dual nature of f -electron in uranium-based compounds was also observed. This duality might be driven by the interplay between multiple microscopic origins: Hund's coupling, spin-orbit coupling, and Coulomb interaction. Furthermore, it could potentially result in orbital-selective partial localized phases. To motivate this study, we present a summary of prior experimental findings, microscopic origins, and theoretical investigations.

Chapter 9 covers the most key theoretical aspects of this section. At first, we present our model Hamiltonian, and thereafter, we present the rotationally invariant slave boson (RISB) approach with mean-field approximations. Finally, we will present the system of self-consistent equations that need to be solved numerically.

Chapter 10 presents the numerical aspects of our study. Solving RISB equations is time-consuming and prone to numerical errors. Thus, they require special attention. During our study, we have employed multiple numerical schemes to obtain the correct physical ground-state solutions. Here, we describe our local and global reduction schemes in detail.

Chapter 11 presents the results on UPt_3 upon varying the orbital-dependent electronic bandwidth. We will first show and discuss our results using isotropic bandwidth, followed by an analysis of the effect of anisotropies on orbital-dependent electronic bandwidth. Finally, we present our phase diagram with orbital-selective partially localized phases, and we characterize them.

Chapter 12 summarizes the key aspects of this part and discusses the future prospects.

Chapter 1

General introduction

Electrons in a material define the physical properties like magnetic, optical, transport, and electronic, embedded in them. Moreover, these electrons can further interact with each other to give rise to some extraordinary features in so-called strongly correlated material systems (SCES). This strong electron-electron interaction may lead them to have either an itinerant character contributing to the chemical bonding, a localized character with no contribution to chemical bonding or even both, making them dual. Throughout this thesis, this localized versus the itinerant character of electrons will be our central theme.

Within band theory [11], a material is a conductor when it has partially filled energy bands. This condition is fulfilled when it has an odd number of electrons per unit cell. Similarly, if a material has an even number of electrons per unit cell, it will act as an insulator due to fully filled energy bands. The above descriptions through band theory are valid for most materials, where interaction between electrons does not play an essential role in the determination of physical properties like conductivity. Hence, the low-temperature physical properties can be understood through a model like free-electron model [12] in these materials. However, with strong electron-electron interactions, a material with a partially filled band can become an insulator. A concrete example would be V_2O_3 [13], where a transition from metal to an insulator happens due to localization of conducting electrons driven through strong electron-electron Coulomb repulsion at low temperature even with partially filled energy bands. Furthermore, the variation of these electron-electron interactions can further lead the localized character of an electron to an itinerant. This is the case found in many f -electron systems [14, 15] with odd or non-integer number of electrons per unit cell, where the application of external pressure can drive a phase transition with localized to itinerant electrons. Again in f -electron systems, a new paradigm [16, 17] has emerged where $5f$ electrons can acquire dual character: it can have both itinerant and localized features. From this observation, a natural question about the nature of f -electron with the variation of the electron-electron interaction can be raised, which we will be treating in this thesis. Besides from this specific itinerant versus localized

feature, the strong correlation between electrons induces many other phenomena, which we will be presenting below.

1.1 Strongly correlated electron systems

The history of SCES started in the 1930s when transition-metal oxide NiO [18] partially filled d -electron band was found to be an insulator. In the same decade, increasing resistivity was observed in impure gold and silver [19] at low temperatures, which was again unexpected. Later on, Nevill Mott and Rudolf Peierls [20] pointed out the possible role of electron-electron correlations for this insulating behavior in NiO with an odd number of electrons per unit cell, and in 1949 a theory [21] was established based on very-strong Coulomb repulsion. However, increasing resistivity [19] in some impure metals at low temperature remained unsolved for almost three decades. It was only explained three decades later by Jun Kondo [22], naming this effect as the Kondo effect that became a prototype of strongly correlated phenomena. Besides these two historical examples, we could note a series of experimental SCES discoveries, features, and breakthroughs like the first heavy-fermion system [23], first heavy-fermion superconductivity [24], high temperature superconductivity in cuprates [25], non-Fermi liquids [2] quantum phase transitions [26], and ferromagnetic superconductors in $5f$ -electron systems [27].

1.1.1 Large diversity of families of systems with remarkable macroscopic emergent phenomena

In this section, we will present various families of SCES with their macroscopic properties. Let's start with f -electron systems, where quasiparticle mass can reach hundreds of times of bare electron mass. The first f -electron system to be found of this kind was CeAl₃ [23]. Later on, a wide range of $4f$ and $5f$ -electron heavy-fermions were discovered. Figure 1.1 shows this wide range of materials and the universal scaling feature when the so-called Kadowaki-Woods ratio between the A coefficient of the resistivity $\rho(T) = \rho_0 + AT^2$ and the square linear coefficient of the specific heat $\gamma = C_v/T$ is plotted. In addition to heavy-fermion behavior, these systems may present unconventional¹ heavy-fermion superconductivity. The first compounds to be found as heavy-fermion superconductors in $4f$ and $5f$ -systems are CeCu₂Si₂[24] and in UBe₁₃ [28] respectively. Also, a few numbers of $5f$ -systems were also found to have ferromagnetic superconductivity [29] and while might present duality [16, 17, 29].

SCES are also famous for high-temperature superconductivity T_c which can be found in cuprates and iron pnictides. Cuprates remains on the top of the podium

¹Unconventional because it can not be explained by BCS theory

with T_c of 133K [30] at 1 atm and 166 K [31] at 23 GPa. The highest T_c observed in iron pnictides is 55 K [32]. Another example of SCES is vanadates with vanadium sesquioxide V_2O_3 seen as an archetype of the Mott insulator [13]. Indeed, V_2O_3 is metal at high temperatures, and it becomes an insulator at low temperatures due to strong correlations. SCES also exhibit exotic phases like spin-liquids [33] and spin-ice [33, 34], and can be found in pyrochlores oxides family ($R_2Ti_2O_7$, where R^{3+} is a rare earth atom) and spin ladders systems like $Sr_{14-x}Ca_xCu_{24}O_{41}$ [35]. Furthermore, the spin ladders systems like $Sr_{14-x}Ca_xCu_{24}O_{41}$ also exhibit charge density wave phases along with the superconducting phase. Apart from f -electron systems, heavy-fermion behavior can be observed in transition metal oxide such as LiV_2O_4 [36]. As most of SCES, ruthenates like Sr_2RuO_4 can present superconductivity [37]. SCES also include organic conductors like $\kappa - (BEDT - TTF)_2X$ systems [38, 39], or even in cold atoms [40, 41] systems.

Besides the theoretical study and understanding of SCES, the strong correlation in some materials has a real potential to be used in near-future technologies in electronic devices [42] like non-volatile memory, also known as Mottronics [43]. Colossal magnetoresistance [44] and magnetocaloric effect [45] found in manganites [45–48] can be used in spintronics [47, 48] and in magnetic refrigeration technology. Complex oxides like doped lanthanum manganites, we can observe multiferroicity [49] effect, which has its potential use in devices [50, 51]. Of course, there is high T_c superconductivity a wide range of uses like high transmission lines.

1.1.2 Various microscopic mechanisms and interactions

Strong correlations in strongly correlated electron systems come from the interplay and competition between the multiple degrees of freedom of an electron: spin, orbital, lattice, or charge. Coulomb interaction could be the most common interaction that may lead to a variety of spin ordering patterns as well as metal-insulator transition [13]. In iridates [53, 54] or cold atoms [41], spin-orbit coupling may contribute orbital-dependent Mott transition. Orbital-dependent physics may appear from Hund's coupling in multi-orbital SCES like in ruthenates [55–57], and iron pnictides [58, 59], iron chalcogenides or in $5f$ systems [60]. More importantly, there can be a complex interplay between all these couplings, which might necessitate a theoretical treatment.

1.1.3 Appropriate theoretical methods

Exploration of the physical properties of SCES presents a challenge on theoretical sides. To illustrate this challenge, we can note the failure of density functional theory to describe for Mott insulator with partially d -shells [61]. Thus, one needs to choose a method carefully to treat electronic correlations. *Ab-initio* methods like local density

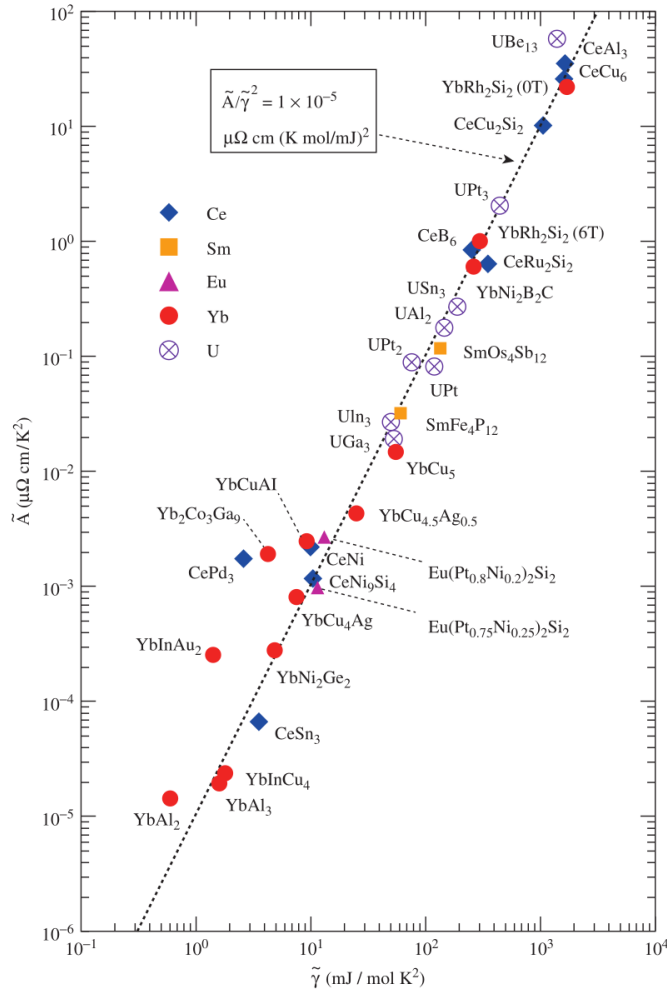


Figure 1.1: Kadowaki–Woods ratio for a wide range of $4f$ and $5f$ -electron heavy-fermion materials with normalized $\tilde{A} = A/(N(N - 1))$ and $\tilde{\gamma} = \gamma/(N(N - 1))$ with ground-state degeneracy N . From [52]

approximation (LDA) + U [62, 63], self-interaction corrected LDA [64], linear muffin-tin orbitals [65, 66], hybrid functional approach [67–69] and generalized gradient approximation [70] could be employed to calculate more accurately the chemical and electronic structure of a material. However, one might need to know some characteristic parameters value, normally experimental data, for a specific material.

Simpler but effective, model-based approaches could be an alternative to *ab-initio* since they tend to capture electron-electron interaction more accurately giving better qualitatively results. One could choose any methods among: slave-bosons [71–74], variational method with Gutzwiller wave function approximation [75], mean-field methods like dynamical mean-field theory [5], exact diagonalization [76], density matrix renormalization group [77], quantum Monte Carlo [78] and cluster perturbation theory [79, 80]. Additionally, both *ab-initio* and model-based method can be mixed for more realistic modelling of electronic properties in real materials. For instance, one can combine dynamical mean-field theory with density functional [6, 81]. DFT+DMFT has been used extensively and successfully to study real materials [82, 83].

1.2 Motivations

In this section of this thesis, we will disclose our motivations and objectives.

1.2.1 Strongly correlated f -electron systems

In this thesis, we focus on the effect of strong electronic correlations present on f -electrons material: the rare earth metals (lanthanides) and the actinides with electronic configurations $[\text{Xe}]4f^n 5d^{0-1} 6s^2$ and $[\text{Rn}] 5f^n 6d^{0-1} 7s^2$ respectively. The whole series of lanthanides and actinides are formed by successive addition of an electron on the $4f$ or $5f$ shells.

From the figure 1.2, we can observe that the wave functions of $4f$ and $5f$ shells are contracted while compared to the wave functions of other electrons in s , p and d shells. Thus, the $4f$ shell is more inner towards the nucleus and spatially localized except in europium, samarium, and ytterbium. Furthermore, the spatial extension of these orbitals shrinks as the atomic number increases, with Ce being more spatially extended for lanthanides. In $4f$ systems, the strong correlation is the result of the interaction between partially filled localized electrons in $4f$ electronic shells and the conduction electrons. In contrast to lanthanides, the spatial extent of $5f$ orbital varies upon atomic number: larger spatial distribution for light actinides [84] whereas for heavy actinides [85] spatial extent is similar to those of lanthanides.

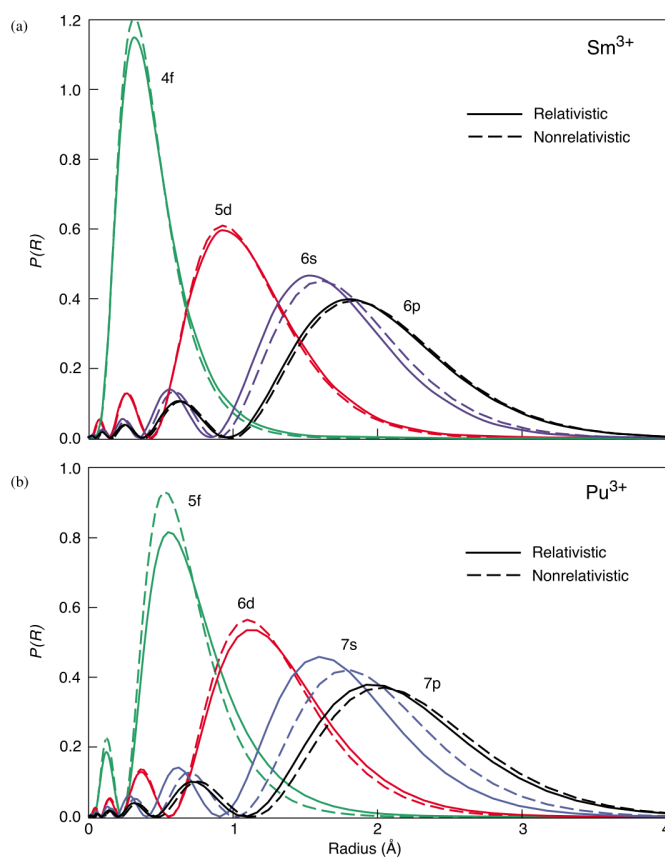


Figure 1.2: Radial extend of $4f$ electrons in Sm^{3+} and Pu^{3+} respectively with both relativistic and nonrelativistic effects. x -axis in radial distance from the nucleus whereas $P(R)$ radial probability to find an electron at a distance r from the nucleus. From [86]

1.2.2 Lattice coherence and local-itinerant duality

In $4f$ and $5f$ systems, the localized f -electrons are immersed in a sea of conduction electrons with which they may interact. At high temperatures, f -electrons remains localized as seen through the observation of Curie Weiss susceptibility. However, at sufficiently low temperatures, strong electronic correlations may arise at the atomic level. Remarkably, a macroscopic coherent state can manifest on periodic lattice despite the short-distance nature of these local correlations. In this thesis, we will study the formation and robustness of this lattice coherence. As a first approach, we conduct this study by diluting the atoms with f -electrons. The dilution can be done through isostructural atomic substitution of the atom with f -electron by the atoms without f -electrons. The second approach for this study consists of varying electronic correlations based up on the application of external parameters like pressure. We address all these questions about the lattice coherence on $4f$ electronic systems in the first part of this thesis. Similarly, the question of duality will be treated on the in uranium alloys in the second part of this thesis.

Part I
Kondo alloys

Chapter 2

An overview of Kondo systems

Kondo systems are the systems where magnetic impurities are randomly distributed in a metallic crystal and interact with conduction electrons. In our case, these metallic impurities are the $4f$ electrons present in rare earth metals. In these systems, the interaction between these localized magnetic impurities and conduction electrons, also known as Kondo effect [87, 88]. This effect can lead to unexpected behaviors [89] at low temperature, rich phase diagrams, non-Fermi liquid behaviors [2], small and large Fermi surfaces [15], and many other emergent phenomenons [90]. In this introductory chapter of part one of this thesis, we will present an overview of Kondo physics following the historical events in the development of Kondo physics while exposing the motivations of this current study.

2.1 Introduction to Kondo physics

2.1.1 Kondo effect as a scattering process

The journey of Kondo physics started with the observation of a minimum resistivity in impure gold [19] (see figure 2.2(a)) and in CuFe [91] in the early 1930s at low temperatures. At that time, this came with a big surprise, since normally, the

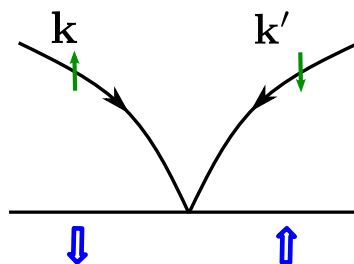


Figure 2.1: Schematic view of spin-flip process during electron scatter in Kondo model.

resistivity decreases with decreasing temperature and tends towards saturation at low temperatures. Later, the logarithm increase of resistivity was observed whenever magnetic impurities are present in the host metal. This effect puzzled for thirty years until Jun Kondo [22] provided an explanation with the assumption that the effect arises through the interaction spins of the localized and conduction electrons. This interaction leads to the model known as the Kondo single-impurity model

$$\mathcal{H} = \sum_{\mathbf{k}} \epsilon_{\mathbf{k}} c_{\mathbf{k}\sigma}^{\dagger} c_{\mathbf{k}\sigma} + J_K \mathbf{S}_I \mathbf{s}_c(0), \quad (2.1)$$

where $c_{\mathbf{k}\sigma}^{\dagger}$ ($c_{\mathbf{k}\sigma}$) describe creation (annihilation) operators of conduction electrons with spin $\sigma = \uparrow, \downarrow$ and momentum \mathbf{k} . $\epsilon_{\mathbf{k}}$ is non-interacting dispersion. \mathbf{S}_I is the impurity spin, and $\mathbf{s}_c(0)$ is the conduction electron spin density at the impurity site with $J_K > 0$ being antiferromagnetic coupling. The resistivity in ordinary metals originates from the scattering processes where the phonon contribution is proportional to T^5 , dominating at high temperatures and the electron-electron contribution of the order T^2 , characterizing the Fermi liquid state. In addition to these contributions, the scattering of conduction electrons from the impurity is also considered through the spin-flip process. In the later process, the electron spin can flip together with a simultaneous spin-flip of the impurity. Schematic representation of spin process can be found in the figure 2.1. Within model 2.1 and Born approximations, an expression of resistivity for impurity scattering part ¹ is obtained

$$R_{imp} = R_0 \left[1 - \frac{2J_K \rho}{N} \log\left(\frac{k_B T}{W}\right) + \dots \right], \quad (2.2)$$

where R_0 is temperature-independent residual resistivity from Born approximation and W electronic bandwidth. For antiferromagnetic coupling $J_K > 0$ and for $k_B T \gg W$, the resistance will increase logarithmically. However, the expression (2.2) contain the problem that it diverges as $T \rightarrow 0$. A year after Jun Kondo explanation, Abrikosov extended the previous calculation by calculating all the terms given by $[(J_K \rho / N) \log(k_B T / W)]^n$ which gave rise to even strong divergence at $T \rightarrow 0$. Through the summation of leading terms, he obtained

$$R_{imp} = \frac{R_0}{[1 + J_K \rho \log(\frac{k_B T}{W})]^2}. \quad (2.3)$$

One can remark that the above equation (2.3) diverges at a characteristic temperature which is expressed as

$$k_B T_K \approx W \exp(-1/J_K \rho). \quad (2.4)$$

Thus, the characteristic temperature T_K determined from the expression (2.4) is the so-called Kondo temperature.

¹A demonstration can be found in chapter four in [92]

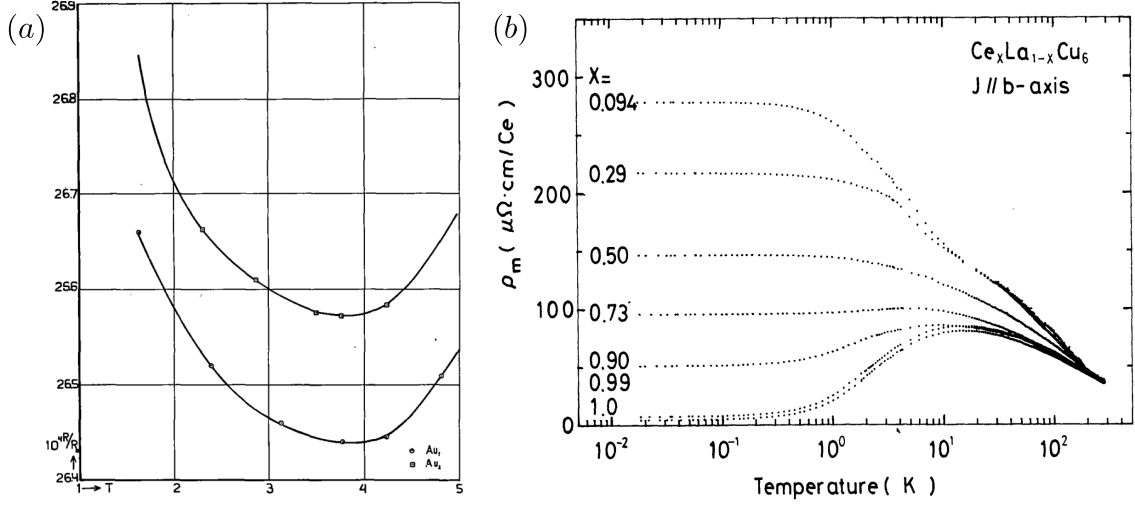


Figure 2.2: Two historical examples showing Kondo effect. (a) Resistivity of impure gold from 1 K to 5 K where we observe a minimum resistivity around 4 K, extracted from [19]. (b) Resistivity of $\text{Ce}_x\text{La}_{1-x}\text{Cu}_6$ series with Ce-La substitution. Single-impurity Kondo effect can be seen at $x = 0.094$ and multi-impurity at $x = 1.0$, extracted from [89].

In order to study the low energy characteristics, Anderson and his co-workers [93–95] used a new approach based on scaling known as poor’s man scaling, where high-energy excitations are eliminated gradually. The effect of eliminated states is retained in a set of energy-dependent running couplings $J_K(W)$ in order to preserve the low-energy behavior of the system. They found an expression of Kondo temperature similar to equation (2.4), but with a pre-factor $\sqrt{J_K\rho}$. From this scaling approach, few conclusions can be drawn: physics is governed by scaling independent Kondo temperature T_K , and different systems have the same low energy behavior.

The theory developed from the perturbation theory progressively breaks at low temperatures. Similarly, all the analytical methods starting from the high-temperature region break down near T_K . With a severe need to understand the low energy characteristics, Wilson developed a non-perturbative numerical normalization group [96] which showed that when the Kondo interacting becomes large and below the Kondo temperature T_K , the ground-state is marked by the formation of spin-singlet states between the conduction band electrons and the local impurity spin. In his study, he also found that the ratio of magnetic susceptibility χ to Sommerfeld coefficient γ was two, which is twice the value observed for a non-interacting system.

Nozières [97, 98] also provided the essentials of the ground-state physical properties at the strong coupling regime (when $J_K \rightarrow \infty$). In his study, the impurity is bound to the conduction electrons and forms a singlet state, and is decoupled from the rest of the system. It acts only as a scattering center for the conduction electrons. Since the coupling is large but not infinite, the conduction electrons can polarize the

singlet, which can again affect another electron. In this way, a "local Fermi liquid" can be formed through local electron-electron interaction. This single-impurity "local Fermi liquid", analogous to Landau's Fermi liquid theory where the resistivity curves behave as $\rho(T) = \rho_0 + AT^2$, specific heat behaves as $C = \gamma T$ and magnetic susceptibility behave as $\chi(T) = \chi_0 - \alpha T^2$. This was observed experimentally in a lot of diluted Kondo alloys [99–101].

Finally, almost 50 years later, the single-impurity Kondo problem was solved exactly [102, 103] by using the Bethe ansatz. The exact solution confirmed the singlet ground state calculated by Wilson and the local Fermi liquid theory elaborated by Nozières.

2.1.2 From single-impurity to Kondo lattice

In the 1970s, the experimental realizations of a new class of systems based on rare earth metals gave rise to new phenomena due to the presence of multiple impurities and the correlations generated by them. Concurrently, a series of theoretical developments were made to explain the physics of multi-impurity systems. Thus, in this section, we will present an overview of the physics of multi-impurity Kondo systems.

2.1.2.1 Magnetism versus Kondo: Doniach's argument

The complexity in Kondo systems increases with the increasing number of impurities. Indeed, the impurities can interact with each other via Ruderman-Kittel-Kasuya-Yosida (RKKY) interaction. Doniach [104] argued the scaling behaviors of this RKKY interaction in multi-impurity systems. In his paper, he showed that there are two competing energy scales in Kondo systems proportional to the Kondo coupling J_K . The magnetically ordered phase competes with the paramagnetic Kondo phase with two different temperature scales: Kondo energy scales as $T_K \propto \frac{1}{\rho_0} e^{-1/J_K \rho_0}$ whereas the Ruderman-Kittel-Kasuya-Yoshida state (RKKY) inter-impurity magnetic interaction scales as $T_{RKKY} \propto J_K^2 \rho_0$. Indeed, magnetic order is stabilized when the strength of the Kondo interaction, i.e. the corresponding T_K , is relatively small. Figure 2.3 resumes schematic view of this competition in a phase diagram. This picture was confirmed through multiple theoretical studies [105–111].

Later based on Doniach argument, another kind of quantum criticality was proposed [112–117] where we observe the breakdown of Kondo effect with change of localized to itinerant behavior of impurity spins. Indeed, a system can undergo a phase transition at zero temperature upon application of external parameters due to quantum fluctuations, known as quantum phase transition [26]. In Kondo lattice this can be done through the application of pressure like in CeRu_2Ge_2 [118, 119], external field like in YbRh_2Si_2 [120] or substitution like in $\text{CeCu}_{6-x}\text{Au}_x$ [121], is of second-order nature. This transition at $T = 0$ at the quantum critical point (QCP), separates a

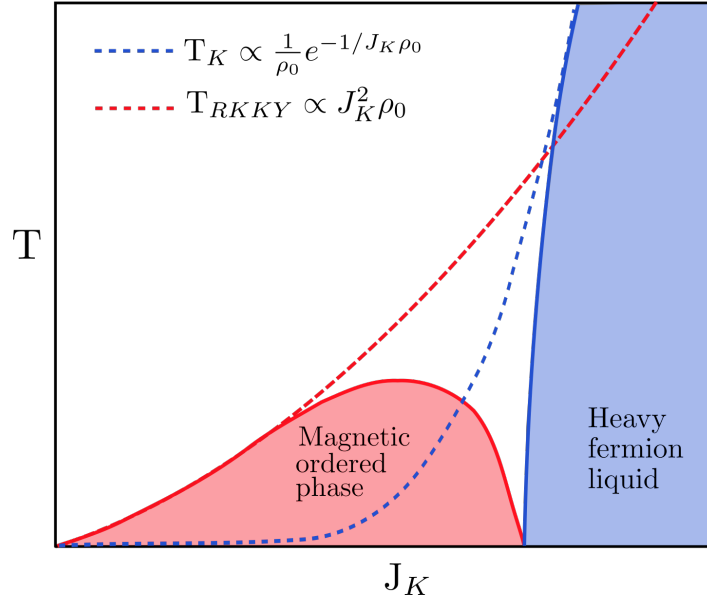


Figure 2.3: Schematic view of Doniach's phase diagram. Blue line indicate Kondo temperature T_K and red line indicate magnetic order temperature scale T_{RKKY} .

magnetically ordered phase from the non-ordered phase. The two separated phases on two sides of QCP compete with each other with similar energy scales, and in its vicinity a non-Fermi liquid behavior [2, 118, 122] can be observed. However, mostly this QCP is hidden by a superconducting dome [24]. The microscopic nature and mechanism of QPT seem an interesting subject to explore, but it remains out of the scope of this thesis.

2.1.2.2 Effect of electronic filling: Nozières's exhaustion problem and coherence formation

The physical properties of the impurity scarce Kondo system can be understood in terms of a single-impurity scenario. However, in lattice systems, a coherent macroscopic Fermi liquid ground state can be realized where localized quantum magnetic impurities contribute to the formation of non-local, i.e. Bloch waves, fermionic quasiparticle excitations. A question about the mechanism of formation of this coherent Fermi liquid Kondo ground state can be raised when the concentration of magnetic impurities is larger than the concentration of conduction electrons. This was the question of 'exhaustion' raised by Nozières [98, 123]. Photoemission [124] results on Kondo lattice showed that the spectral weights and the Kondo resonance at E_F were inconsistent with the description of the single-impurity model with the temperature scale T_K . Thus, he proposed that there are two energy scales, the Kondo temperature T_K and a coherence temperature T^* lower than T_K . This proposition was discussed in many papers, and authors now agree that the ratio of these two energy scales depends only on the band filling n_c [125–129].

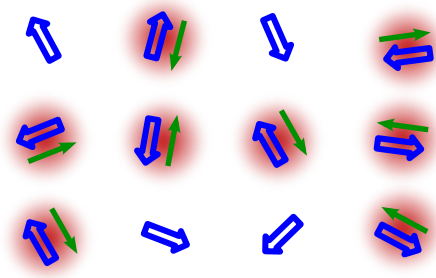


Figure 2.4: Schematic representation of Kondo lattice with impurity concentration x greater than electronic filling n_c in large Kondo coupling scenario. Impurity spins are represented by blue double arrows and conduction electrons are represented by green arrows. Red glow represent the formation of spin-singlet formation between impurity spins and conduction spins screening the local moments.

The formation of the coherence macroscopic phase influences the transport properties. For instance, figure 2.2 shows the resistivity for $\text{Ce}_x\text{La}_{1-x}\text{Cu}_6$. For low Ce concentrations, a saturation of maximum resistivity is observed as $T \rightarrow 0$. For high Ce concentrations, the resistivity gets maximum around coherence temperature T^* , and then it starts to decrease for lower temperatures. The difference in these two behaviors can be understood from the coherence formation in the lattice. At low temperatures, the screened moments become strong scatters, thus the rise in resistivity is observed at first. Below, coherence temperature T^* , coherent scattering of the Kondo singlets takes place with the conservation of momentum, this leads to the decrease of resistivity after a maximum of around T^* . Furthermore, this decrease in resistivity at low temperature shows the characteristic Fermi liquid T^2 dependence.

In the coherent phase, f -electron levels may enter the description of the Fermi surface, which enlarges the Fermi surface. Experimentally, this enlargement of the Fermi surface can be observed from photoemission experiments, for example, the figure 2.5 presents a large Fermi surface of Kondo lattice YbRh_2Si_2 obtained through ARPES for $T < T_K$. Also, at low temperatures, the local density of states at Fermi level $\rho(E_F)$ presents a distinct large peak also known as Kondo resonance [130–132]. In order to understand the coherence formation and the large Fermi surface in Kondo lattice, we should at first consider the case of large Kondo coupling as in the exact strong-coupling treatment [133] of Kondo lattice. Here, we have $N_f = Nx$ number of Kondo impurities on N sites and $N_c = Nn_c$ number of conduction electrons. Since, every conduction electron is bound to an impurity spin, which gives us $N_f - N_c$ number of unscreened impurity spins per site. Knowing this, we can deduce that the conduction electrons can only hop from the impurity bound site to the bachelor impurity site. We could now think the other way around: the effective charge carriers are the holes from the site with the unscreened Kondo spin. In this case, we can deduce that the number of quasiparticles would be $2N_f - (N_f - n_c) = N_f + N_c$, where the two come from spin degeneracy. This also shows that the observation of enlarged

Fermi surface (see figure 2.5) comes from the participation of impurity electron in its formation, as per Luttinger's theorem [134]. A schematic representation is presented in the figure 2.4.

The coherent Fermi liquid phase can also be established from the magnetically ordered ground state in the Kondo lattice. This can be done by increasing the Kondo coupling, applying external pressure. Let's take a concrete example of CeRu_2Ge_2 for the illustration. CeRu_2Ge_2 is ferromagnetic with Curie temperature of 8 K, and Kondo temperature of 1.9 K. This low T_K implies low Kondo coupling J_K . By applying pressure of 76 kbar [118], a complete suppression of magnetically ordered phase is observed, followed by coherent Kondo Fermi liquid phase with enhanced effective masse.

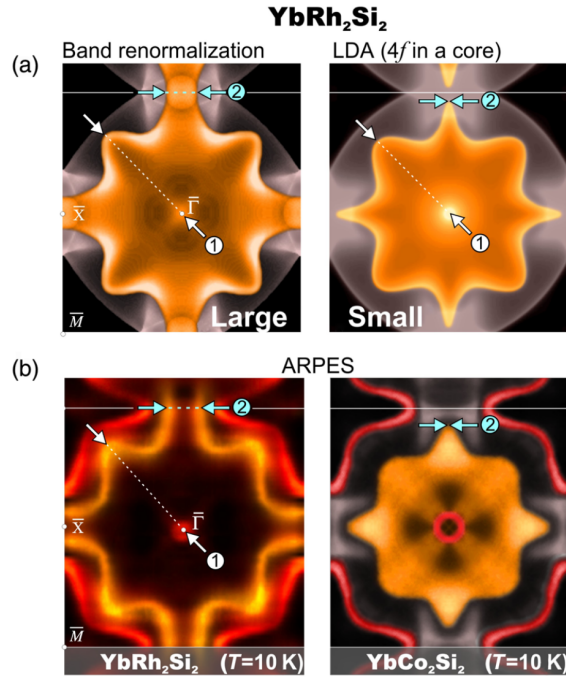


Figure 2.5: Left: large Fermi surface of YbRh_2Si_2 seen through (a) band renormalization calculation and (b) ARPES, where f -electron enter the description of Fermi surface at the temperature $T < T_K$. Right: small Fermi surface of YbCo_2Si_2 (a) LDA calculation and (b) ARPES, at the temperature $T > T_K$. From [135]

2.2 Kondo substitution in Kondo alloys

In Kondo alloys, the number of Kondo impurities can be diminished through the substitution of Kondo atoms with magnetic impurities by non-magnetic atoms. This substitution can break the lattice coherence and can induce change in the Fermi surface structure. In this section, we present different aspects of Kondo substitution related to the lattice coherence and its breakdown.

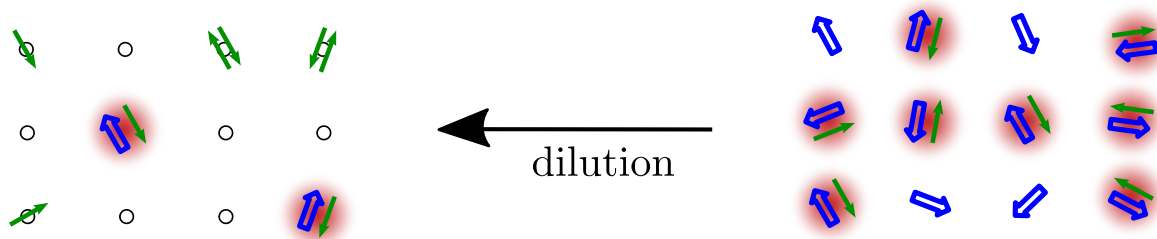


Figure 2.6: Schematic representation of dilution of magnetic impurities. In both case, impurity spin (in blue arrow) forms a spin-singlet with conduction spin, represented by red glow. Right: the conduction electrons hop from singlet site to bachelor site, left: the conduction electrons hops from non-magnetic site to non-magnetic site.

2.2.1 Strong coupling picture

With a description of the large Fermi surface in Kondo lattice obtained, we could now deplete Kondo atoms. This will reduce the number of Kondo impurities N_f while the number of conduction electrons N_c remains the same. When $N_f < N_c$ upon dilution of magnetic impurities, each impurity still captures one conduction electron by forming Kondo singlets. This leaves only $N_c - N_f$ free conduction electrons, which can hop freely only on sites without magnetic impurity. In this case, the Fermi surface contains only $N_c - N_f$ free electrons, thus the Fermi surface is considerably reduced. This scenario is illustrated in the figure 2.6. It has been proposed that the transition between large and small Fermi surfaces happens when $N_f = N_c$ [136].

2.2.2 Weak coupling limit

The theoretical works predict a fundamental difference between dense and dilute Kondo alloys. But, this strong coupling does not represent the experimental reality where Kondo coupling can not be infinity. Thus, one must study the limit of intermediate to weak coupling limit. A study [137, 138] on weak coupling limit was conducted on the Bethe lattice through the adapted version of the statistical DMFT method [139, 140] and with matrix DMFT [141] to treat the Kondo substitution with the disorder. In that study, the neighborhood fluctuations and low dimensionality issues were analyzed through the local potential scatterings, a site-dependent effective local energy level. For weak coupling, local potential scattering showed a smooth crossover from the dilute to dense impurity concentration regime. This was in contrast with the strong coupling picture, where a clear separation of dilute and dense regimes was obtained. Furthermore, for intermediate values of impurity concentration x , the distribution local potential scattering could be found outside the non-interacting electronic bandwidth, showing the possible breakdown of Luttinger's theorem [134].

2.2.3 Experimental realization of lattice coherence breakdown

In order to show the lattice coherence breakdown, let's take the previous example of CeCu_6 (see figure 2.2(b)) where magnetic Ce is substituted by non-magnetic and iso-electronic La atom. In this particular example, one can follow the gradual breakdown of coherence as Ce atoms get depleted by following the resistivity curves. The breakdown of Kondo coherence also marks the change of the Fermi surface from large to small. This is because the singlet forming f -electrons does not participate in the Fermi surface. Similarly, the enhanced effective mass becomes far lesser enhanced.

Substitution of Kondo atoms can also generate pressure effects in addition to the dilution of Kondo impurities. Ce atoms with the ionic radius of 101 pm are slightly smaller than La atoms with the ionic radius of 103.2 pm [142]. Thus Ce-La substitution increases the volume of the cell without altering the lattice structure. The increase in cell volume has the same effect as negative pressure, which decreases J_K and favors the magnetically ordered phase. A concrete example would be the case of $\text{Ce}_x\text{La}_{1-x}\text{Ru}_2\text{Si}_2$ [119] series where only 8% of Ce substitution generates a phase transition from coherent Kondo to antiferromagnetic phase.

In addition to cell volume change, the Kondo substitution can generate substitutional disorder. This disorder can also be responsible for the breakdown of Kondo coherence, along with phase transition from coherent Kondo magnetically ordered phase or to a single-impurity local Fermi liquid regime. Non-Fermi liquid behavior [2], a deviation from Fermi liquid properties, can be observed in disordered f -electron system with substitution [143]. In disordered Kondo system $\text{Ce}_x\text{La}_{1-x}\text{Ni}_2\text{Ge}_2$ [101] series, no magnetic ordering was observed upon magnetic dilution, but the coherent Fermi liquid in dense Kondo regime get replaced by the non-Fermi liquid state before local Fermi liquid state at the very dilute regime. The disorder may be one of the possible origins of this non-Fermi liquid behavior, without ignoring the fact the non-Fermi liquid behavior can appear in the vicinity of magnetic phase transition.

Kondo substitution can also break the ground-state magnetic phase present in many Kondo lattices like antiferromagnetism in CeCu_2Ge_2 [144] or ferromagnetism like in CeRu_2Ge_2 [118] ground-state. For instance, the substitution in CeCu_2Ge_2 [100] series found that the antiferromagnetic phase survives up to dilution state with $x \approx 0.8$ and further dilution $x \approx 0.03$ led to single-impurity behavior. Similar results were seen on $\text{Ce}_x\text{La}_{1-x}\text{Ni}_2\text{Ge}_2$ [101] series at very dilute case, even though CeNi_2Ge_2 has a paramagnetic ground-state. Compiling all the observations, we can deduce the following possible scenarios with substitution: coherent paramagnetic Kondo phase (dense Kondo) leading to single-impurity Kondo regime, coherent paramagnetic Kondo phase to magnetically ordered phase, coherent paramagnetic Kondo phase to non-Fermi liquid phase to single-impurity Kondo regime, magnetically ordered phase to single-impurity Kondo regime.

2.3 Motivations and objectives

Crucial differences between dilute and dense regimes were observed through DMFT on Bethe lattice at strong coupling regime [136, 141], through finite-size calculations [145], Monte Carlo simulations [146–148], numerical renormalization group [149], or local-moment approach [150, 151] and also through statistical DMFT by analyzing local potential scatterings [137]. However, these studies lacked a systematic study of the Fermi surface with the depletion of Kondo atoms which we will be addressing in this work. Also, in this thesis, we will consider the possibility of having a magnetically ordered phase in order to verify Doniach’s argument with Kondo substitution. For this particular study, we will consider 1D, 2D, and 3D systems. The possible experimental signatures of coherence breakdown between dilute and dense Kondo regimes through photoemission will be also analyzed on 2D system. We also analyze local potential scattering and the possibility of charge ordering. More importantly, each of our studies will be considered with the possibility of having experimental realizations. This part is organized as follows:

The next chapter 3 is dedicated to the methodical and numerical aspect of Kondo alloys. There, we present two matrix DMFT methods: one for the paramagnetic Kondo phase and the other for the magnetically ordered phase. The DMFT method for the magnetically ordered phase is one of the original works of this thesis, which can be seen as an extension of previous DMFT [5] and matrix DMFT [141]. Again, in this chapter, we will present our approach to decouple the Kondo interactions and the numerical algorithm.

Chapter 4 present the results concerning the magnetic phase diagram of Kondo alloys upon substitution using DMFT. The pertinence of our results will be compared with experimental data of cerium-lanthanum substitution and with Doniach’s picture.

Chapter 5 will be the core chapter of this part where we search various signatures of lattice coherence breakdown through photoemission. Systematic studies will be done with magnetic impurity concentration x , electronic filling n_c , and the Kondo coupling strength T_K . We will analyze the Fermi surfaces, the effective masses, density of states, and the ARPES derived bands along with the disorder effect.

In chapter 6, we present and analyze our results on local potential scattering and charge order. This chapter has two motivations: one to produce the pertinence of our results with previous studies [137, 138] and the other to support the results obtained in the chapter 5 for coherence breakdown.

Chapter 7 resumes this study and presents the future perspectives.

Chapter 3

Model, method and approximations

This chapter is dedicated to the theoretical aspects of Kondo alloys. First, we start with the presentation of our model Hamiltonian, followed by the dynamical mean-field theory, which treats the disorder. Thereafter, we derive our self-consistent equations through mean-field approximations on Kondo interaction, and finally, we present our method of their numerical resolution.

3.1 The Kondo alloy model

We consider the Kondo alloy model (KAM)

$$\mathcal{H} = \sum_{ij\sigma} (t_{ij} - \mu\delta_{ij}) c_{i\sigma}^\dagger c_{j\sigma} + J_K \sum_{i \in \mathcal{K}} \mathbf{S}_i \mathbf{s}_i, \quad (3.1)$$

where $c_{i\sigma}^{(\dagger)}$ corresponds to annihilation (creation) operators for conduction electrons on a site i with spin $\sigma = \uparrow, \downarrow$. $J_K > 0$ is the local Kondo antiferromagnetic interaction between the local spin density of conduction electrons \mathbf{s}_i , and quantum spin 1/2 operators \mathbf{S}_i representing Kondo impurities. The Kondo impurities are distributed randomly with a site concentration x on a sub-part Kondo-sites \mathcal{K} of the periodic lattice with N sites. The complementary non-Kondo sites, with concentration $1 - x$, will be denoted \mathcal{N} . μ is the chemical potential fixing the electronic filling n_c per site. Despite the disordered nature of Kondo alloys, the nearest-neighbor inter-site electronic hopping energy t_{ij} remains constant, $t_{ij} = t$, respectively from the random nature \mathcal{K} or \mathcal{N} of sites i and j . In this model, each local Kondo spin describes a local $4f^1$ electronic state (Ce-based materials) or a $4f^{13}$ hole state (Yb-based materials) with fixed valence. Thus, every \mathcal{K} -site will have exactly one impurity.

3.2 Treatment of disorder due to Kondo impurity substitution

The Eq. (3.1) describes the randomness of the distribution of Kondo atoms during Kondo substitutional. Thus, an appropriate method is required to treat the disorder generated due to substitutional randomness. In our case, we have opted dynamical mean-field theory [5] method. However, below we present a short selection of available methods.

3.2.1 An overview of methods

Multiple methods can take account of disorder presence in alloys and depends upon the considered systems. For example, exact diagonalization [152, 153] works only for small systems. Density-matrix renormalization group [154] is efficient to obtain the low-energy properties for low-dimensional systems. We can also note real-space variational Gutzwiller wave functions [155], quantum monte carlo [156] methods, and Hartree-Fock based diagonalization [157] can be used to simulate disordered systems. And finally, there is dynamical mean-field theory [5, 141] which we will be using in this part of this thesis.

3.2.2 A brief introduction to dynamical mean-field theory (DMFT)

A simple but effective mean-field theory can be employed in order to have a qualitative insight into physical properties. A well-known mean-field approach is the Weiss mean-field theory, which is a static mean-field approach. However, the static mean-field approximations are unable to capture a complete picture of the effect of correlations and also suffer from drawbacks [158]. This leads us to a dynamical mean-field theory (DMFT) where the fluctuation due to correlations are treated dynamically. The conceptual DMFT framework was developed Metzner and Vollhardt [159], Kotliar and Georges [160]. Later DMFT was applied to numerous correlated models describing strongly correlated systems [5].

DMFT makes use of infinite dimension or coordination $d, Z = \infty$ where a model defined in a lattice is reduced to a single site local problem embedded into a dynamical mean-field generated by other fermions. In DMFT, the mean-field is dynamical, and the quantum fluctuations are taken into account at the local level. In SCES, DMFT is a very versatile method that can be used to study the effect of coupling, electronic fillings, densities, and temperature on a system. It has been used extensively and has been successful to study Metal insulator transitions [5, 161, 162], disorder [149, 163–167], to generate phase diagrams and ARPES properties [81]. For a much better accurate understanding of electronic properties in real materials, the DMFT method has also been combined with ab-initio methods [6, 81]. This com-

bined method DFT+DMFT has been used extensively in real materials study [82, 83].

3.2.3 Matrix DMFT/CPA

In this part of this chapter, we will extend the matrix DMFT/CPA formalism initially developed in [5, 141] to treat the effect of randomness and disorder in binary Kondo alloys with a possibility to include the magnetically ordered (MO) phases. One of the key points of our approach is that it permits us to investigate disorder in Kondo alloys at finite temperature, whereas is not possible in a static mean-field approach. At first, we will start by detailing the matrix DMFT/CPA formalism for the paramagnetic phase. Thereafter, we explain matrix DMFT formalism for a bipartite system for Néel ordered antiferromagnetic phase.

3.2.3.1 Paramagnetic Kondo phase

In this section, we detail our matrix DMFT/CPA formalism to treat paramagnetic Kondo phase for Kondo alloys which was initially developed in [141]. In order to capture the alloying effect, we remap the single local site scheme [5] into two local site problems which can be either Kondo site (\mathcal{K} -site) or non-Kondo site (\mathcal{N} -site). This gives us the Eq. (3.1) as

$$\mathcal{H} = \sum_{ij\sigma} (t_{ij} - \mu\delta_{ij}) c_{i\sigma}^\dagger c_{j\sigma} + J_K \sum_{i \in \mathcal{K}} \mathbf{S}_i \mathbf{s}_i . \quad (3.2)$$

The term on the right-hand side of the Eq. (3.2) represents local Kondo impurities on a fixed subset \mathcal{K} (Kondo) of lattice sites, which have been randomly distributed with a site concentration x . To take account of all the configurations, we introduced the projection operators as $\mathbf{P}_i^\dagger = \begin{pmatrix} \hat{x}_i & \hat{y}_i \end{pmatrix}$ and $\mathbf{P}_i = \begin{pmatrix} \hat{x}_i \\ \hat{y}_i \end{pmatrix}$, where $\hat{x}_i = 1 - \hat{y}_i$ equals to 1 if i is an \mathcal{K} -site site or '0' otherwise. These projection operators make possible to take account of various configuration possibilities between Thus, we rewrite the KAM Eq. (3.2) as

$$H = \sum_{ij\sigma} \gamma_{ij} \mathbf{P}_i^\dagger \mathbf{W} \mathbf{P}_j c_{i\sigma}^\dagger c_{j\sigma} + J_K \sum_i \hat{x}_i \mathbf{S}_i \mathbf{s}_i , \quad (3.3)$$

where $\mathbf{W} = \begin{pmatrix} t & t \\ t & t \end{pmatrix}$ is transfer matrix. γ_{ij} is the structure factor of the underlying periodic lattice such that the non-interacting dispersion is given by $\epsilon_{\mathbf{k}} = \sum_{ij} \gamma_{ij} t_{ij} e^{i\mathbf{k}(\mathbf{R}_j - \mathbf{R}_i)}$. Furthermore, we can write the action corresponding to the Eq. (3.3)

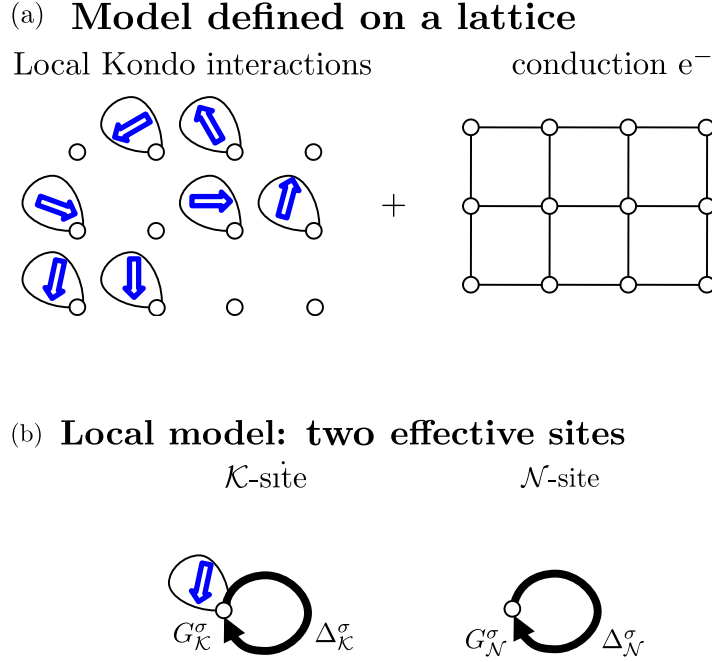


Figure 3.1: Schematic view of matrix-DMFT approach of mapping a lattice problem (a) into a two local site local problem (b).

$$S = - \sum_{ij\sigma} \int_0^\beta d\tau c_{i\sigma}^\dagger(\tau) \{ \gamma_{ij} \mathbf{P}_i^\dagger \mathbf{W} \mathbf{P}_j - (\partial_\tau - \mu) \delta_{ij} \} c_{j\sigma}(\tau) - J_K \sum_i \int_0^\beta d\tau \hat{x}_i \mathbf{S}_i(\tau) \mathbf{s}_i(\tau). \quad (3.4)$$

In the above equation, $c_{i\sigma}^\dagger(\tau)$ and $c_{j\sigma}(\tau)$ are Grassmann variables which follows anti-commutation relation, but they aren't fermionic operators as in 3.3 while τ represents imaginary time. Equally, we write the partition function related to the action (3.4) as

$$\mathcal{Z} = \Pi_i \text{Tr}_i[\mathcal{T}_\tau e^S], \quad (3.5)$$

where \mathcal{T}_τ describes chronological order in imaginary time variable. Following DMFT formalism, the next step to map the lattice problem into a two local sites effective problem as in figure 3.1.

3.2.3.1.1 Local effective action and cavity method Here, a local site can be either \mathcal{K} -site or \mathcal{N} -site which is tagged by the index a . The action (3.4) can be further split

into two different parts as $S = S_{loc}^a + S^{(a)}$

$$\begin{aligned}
 S &= S_{loc}^a + S^{(a)} \\
 &= - \sum_{\sigma} \int_0^{\beta} d\tau c_{a\sigma}^{\dagger}(\tau) (\partial_{\tau} - \mu) c_{a\sigma}(\tau) - J_K \int_0^{\beta} d\tau \hat{x}_a \mathbf{S}_a(\tau) \mathbf{s}_a(\tau) \\
 &\quad - \sum_{j\sigma} \int_0^{\beta} d\tau \{ \gamma_{aj} \mathbf{P}_a^{\dagger} \mathbf{W} \mathbf{P}_j c_{a\sigma}^{\dagger}(\tau) c_{j\sigma}(\tau) + \gamma_{ja} \mathbf{P}_j^{\dagger} \mathbf{W} \mathbf{P}_a c_{j\sigma}^{\dagger}(\tau) c_{a\sigma}(\tau) \} + S^{(a)}. \quad (3.6)
 \end{aligned}$$

(3.7)

The term S_{loc}^a includes all the interactions including the local site a and the cavity term $S^{(a)}$ include all the contributions that are not taken account by the term S_{loc}^a . The partition function is expressed as $\mathcal{Z} = e^{\beta \mathcal{F}^{(a)}} \text{Tr}_a [\mathcal{T}_{\tau} e^{S_{loc}^a}]$, where $\mathcal{F}^{(a)} = \frac{1}{\beta} \ln(\prod_{i \neq a} \text{Tr}_i [e^{S^{(0)}}])$ is the free energy in the presence of the cavity. The term S_{loc}^a is rewritten as

$$S_{loc}^a = \sum_{\sigma} \int_0^{\beta} d\tau c_{a\sigma}^{\dagger}(\tau) (\partial_{\tau} - \mu) c_{a\sigma}(\tau) - J_K \int_0^{\beta} d\tau \hat{x}_a \mathbf{S}_a(\tau) \mathbf{s}_a(\tau) + S_{\Delta}, \quad (3.8)$$

where $S_{\Delta} = \ln \langle \exp(- \sum_{j\sigma} \int_0^{\beta} d\tau \{ \gamma_{aj} \mathbf{P}_a^{\dagger} \mathbf{W} \mathbf{P}_j c_{a\sigma}^{\dagger}(\tau) c_{j\sigma}(\tau) + \gamma_{ja} \mathbf{P}_j^{\dagger} \mathbf{W} \mathbf{P}_a c_{j\sigma}^{\dagger}(\tau) c_{a\sigma}(\tau) \}) \rangle_{(a)}$, with $\langle \dots \rangle_{(a)}$ denotes average value in the presence of the cavity.

3.2.3.1.2 Limit of infinite coordination number ($z = \infty$) The next step is to evaluate the newly expressed dynamical local bath term S_{Δ} in the limit of large coordination (z) number. In the limit of infinite dimensions or, equivalently, of infinite coordination number $z \rightarrow \infty$, DMFT becomes exact as a mean-field theory in classical statistical mechanics. In this case, one can neglect spatial fluctuation in the system, considering only on-site dynamical fluctuations.

So at first, we rescale the hopping parameter as $\tilde{t}_{ij} = \frac{t_{ij}}{\sqrt{z}}$ in order to have finite average kinetic energy in this limit [168]. Similarly, the transfer matrix \mathbf{W} will be also rescaled as $\tilde{\mathbf{W}} = \mathbf{W}/\sqrt{z}$. Now, the average value $\langle \dots \rangle_{(a)}$ is calculated by cumulant development as $S_{\Delta} = \sum_{n=1}^{\infty} \frac{C_n}{n!}$.

The first order cumulant is the average value of the expression (3.8) and since the average value Grassmann variables $\langle c_{j\sigma}(\tau) \rangle = 0$ and $\langle c_{j\sigma}^{\dagger}(\tau) \rangle = 0$ due to the disorder nature of the phase, the $C_1 = - \sum_{j\sigma} \int_0^{\beta} d\tau \{ \mathbf{P}_a^{\dagger} \tilde{\mathbf{W}} \mathbf{P}_j c_{a\sigma}^{\dagger}(\tau) \langle c_{j\sigma}(\tau) \rangle + \mathbf{P}_j^{\dagger} \tilde{\mathbf{W}} \mathbf{P}_a \langle c_{j\sigma}^{\dagger}(\tau) \rangle c_{a\sigma}(\tau) \} = 0$ and equally all the impair order terms $C_{2n+1} = 0$. Furthermore, the pair order terms $C_{2n} \sim 1/z^{n-1}$ when $z \rightarrow \infty$. Thus, the dynamical bath term can be expressed as

$$\begin{aligned}
 S_{\Delta} &= \frac{1}{2} = - \int_0^{\beta} \partial\tau \int_0^{\beta} \partial\tau' \sum_{ij\sigma} \gamma_{ai} \gamma_{ja} c_{a\sigma}^{\dagger}(\tau) \mathbf{P}_a^{\dagger} \tilde{\mathbf{W}} \langle \mathbf{P}_i \mathbf{P}_j^{\dagger} c_{i\sigma}(\tau) c_{j\sigma}^{\dagger}(\tau') \rangle_{(a)} \tilde{\mathbf{W}} \mathbf{P}_a c_{a\sigma}(\tau') \\
 &= - \int_0^{\beta} \partial\tau \int_0^{\beta} \partial\tau' \sum_{\sigma} c_{a\sigma}^{\dagger}(\tau) \mathbf{P}_a^{\dagger} \Delta_a^{\sigma}(\tau - \tau') \mathbf{P}_a c_{a\sigma}(\tau'), \quad (3.9)
 \end{aligned}$$

where $\Delta_a^{\sigma}(\tau - \tau') = \sum_{ij} \gamma_{ai} \gamma_{ja} \tilde{\mathbf{W}} \langle \mathbf{P}_i \mathbf{P}_j^{\dagger} c_{i\sigma}(\tau) c_{j\sigma}^{\dagger}(\tau') \rangle_{(a)} \tilde{\mathbf{W}} = \sum_{ij} \tilde{\mathbf{W}} \mathbf{G}_{ij}^{(a)} \tilde{\mathbf{W}}$ is the dynamical local bath.

3.2.3.1.3 Determination of dynamical local bath and local action Here, we define a Green's function as $G_{ij}^{\sigma}(\tau - \tau') = -\langle T_{\tau} c_{i\sigma}^{\dagger}(\tau) c_{j\sigma}(\tau') \rangle$. Thus, the next step of this formalism to establish an expression of dynamical local bath $\Delta_a^{\sigma}(\tau - \tau')$. To do so, we need to redefine the Green's function in the presence of the cavity to the Green's function without the cavity. For that, we do a diagrammatic expansion of the cavity correlation function along with all the paths and excluding the paths passing through site a . We also define a local propagator $\Pi_{ii}^{\sigma}(\tau - \tau')$ which contains all the local correlations. With the help of Fourier transform as $G(\tau - \tau') = \frac{1}{\beta} \sum_{i\omega_n} e^{-i\omega_n(\tau - \tau')} G(i\omega_n)$, all the Green's function as well as local propagators can be expressed in terms of fermionic Matsubara frequencies.

Since, we treat a paramagnetic phase and both $G_{ij}^{\sigma}(i\omega)$ and the local propagator $\Pi_{ii}^{\sigma}(i\omega)$ are diagonals on spin, we omit the spin index. We also escape $i\omega$ from now in order to simplify the reading. We express the correlation Green function G_{ij}^{σ} with the sum of all the direct paths leading $i \rightarrow j$ as

$$G_{ij} = \sum_{\text{all paths}} \Pi_{ii} \gamma_{ii_1} \mathbf{P}_{i_1}^{\dagger} \tilde{\mathbf{W}} \mathbf{P}_{i_1} \Pi_{i_1 i_2} \gamma_{i_1 i_2} \mathbf{P}_{i_2}^{\dagger} \tilde{\mathbf{W}} \mathbf{P}_{i_2} \dots \Pi_{i_p i_{p-1}} \gamma_{i_{p-1} i_p} \mathbf{P}_{i_p}^{\dagger} \tilde{\mathbf{W}} \mathbf{P}_{i_p} \Pi_{i_p j} \mathbf{P}_{ij}, \quad (3.10)$$

We introduced site-dependent Green's function matrix as

$$\mathbf{P}_i G_{ij} \mathbf{P}_j^{\dagger} = \begin{pmatrix} \hat{x}_i \hat{x}_j G_{ij} & \hat{x}_i \hat{y}_j G_{ij} \\ \hat{y}_i \hat{x}_j G_{ij} & \hat{y}_i \hat{y}_j G_{ij} \end{pmatrix}. \quad (3.11)$$

Multiplying the Eq. (3.10) by \mathbf{P}_i on left side and \mathbf{P}_j^{\dagger} on the right side and by taking the average over disorder denoted by $\langle \dots \rangle_{dis}$, we get

$$\langle \mathbf{G}_{ij} \rangle_{dis} = \langle \mathbf{P}_i G_{ij} \mathbf{P}_j^{\dagger} \rangle_{dis} = \sum_{\text{all paths}} \langle \mathbf{P}_i \Pi_{ii} \gamma_{ii_1} \mathbf{P}_{i_1}^{\dagger} \tilde{\mathbf{W}} \mathbf{P}_{i_1} \Pi_{i_1 i_2} \gamma_{i_1 i_2} \mathbf{P}_{i_2}^{\dagger} \tilde{\mathbf{W}} \mathbf{P}_{i_2} \dots \Pi_{i_p i_{p-1}} \gamma_{i_{p-1} i_p} \mathbf{P}_{i_p}^{\dagger} \tilde{\mathbf{W}} \mathbf{P}_{i_p} \Pi_{i_p j} \mathbf{P}_{ij} \rangle_{dis}. \quad (3.12)$$

Since we consider only direct paths connecting $i \rightarrow j$ and a site can be either \mathcal{K}

or \mathcal{N} -site, the above-average value \mathbf{G}_{ij} lead to

$$\langle \mathbf{G}_{ij} \rangle_{dis} = \sum_{allpaths} \Pi_0 \gamma_{ii_1} \tilde{\mathbf{W}} \Pi_0 \gamma_{i_1 i_2} \tilde{\mathbf{W}} \dots \Pi_0 \gamma_{i_p j} \tilde{\mathbf{W}} \Pi_0, \quad (3.13)$$

with $\Pi_0 = \langle \mathbf{P}_i \Pi_{ii} \mathbf{P}_i^\dagger \rangle_{dis}$. From the diagrammatic expansion, one can obtain a Dyson like equation as (see appendix B.1)

$$\langle \mathbf{G}_{ij} \rangle_{dis} = \Pi_0 (\delta_{ij} + \sum_l \gamma_{il} \mathbf{W} \langle \mathbf{G}_{lj} \rangle_{dis}). \quad (3.14)$$

3.2.3.1.4 Local Green's function We introduce disordered-averaged local Green's matrix as

$$\mathbf{G}_{loc} = \langle \mathbf{G}_{ii} \rangle_{dis} = \begin{pmatrix} x G_{\mathcal{K}} & 0 \\ 0 & (1-x) G_{\mathcal{N}} \end{pmatrix}, \quad (3.15)$$

where $G_{\mathcal{K}}$ and $G_{\mathcal{N}}$ are the local Green's functions for site \mathcal{K} and \mathcal{N} -site respectively. Further, we define the Green's function in reciprocal \mathbf{k} space through Fourier transform as $\mathbf{G}_{\mathbf{k}} = \sum_{\mathbf{k}} \langle \mathbf{G}_{ij} \rangle_{dis} e^{i\mathbf{k}(\mathbf{R}_j - \mathbf{R}_i)}$. Using the Fourier transform and the Eq. (3.14), we obtain

$$\mathbf{G}_{\mathbf{k}}^{-1} = \Pi_0^{-1} - \mathbf{E}_{\mathbf{k}}, \quad (3.16)$$

where $\mathbf{E}_{\mathbf{k}}$ is dispersion matrix as

$$\mathbf{E}_{\mathbf{k}} = \begin{pmatrix} \epsilon_{\mathbf{k}} & \epsilon_{\mathbf{k}} \\ \epsilon_{\mathbf{k}} & \epsilon_{\mathbf{k}} \end{pmatrix}. \quad (3.17)$$

Furthermore, the transformation of Green's function from imaginary time τ to Matsubara frequency ($i\omega_n$) is obtained through Fourier transformation as $G(\tau - \tau') = \frac{1}{\beta} \sum_{i\omega_n} e^{-i\omega_n(\tau - \tau')} G(i\omega_n)$. Thus, we can now express the local Green's function matrix in terms of Green's function in reciprocal \mathbf{k} space as

$$\mathbf{G}_{loc}(i\omega) = \sum_{\mathbf{k}} \mathbf{G}_{\mathbf{k}}(i\omega), \quad (3.18)$$

where $i\omega_n = i\pi T(2n+1)$ is fermionic Matsubara frequency, while T is the temperature of the system.

$$\mathbf{G}_{loc}(i\omega) = \sum_{\mathbf{k}} \Pi_0^{-1}(i\omega) - \mathbf{E}_{\mathbf{k}}. \quad (3.19)$$

3.2.3.2 Dynamical local bath

Like in the standard DMFT formalism, the relation between local Green's function with cavity and without cavity is expressed as

$$\langle \mathbf{P}_i \mathbf{G}_{ij}^{(a)} \mathbf{P}_j^\dagger \rangle_{dis} = \langle \mathbf{G}_{ij}^{(a)} \rangle_{dis} = \langle \mathbf{G}_{ij} \rangle_{dis} - \langle \mathbf{G}_{ia} \rangle \mathbf{G}_{loc}^{-1} \langle \mathbf{G}_{aj} \rangle_{dis}. \quad (3.20)$$

Inserting the Eq. (3.20) into the equation of dynamical local bath in (3.9)

$$\Delta(i\omega_n) = \sum_{ij} \gamma_{ai} \gamma_{ja} \tilde{\mathbf{W}} \langle \mathbf{G}_{ij}^{(a)} \rangle_{dis} \tilde{\mathbf{W}} - \left(\sum_i \gamma_{ia} \tilde{\mathbf{W}} \langle \mathbf{G}_{ai} \rangle \right) \mathbf{G}_{loc}^{-1} \left(\sum_j \gamma_{ja} \tilde{\mathbf{W}} \langle \mathbf{G}_{aj} \rangle \right). \quad (3.21)$$

From now, we can follow the standard DMFT formalism, and after some straightforward algebraic steps, we obtain

$$\Delta(i\omega) = [[\mathbf{\Pi}_0(i\omega)]^{-1} - [\mathbf{G}_{loc}(i\omega)]^{-1}]. \quad (3.22)$$

3.2.3.2.1 Self-consistent equations At the end, the our self-consistent equation for local Green's matrix becomes

$$\mathbf{G}_{loc}(i\omega) = \sum_{\mathbf{k}} [(i\omega + \mu)\mathbf{I} - \mathbf{K}(i\omega) + \mathbf{G}_{loc}(i\omega)^{-1} - \mathbf{E}_{\mathbf{k}}]^{-1} \quad (3.23)$$

$$= \sum_{\mathbf{k}} [(i\omega + \mu) \begin{pmatrix} 1 & 0 \\ 0 & 1 \end{pmatrix} - \begin{pmatrix} \kappa_{\mathcal{K}} & \kappa_{\mathcal{K}\mathcal{N}} \\ \kappa_{\mathcal{N}\mathcal{K}} & \kappa_{\mathcal{N}} \end{pmatrix} + \begin{pmatrix} xG_{\mathcal{K}} & 0 \\ 0 & (1-x)G_{\mathcal{N}} \end{pmatrix}^{-1} - \begin{pmatrix} \epsilon_{\mathbf{k}} & \epsilon_{\mathbf{k}} \\ \epsilon_{\mathbf{k}} & \epsilon_{\mathbf{k}} \end{pmatrix}]^{-1}, \quad (3.24)$$

where, $\mathbf{K}(i\omega) = \mathbf{\Sigma}(i\omega) + [\mathbf{G}_{loc}(i\omega)]^{-1}$. $\mathbf{\Sigma}(i\omega)$ is self-energy matrix, is related to local propagator $\mathbf{\Pi}_0(i\omega) = i\omega + \mu - \mathbf{\Sigma}(i\omega)$. After some lines of algebraic operations, we get our final results is: where $\det(i\omega) = (i\omega + \mu - \kappa_{\mathcal{K}}(i\omega) + \frac{1}{xG_{\mathcal{K}}(i\omega)} - \epsilon_{\mathbf{k}})(i\omega + \mu - \kappa_{\mathcal{N}}(i\omega) + \frac{1}{(1-x)G_{\mathcal{N}}(i\omega)} - \epsilon_{\mathbf{k}}) - (\kappa_{\mathcal{K}\mathcal{N}}(i\omega) + \epsilon_{\mathbf{k}})^2$ and knowing $\Delta_{\mathcal{K}}(i\omega) = i\omega + \mu - \kappa_{\mathcal{K}}$ and $\Delta_{\mathcal{N}}(i\omega) = i\omega + \mu - \kappa_{\mathcal{N}}$, our three self-consistent equations are :

$$xG_{\mathcal{K}}(i\omega) = \sum_{\mathbf{k}} \frac{1}{\det(i\omega)} (\Delta_{\mathcal{N}}(i\omega) + \frac{1}{(1-x)G_{\mathcal{N}}(i\omega)} - \epsilon_{\mathbf{k}}), \quad (3.25)$$

$$0 = \sum_{\mathbf{k}} \frac{(\kappa_{\mathcal{K}\mathcal{N}} + \epsilon_{\mathbf{k}})}{\det(i\omega)}, \quad (3.26)$$

$$(1-x)G_{\mathcal{N}}(i\omega) = \sum_{\mathbf{k}} \frac{1}{\det(i\omega)} (\Delta_{\mathcal{K}}(i\omega) + \frac{1}{xG_{\mathcal{K}}(i\omega)} - \epsilon_{\mathbf{k}}). \quad (3.27)$$

with

$$\kappa_{\mathcal{KN}}(i\omega) = -\frac{1 - 2x + x(i\omega + \mu - \Sigma_{\mathcal{K}})G_{\mathcal{K}} - (1 - x)(i\omega + \mu)G_{\mathcal{N}}}{xG_{\mathcal{K}} - (1 - x)G_{\mathcal{N}}}, \quad (3.28)$$

where $G_{\mathcal{K}}$ and $G_{\mathcal{N}}$ is obtained from local effective action for \mathcal{K} and \mathcal{N} site.

3.2.3.2.2 Local actions Local Green's functions for $G_{\mathcal{K}}(i\omega)$ \mathcal{K} -sites and for $G_{\mathcal{N}}(i\omega)$ \mathcal{N} -sites are obtained respectively from the local actions below

$$S_{\mathcal{K}} = -\int_0^\beta d\tau \int_0^\beta d\tau' \sum_{\sigma} \partial\tau' c_{\mathcal{K}\sigma}^\dagger(\tau) ((\partial_t - \mu)\delta(\tau - \tau') + \Delta_{\mathcal{K}}^\sigma(\tau - \tau')) c_{\mathcal{K}\sigma}(\tau'),$$

$$-J_{\mathcal{K}} \int_0^\beta d\tau \mathbf{S}_a(\tau) \mathbf{s}_a(\tau) \quad (3.29)$$

$$S_{\mathcal{N}} = -\int_0^\beta d\tau \int_0^\beta d\tau' \sum_{\sigma} \partial\tau' c_{\mathcal{N}\sigma}^\dagger(\tau) ((\partial_t - \mu)\delta(\tau - \tau') + \Delta_{\mathcal{N}}^\sigma(\tau - \tau')) c_{\mathcal{N}\sigma}(\tau'). \quad (3.30)$$

3.2.3.3 Antiferromagnetic phase

Matrix DMFT/CPA formalism detailed in the previous section (3.2.3) is designed to treat only the paramagnetic Kondo phase. Thus, to take account of the magnetically ordered phase, we have generalized the previous approach. To do so, we consider a bipartite lattice where a unit cell is composed of two lattice sites (see figure 3.2). Thus, we have remapped two local sites schemes to four local site problems (see figure 3.3) belonging to two sub-lattices A or B on a bipartite lattice.

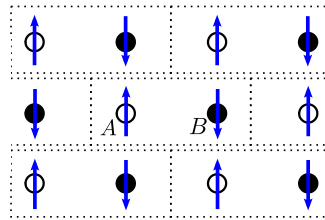


Figure 3.2: Figure illustrating the bipartite nature of the lattice for a Néel ordered antiferromagnetic phase. Dotted rectangle in the figure represent a unit cell composed two lattice sites belonging to each sublattices A and B .

In this new mapping scheme, a local site can be either Kondo (\mathcal{K}) or non-Kondo (\mathcal{N}) marked by index a , and it can either belong to sublattice A or B which is marked by index α . So all together, we have four local site problems (see figure 3.3), which makes it more complex than it was initially. But further, we show that these four local

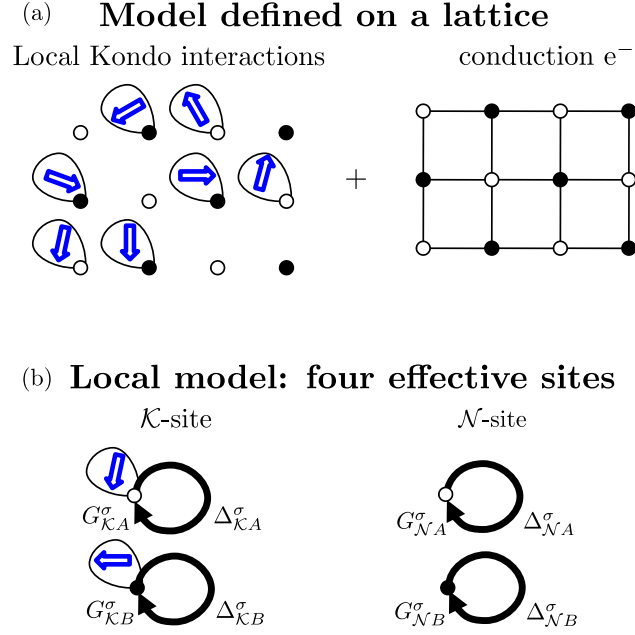


Figure 3.3: Schematic view of the generalized matrix-DMFT approach of mapping a lattice problem (a) onto four effective sites (b) in a bipartite system interacting with dynamical effective local bath in each case, where \bullet denotes sub-lattice A and \circ denotes sub-lattice B, red arrows are Kondo impurity spins, and the black arrows denotes the dynamical local baths.

sites problem can be reduced into two local sites problems, using the symmetries of the phases considered.

3.2.3.4 Local Green's function

The formalism here is similar to that in section (3.2.3) up to average over the disorder of Green's functions. The details of the calculations can be found in the appendix B.1. We rewrite the Dyson-like equation in \mathbf{k} -space

$$\mathbf{G}_{\mathbf{k}\mathbf{k}'}^\sigma = \mathbf{\Pi}_{\mathbf{k}'-\mathbf{k}}^\sigma + \sum_{\mathbf{k}''} \mathbf{\Pi}_{\mathbf{k}''-\mathbf{k}}^\sigma \gamma_{\mathbf{k}''} \mathbf{G}_{\mathbf{k}''\mathbf{k}'}^\sigma. \quad (3.31)$$

Due to the bipartite nature of lattice, we define the local propagator of a site in sublattice A as $\mathbf{\Pi}_A$ and a site in sublattice B as $\mathbf{\Pi}_B$. By considering the bipartite nature of the lattice and developing the expression (3.31) over the Reduced Brillouin zone (RBZ), we get a (4×4) matrix equation

$$\bar{\mathbf{G}}_{\mathbf{k}\mathbf{k}'}^\sigma = \begin{pmatrix} \mathbf{G}_{\mathbf{k}\mathbf{k}'}^\sigma & \mathbf{G}_{\mathbf{k}\mathbf{k}'+\mathbf{Q}}^\sigma \\ \mathbf{G}_{\mathbf{k}+\mathbf{Q}\mathbf{k}'}^\sigma & \mathbf{G}_{\mathbf{k}+\mathbf{Q}\mathbf{k}'+\mathbf{Q}}^\sigma \end{pmatrix} = \left\{ \begin{pmatrix} \mathbf{\Pi}_\sigma^+ & \mathbf{\Pi}_\sigma^- \\ \mathbf{\Pi}_\sigma^- & \mathbf{\Pi}_\sigma^+ \end{pmatrix}^{-1} - \begin{pmatrix} \mathbf{E}_\mathbf{k} & 0 \\ 0 & \mathbf{E}_{\mathbf{k}+\mathbf{Q}} \end{pmatrix} \right\}^{-1} \delta_{\mathbf{k}\mathbf{k}'}, \quad (3.32)$$

where $\Pi_{\sigma}^{+} = \frac{\Pi_N^{\sigma} + \Pi_B^{\sigma}}{2}$ and $\Pi_{\sigma}^{-} = \frac{\Pi_N^{\sigma} - \Pi_B^{\sigma}}{2}$ and $\mathbf{k}\mathbf{k}' \in \text{RBZ}$ and \mathbf{Q} is order vector of considered phase. $\bar{\mathbf{G}}_{\mathbf{k}\mathbf{k}'}$ is a tensor with it's each element is a (2×2) matrix. The details of the calculations to obtain the Eq. (3.32) can be found in the appendix B.2.

Similarly, we have two disordered-averaged local Green's matrix for two sublattices A and B as $\mathbf{G}_{loc,A}^{\sigma}$ and $\mathbf{G}_{loc,B}^{\sigma}$ respectively. From these two (2×2) local Green's matrices, we define a (4×4) local Green's matrices as

$$\bar{\mathbf{G}}_{loc}^{\sigma} = \begin{pmatrix} \mathbf{G}_{loc,A}^{\sigma} & \mathbf{0} \\ \mathbf{0} & \mathbf{G}_{loc,B}^{\sigma} \end{pmatrix}. \quad (3.33)$$

Here, the unit cell is two times larger than the original, thus the Brillouin zone is reduced by two folds. So expanding the over \mathbf{k} to reduced Brillouin zone (RBZ), we get

$$\mathbf{G}_{loc,A}^{\sigma} = \frac{1}{N} \sum_{\mathbf{k} \in \text{RBZ}} \{ \mathbf{G}_{\mathbf{k}\mathbf{k}}^{\sigma} + \mathbf{G}_{\mathbf{k}\mathbf{k}+\mathbf{Q}}^{\sigma} + \mathbf{G}_{\mathbf{k}+\mathbf{Q}\mathbf{k}}^{\sigma} + \mathbf{G}_{\mathbf{k}+\mathbf{Q}\mathbf{k}+\mathbf{Q}}^{\sigma} \}, \quad (3.34)$$

$$\mathbf{G}_{loc,B}^{\sigma} = \frac{1}{N} \sum_{\mathbf{k} \in \text{RBZ}} \{ \mathbf{G}_{\mathbf{k}\mathbf{k}}^{\sigma} - \mathbf{G}_{\mathbf{k}\mathbf{k}+\mathbf{Q}}^{\sigma} - \mathbf{G}_{\mathbf{k}+\mathbf{Q}\mathbf{k}}^{\sigma} + \mathbf{G}_{\mathbf{k}+\mathbf{Q}\mathbf{k}+\mathbf{Q}}^{\sigma} \}. \quad (3.35)$$

$$(3.36)$$

Expressing the (4×4) local Green's matrix with the help of the equations (3.34) and (3.35) and (3.32), and with some algebraic calculation (see appendix B.4), we get

$$\bar{\mathbf{G}}_{loc}^{\sigma} = \frac{2}{N} \sum_{\mathbf{k} \in \text{RBZ}} \begin{pmatrix} [[\Pi_A^{\sigma}]^{-1} - \mathbf{E}_{\mathbf{k}} \Pi_B^{\sigma} \mathbf{E}_{\mathbf{k}}]^{-1} & \mathbf{0} \\ \mathbf{0} & [[\Pi_B^{\sigma}]^{-1} - \mathbf{E}_{\mathbf{k}} \Pi_A^{\sigma} \mathbf{E}_{\mathbf{k}}]^{-1} \end{pmatrix}. \quad (3.37)$$

Finally, we deduce the expression for the local Green's matrix as

$$\mathbf{G}_{loc,\alpha}^{\sigma}(i\omega_n) = \frac{2}{N} \sum_{\mathbf{k} \in \text{RBZ}} [\Pi_{\alpha}^{\sigma}(i\omega_n)]^{-1} - \mathbf{E}_{\mathbf{k}} \Pi_{\alpha}^{\sigma}(i\omega_n) \mathbf{E}_{\mathbf{k}}]^{-1}. \quad (3.38)$$

3.2.3.4.1 Determination of dynamical local bath Similarly, as in paramagnetic case, the dynamical local bath is for bipartite lattice is expressed as

$$\Delta^{\sigma} = \sum_{ij} \gamma_{i\alpha} \gamma_{\alpha j} \mathbf{W} \langle \mathbf{G}_{ij}^{(\alpha)} \rangle_{dis} \mathbf{W}. \quad (3.39)$$

Here, a cavity site can belongs to either sublattice A or B tagged by index α . As before, we define (4×4) dynamical local bath matrix as

$$\bar{\Delta} = \begin{pmatrix} \Delta_A^\sigma & \mathbf{0} \\ \mathbf{0} & \Delta_B^\sigma \end{pmatrix}. \quad (3.40)$$

Knowing the relation $\langle \mathbf{G}_{ij}^{(\alpha)} \rangle_{dis} = \langle \mathbf{G}_{ij} \rangle_{dis} - \langle \mathbf{G}_{i\alpha} \rangle \mathbf{G}_{loc}^{-1} \langle \mathbf{G}_{\alpha j} \rangle_{dis}$ which relates the disorder-averaged Green's function to the disorder-averaged Green's function in the presence of the cavity and putting int the expression (3.40) and with some algebraic manipulations (see appendix...), we get

$$\bar{\Delta} = \begin{pmatrix} [\mathbf{\Pi}_A^\sigma]^{-1} & \mathbf{0} \\ \mathbf{0} & [\mathbf{\Pi}_B^\sigma]^{-1} \end{pmatrix} - \begin{pmatrix} [\mathbf{G}_{loc,A}^\sigma]^{-1} & \mathbf{0} \\ \mathbf{0} & [\mathbf{G}_{loc,B}^\sigma]^{-1} \end{pmatrix}. \quad (3.41)$$

The above Eq. (3.41) is further simplified to

$$\Delta^\sigma = [\mathbf{\Pi}_\alpha^\sigma]^{-1} - [\mathbf{G}_{loc,\alpha}^\sigma]^{-1}. \quad (3.42)$$

The detailed step-by-step calculations can be found in the appendix B.5.

3.2.3.4.2 Self-consistent equations In order to study the disordered binary Kondo alloy problem, we need to solve the self-consistent equations numerically. The self-consistent equations are determined from the matrix Eq. (3.38) and are presented below

$$xG_{\mathcal{K}\alpha}^\sigma = \frac{2}{N} \sum_{\mathbf{k} \in \text{RBZ}} \frac{1}{D_{\mathbf{k}}^\sigma} \{ \Delta_{N\alpha}^\sigma + ((1-x)G_{N\alpha}^\sigma)^{-1} - H_{\mathbf{k}\bar{\alpha}}^\sigma \}, \quad (3.43)$$

$$0 = \frac{2}{N} \sum_{\mathbf{k} \in \text{RBZ}} \frac{1}{D_{\mathbf{k}}^\sigma} \{ \kappa_{\mathcal{K}N\alpha}^\sigma + H_{\mathbf{k}\bar{\alpha}}^\sigma \}, \quad (3.44)$$

$$(1-x)G_{N\alpha}^\sigma = \frac{2}{N} \sum_{\mathbf{k} \in \text{RBZ}} \frac{1}{D_{\mathbf{k}}^\sigma} \{ \Delta_{\mathcal{K}\alpha}^\sigma + (xG_{\mathcal{K}\alpha}^\sigma)^{-1} - H_{\mathbf{k}\bar{\alpha}}^\sigma \}, \quad (3.45)$$

where $H_{\mathbf{k}\bar{\alpha}}^\sigma = \frac{\epsilon_{\mathbf{k}}^2}{(\det)_{\bar{\alpha}}^\sigma} (\Delta_{\mathcal{K}\bar{\alpha}}^\sigma + \Delta_{N\bar{\alpha}}^\sigma + (xG_{\mathcal{K}\bar{\alpha}}^\sigma)^{-1} + ((1-x)G_{N\bar{\alpha}}^\sigma)^{-1} + 2\kappa_{\mathcal{K}N\bar{\alpha}}^\sigma)$ and $D_{\mathbf{k}}^\sigma = (\Delta_{\mathcal{K}\alpha}^\sigma + (xG_{\mathcal{K}\alpha}^\sigma)^{-1} - H_{\mathbf{k}\bar{\alpha}}^\sigma)(\Delta_{N\alpha}^\sigma + ((1-x)G_{N\alpha}^\sigma)^{-1} - H_{\mathbf{k}\bar{\alpha}}^\sigma) - (\kappa_{\mathcal{K}N,\alpha}^\sigma + H_{\mathbf{k}\bar{\alpha}}^\sigma)^2$ with

$$\kappa_{\mathcal{K}N\alpha}^\sigma = -\frac{1 - 2x + x(i\omega + \mu - \Sigma_{\mathcal{K}\alpha}^\sigma)G_{\mathcal{K}\alpha}^\sigma - (1-x)(i\omega + \mu)G_{N\alpha}^\sigma}{xG_{\mathcal{K}\alpha}^\sigma - (1-x)G_{N\alpha}^\sigma}. \quad (3.46)$$

3.3 Treatment of local Kondo interaction

Within DMFT formalism, one has to use a local impurity solver to resolve DMFT/CPA self-consistent equations as in section (3.2.3) and (3.2.3.3) representing many-body problem defined by the local effective action on a Kondo site, Eq. 3.29.

3.3.1 An overview of methods

In order to treat an interaction, one needs to choose an adapted impurity solver to that interaction keeping in mind the goal of the study. Each decoupling can have its own advantages like in the continuous-time quantum Monte Carlo method (CTQMC) [169] which is particularly applicable for multiband and time-dependent correlations. CTQMC suffers from potential sign problems and slow convergence. One can also employ density-matrix renormalization group [170, 171] for low dimensional quantum problems. Dynamical cluster approximation [172] is a technique that includes short-ranged dynamical correlations in addition to the local dynamics of the dynamical mean-field approximation while preserving causality. One can also choose the numerical renormalization group approach [173] for quantum impurity systems. There are approximate solvers like non-crossing approximation [174] which are fast but not exact.

Here, we employ mean-field approximations as local impurity solvers to describe both purely magnetically ordered and pure Kondo paramagnetic phases. Indeed, we want to focus on the physical observable like the ARPES and PES signatures of these different phases along with effective masses of quasi-particles that may emerge from the KAM. The aim is to investigate the effect of Kondo alloying and the effect of disorder, focusing on the change in Fermi surface structure via ARPES signatures, decoherence effects, and discontinuity of effective masses. We thus use the Weiss mean-field approximation for MO phases while Kondo mean-field approximation for pure paramagnetic Kondo phase since it was previously successfully used before [105, 113, 126, 138]. Below, we present the two different mean-field approaches.

3.3.2 Magnetically ordered phases: Weiss mean-field approximation

Weiss mean-field channel is used to solve the action (?? while assuming a magnetically ordered phase. We restrict our study to pure ordered phase ignoring the possibility of mixed phases where the Kondo effect and magnetic order might co-exist. Furthermore, we assume that the magnetic order is either ferromagnetic (F) or staggered antiferromagnetic (AF). Invoking the $A \leftrightarrow B$ symmetries of these phases as in table 4.1, the single site effective DMFT/CPA action can be solved assuming this site belongs to the sublattice A . Consequently, hereafter, in this section, we consider only $\alpha = A$, and we omit the α index.

The Kondo interaction is decoupled using the standard Weiss mean-field approximation as $\mathbf{S} \cdot \mathbf{s} \approx \langle S^z \rangle s^z + S^z \langle s^z \rangle - \langle S^z \rangle \langle s^z \rangle$ which leads us to the local magnetizations $m_f \equiv \langle S^z \rangle$, and $m_c \equiv \langle s^z \rangle = \frac{1}{2} \sum_{\sigma} \sigma_z \langle c_{\sigma}^{\dagger} c_{\sigma} \rangle$ as order parameters on a Kondo site belonging to the sublattice A . The local effective action (3.29) becomes quadratic, and the local Green function on a \mathcal{K} -site can be expressed explicitly in terms of the bath and order parameters as

$$G_{\mathcal{K}}^{\sigma}(i\omega) = \frac{1}{i\omega + \mu - \Delta^{\sigma}(i\omega) - \sigma J_K \frac{m_f}{2}}. \quad (3.47)$$

Finally, to complete the general DMFT/CPA self-consistent equations described in section 3.2.3.3 which relate the local Green functions and the dynamical bath, the chemical potential μ and the order parameters m_f and m_c are determined by solving the following self-consistent equations:

$$n_c = x \frac{1}{\beta} \sum_{i\omega} G_{\mathcal{K}\sigma}(i\omega) + (1-x) \frac{1}{\beta} \sum_{i\omega} G_{\mathcal{N}\sigma}(i\omega), \quad (3.48)$$

$$m_c = \frac{1}{2\beta} \sum_{i\omega, \sigma} \sigma G_{\mathcal{K}\sigma}(i\omega), \quad (3.49)$$

$$m_f = -\frac{1}{2} \tanh\left(\frac{\beta m_c J_K}{2}\right). \quad (3.50)$$

These equations (3.48, 3.49, 3.50) are solved self-consistently using the DMFT in order to find the self-consistent solutions for μ , m_f and m_c .

3.3.3 Paramagnetic Kondo phases: "large N" slave-bosons mean-field approximation

Like above, the Kondo interaction is decoupled using mean-field to solve the local effective action on a \mathcal{K} -site, which is given by Eq. (3.29) assuming a paramagnetic Kondo correlated state. We neglect again the possibility that magnetic order might co-exist with Kondo local strong correlations. Consequently, hereafter, in this section, we omit the α sublattice index. We follow the standard mean-field approximation as introduced by Lacroix and Cyrot in ([105]), which is analogous to the "large N" expansion or slave boson approximation developed by Coleman in ([175]) and Read and Newns in ([176]).

At first, we start by representing Kondo spin operator within Abrikosov's fermionic representation $\mathbf{S}^{\sigma\sigma'} = f_{\sigma}^{\dagger} f_{\sigma'} - \delta_{\sigma\sigma'}/2$. Thereafter, the Kondo interaction in Eq. (3.29)

is mapped and decoupled as

$$\mathbf{S} \cdot \mathbf{s} \rightarrow \frac{1}{2} \sum_{\sigma\sigma'} c_{\mathcal{K}\sigma}^\dagger c_{\mathcal{K}\sigma'} f_{\sigma'}^\dagger f_{\sigma} \quad (3.51)$$

$$\approx \frac{1}{2} \sum_{\sigma\sigma'} \langle c_{\mathcal{K}\sigma}^\dagger f_{\sigma} \rangle f_{\sigma'}^\dagger c_{\mathcal{K}\sigma'} + \langle f_{\sigma'}^\dagger c_{\mathcal{K}\sigma'} \rangle c_{\mathcal{K}\sigma}^\dagger f_{\sigma} - \langle f_{\sigma'}^\dagger c_{\mathcal{K}\sigma'} \rangle \langle c_{\mathcal{K}\sigma}^\dagger f_{\sigma} \rangle. \quad (3.52)$$

The mean-field description as in Eq. (3.52) results in an emergent effective hybridization between the conduction electrons and the Abrikosov fermions, $r = \frac{J_K}{2} \sum_{\sigma} \langle c_{\mathcal{K}\sigma}^\dagger f_{\sigma} \rangle$, which can be identified as an order parameter for the Kondo phase. An additional constraint $\sum_{\sigma} f_{\sigma}^\dagger f_{\sigma} = 1$ restricts the number of Abrikosov fermions to one, which are imposed by introducing a Lagrange parameter $\lambda(\tau)$. With the mean-field approximation, λ is assumed to be constant and determined self-consistently in order to satisfy the f occupancy constraint on average.

Since here we are considering the paramagnetic Kondo phase, for the sake of clarity, hereafter we skip the spin index σ . The local effective action (3.29) becomes quadratic and the local Green function on a \mathcal{K} -site can be expressed explicitly in terms of the bath and order parameters as

$$G_{\mathcal{K}}(i\omega) = \frac{1}{i\omega + \mu - \Delta_{\sigma}(i\omega) - \frac{r^2}{i\omega + \lambda}}. \quad (3.53)$$

For a non-Kondo site, the Green function can be obtained directly from the electronic bath Δ

$$G_{\mathcal{N}}^c = \frac{1}{i\omega + \mu - \Delta(i\omega)}. \quad (3.54)$$

The Kondo self-energy involved in Eq. (3.53) thus has a pole singularity $\Sigma_{\mathcal{K}}(i\omega) = \frac{r^2}{i\omega + \lambda}$ which captures several relevant aspects of Kondo physics.

Finally, to complete the general DMFT/CPA self-consistent equations described in section 3.2.3 which relate the local Green functions and the dynamical bath, the chemical potential μ , the order parameter r , and the Lagrange multiplier λ are determined by solving the following self-consistent equations:

$$n_c = x \frac{2}{\beta} \sum_{i\omega} G_{\mathcal{K}}(i\omega) + (1-x) \frac{2}{\beta} \sum_{i\omega} G_{\mathcal{N}}(i\omega), \quad (3.55)$$

$$\frac{r}{J_K} = -\frac{r}{\beta} \sum_{i\omega} \frac{G_{\mathcal{K}}(i\omega)}{i\omega + \lambda}, \quad (3.56)$$

$$1 = \frac{2}{\beta} \sum_{i\omega} \frac{r^2 G_{\mathcal{K}}(i\omega)}{(i\omega + \lambda)^2}. \quad (3.57)$$

In this mean-field description, r is an order parameter for the Kondo param-

agnetic phase. It describes the low temperature magnetic entanglement between conduction electrons and Kondo impurities spins. The Kondo crossover temperature is replaced by a transition at Kondo temperature T_K , defined as the temperature where r continuously vanishes. It can be computed from J_K by solving the equation $\frac{1}{J_K} = -\frac{1}{\beta} \sum_{i\omega} \frac{G_0(i\omega)}{i\omega}$, where $G_0(i\omega)$ is the non-interacting Green's function and is independent on x , as discussed in[141]. The equations (3.55, 3.56, 3.57) are solved self-consistently to find the self-consistent solutions for μ , λ and r .

3.4 Numerical approach and algorithm scheme

Two different DMFT loops were used to solve numerically paramagnetic Kondo phase and magnetically ordered phases as depicted on figures 3.4a and 3.4b respectively. DMFT full self-consistency was obtained using imaginary Matsubara fermionic frequencies to determine the effective dynamical electronic bath and the mean-field order parameters. Due to the constraints over computational power and time-limit, we introduced a cut-off frequency that was taken much larger than the bandwidth of the system, and the finite temperature introduced was taken at least 80 times smaller than T_K . Thus, the solutions described here correspond to the possible ground states.

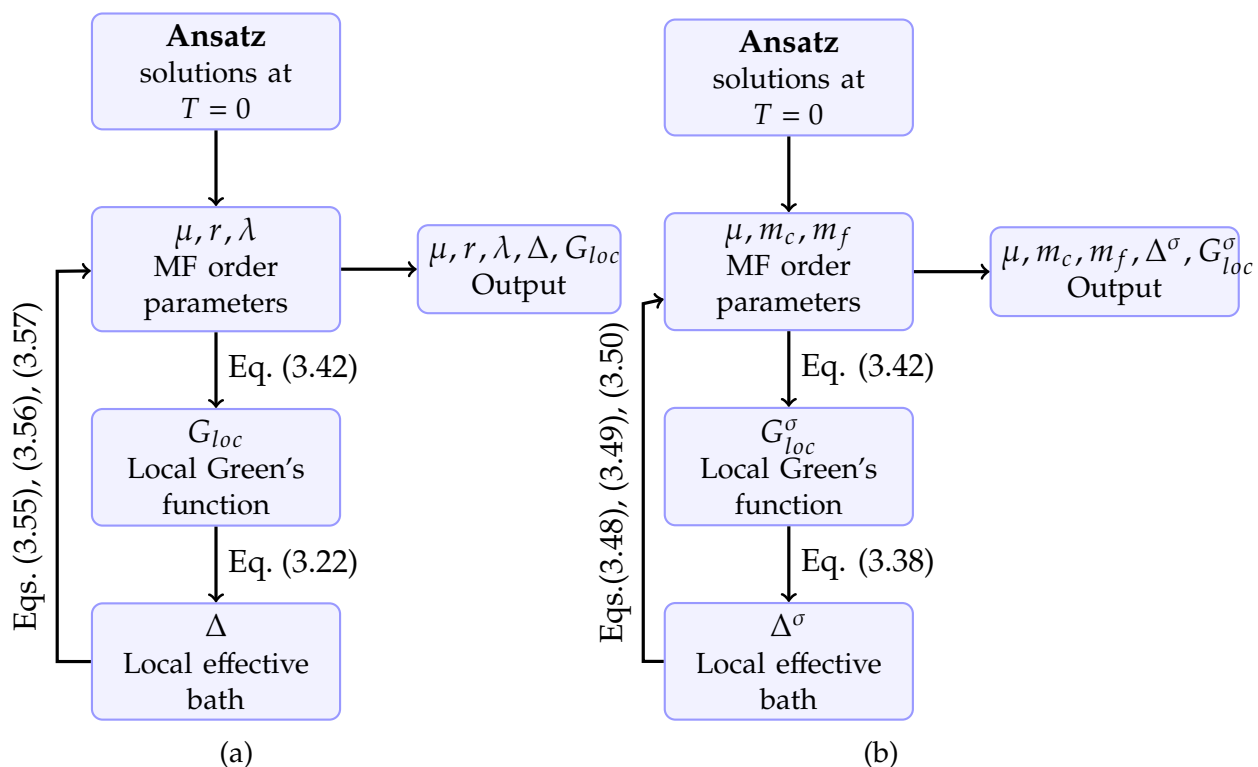


Figure 3.4: (3.4a) DMFT loop for paramagnetic Kondo phase and (3.4b) for magnetically ordered phases

We describe our numerical approach in the following steps below:

- i)* We start with our solution obtained for $T = 0$ as ansatz at $x = 1$ or with the solution obtained when $J_K = 0$.
- ii)* $G_{\mathcal{K},\alpha}^\sigma$ and $G_{\mathcal{N},\alpha}^\sigma$ are actualized from the Eq. (3.42).
- iii)* From the actualized $G_{\mathcal{K},\alpha}^\sigma$ and $G_{\mathcal{N},\alpha'}^\sigma$ we compute new dynamical local bath ($\Delta_\alpha^\sigma(i\omega)$) from Eq. (3.38). We iterate until convergence for the order parameters.
- iv)* We evaluate our new MF orders parameter form the set of equations (3.55,3.56,3.57) or (3.48,3.49,3.50) for a given phase.

Chapter 4

Magnetic phase diagrams of Kondo alloys

Kondo alloys present very rich phase diagrams, and these phase diagrams depend upon various parameters. In this chapter, we analyze experimental and theoretical phase diagrams of Kondo alloys considering three parameters: the Kondo coupling between magnetic impurities and conduction electrons J_K , the electronic filling n_c , and the concentration of magnetic impurities x . At first, we start by presenting the state-of-the-art on both experimental and theoretical aspects of phase diagrams of Kondo alloys. Later, we present and discuss our results on the ground state phase diagrams obtained for Kondo lattice ($x = 1.0$) and with substitution.

4.1 A state of the art

4.1.1 Experimental phase diagrams

Decades of experiments in Kondo alloys revealed that various types of ground states could be stabilized with a large diversity of unconventional quantum phases and behaviors [177]. The unconventional phase includes unconventional superconductivity [178, 179] like in heavy-fermion compound CeCu_2Si_2 [24, 180], heavy-fermion paramagnetic phase, metallic spin-liquid [181] and also non-Fermi liquid phases [2]. They also exhibit more conventional magnetically ordered phases such as antiferromagnetic phases like in CeCu_2Ge_2 [100, 182, 183] or ferromagnetic phase like in CeRu_2Ge_2 [118]. Furthermore, a phase transition can be obtained by the application of pressure or atomic substitution from these conventional or unconventional phases. Below, we present an experimental overview of these parameters on various Kondo alloys.

4.1.1.1 Mechanical pressure as tuning parameter

In chapter 2, we have presented Doniach's argument explaining the stabilization of magnetically ordered phases at low Kondo coupling. This Doniach's argument was verified experimentally for a multitude of Kondo lattices where the Kondo coupling J_K was controlled by applying pressure. The applied pressure can be either external mechanical pressure, negative pressure through hydrogenation, or negative or positive chemical pressure through atomic substitution. The application of external pressure usually reduces the volume of lattice, which consequently increases the Kondo interaction. Thus, this increase in Kondo interaction can yield a phase transition from a magnetic phase to a paramagnetic phase. For instance, application of pressure in Ce-based Kondo alloys like in CeRu_2Ge_2 [118] or in CeAu_2Si_2 [184] changed the magnetically ordered ground state present at atmospheric pressure into heavy-fermion paramagnetic phase. Meanwhile, the scaling of the Kondo temperature [118] was also in good agreement with Doniach's argument. Other than the positive external pressure, a negative pressure also can be applied from hydrogenation. For example, the hydrogenation in CeRuSi [185] led to the transition from paramagnetic heavy-fermion phase to antiferromagnetic phase.

Application of pressure is not limited to magnetic to non-magnetic transition but can also reveal unconventional phases. Indeed, pressure-induced superconductivity was found in Ce based compounds like CeRh_2Si_2 [186], CePtSi_2 [187], CeRhIn_5 [188] or CeNiGe_3 [189] and unusual nonmagnetic ordered state in CeCoSi [190]. Pressure can also induce breakdown of Fermi liquid properties like in CeRu_2Ge_2 [118].

4.1.1.2 Substitution as tuning parameter

In Kondo alloys, one can substitute either the rare-earth atom, transition metal, or metalloid atom. Each of these substitutions can act as a tuning parameter which we will be presenting below.

4.1.1.2.1 Transition metal or metalloid substitution In most cases, Cerium-based Kondo alloys are of type CeT_aX_b where T is a transition metal like Ru and X is a metalloid such as Si or Ge. Apart from rare-earth atoms, in these alloys, we can substitute either a transition metal atom or metalloid atom with another atom of the same group of the periodic table. This substitution can modify the Kondo coupling and the electronic filling at the same time, even though the electronic is difficult to evaluate experimentally. Thus, these substitutions can act as a tuning parameter. An example of a magnetic phase diagram through metalloid substitution is presented in the figure 4.1 where Si atoms are substituted by Ge atoms (extracted from [119]). This Si-Ge substitution generated a cascade of magnetic phase transitions from ferromagnetic to two different antiferromagnetic phases and paramagnetic phase at the end. A cascade of phase transitions is expected with

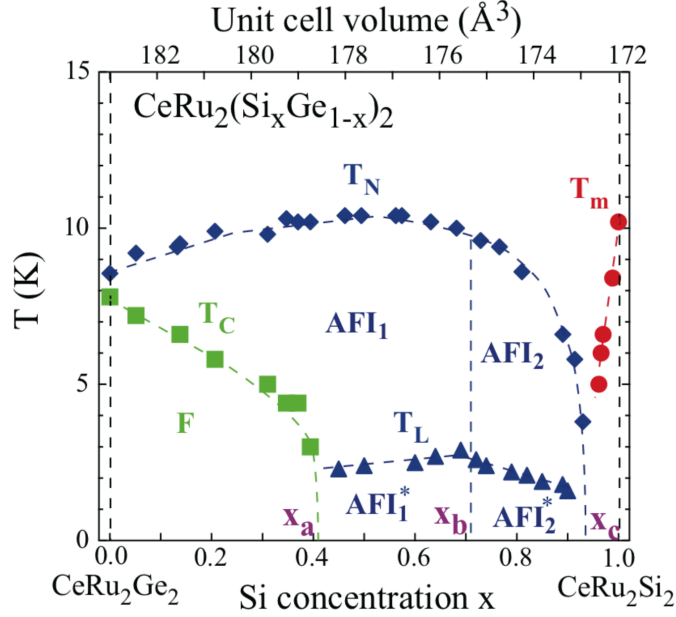


Figure 4.1: Magnetic phase diagram of $\text{CeRu}_2(\text{Si}_x\text{Ge}_{1-x})$. Substitution of Si by Ge increases the unit cell volume. A cascade of magnetic to non-magnetic phase transition is observed for increase Si concentration. From [119]

varying electronic filling (see section 4.3.1). In other experiment, Si-Ge substitution conducted on $\text{CeNi}(\text{Si}_x\text{Ge}_{2-x})$ [191] series led to non-Fermi liquid behavior at the concentration $x = 1$, but globally phase diagram [192] was consistent with Doniach argument. Regarding transition metal substitution, Ru-Co substitution in $\text{CeRu}_{2-x}\text{Co}_x\text{Ge}_2$ [193] showed a smooth crossover from RKKY to Kondo regime with increasing x . Cu-Ni substitution in CeCu_2Si_2 [194] suppressed both antiferromagnetic fluctuations and superconductivity, and it led to a dramatic crossover from the HF regime to the intermediate-valence regime with progressive Ni doping.

4.1.1.2.2 Rare earth metal substitution In Kondo systems, the concentration of Kondo impurities x is another relevant parameter besides the electronic filling n_c and pressure. Continuous tuning of x can be realized experimentally in Kondo alloys heavy-fermions by isostructural substitution of a magnetic rare-earth atom with a non-magnetic one. This induces remarkable changes in macroscopic physical properties, and the dilution of magnetic impurities from the Kondo lattice can yield a phase transition. As La atom is slightly larger than Ce atom, Ce-La isostructural substitution enlarges the crystal volume, thus reducing the Kondo coupling. One can imagine that this reduction of Kondo coupling can lead from paramagnetic phase to magnetic ordered phase transition. Indeed, this was observed for $\text{Ce}_x\text{La}_{1-x}\text{Ru}_2\text{Si}_2$ [119] where the dilution of magnetic impurities led to a phase transition from paramagnetic to magnetically ordered phase. This is not always true since in $\text{Ce}_x\text{La}_{1-x}\text{Cu}_2\text{Ge}_2$ [100] series a phase transition from antiferromagnetic

(AF) to paramagnetic (PM) was observed. Another Ce-La substitution in the series $Ce_xLa_{1-x}Cu_6$ [89, 195] revealed an evolution from coherent dense Kondo lattice regime to dilute Kondo regime whereas in the series $Ce_xLa_{1-x}FePO$ [196] coexistence of spin glass with dilute Kondo regime is observed. Other types of rare-earth substitutions can also unexpected result like Fermi-surface instabilities in unconventional superconductors like $Ce_xYb_{1-x}CoIn_5$ [197] and $Nd_{2-x}Ce_xCuO_4$ [198].

The Fermi liquid properties were seen from resistivity measurements for $Ce_xLa_{1-x}Pt_2Si_2$ [99] and $Ce_xLa_{1-x}Cu_2Ge_2$ [100] series. But in multiple cases, Ce-La substitution led to non-Fermi liquid behavior [122]. Such as for $Ce_xLa_{1-x}Ni_2Ge_2$ [101] and $Ce_xLa_{1-x}PtIn$ [199] series, substitution led to dense-dilute transition along with non-Fermi liquid behavior. In some Ce-La substitution, Fermi liquid properties were not consistent over different physical quantities. This is the case for Ce-La substitution in $Ce_xLa_{1-x}Ni_9Ge_4$ [200, 201] where non-Fermi liquid behavior was observed in specific heat measurements while Fermi liquid behavior in magnetic susceptibility. This raises an additional question about the origin of these non-Fermi liquid behaviors upon dilution. These handfuls of examples clearly show that Ce-La substitution can considerably alter the behavior of physical quantities, which also motivates our study of binary Kondo alloys of this thesis.

4.1.2 Phase diagrams through various theoretical approaches

Another pertinent parameter besides pressure is the electronic filling (n_c). Various theoretical studies revealed Doniach-like phase diagrams [105, 106, 202, 203]. Multiple theoretical techniques were employed in order to explore the effect of n_c for Kondo lattice model (KLM) like for one-dimensional systems by exact diagonalization [129], by density matrix renormalization group [204–206], by a unitary transformation involving a bosonization of delocalized conduction electrons [207], for two-dimensional systems by DMFT with numerical renormalization group [111, 208, 209], cellular dynamical mean-field theory and variational Monte Carlo [210] and by dynamical cluster approach [211] and for three-dimensional systems by mean-field [105]. Some the theoretical studies [109, 212, 213] in Kondo lattice model also pointed out that magnetic order can coexist with Kondo effect.

Important attention was also focused on the issue of coherence in the paramagnetic phase of dense Kondo systems. The robustness of a coherent Kondo state has then been investigated in the framework of the Kondo lattice model by several complementary theoretical approaches [123, 125–129, 133, 214–217].

4.2 Symmetries considerations for numerical calculations

In our study of Kondo alloys, we consider only pure paramagnetic Kondo phase (K), pure ferromagnetic phase (F) or antiferromagnetic (AFII) phase with purely staggered Néel order with ordering vector $\mathbf{Q} = (\pi, \pi)$. Using the DMFT method, the lattice problem has been mapped onto four single-site effective problems that account for the possible local correlations, $a = \mathcal{N}$ or \mathcal{K} , on sublattice $\alpha = A$ or B. For different reasons, in each case, we can restrict the problem to two effective sites.

Transformations	invariance		
	K	F	AFII
$A \rightarrow B$			
$\sigma \rightarrow \bar{\sigma}$	yes	no	yes
$A \rightarrow B$			
$\sigma \rightarrow \sigma$	yes	yes	no
$A \rightarrow A$			
$\sigma \rightarrow \bar{\sigma}$	yes	no	no

Table 4.1: Table that resumes local Green's function invariance according to the transformations for K, F and AFII phases

In table 4.1, we analyze the symmetry properties of the various phases that we consider. Sites A and B are equivalent for Kondo decoupled F and K phases, and there we recover the two effective sites dynamical approach as developed in [141]. As AF phase with Néel order obeys the transformations ($A \rightarrow B, \sigma \rightarrow \bar{\sigma}$), the basis and the Green's function remains invariant through this transformation. Thus, the correlation functions for a site in sublattice A with spin σ are equivalent to the correlation functions for a site in sublattice B with spin $\bar{\sigma}$. Therefore, evaluating Green's functions for a site in sublattice A or B with spin σ and $\bar{\sigma}$ is sufficient to study the AFII phase. So again, we bring back two effective sites dynamical approach instead of four effective sites.

4.3 Results: ground-state phase diagram

In this section, we present and discuss the ground state phase diagrams obtained for periodic Kondo lattice as well as for Kondo alloys for electronic filling $n_c = 0.30, 0.70$ and 0.90 . In each case, the phase diagrams were obtained by comparing the energies of each considered phase. The expressions to compute the energies of each phase are detailed in the appendix A. At First, we studied the phase diagrams for periodic Kondo lattice for 1D 'chain', 2D 'square', and 3D 'cubic' lattices. We reproduced

the existing results, which validated our method. Thereafter, we studied the phase diagrams of Kondo alloys by varying the Kondo atom concentration x .

4.3.1 Tuning of n_c and T_K for periodic Kondo lattice

	\mathbf{Q}_0^{AFI}	\mathbf{Q}_0^{AFII}	\mathbf{Q}_0^{AFIII}
1D	π		
2D	$(\pi, 0)$	(π, π)	
3D	$(0, 0, \pi)$	$(\pi, \pi, 0)$	(π, π, π)

Table 4.2: commensurate AF phases with and their respective wave ordering vectors.

In order to validate our DMFT approach, we calculated the solutions for paramagnetic Kondo phase (K), ferromagnetic phase (F), and commensurate antiferromagnetic phases for periodic 1D ‘chain’, 2D ‘square’ and 3D ‘cubic’ Kondo lattices without using DMFT algorithm at $T = 0$ with varying n_c . We then studied the same problem for the 2D ‘square’ lattice using the DMFT algorithm. We came up with the same results. However, we didn’t calculate the solutions below $n_c < 0.25$ with DMFT because the algorithm becomes more time-consuming. We have equally omitted to evaluate AF I in our DMFT calculations, however, it doesn’t change the qualitative results.

Figure 4.2 shows the phase diagrams obtained for 1D ‘chain’, 2D ‘square’ and 3D ‘cubic’ lattices at $T = 0$ with K, F and AF phases with several commensurate antiferromagnetic phases (see table 4.2). The ground-state phase diagrams are consistent with Doniach’s Phase diagram [104]. Three distinct phases can be seen for 1D lattice with magnetic phase dominates at small $\frac{J_K}{W}$ and Kondo phase is observed at large $\frac{J_K}{W}$. At half-filling, the transition between AF to Kondo phase occurs around $\frac{J_K}{W} \simeq 0.40$, and it gradually decreases with n_c . With decreasing n_c at $n_c \approx 0.62$, transition from AF to F is observed. Further reduction of n_c saturates the ferromagnetic phase, and it is stabilized for low electronic filling. The phase diagram obtained for 2D square lattice is remarkably similar to that obtained by Lacroix and Bernhard [109]. At half-filling a transition between K and AFII is obtained at around $\frac{J_K}{W} \simeq 0.20$ at a similar value obtained in [218]. The transition from AFII to F is observed at $n_c = 0.57$, similar as in [106, 109]. The transition between AFII and AF I is observed at around $n_c \simeq 0.68$ whereas AF I \rightarrow F is observed at $n_c \simeq 0.28$. In [111], a stripped magnetism was observed at $0.32 < n_c < 0.65$ which is quite similar to the region ($0.28 < n_c < 0.68$) where our AF I is stabilized. Similar observations for 3D ‘cubic’ lattice were observed. When the number of conducting electrons n_c is low, saturated F phase is observed up-to $\frac{J_K}{W} \simeq 1.0$ which is followed by Kondo phase afterwards. At half filling, the transition AFIII \rightarrow K, occurs at $\frac{J_K}{W} \simeq 0.18$ as in [219].

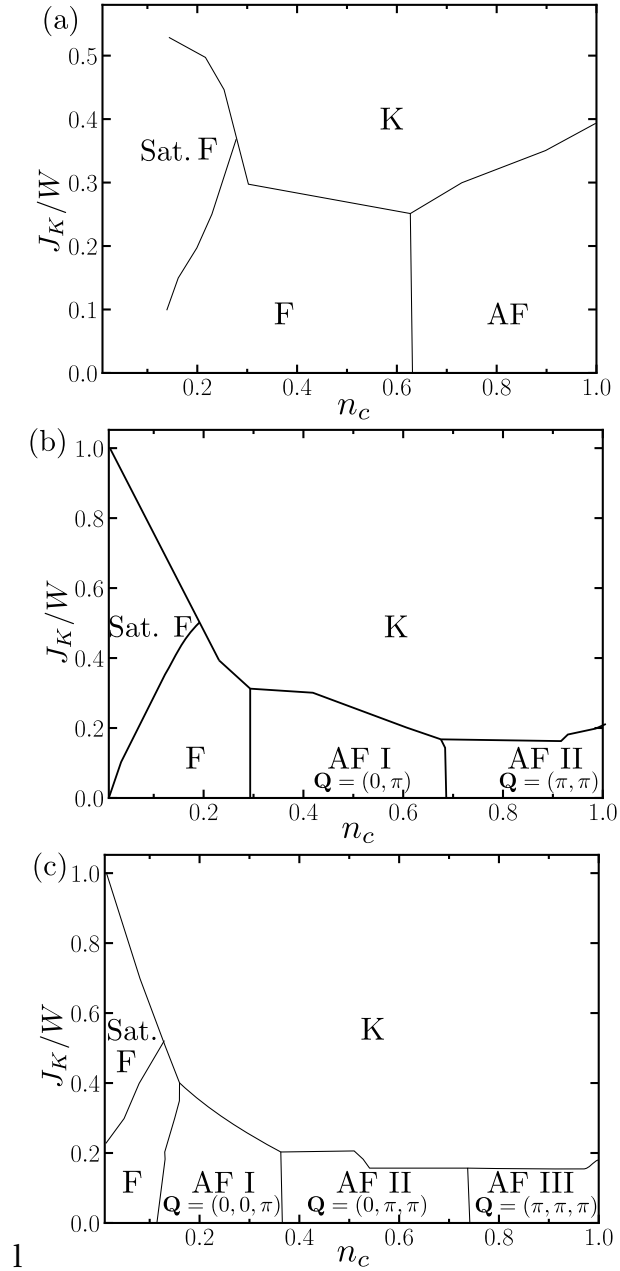


Figure 4.2: phase diagrams (a) 1D 'chain', (b) 2D 'square', (c) 3D 'cubic' lattices at $T = 0$. K = paramagnetic Kondo phase, F = ferromagnetic phase, sat. F = saturated ferromagnetic phase and AF = antiferromagnetic phase

Whereas the transitions AFIII \rightarrow AFII, AFII \rightarrow AF I and AF I \rightarrow F occurs around $n_c \simeq 0.73, 0.36, 0.11$ receptively for low $\frac{J_K}{W}$.

In summary, a cascade of antiferromagnetic phases to ferromagnetic phases is observed as we move from higher n_c to lower n_c in each case for low J_K/W , and paramagnetic Kondo phase is observed for higher J_K/W . Since all three phases diagrams have the same form, we will concentrate only on the 2D square lattice to study the effect of dilution of magnetic impurities.

4.3.2 Tuning of x and T_K at fixed n_c for Kondo alloys

We used the DMFT algorithm to study binary Kondo alloys for the concentrations $x \in [0.01, 1]$ for different n_c with different couplings J_K considering pure K, F, and AFII phases. We present in the figure 4.3 the ground-state phase diagrams obtained for $n_c = 0.90$ and 0.30 . Here, the strength of the Kondo interaction is represented by the ratio between the corresponding Kondo temperature T_K and the non-interacting electronic bandwidth W . All three-phase diagrams present similar forms and are Doniach-like: at low Kondo temperature (T_K) MO phase is found to be the ground state, and this MO phase is suppressed by the paramagnetic Kondo phase at higher T_K .

4.4 Discussion: comparison with experimental data

The above phase diagrams are compatible with the phase diagrams of some alloys as $\text{Ce}_x\text{La}_{1-x}\text{Ru}_2\text{Si}_2$ [119] where substitution of Ce with La give rises to MO, $\text{Ce}_x\text{La}_{1-x}\text{Cu}_2\text{Ge}_2$ [100] where antiferromagnetic phase was seen up-to very low concentration of Ce, and $\text{Ce}_x\text{La}_{1-x}\text{Pt}_2\text{Si}_2$ [99] paramagnetic Kondo phase persists with substitution. In the real isostructural Ce-La substitution series, experiments show that the strength of the Kondo interaction decreases when decreasing Cerium concentration. The opposite monotonic variation of T_K with x is observed with Ytterbium-based Kondo alloys. This is due to the effective pressure effect that is related, with the difference of lattice parameters between Ce- (or Yb-) and La-based (or Lu-) compounds. Therefore, in order to provide a scenario for real Kondo alloys, using the $(x-T_K)$ phase diagrams depicted in figure 4.3, one has to characterize Ce-La substitution with a non-constant but rather monotonous line.

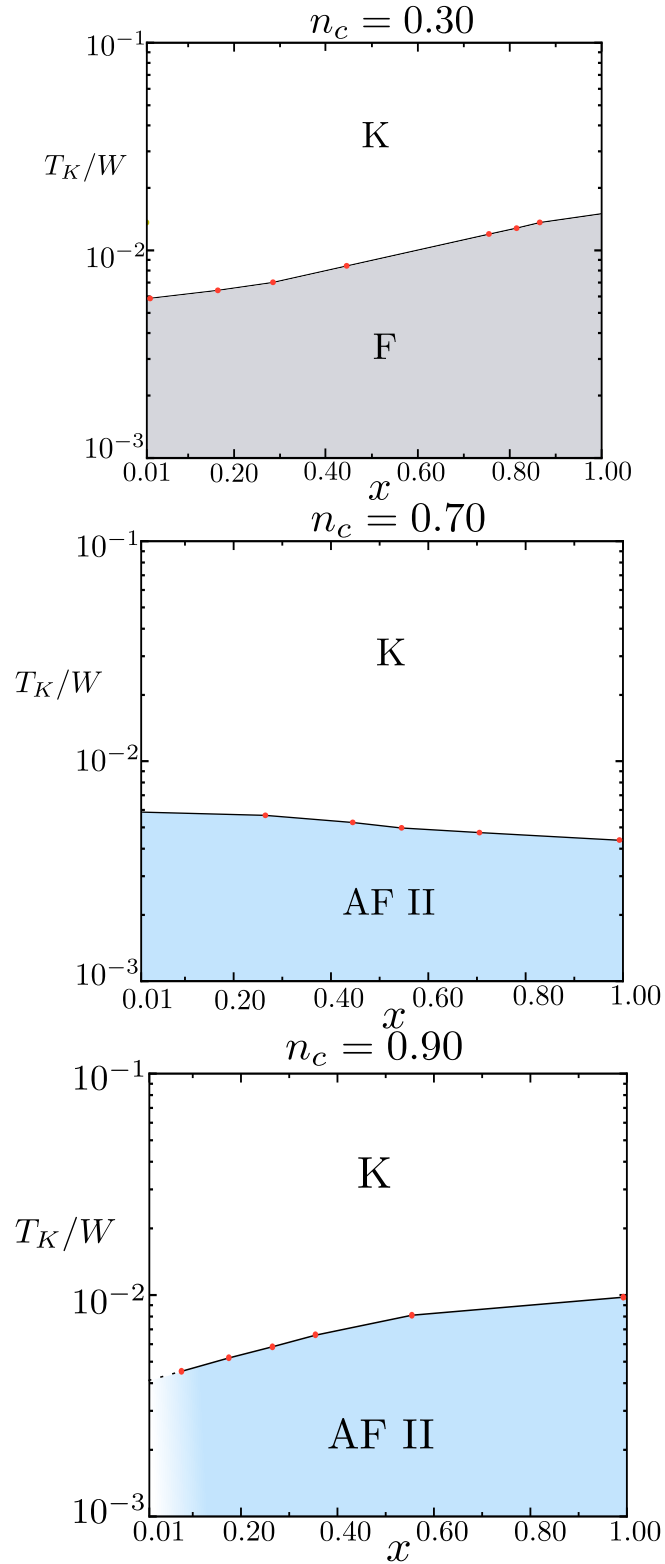


Figure 4.3: from left to right: ground state phase diagrams of the Kondo alloys for $n_c=0.30$, 0.70 and 0.90 . AFII = Néel ordered anti-ferromagnetic phase, and F = ferromagnetic phase

Our results suggest a coherent scenario for Ce-La substitution in various Ce-based

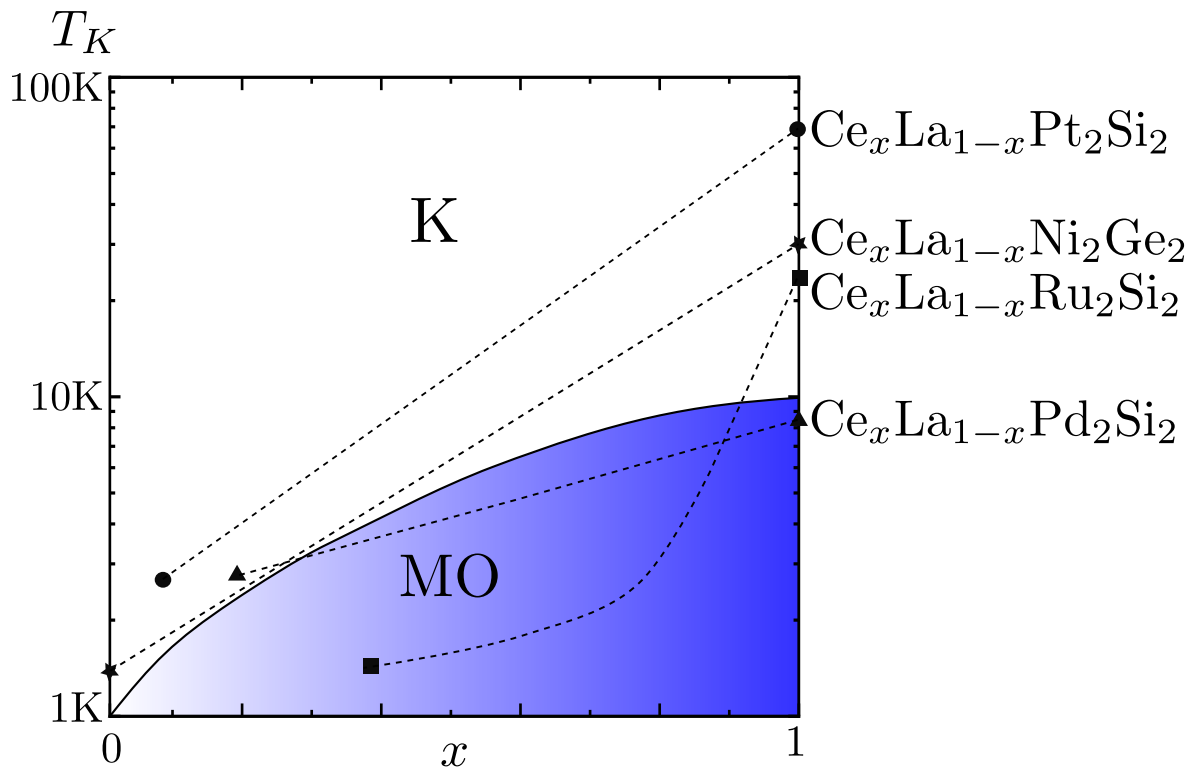


Figure 4.4: Schematic description of the Kondo alloys phase diagrams depicted on figure 4.3, with Kondo (K) and magnetically ordered (MO) phases. In order to fix the energy scale, the K-MO transition is arbitrarily chosen to be realized here at $T_K \approx 10$ Kelvin for the Kondo lattice ($x = 1$) and at around 1 Kelvin in the dilute limit $x \ll 1$. Dashed lines describe four examples of Kondo alloys: $\text{Ce}_x\text{La}_{1-x}\text{Pt}_2\text{Si}_2$ (circle), $\text{Ce}_x\text{La}_{1-x}\text{Ni}_2\text{Ge}_2$ (star), $\text{Ce}_x\text{La}_{1-x}\text{Ru}_2\text{Si}_2$ (square) and $\text{Ce}_x\text{La}_{1-x}\text{Pd}_2\text{Si}_2$ (triangle).

HF materials. Here, we focus only on 122-family, but the scenario isn't restricted to these compounds, and we expect that it can be much more general. Figure 4.4 is the generalized phase diagram obtained through our DMFT calculations where we have placed a few Ce-based 122-family HF materials. For several of Kondo lattice ($x = 1$) 122 compounds, the Doniach argument is consistent with the occurrence of magnetically ordered ground state when the strength of the Kondo coupling T_K becomes smaller than about 10 Kelvin. We can thus depict various Kondo alloys on a single schematic phase diagram, where the energy scale is arbitrarily fixed (see figure 4.4). For $\text{Ce}_x\text{La}_{1-x}\text{Pt}_2\text{Si}_2$, the paramagnetic phase persists with substitution, with T_K decreasing from 70 K ($x = 1$) to 2.6 ± 0.6 K ($x = 0.10$) [99]. For $\text{Ce}_x\text{La}_{1-x}\text{Ni}_2\text{Ge}_2$, the ground state also remains paramagnetic, but the Kondo interaction is smaller, from 30 K for $x = 1$ to 1 K for $x = 0.01$ [101]. Invoking the present scenario, the vicinity of a magnetically ordered phase at intermediate Ce concentration might explain the non-Fermi liquid behavior that has been reported for this Kondo alloy [101]. For $\text{Ce}_x\text{La}_{1-x}\text{Ru}_2\text{Si}_2$, the Kondo lattice ($x = 1$) is paramagnetic with $T_K = 24$ K, but an antiferromagnetic ground state is stabilized below the critical concentration $x = 0.91$ [119] and down to the smallest concentrations for which this alloy was synthesized. The Kondo lattice CePd_2Si_2 , which is characterized by a smaller $T_K = 9$ K, has an antiferromagnetic ground state with a Néel temperature $T_N = 9.9$ K. For $\text{Ce}_x\text{La}_{1-x}\text{Pd}_2\text{Si}_2$, the antiferromagnetic phase is observed when $x > 0.75$, but a paramagnetic Kondo ground state is obtained at lower Cerium concentrations, with T_K decreasing down to 2.8 K for $x = 0.20$ [220]. Another example of 122 Ce-La substituted compound has a similar behavior as CePd_2Si_2 : the Kondo alloy $\text{Ce}_x\text{La}_{1-x}\text{Cu}_2\text{Ge}_2$ was indeed reported to be antiferromagnetic with $T_N = 4.1$ K and $T_K = 4$ K for $x = 1$, and a surprising persistence of antiferromagnetic order down to $x = 0.10$ [100]. Our present scenario might also explain this persistence. Of course, the quantitative energy scale used for the schematic figure 4.4 was chosen arbitrarily to mimic various 122 Ce-based compounds in a coherent scenario. However, we expect that the qualitative properties observed experimentally should remain universal beyond the specific cases that are analyzed here.

Chapter 5

Photo-emission properties of Kondo alloys

In this chapter, we present our results on the photo-emission properties of Kondo alloys upon the dilution of Kondo impurities for a large range of Kondo coupling and three electronic fillings $n_c = 0.30, 0.70$ and 0.90 . For this, we will analyze the photo-emission spectrum in terms of Fermi surfaces, band-structure and density of states, and effective mass focusing on the paramagnetic Kondo phase. This analysis will further complete the phase diagram presented in chapter 5.

5.1 A state of the art

The angle-resolved photoemission spectroscopy (ARPES) technique is based on the photoelectric effect described a century ago. In this technique, a photon of sufficient energy is projected to the crystal, which ejects an electron from the material, following the absorption of an X-ray photon. By measuring the kinetic energy and angle distributions of the emitted photoelectrons, the technique can map the electronic band structure and Fermi surfaces of the system. ARPES is used to characterize materials because it gives access directly to the Fermi surface topology and band structure. On Kondo alloys, it was first Park *et al.* [221] conducted ARPES experiments on multiple Ce-based Kondo lattice systems, since then this probe was employed extensively to study the electronic structure of correlated electronic systems [15]. These experimental technics have already been proven to be very useful to investigate the physics of f -electron systems, including Kondo alloys [15, 222].

Enlargement of Fermi surface due to the coherent participation of $4f$ electrons are directly observed by ARPES experiments on varieties of Kondo lattice systems. The ARPES experiments carried on varieties of Kondo lattice systems like CeRu_2Si_2 [223–225], CeRu_2Ge_2 [226], CeBi [227], CeNiSn [228] and YbRh_2Si_2 [135, 229, 230] showed

large Fermi surfaces due to the coherent participation of $4f$ electrons. ARPES can also reveal anisotropic properties present in some Kondo alloys. For example, soft x-ray ARPES revealed anisotropic Fermi surface structures: large along $\Gamma - X$ direction for CeRu_2Si_2 [231] and smaller along with other directions. Meanwhile, LaRu_2Si_2 showed a smaller Fermi surface as predicted through model calculations (see figure 5.1). Additionally, photoemission spectroscopy experiments also revealed limitations of the single impurity models for describing dense Kondo systems [124, 232, 233]. However, a complete picture of the evolution of large Fermi surface for dense Kondo to small Fermi surface in dilute Kondo upon dilution remains still an open question.

ARPES can give access directly also to the band structure, and angle-integrated photoemission spectroscopy gives access to the density of states of a crystal. In Kondo lattice, ARPES experiment [223] on CeRu_2Si_2 and URu_2Si_2 indicated $f - d$ band mixing at low temperatures and exclusions of f -electrons in the Fermi surface above T_K . While in $\text{CeCoGe}_{1.2}\text{Si}_{0.8}$ [234] the heavy hybridized conduction band as well as dispersive Kondo resonance peaks were observed directly. In another ARPES experiment, similar band structures were obtained on both Kondo lattice CeRh_2Si_2 and in Ce-La substituted Kondo alloy $\text{Ce}_{0.84}\text{La}_{0.16}\text{Ru}_2\text{Si}_2$ [235]. This similarity was astonishing because below the critical concentration $x = 0.07$, the antiferromagnetic phase appears. Similarly in the band structure before and after the critical concentration indicates that the change in band structure might be continuous across x_c . ARPES in CeRh_2Si_2 [236] also revealed the surface and bulk hybridization in antiferromagnetic Kondo lattice.

Important works were also done in theoretical part to determine the electronic structures of Kondo alloys either by *ab-initio* methods like DFT, linear muffin-tin orbital [66, 237], or DMFT/DMFT+*ab-initio* calculations [81]. Fermi surface obtained through *ab-initio* calculations were consistent with ARPES derived Fermi surfaces [227, 229, 230, 238]. Combined DMFT and DFT method was employed to study temperature dependent Fermi surface in multiple cases [239–242].

5.2 Theoretical approach for disordered systems

Some physical quantities like the density of states, spectral function, and effective masses, showing the electronic structure of a system can be extracted directly from local self-energy. Since the system that we are studying is disordered and random, one must include all the processes of creation and annihilation of a fermion that goes from one type of site to another type of site. In our case, we have four different processes: Kondo site to Kondo site, Kondo site to non-Kondo site, non-Kondo site to Kondo site and non-Kondo site to non-Kondo site. Below, we obtain a disordered-averaged one-body Green's function from these four different processes. This disordered-averaged one-body Green's function will be used to obtain photoe-

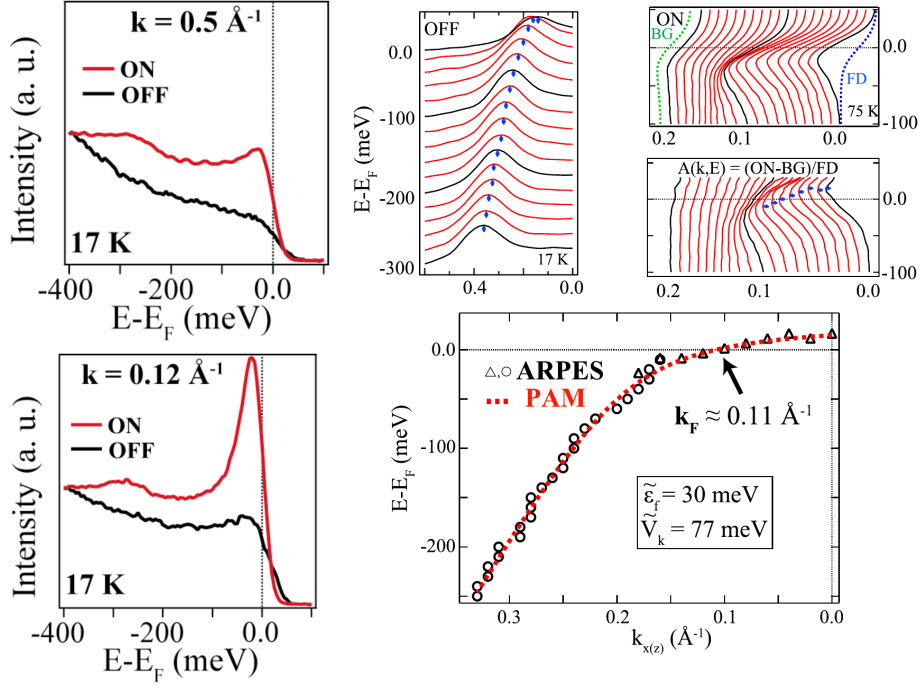


Figure 5.1: Left figures: Electronic density curve showing Kondo resonance peak (below) at on-resonance ARPES spectra. Right figure: Comparison of ARPES derived hybridized band and PAM hybridized band. From [231].

mission signals.

5.2.1 Disorder averaged one-body Green's function

Here, we will derive the expression for one-body Green's function for paramagnetic Kondo phase. In pure Kondo phase the sub-lattices A and B are equivalent and doesn't depend on spin σ , the sites α and $\bar{\alpha}$ are equivalent which gives makes the local propagator equivalent for each site $[\Pi_{\alpha}(i\omega_n)]^{-1} = [\Pi_{\bar{\alpha}}(i\omega_n)]^{-1} = [\Pi_0(i\omega_n)]^{-1}$ and similarly the dynamical local bath for the sites α and $\bar{\alpha}$ are equivalent, hence $\Delta_{\alpha}(i\omega_n) = \Delta_{\bar{\alpha}}(i\omega_n) = \Delta(i\omega_n)$. We recover the equation for $\mathbf{G}_{loc}^{\sigma}(i\omega_n)$ as in [141]

$$\mathbf{G}_{loc}(i\omega_n) = \sum_{\mathbf{k}} \mathbf{G}(\mathbf{k}, i\omega_n) = \sum_{\mathbf{k}} [[\Pi_{0\sigma}(i\omega_n)]^{-1} - \mathbf{W}_{\mathbf{k}}]^{-1}, \quad (5.1)$$

with $[\Pi_{0\sigma}(i\omega_n)]^{-1} = (i\omega_n + \mu)I - \Sigma_{\sigma}(i\omega_n)$, where I is 2×2 identity matrix. Following the steps as in [141], disordered-averaged \mathbf{K} -dependent 2×2 Green's function matrix $\mathbf{G}(\mathbf{k}, i\omega_n)$ can be expressed as

$$\mathbf{G}(\mathbf{k}, i\omega_n) = \begin{pmatrix} \frac{i\omega_n + \mu - \Sigma_{\mathcal{K}}(i\omega_n) - (1-x)\Delta(i\omega_n)}{x} - \epsilon_{\mathbf{k}} & \Delta(i\omega_n) - \epsilon_{\mathbf{k}} \\ \Delta(i\omega_n) - \epsilon_{\mathbf{k}} & \frac{i\omega_n + \mu - x\Delta(i\omega_n)}{1-x} - \epsilon_{\mathbf{k}} \end{pmatrix}^{-1}, \quad (5.2)$$

where, self-energy Kondo $\Sigma_{\mathcal{K}}(i\omega_n) = \frac{r^2}{i\omega_n + \lambda}$. Inverting this (2×2) matrix, we get the matrix elements of $\mathbf{G}(\mathbf{k}, i\omega_n)$. We sum up all the four matrix elements of the matrix (5.2) defining the four different processes to get our one-body Green's function as

$$\mathcal{G}(\mathbf{k}, i\omega_n) = G_{\mathcal{K}\mathcal{K}}(\mathbf{k}, i\omega_n) + G_{\mathcal{K}\mathcal{N}}(\mathbf{k}, i\omega_n) + G_{\mathcal{N}\mathcal{K}}(\mathbf{k}, i\omega_n) + G_{\mathcal{N}\mathcal{N}}(\mathbf{k}, i\omega_n), \quad (5.3)$$

where $G_{\mathcal{K}\mathcal{K}}(\mathbf{k}, i\omega_n)$, $G_{\mathcal{K}\mathcal{N}}(\mathbf{k}, i\omega_n)$, $G_{\mathcal{N}\mathcal{K}}(\mathbf{k}, i\omega_n)$ and $G_{\mathcal{N}\mathcal{N}}(\mathbf{k}, i\omega_n)$ are the matrix elements of the matrix (5.2). With a some straight forward algebraic manipulations, we obtain an expression analogous to one-body interacting Green's function as

$$\mathcal{G}(\mathbf{k}, i\omega_n) = (i\omega_n + \mu - \Sigma_{Alloy}(i\omega_n) - \epsilon_{\mathbf{k}})^{-1}. \quad (5.4)$$

where the self-energy is expressed with the help of Kondo self-energy $\Sigma_{\mathbf{k}}(i\omega_n) = r^2/(i\omega_n + \lambda)$ alloy as

$$\Sigma_{alloy}(i\omega_n) = \frac{x}{\Sigma_{\mathcal{K}}^{-1}(i\omega_n) - (1-x)G_{\mathcal{N}}(i\omega_n)}. \quad (5.5)$$

We can easily verify that this one-body Green's function (Eq. 5.4) reproduces standard results at several limits. At extreme dilute limit ($x = 0$), we obtain non-interaction Green's function $G_0(\mathbf{k}, i\omega_n) = 1/(i\omega_n + \mu - \epsilon_{\mathbf{k}})$ whereas when $x = 1$, we obtain $G(\mathbf{k}, i\omega_n) = 1/(i\omega_n + \mu - \Sigma_{\mathcal{K}}(i\omega_n) - \epsilon_{\mathbf{k}})$. Thus, one-body Green's function take account all the processes relates both \mathcal{K} and \mathcal{N} sites. All the observable properties related to our system is confined into Σ_{alloy} . So now, we present below the definitions and expressions of some quantities that we have analyzed in this chapter.

5.2.2 Spectral function and Fermi surface

In non-interacting system, the spectral function is defined as

$$\mathcal{A}_0(\mathbf{k}, \omega) = \delta(\omega - \epsilon_{\mathbf{k}}), \quad (5.6)$$

with δ being delta Dirac function. Similarly, in this study, we define the spectral function at a frequency ω and a wave-vector \mathbf{k} from the disorder-averaged one-body Green's function as

$$\mathcal{A}(\mathbf{k}, \omega) = -\frac{1}{\Pi} \text{Im}(\mathcal{G}(\mathbf{k}, \omega + i\eta^+)). \quad (5.7)$$

where η is an infinitesimal positive number. The Fermi surface for a system is obtained from the equation 5.7 by evaluating it at Fermi level $\omega = 0$ over first the Brillouin zone.

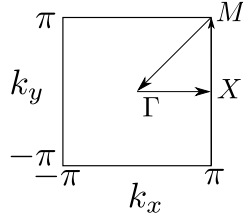


Figure 5.2: First Brillouin zone of the square lattice, with indications of the points $\Gamma = (0, 0)$, $X = (0, \pi)$, and $M = (\pi, \pi)$.

5.2.3 Local density of states

Another quantity that we can obtain from one-particle Green function is density of states (d.o.s). The d.o.s is obtained by a summation of spectral function (Eq. 5.6) over all \mathbf{k} .

$$\rho(\omega) = \frac{1}{V} \int_{\mathbf{k}} \mathcal{A}(\mathbf{k}, \omega) d\mathbf{k}, \quad (5.8)$$

where V is the volume of Brillouin zone. This quantity can be obtained from angle integrated photoemission spectroscopy.

5.2.4 Local self-energy and effective mass

In this chapter, we are also interested in the effective mass of quasiparticles. This quantity can be obtained through self-energy. At low-energy, the Taylor expansion of self-energy can be written in as

$$\Sigma(\omega) = \Sigma(0) + \omega \left. \frac{\partial \Sigma(\omega)}{\partial \omega} \right|_{\omega=0} + O(\omega^2) \quad (5.9)$$

$$= \Sigma(0) + (1 - m^*)\omega + O(\omega^2), \quad (5.10)$$

where m^* is effective mass and is defined as

$$\frac{m^*}{m} = 1 - \left. \frac{\partial \Re(\Sigma(\omega))}{\partial \omega} \right|_{\omega=0}. \quad (5.11)$$

5.3 Results: Spectral function and electronic density of states

In this section, we analyze the spectral function $\mathcal{A}(\mathbf{k}, \omega)$, which is related ARPES signal and the local electronic density of states with a focus on the specific signatures of the transitions and crossovers in the paramagnetic Kondo phases. In particular, we address the issues of one-branch versus multi-branches dispersion in spectral function along with gap-less, pseudogapped, or gapped local electronic density of states. We solved the self-consistent equations (3.25, 3.26 and 3.27) for various

electronic fillings, and we obtained similar qualitative results in all cases. Therefore here, we choose $n_c = 0.70$ to present an overview of different situations depending on x and T_K . Overall we identify two different scenarii depending on the strength of the Kondo interaction: the relatively high T_K regime (see figure 5.3) and the relatively small T_K regime (see figure 5.4), typically separated by a threshold corresponding to T_K around $W/10$.

In both cases, the dilute Kondo limit ($x \ll 1$) and the dense Kondo limit ($x = 1$) generate usual results. The dilute Kondo limit ($x \ll 1$) reproduces the non-interacting electronic structure, which is characterized here by a well-defined single branch electronic dispersion and a density of states with a van-Hove singularity usual for the square lattice. The Kondo lattice limit ($x = 1$) also presents universal signatures with two branches resulting from the effective hybridization between conduction electrons and the local levels associated with Kondo spins. The resulting density of states also presents a gap. For intermediate concentrations x , the situation depends on the strength of the Kondo interaction.

5.3.1 Evidence for a Lifshitz-like transition in the Kondo phase at large T_K

The numerical results obtained for various Kondo impurity concentrations at relatively large Kondo coupling $T_K/W = 0.169$ are presented in the figure 5.3. In the intermediate concentration regime, as long as $x > n_c$, the dilution of Kondo impurities does not close the hybridization gap characterizing the coherent dense regime. Since we have fixed $n_c < 1$ in the dense case, the Fermi level is inside the lower band. When decreasing x , a third band starts to be formed inside the gap, and a transition from dense to dilute Kondo regimes occurs at $x = n_c$. This transition is marked by the shift of the Fermi level from the lower band to the third band. Upon further dilution of Kondo impurities in the regime $x < n_c$, the hybridization gap is filled giving rise to three branches structures separated by two pseudogaps.

Let us consider at first $x > n_c$ regime in order to understand the formation of the third band and the breakdown of the coherence of the Kondo impurities. In this dense regime and at strong Kondo coupling, the KAM can be mapped onto an effective Hubbard model where quasiparticles are the unscreened Kondo impurities [133, 243–245]. The corresponding “Coulomb repulsion” in this case of the order T_K which is very large compared to W . Apart from half-filling which corresponds to a Kondo insulator for $x = 1$, the system is a strongly correlated metal. Considering particle-hole general symmetry, let us depict a situation where the effective Fermi level is inside the lower band. The gapped local d.o.s characterizing Kondo lattices at large T_K reflects the two Hubbard bands separated by an energy of the order of T_K and the states in the upper Hubbard band correspond to singlet-triplet excitations. Dilution of Kondo atoms in the dense regime ($n_c < x < 1$) changes the

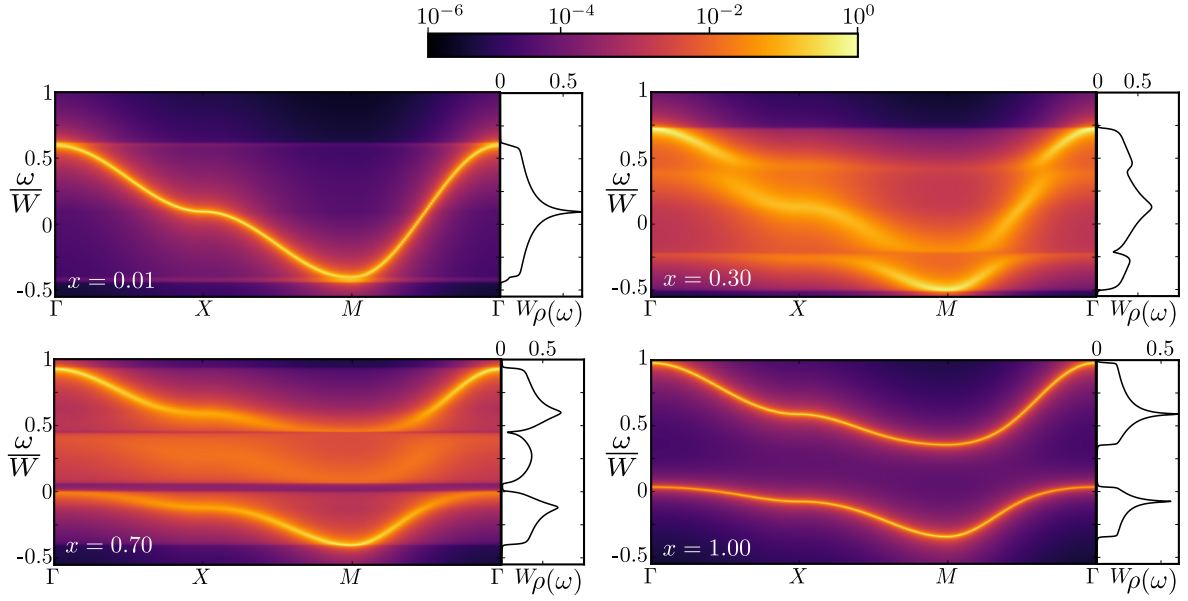


Figure 5.3: Spectral function evaluated for $n_c = 0.70$ at relatively strong coupling $T_K/W = 0.169$ for Kondo impurity concentrations $x = 0.01, 0.30, 0.70,$ and 1.00 . The wavevector \mathbf{k} axis corresponds to the high symmetry lines $\Gamma - X - M - \Gamma$ in the square lattice first Brillouin zone (see figure 5.2). The corresponding electronic density of states $\rho(\omega)$ is plotted on the right side. Each individual cases of this figure are indicated in the phase diagram depicted in the figure 5.9.

number of carriers and the Fermi level gets closer to the upper edge of the effective Hubbard band. The transition realized at $x = n_c$ for strong Kondo interaction may thus be analogous to a doping-induced Mott transition [13], which also presents the formation of a quasiparticle peak inside the Hubbard gap. However, the effective model is different for $x < n_c$: in this dilute regime and for strong Kondo interaction, quasiparticles emerge from the supernumerary conduction electrons which do not form Kondo singlets. The third central band may be associated with the motion of these conduction electrons on the non-Kondo sites. When decreasing x , this third band (see $x = 0.30$ in the figure 5.3) looks like the $x = 0.01$ band but distorted. This is consistent with previous argument about the origin of the third band since in the both cases, most of the sites are non-Kondo. Thus in the extreme dilute case, the d.o.s of non-interacting 2D square lattice is recovered while the lower and the upper Kondo-related bands disappear. Further, the states in the fully occupied lower band represent the electrons forming singlets on Kondo sites whereas the upper unoccupied band corresponds to excitations of a second electron on a Kondo site.

5.3.2 Evidence for a new critical concentration at low T_K

We now focus on the output of spectral function obtained for the relatively small Kondo coupling case. Figure 5.4 illustrates the results obtained for $T_K/W = 0.019$. We observe that the two branches structure characterizing the dense Kondo state is

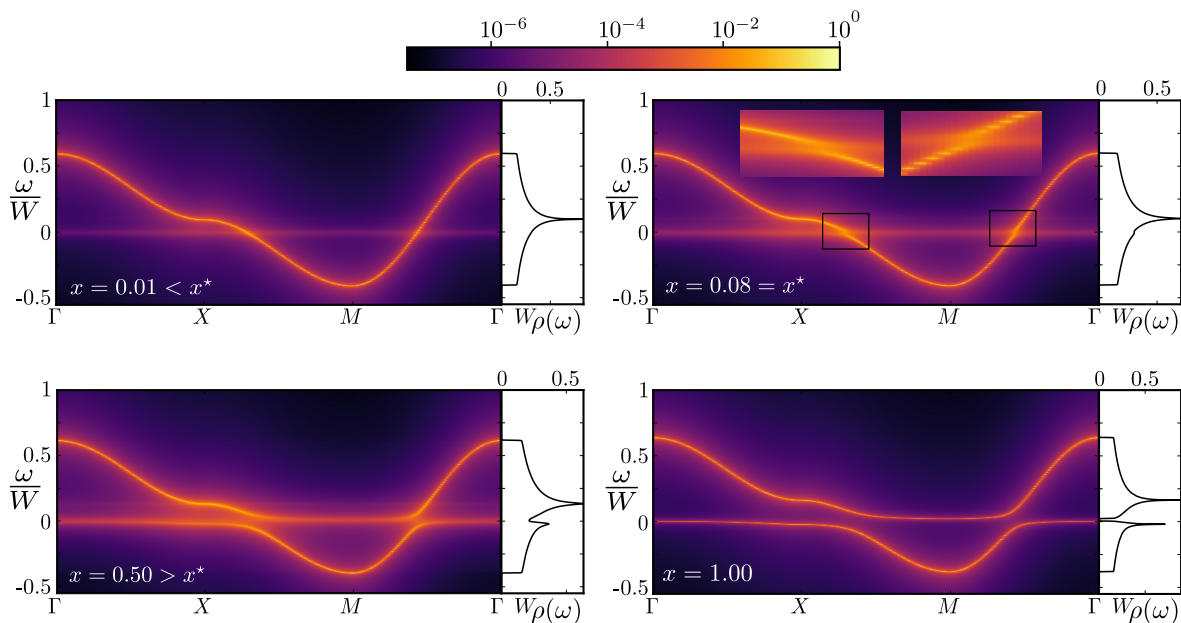


Figure 5.4: Spectral function evaluated for $n_c = 0.70$ at relatively small coupling $T_K/W = 0.019$ for Kondo impurity concentrations $x = 0.01, 0.08, 0.50,$ and 1.00 with $x^* = 0.08$. The wavevector \mathbf{k} axis corresponds to the high symmetry lines $\Gamma - X - M - \Gamma$ in the square lattice first Brillouin zone (see figure 5.2). The corresponding electronic density of states $\rho(\omega)$ is plotted on the right side. Each individual case of this f are indicated in the phase diagram depicted in the figure 5.9.

preserved upon dilution even for $x < n_c$. Furthermore, the effect of disorder-related decoherence is maximum at around $x = n_c$ which leads to a broadening of the branches as well as a reduction of the quasiparticle lifetime. This maximum decoherence also results in a partial filling of the hybridization gap leaving a pseudogap near the Fermi level. Upon further dilution of Kondo atoms, the two branches merge to form a single branch structure along with the disappearance of the pseudogap. This occurs at a critical concentration x^* which depends on the strength of the Kondo interaction. We find that $x^* \ll n_c$ at very small T_K , and $x^* \rightarrow n_c$ when T_K approaches around $W/10$.

5.4 Results: Fermi surface

In this section we analyze the experimental signatures in the Fermi surfaces obtained from the spectral function $\mathcal{A}(\mathbf{k}, i\omega = i0^+)$. Figure 5.5 depicts the Fermi surface spectra computed for a paramagnetic Kondo ground state within broad ranges of x and n_c . For all values considered for the Kondo interaction and the electronic filling, we find that the Fermi surface of the Kondo lattice ($x = 1$) is large, and it includes the contributions from both the conduction electrons and the Kondo spins. This universal feature is in good agreement with previous theoretical and experimental results [15, 135, 222–230]. It can be well understood in terms of the Luttinger theorem,

which stipulates that all fermionic degrees of freedom participate in the formation of the Fermi liquid ground state.

5.4.1 Fermi surface in the Kondo phases: coherence breakdown

We now focus on the possible breakdown of this coherent Kondo lattice state when decreasing x . For a relatively strong Kondo interaction ($T_K/W = 0.175$) we observe the Lifshitz-like transition at $x = n_c$ that was predicted in [136]. In this case, the spectral function corresponds to relatively long lifetime quasiparticles with a well-defined Fermi surface (excepted at the transition). Figure 5.6 shows clearly this discontinuity of Fermi surface at $T_K/W = 0.175$. In this case, the volume of the Fermi-surface shrinks when increasing x in the dilute regime $x < n_c$, and it increases with x in the dense regime $x > n_c$. This feature is consistent with the fact that Kondo impurities behave as hole-dopant for $x < n_c$ and particle-dopant for $x > n_c$.

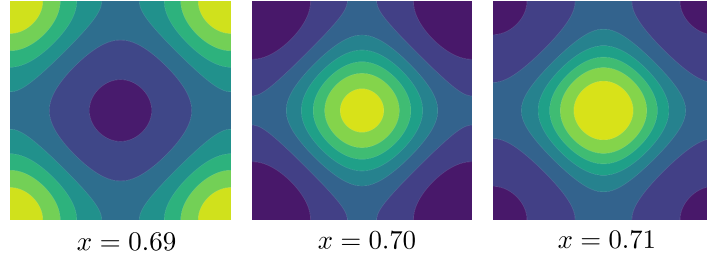


Figure 5.6: Fermi surface structure for $T_K/W = 0.175$ for $n_c = 0.70$ at $x = n_c - 0.1$, $x = n_c$ and $x = n_c + 0.1$ from left to right. A clear evidence of Lifshitz-like transition is marked by the discontinuity of Fermi surface at $x = n_c$.

For $T_K/W = 0.082$, and 0.0058 , the evolution of the Fermi surface along with concentration x is more gradual, and the Lifshitz-like transition around $x = n_c$ seems to become a crossover at lower values of T_K . Furthermore, the broadening of the Fermi surface spectra around the Fermi wavevectors is maximal around $x = n_c$ due to disorder-related decoherence.

Fermi surface spectra provide apparent signatures of the Kondo lattice coherence breakdown transition at $x = n_c$, especially for systems with relatively strong Kondo interaction, corresponding to T_K typically larger than $W/10$. This Lifshitz like transition separating dense and dilute Kondo phases at $x = n_c$ becomes a crossover for smaller T_K . At small T_K , we identified another critical concentration from the spectral functions (see section 5.3) at x^* characterizing the merging of two spectral function branches. However, the Fermi surfaces at figure 5.5 do not present clear signatures of any characterized feature at or around this critical concentration x^* . This is not surprising since the electronic excitation spectrum is not accessible from the Fermi surfaces.

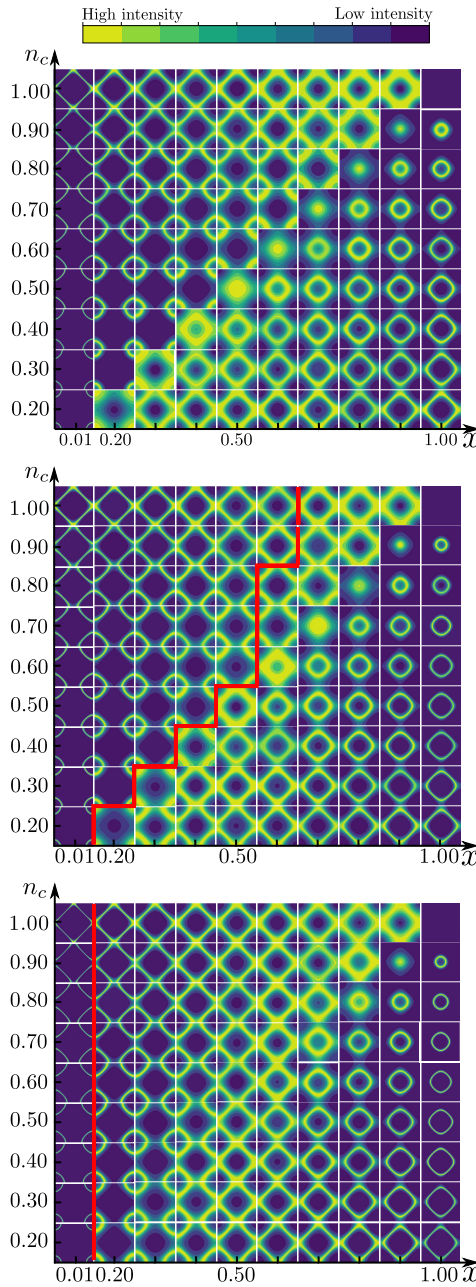


Figure 5.5: FS spectra assuming a Kondo paramagnetic ground state for $x = 0.01, 0.20, 0.30, 0.40, 0.50, 0.60, 0.70, 0.80, 0.90, 1.00$ (from left to right) and $n_c = 0.20, 0.30, 0.40, 0.50, 0.60, 0.70, 0.80, 0.90, 1.00$ (from bottom to top). Each square corresponds to the first Brillouin zone of the square lattice (see figure 5.2). From top to bottom, $T_K/W = 0.175, 0.082$, and 0.0058 : the Lifshitz-like transition around $x = n_c$ is observed for a sufficiently strong Kondo interaction, and it becomes a gradual crossover for smaller values of the interaction. The red lines for $T_K/W = 0.082$ and 0.0058 separates the regimes $x < x^*$ and $x > x^*$. In both cases, x^* increases with increasing n_c . However, for $T_K/W = 0.0058$, this is not visible because x^* lies between $x = 0.01$ and $x = 0.20$ for all values of n_c considered.

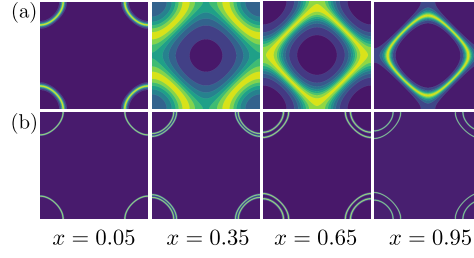


Figure 5.7: Fermi surface spectra for $n_c = 0.30$ and $x = 0.05, 0.35, 0.65$ and 0.95 . (a) $T_K/W = 0.012$ with Kondo ground states: we observe signatures of a breakdown of coherence associated with a change of topology in the Fermi-surface. (b) $T_K/W = 0.0031$ with ferromagnetic ground states: we observe Zeeman splitting effect only.

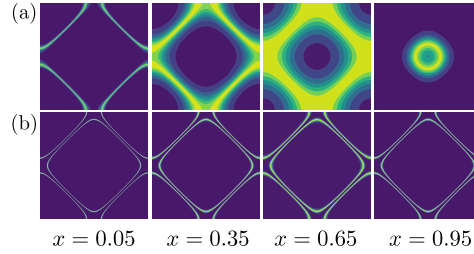


Figure 5.8: Fermi surface spectra for $n_c = 0.90$, and $x = 0.05, 0.35, 0.65$ and 0.95 . (a) $T_K/W = 0.0143$ with Kondo ground states: we observe signatures of a breakdown of coherence associated with a change of topology in the Fermi-surface. (b) $T_K/W = 0.0045$ with antiferromagnetic ground states: we observe only the folding of the Fermi-surface which results from the staggered Néel ordering.

5.4.2 Fermi surface in the magnetically ordered phases

We also studied the Fermi surfaces in the magnetically ordered phases of Kondo alloys, as depicted in figure 5.7 (for $n_c = 0.30$, where the small Kondo coupling ground state is ferromagnetic) and in figure 5.8 (for $n_c = 0.90$, where the small Kondo coupling ground state is antiferromagnetic). The Zeeman splitting is obtained, and we are also able to reproduce the folding of the Brillouin zone in the Néel antiferromagnetic state as in [246]. For both magnetically ordered states, we find that the evolution of the Fermi surface is either absent or very smooth and gradual upon varying x . This result is in contrast with the coherence breakdown which is predicted in the Kondo phases. A possible explanation for this difference may be obtained by considering the Kondo lattice limit ($x = 1$). In this case, Kondo spins contribute to the formation of a large Fermi surface for the Kondo coherent state, while they do not contribute for the magnetically ordered states. The breakdown of coherence which is depicted here in Fermi surfaces spectra for the Kondo phase is thus related to the contribution of Kondo ions to forming strongly correlated fermionic quasiparticles. This breakdown of coherence is different from the breakdown of Kondo effect that distinguishes Kondo phases from pure magnetically ordered phases. Indeed, Kondo

effect is still present in the non-coherent dilute Kondo phase. In our calculations, we did not consider the possibility of mixed states where magnetic order might coexist with Kondo effect. For such states, we expect coherence breakdown signatures that might be concomitant with Fermi surface reconstructions resulting from magnetic order.

5.5 Results: emergence of two transitions in the paramagnetic Kondo phases

The phase diagram of the KAM is depicted in figure 5.9. It was obtained by comparing the energies of each phase considered: paramagnetic Kondo, antiferromagnetic and ferromagnetic phases. From these phase diagrams, we observe that in the region with small values of Kondo coupling, the long-range magnetically ordered phases are stabilized. Their competitions and their stabilities for the KAM, which is consistent with Doniach argument, was discussed elsewhere [247]. For small to intermediate values of T_K , a paramagnetic Kondo phase with three distinct zones are identified: a dilute Kondo at $x \ll 1$, a dense Kondo at $x \approx 1$ separated by a large zone of intermediate state $x^* < x < n_c$. When increasing the Kondo coupling, x^* tends towards n_c and for strong coupling only dilute and dense Kondo phases are obtained, separated by a Lifshitz transition.

Now, we analyze the different regions of paramagnetic Kondo phases by means of effective self-energy $\Sigma_{Alloy}(\omega)$ and its corresponding effective mass m^* with a focus on spectral function, which is related to experimental observation of ARPES signals. The transition observed in the Fermi surfaces (see section 5.4) at $x = n_c$ for sufficiently large values of Kondo coupling is characterized by a discontinuity of $\Sigma_{Alloy}(\omega = 0)$ (solid line in figure 5.9). Since the real part of the self-energy is related with a rescaling of the Fermi level, we interpret this transition as a signature of the Lifshitz transition that was predicted elsewhere [136] from a strong coupling approach of the Kondo alloy: for $x > n_c$, all magnetic degrees of freedom from conduction electrons are frozen by Kondo singlets formation. The Fermi liquid quasiparticles in this coherent dense regime are formed by the remaining degrees of freedom from unscreened Kondo impurities. In the dilute regime $x < n_c$, the microscopic nature of quasiparticles is different and emerges from unscreened conduction electrons. Our result shows that this strong coupling picture may be realized for $T_K \gtrsim \frac{W}{10}$. Therefore, in order to observe a signature of coherence breakdown at $x = n_c$ from ARPES experiments on Kondo alloys, one would need to consider f -electron compounds with relatively large Kondo temperatures. In this case, a valence fluctuation or valence transition might also become relevant as well but this issue is beyond the scope of the present work.

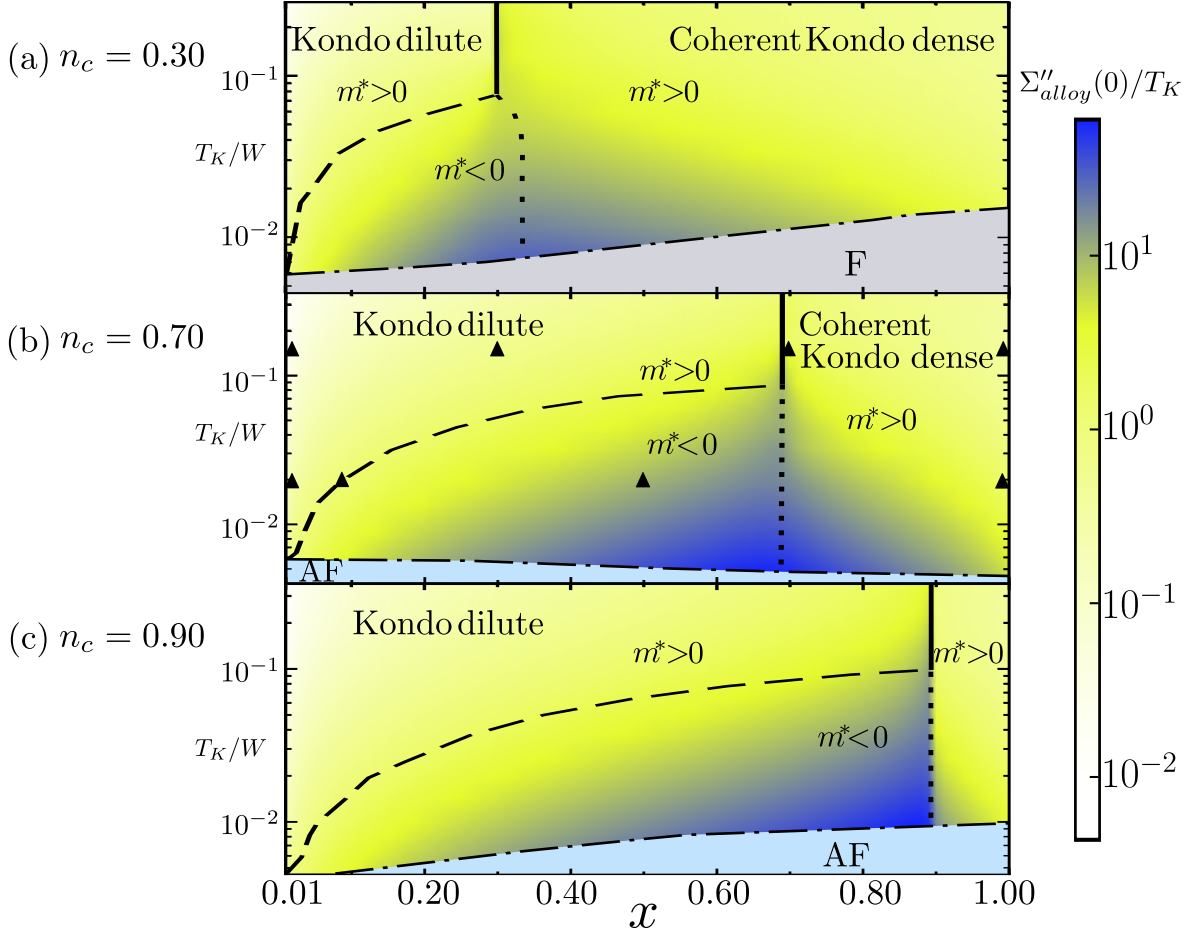


Figure 5.9: Ground state phase diagram of the KAM as functions of x and T_K/W for (a) $n_c = 0.30$, (b) $n_c = 0.70$ and (c) $n_c = 0.90$. (▲) indicates the individual cases presented in the figure 5.3 and figure 5.4 for $n_c = 0.70$. In the Kondo phases the solid line indicates the discontinuity of the self-energy observed at $x = n_c$ for sufficiently strong T_K . This transition from the dense coherent Kondo phase becomes a crossover marked by an inflection in the self energy at smaller T_K (dotted line), and a significant increase in the intensity of imaginary part of the self-energy (color or black and white gradient). A continuous vanishing of the effective mass m^* is obtained at concentration x^* (dashed line), and we find $m^* < 0$ in the intermediate region $x^* < x < n_c$. We also solved the DMFT equations obtained for a Bethe lattice, considering the Kondo paramagnetic solution only and the same values of model parameters as depicted here. Results for Bethe lattice can be found in the appendix C.2. We were not able to distinguish the figures corresponding to the Bethe lattice from the ones depicted here for the 2D square lattice. This strong similarity excludes several interpretations that might invoke specificities of the lattice structure.

Hereafter, we analyze different situations with smaller Kondo coupling. The transition predicted at $x = n_c$ separating dense and dilute Kondo regimes becomes a crossover at smaller coupling and the quasiparticle lifetime is significantly shortened due to disorder incoherence effects. Indeed, the self-energy is found to be continuous and characterized by an inflection around this crossover $x = n_c$ (dotted line in figure 5.9, see also figure 5.10).

Whereas, the imaginary part, $\Sigma''_{Alloy}(0)$, which is relatively small at strong cou-

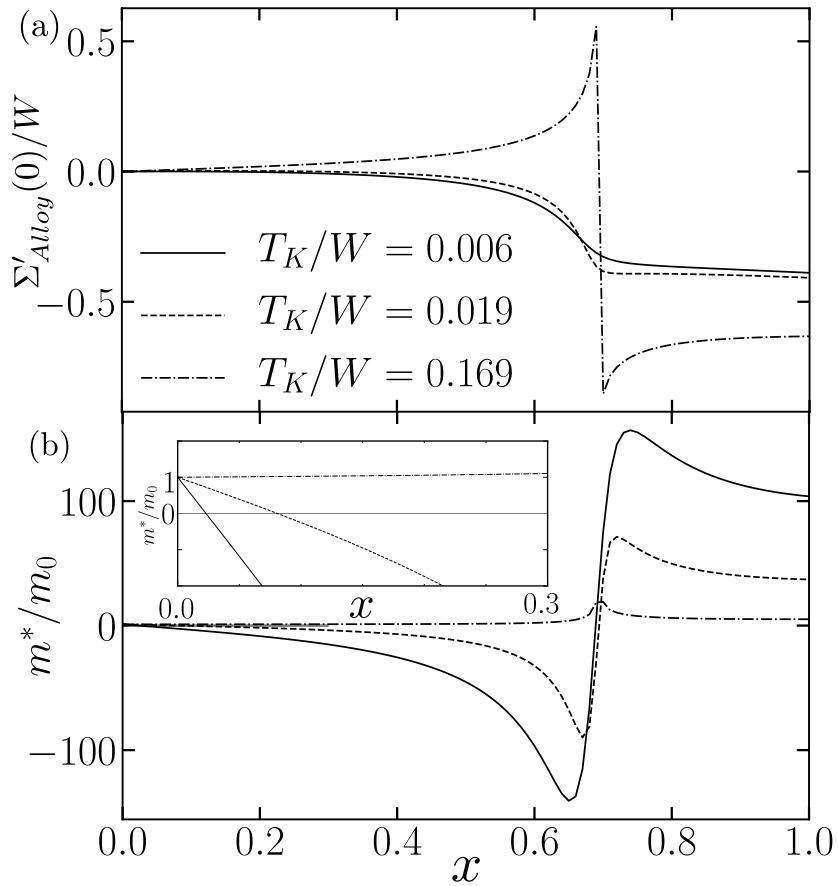


Figure 5.10: (a) Real part of the self-energy $\Sigma'_{Alloy}(0)/W$, (b) Effective mass m^*/m_0 as functions of x , for $n_c = 0.70$. Different Kondo temperatures have been used for the numerics, illustrating the transition (at strong T_K) and crossover (at smaller T_K) obtained around $x = n_c$. The inset in (b) is a focus around the critical concentration x^* which is characterized by a vanishing of m^* when T_K relatively small. At intermediate concentrations $x^* < x < n_c$ we find $m^* < 0$.

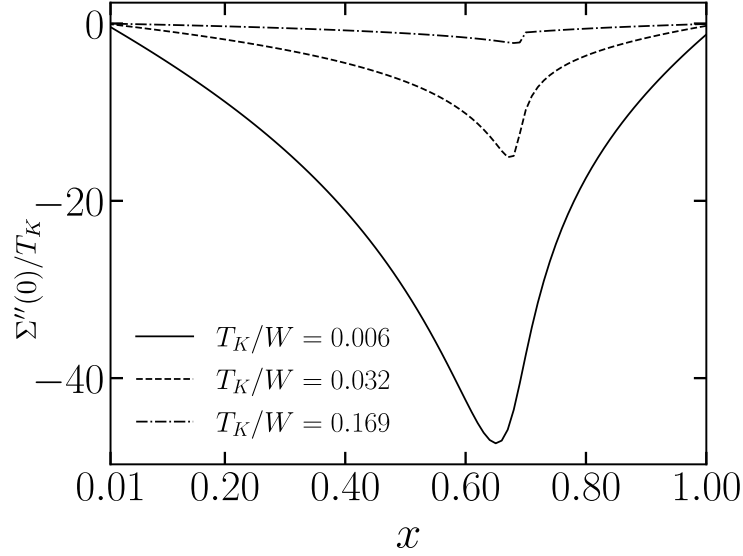


Figure 5.11: Imaginary part of self-energy $\Sigma''(0)/T_K$ for $T_K/W = 0.169, 0.019$ and 0.006 . $\Sigma''(0)/T_K$ is negative and increases with increasing T_K with a maximum at $x = n_c$.

pling, becomes large around this crossover at smaller coupling (see color/black-white gradient in figure 5.9).

In agreement with the spectral function analysis of section 5.3 for intermediate values of Kondo coupling, we found a third intermediate phase, which is separated from the dilute phase by a transition line in the $x - T_K$ phase diagram: at the critical concentration x^* , the effective mass m^* vanishes continuously. This transition separates the very dilute regime ($x < x^*$) with $m^* > 0$ from an intermediate regime ($x^* < x < n_c$) characterized by $m^* < 0$ (see inset of figure 5.10 and dashed line in figure 5.9). From our numerical data, we found a power law relation $T_K/W \propto (x^*)^\gamma$ with an exponent $\gamma < 1$ and the exponent itself depends on the filling n_c .

We found $\gamma = 0.71, 0.78$ and 0.83 for $n_c = 0.30, 0.70$ and 0.90 respectively as shown in the figure 5.12. This transition produces signatures in spectral function (see section 5.3) where two branches merge to one branch at x^* (see figure 5.4). Meanwhile, Fermi surface structures (see figure 5.5) do not show a clear signature of x^* . Keeping in mind that the dispersion relation is $\omega + \mu - \Sigma_{Alloy}(\omega) = \epsilon_{\mathbf{k}}$, the frequency dependence of the real part $\omega - \Sigma'_{Alloy}(\omega) + \Sigma'_{Alloy}(0)$ is represented in figure 5.13. We can thus interpret the transition at $x = x^*$ as the gradual formation (or extinction) of extra branches in the one-electron excitations, as suggested by the low-frequency dependence of this quantity, which changes from locally monotonous (at $x < x^*$) to locally non-monotonous (at $x > x^*$). The second branch could then be associated with coherent and dispersive singlet-triplet excitations that may propagate. Such triplet excitations are gaped out at strong Kondo coupling, but they

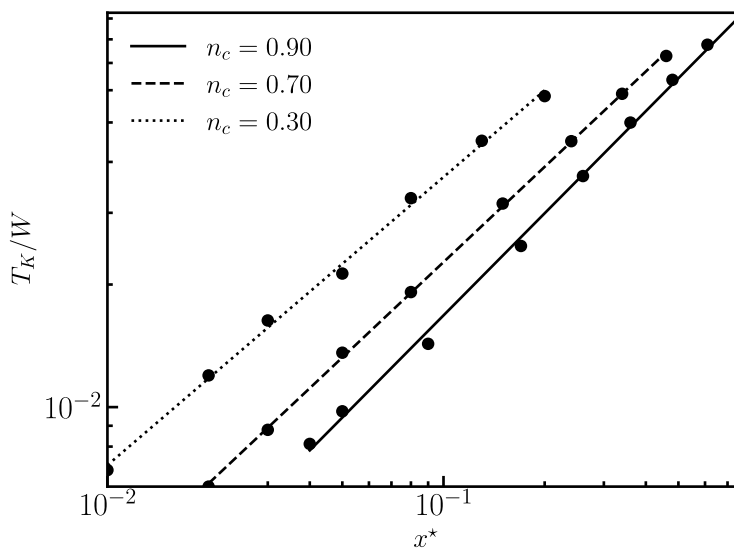


Figure 5.12: Evolution of the critical concentration x^* with respect to the Kondo coupling T_K/W presented here on $\log - \log$ scale. Solid line represent $n_c = 0.90$, dashed line represent $n_c = 0.70$ and dotted line represent $n_c = 0.30$ with a slope γ of 0.83 ± 0.013 , 0.78 ± 0.006 , and 0.71 ± 0.016 respectively.

might also reveal a pseudogap in PES at smaller Kondo coupling as analyzed in the section 5.3. This intermediate state is thus a precursor to the coherent state which is realized around $x \approx 1$. It is very interesting to see that such a pre-coherent state may start being formed at a relatively small concentration x^* .

Imaginary part of self-energy $\Sigma''(0)/T_K$ is presented in the figure 5.11. We quickly remark that $\Sigma''(0)/T_K < 0$, which shows that our calculation respects the causality. We could also observe that the $\Sigma''(0)/T_K$ increases considerably with increasing T_K while getting maximum value at $x = n_c$. This shows us that finite lifetime of quasiparticle is minimum at $x = n_c$. However, two very important features could make the transition at x^* observable experimentally: first, the imaginary part of $\Sigma''_{Alloy}(0)$ remains relatively small around x^* (see color/black-white gradient in figure 5.9 and figure 5.11). We can thus expect that the excitations are long lifetime quasiparticles that could be revealed by photo-emission. Secondly, x^* depends on the strength of the Kondo interaction. We may thus expect that this transition could be tuned by applying pressure on a compound with a fixed concentration x . Of course, we are aware that mechanical pressure is not fully compatible with ARPES experiments. However, since the underlying phenomenon is a transition in the one-electron excitation spectrum, we may expect signatures in other sorts of experiments that could be realized under pressure, e.g., Raman spectroscopy.

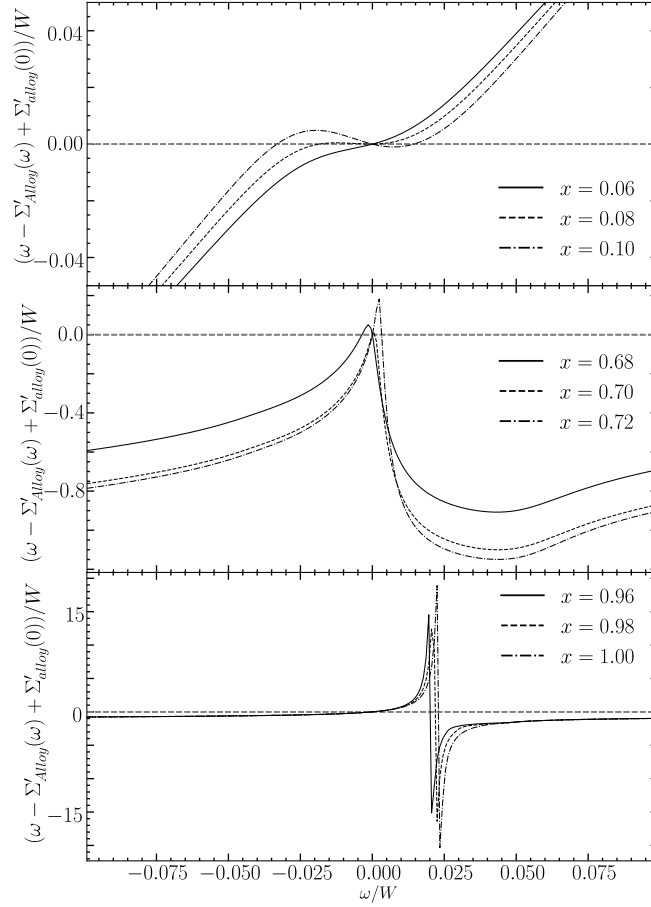


Figure 5.13: Frequency dependence of the real part of the self-energy, $\omega - \Sigma'_{Alloy}(\omega) + \Sigma'_{Alloy}(0)$ for $n_c = 0.70$ and $T_K = 0.019$. Top: for x in the vicinity of the critical point $x^* = 0.08$ which is characterized by $m^* = 0$, we observe the emergence of a non-monotonicity at low energy. This leads to the gradual formation of a multiple-branches dispersion for $x > x^*$. Center: for x in the vicinity of n_c , the maximum is realized at $\omega < 0$ for $x < n_c$ and at $\omega > 0$ for $x > n_c$ resulting in a second change of sign of m^* . Bottom: for x close to 1, we observe signatures of the singularity $\Sigma_K(\omega) = \frac{r^2}{\omega + \lambda}$ which is obtained in the mean-field approximation for the Kondo lattice. The non-monotonicity obtained at lower concentrations is reminiscent of this singularity, and we expect this feature to survive qualitatively beyond the mean-field approximation.

5.6 Discussion

Our results confirm the existence of a transition at $x = n_c$ between a coherent dense Kondo regime (for $x > n_c$) and a dilute Kondo regime (for $x < n_c$) [136]. This Lifshitz-like transition may be observed in ARPES experiments through the analysis of Fermi surface for Kondo alloys with a Kondo temperature higher than about 1/10 bandwidth. A shrinking of the Fermi-surface is expected when increasing x

in the dilute regime, while the Fermi surface is enlarged with x , in connection with the Luttinger theorem, in the coherent dense Kondo regime. It could be obtained experimentally in the materials with a relatively large T_K . We have also shown that this transition at $x = n_c$ becomes a crossover at smaller values of Kondo interaction.

While Doniach argument is recovered, with magnetically ordered ground states stabilized at very small Kondo coupling, we identified a broad region of parameters where an intermediate paramagnetic Kondo state can be stabilized. This corresponds to values of T_K between $W/100$ and $W/10$ with the regime of concentrations $x^* < x < n_c$ which can be realized in a large variety of heavy-fermion Kondo systems. Unlike the dilute and the dense Kondo states, this intermediate phase is characterized by a negative effective mass. Here, the negative effective mass does not mean instability, but it is rather a Fermi liquid phase. It corresponds to the emergence of an extra branch in the electronic dispersion and a formation of a pseudogap in the local density of states at $x > x^*$.

We also analyze the effects of decoherence resulting from disorder, which may spoil the possibilities of analyzing ARPES signals. We find that these effects are relatively small at strong Kondo coupling, which may make possible the observability of the transition at $x = n_c$. However, this requires compounds with a relatively large value of T_K . At smaller values of Kondo interaction, disorder-induced decoherence may become significant, with a maximal effect around $x = n_c$. This disorder-induced decoherence reduces the opportunities of observing signatures in the Fermi surface at $x = n_c$ for small coupling. We still expect relatively well-defined quasiparticles around $x = x^*$ even though contrary to the transition at $x = n_c$, the transition at $x = x^*$ cannot be observed directly from the Fermi surface structures. We considered an infinite coordination number, the fluctuations in neighboring atoms configurations [138] in our calculations are neglected. This might induce fluctuations of the local effective Kondo hybridization [165, 166, 248], resulting in additional broadening of spectral function. Indeed, the experiments involving low energy excitations (e.g. ARPES) are more appropriate. This opens rich perspectives for experimental investigations of the breakdown of coherence on Kondo alloys. Since we predict that x^* varies with the strength of the Kondo interaction, this transition might be realized not only by atomic substitution but also by applying pressure in a Kondo alloy with fixed stoichiometry (i.e. fixed x and n_c).

Chapter 6

Local potential scattering and charge inhomogeneity in Kondo alloys

In this chapter, we will present our results on local potential scattering and charge inhomogeneities in order to characterize the dilute and dense Kondo regimes. Similar to the previous chapter 5, here we will analyze different quantities with large Kondo coupling and also with Kondo coupling for various electronic filling upon the dilution of Kondo impurities. This will permit us to further characterize the critical concentrations at $x = n_c$ and $x = x^*$ seen through the photo-emission spectrum.

6.1 Introduction

6.1.1 Local potential scattering

We define local potential scattering (LPS) $S_a(i\omega)$ as

$$G_a^{cc}(i\omega) = G_0(i\omega + S_a(i\omega)) , \quad (6.1)$$

where the index a denotes either \mathcal{K} -site or \mathcal{N} -site, $G_0(i\omega) = 1/(i\omega - \epsilon_{\mathbf{k}})$ is non-interacting Green's function and $G_a^{cc}(i\omega)$ is local Green's function for conduction electrons as expressed in the equations (3.53 - 3.54). $S_a(i\omega)$ is a site dependent complex quantity with its real part can be seen as an effective energy level of conduction electron on a given site with respect to the non-interacting bandwidth. By comparing this real part with the chemical potential $\mu_0(n_c)$ for non-interacting electrons with n_c electronic filling as defined by the Eq. (6.2), we can deduce hole-dopant or particle-dopant nature of the quasiparticles.

$$n_c = \int_{-W/2}^{\mu_0(n_c)} \rho_0(\omega) d\omega \quad (6.2)$$

Furthermore, the imaginary part of $S_a(i\omega)$ is linked with the quasiparticle's

lifetime. Thus, one can extract the information about localized or itinerant behavior of f -electrons depending upon the position of the $S_a(i\omega)$ to the non-interacting bandwidth.

In this chapter, we will only concentrate on static part of LPS at zero frequency. Thus, we define

$$S_a(0) = S'_a + iS''_a, \quad (6.3)$$

where S'_a and S''_a are real and imaginary part of $S_a(0)$.

Local potential scattering was previously studied for Bethe lattice in [138] in the Kondo alloy model using two complementary DMFT and stat-DMFT approaches while taking account of structural disorder fluctuations due to impurity substitution. In their study, they found that the real part of the LPS can shift outside the non-interacting electronic bandwidth while depleting Kondo sites. They also found a clear signature of Kondo lattice coherence breakdown $x = n_c$ marking emergence of two Fermi liquid phases: a coherent Fermi liquid for $x > n_c$ and a local Fermi liquid $x < n_c$ at strong J_K .

6.1.2 Charge inhomogeneity

It was first in 1934, Wigner [249] introduced the concept of charge ordering, the long-range ordered pattern of electron density, in the gas of electrons. Following its first introduction, numerous systems [250] have been found showing charge ordering. In strongly correlated systems, charge ordering is found in transition metal compounds like in manganates [251, 252]. Again in SCES, charge ordering is found to cause multiferroicity [253] in some groups of strongly correlated systems. Regarding f -electron systems, the charge ordering is less common but can occur in the systems where the intersite Coulomb interaction may be strong enough to lead to a 4f-charge disproportionate like in Yb_4As_3 [254, 255].

Charge order was studied previously in Kondo lattice system [208] at quarter filling using DMFT where the paramagnetic charge-ordered state was found for small coupling strengths for a bipartite Bethe lattice, and it vanishes as a first-order phase transition for strong coupling. In this study, the charge order was found to be an insulator. Further, charge order was also studied in a two-dimensional Kondo Lattice Model [210] using two complementary approaches: variational Monte Carlo method [78] for the ground state and cellular dynamical mean-field theory [256]. In their study, they found charge order as an insulator at quarter filling.

In this part of this chapter, inspired from previous studies of charge order, we will analyze charge inhomogeneities present between Kondo and non-Kondo sites. Thus, we define the charge occupation for each type of site as

$$n_a = \frac{1}{\beta} \sum_{i\omega} G_a^{cc}(i\omega), \quad (6.4)$$

where the occupation $n_{\mathcal{K}}$ and $n_{\mathcal{N}}$ satisfies a sum rule $n_c = xn_{\mathcal{K}} + (1 - x)n_{\mathcal{N}}$.

6.2 Results: Local Potential scattering

Here, we present our LPS results at Fermi level ($\omega = 0$) for 2D square lattice, however, supplementary calculations for Bethe lattice were also performed, and we got similar results as obtained in [138], and are presented in the appendix C.3. As before in the chapter 5, we consider two Kondo coupling: a relatively large Kondo coupling $T_K/W = 0.169$ and an intermediate Kondo coupling $T_K/W = 0.019$ in order to analyze LPS to find additional signatures of the critical concentrations $x = x^*$ where the cancellation of effective mass m^* occurs (see section 5.3) and $x = n_c$ where Lifshitz-like transition occurs (see chapter 5.4).

6.2.1 Large T_K case

At first, we focus on a large Kondo coupling scenario with $T_K/W = 0.169$ for $n_c = 0.70$ where evidence of Lifshitz-like transition was observed through the analysis of Fermi surface structures (see section 5.4). Figure 6.1 represents the results for the LPS at Fermi level for large coupling. An obvious limit to analyze should be the Kondo lattice limit ($x \simeq 1$). At Kondo lattice limit ($x \simeq 1$), the real part $S'_{\mathcal{N}}$ is situated outside the electronic bandwidth with finite positive imaginary part, and the real part $S'_{\mathcal{K}}$ is inside the electronic bandwidth with the negligible but non-negative imaginary part. One should notice that $S'_{\mathcal{K}}$ is almost constant for the concentrations $x > n_c$. This shows the extent of coherence of coherent dense regime up to the concentration $x > n_c$ as in [138] for Bethe lattice at finite J_K . For $x = 1.00$, S' equals to the chemical potential of non-interacting electrons $\mu_0(n_c + 1)$, with $n_c + 1$ electronic filling. This corresponds to the large Fermi surface verifying the Luttinger 'theorem' [134] where all the fermionic degree of freedoms participates in the formation of the Fermi surface. Upon dilution, at $x = n_c$, both quantities $S_{\mathcal{K}}$ and $S_{\mathcal{N}}$ presents discontinuities.

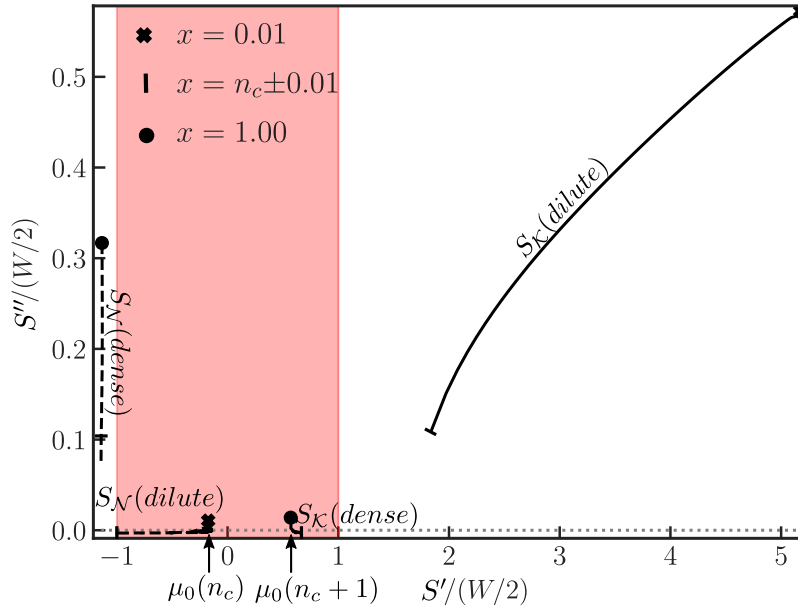


Figure 6.1: Evolution of local potential scattering $S_a(0)$ for $n_c = 0.70$ relatively large Kondo coupling $T_K/W = 0.169$ represented on Argand diagram. Solid line represent LPS for \mathcal{K} -site whereas dashed line represent LPS for \mathcal{N} -site. (•) indicates Kondo lattice ($x = 1.00$), short vertical solid line indicates the concentrations $x = n_c \pm 0.01$ and (•) the most diluted case ($x = 0.01$). Light red background highlights the electronic bandwidth W .

At $x < n_c$, $S'_{\mathcal{K}}$ crosses out the non-interacting bandwidth through the upper limit while $S'_{\mathcal{N}}$ enters inside the non-interacting bandwidth through lower limit. Interestingly, $S''_{\mathcal{K}}$ acquire a finite value whereas $S''_{\mathcal{N}}$ cancels out. For $x \ll n_c$, $S'_{\mathcal{N}}$ coincide with the chemical potential $\mu_0(n_c)$ corresponding to a small Fermi surface. In contrast to the previous calculations in [138] for the Bethe lattice, here we did not observe the change of sign in the imaginary part of LPS for either \mathcal{K} -site or for \mathcal{N} -site.

6.2.2 Low T_K case

From our previous analysis of spectral function in the low Kondo coupling case, we had identified a new critical concentration x^* where the cancellation of effective mass happens. Here, we present and analyze results for the same value of $T_K/W = 0.019$ and for $n_c = 0.70$. Figure 6.2 present the LPS for \mathcal{K} -site and \mathcal{N} -site for low T_K case. As soon as we compare the figure 6.2 for low T_K case with the figure 6.1 for large T_K , we find two clear differences: *i*) the discontinuity at $x = n_c$ for both $S'_{\mathcal{K}}$ and $S'_{\mathcal{N}}$ disappears and *ii*) $S'_{\mathcal{N}}$ is always situated inside the electronic bandwidth. Like for the large T_K , at $x = 1.00$, $S'_{\mathcal{K}}$ corresponds to $\mu_0(n_c + 1)$ showing that the Luttinger

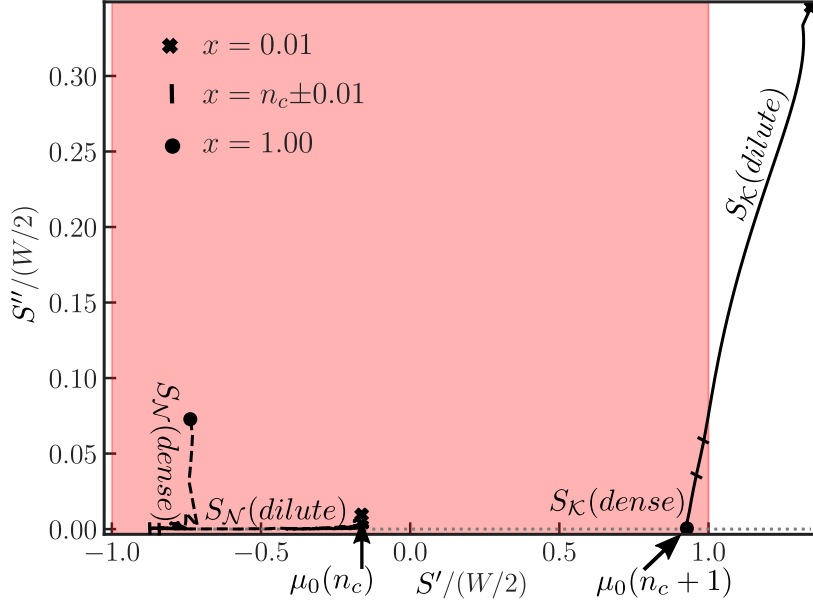


Figure 6.2: Evolution of local potential scattering $S_a(0)$ for $n_c = 0.70$ relatively low coupling $T_K/W = 0.019$ represented on Argand diagram. Solid line represent LPS for \mathcal{K} -site whereas dashed line represent LPS for \mathcal{N} -site. (\bullet) indicates Kondo lattice ($x = 1.00$), short vertical solid line indicates the concentrations $x = n_c \pm 0.01$ and (\ast) the most diluted case ($x = 0.01$). Light red background highlights the electronic bandwidth W .

theorem is still verified. Even though the discontinuity at $x = n_c$ disappears, $S'_{\mathcal{K}}$ crosses the upper limit shortly after $x = n_c$ marking the extent of coherence of Kondo lattice. Thus, this disappearance of discontinuity at $x = n_c$ translates the transformation of dilute-dense transition into a crossover. Upon further dilution of magnetic impurities at $x \ll n_c$, $S'_{\mathcal{N}}$ corresponds to the chemical potential $\mu_0(n_c)$ and also $S''_{\mathcal{N}}$ cancels out. LPS clearly presents evidence of Lifshitz-like transition, but it was unable to present any signatures of the transition at $x = x^\ast$.

6.3 Results: Charge inhomogeneity

In this section, we present our results on the average charge occupation and its average distribution over the randomly distributed \mathcal{K} -sites and \mathcal{N} -sites to study further the critical concentrations: $x = n_c$ and x^\ast in paramagnetic Kondo phase. We also analyze the distribution of charge between the Kondo sites and non-Kondo sites concerning the impurity concentration x and electronic filling n_c . It permits us to study the distribution of charge inhomogeneity with the alloying effect.

Let us first start by analyzing the infinite $J_K \rightarrow \infty$ case. In this case, we can derive

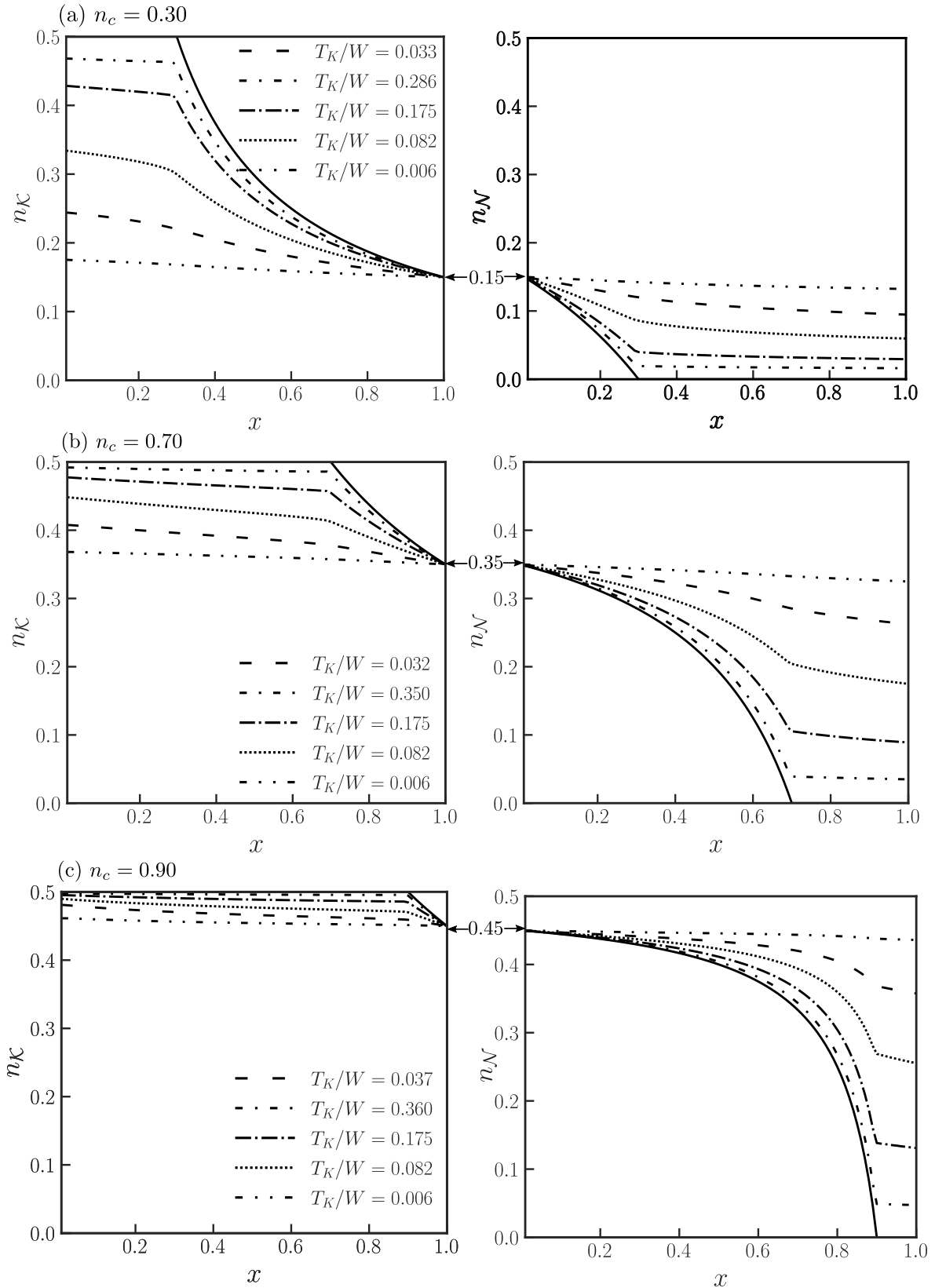


Figure 6.3: Charge occupation on \mathcal{K} and \mathcal{N} -sites with the dilution of magnetic impurities x for different Kondo temperature T_K . Left: occupation for Kondo site, Right: occupation for non-Kondo site. The solid lines represent theoretical values expected for $T_K/W \rightarrow \infty$. $n_{\mathcal{K}}$ and $n_{\mathcal{N}}$ verifies the sum rule as: $x n_{\mathcal{K}} + (1 - x) n_{\mathcal{N}} = n_c$.

two relations for charge occupations in two different regimes: $x < n_c$ and $x > n_c$ and is presented in the Eq 6.5.

$$\begin{aligned}
 & x < n_c , & & x > n_c , \\
 & n_{\mathcal{K}} = 0.5 , & & n_{\mathcal{N}} = 0 , \\
 & xn_{\mathcal{K}} + (1-x)n_{\mathcal{N}} = n_c/2 , & & xn_{\mathcal{K}} + (1-x)n_{\mathcal{N}} = n_c/2 , \\
 & \text{gives } n_{\mathcal{N}} = n_c - x/2(1-x) . & & \text{gives } n_{\mathcal{K}} = n_c/2x .
 \end{aligned} \tag{6.5}$$

From the above figure 6.3, we can observe that at the large Kondo coupling $T_K/W = 0.350$, our results follow the theoretical large Kondo coupling limit (see Eq. 6.5). For dense regime $x > n_c$, the occupation $n_{\mathcal{K}}$ rises steadily upon depleting Kondo atoms up to $x = n_c$, and $n_{\mathcal{N}}$ is zero. This is because all the conduction electrons are occupied, forming singlets with impurities electrons. In our case, $n_{\mathcal{N}}$ is not rigorously zero since the Kondo coupling is not infinite. The dense-dilute transition concentration at $x = n_c$ is marked by a kink in $n_{\mathcal{K}}$ and $n_{\mathcal{N}}$ for the large T_K . For dilute regime $x < n_c$, $n_{\mathcal{N}}$ increases gradually whereas $n_{\mathcal{K}}$ becomes a plateau with a value 0.50. Lowering T_K increases the probability of charge occupation in non-Kondo sites even at $x \approx 1.0$ and suppress the kink present at $x = n_c$. Thus, charge inhomogeneity is present in Kondo alloys between Kondo and non-Kondo sites upon dilution, and the intensity of charge inhomogeneity decreases with decreasing Kondo coupling.

6.4 Discussion

In this chapter, we have analyzed local potential scattering and charge inhomogeneity with substitution to find new signatures of the transitions at $x = x^*$ and $x = n_c$. At first, we can observe that for large Kondo coupling at $x \gtrsim n_c$, $S'_{\mathcal{N}}$ is situated outside and below of non-interacting electronic bandwidth, showing that \mathcal{N} -sites are empty. However, $S'_{\mathcal{K}}$ is found inside the non-electronic bandwidth, with $S'_{\mathcal{K}}$ corresponding to $\mu_0(n_c + 1)$ at $x = 1.00$. This verifies the Luttinger theorem and shows that the occupied Kondo sites behave like particle doping for the concentrations $x \gtrsim n_c$ even for the low T_K . Furthermore, $S''_{\mathcal{K}}$ is very small, indicating the quasiparticles are well-defined with a long lifetime on Kondo sites. This result is concordant with the large Fermi surface and self-energy found in the previous chapter 5 in the dense regime. Upon dilution for large Kondo coupling, at $x \simeq n_c$, $S'_{\mathcal{K}}$ shifts outside above while $S'_{\mathcal{N}}$ enters inside the non-interacting bandwidth. This shows that all the \mathcal{K} -sites are fully occupied and don't contribute to the transport properties. On the other hand, at the very dilute case, $S'_{\mathcal{N}}$ situated inside the non-interacting bandwidth corresponds to $\mu_0(n_c)$, confirming the small Fermi surface. In this case, the quasiparticles in \mathcal{N} -sites are well-defined since $S''_{\mathcal{K}} \simeq 0$. However, as expected, from the charge occupation,

the probability of occupation of non-Kondo sites increases with decreasing T_K even for the dense regime. The transition between dilute and dense Kondo regimes at large T_K happens at $x = n_c$ is marked by a discontinuity in local potential scattering and a sudden rise in occupations of non-Kondo sites. We again confirm that this transition at $x = n_c$ becomes a mere crossover for intermediate to low T_K , since the discontinuities in local potential scattering disappear and the kinks in charge occupations become smoother. In this study, either local potential scattering or charge occupations gave any signatures of the transition at $x = x^*$ or negative effective mass of quasiparticles. This can be understood since the transition at $x = x^*$ is related to the electronic excitation spectrum, thus not accessible at zero energy.

Chapter 7

Conclusion and Perspectives

In this part of the thesis, we have thoroughly studied f -electron substitution in Kondo alloys which permitted us to answer multiple pending questions related to lattice coherence and its breakdown.

For this study, we used DMFT to treat the disorder in combination with the mean-field coupling of the Kondo interaction. Firstly, the study of the paramagnetic phase was carried out by using matrix DMFT, which was already developed previously. However, the study of magnetically ordered phases for the binary alloy with substitution needed its generalization. Thus, we generalized this formalism in order to incorporate magnetically ordered phases with the disorder. On the purely theoretical side, this generalization is an original work of this thesis. Using the above methods, we constructed at first the phase diagram of the Kondo lattice ($x = 1.00$) for the 1D chain, 2D square, and 3D cubic lattices. For this particular study, we considered a wide range of electronic fillings n_c along with low to strong Kondo couplings. The results obtained for all three lattices were consistent with previous studies proving the pertinence of our numerical approach. Thereafter, we diluted the impurity concentration for only 2D square system by tuning x for $n_c = 0.30, 0.70, \text{ and } 0.90$. We obtained a Doniach-like phase diagram with Kondo substitution marked by magnetically ordered phases dominating at low J_K .

Even though this study is theoretical, the experimental relevance of our results was not left behind. Our magnetic phase diagrams of Kondo alloys were compared with the experimental data of Ce-La substitution for various cerium-based heavy-fermions. Our comparisons were consistent, and it provided how the Kondo alloys with the magnetically ordered ground-state like in CeCu_2Ge_2 [100] or the paramagnetic Kondo ground-state like in CePt_2Si_2 [99] can resist the dilution of magnetic impurities.

After the generalization of Doniach's argument to Kondo substitution, our study focuses on the study of the breakdown of the coherent Kondo phase. For this, we analyzed photoemission spectra, local potential scattering, and charge inhomogeneity under dilution while varying Kondo coupling. Predicted results [136] were

obtained for large Kondo coupling on the dense ($x \sim 1.00$) and dilute ($x \sim 0.01$), with large and small Fermi surfaces respectively. Furthermore, the analysis of local potential scattering on Kondo-sites ($S'_{\mathcal{K}}$) confirms the verification of the Luttinger theorem [134] at the dense regime for all the values of Kondo couplings. The transition between the dilute and dense regimes happens around $x = n_c$ for Kondo strength $T_K/W \gtrsim 0.10$. This transition is characterized by Lifshitz-like transition and the shifting of $S'_{\mathcal{K}}$ outside and above the non-interacting bandwidth, revealing that the transport properties are assured only from the movement of electrons on the \mathcal{N} -sites. As T_K/W decreases, the probability of charge occupation at \mathcal{N} -sites increases. Thus, for $T_K/W \lesssim 0.10$, a crossover happens between the dense and dilute regimes. Surprisingly for intermediate to low Kondo strength, the crossover at $x \simeq n_c$ is followed by a vast region where quasiparticles acquire negative-effective masses with two-branches electronic dispersion. In this negative-mass region, $S'_{\mathcal{K}}$ also shifts outside and above the non-interacting bandwidth, as seen for large T_K/W . At the end of this negative effective mass region, we found the presence of a critical concentration x^* where the quasiparticle effective mass cancels out. This critical concentration x^* was characterized by the merging of two the spectral function bands. This result was completely unexpected. Compiling all the information, we constructed more detailed versions of the phase diagram for Kondo alloys for various n_c .

In the continuation of this work, one could explore the optical conductivity in CPA formalism [257–264] to find the signatures of the transitions at x^* and $x = n_c$. Indeed, optical conductivity can provide additional information about particle-hole nature of quasiparticle, spectral weight [265] which is also linked with electron mass and also possible non-Fermi liquid behavior [266]. From a fundamental point of view, this work also suggests the possible emergence of exceptional points at x^* where two dispersive branches merge and m^* vanishes. Recently, the presence of exceptional points along with the Kondo effect was proposed on multiple occasions [90, 267] by theoretical means. In appendix D, we propose an origin of negative mass. This has to be further developed and analyzed in the context of the exceptional point, which makes it another promising perspective of this thesis.

Our extension of matrix DMFT formalism only considers two commensurate magnetically ordered phases: Néel ordered antiferromagnetic phase and ferromagnetic phase. So, in future works, this work can be extended to include other commensurate and non-commensurate magnetically ordered phases. We have also omitted the possibility of having coexisting phases, which has been a subject of study in multiple theoretical studies [109, 111, 213, 268] primarily for Kondo lattices. In future works, the effect of disorder and alloying could be studied on the coexistence of multiple phases.

Experimental consistencies of transition between dilute-dense paramagnetic Kondo phases still remain to be explored. An obvious choice would experiment like ARPES or dHvA can give direct access to the electronic structure and thus can provide di-

rect evidence of our predicted transitions. There might be a need to apply external pressure to cross the transition temperature of $x = x^*$ and $x = n_c$. Knowing that these experimental probes are not fully compatible with the applied external pressure, an alternative option would be Compton scattering. It can be conducted with respect to various experimental conditions like external pressure, atomic substitution, temperature, or magnetic field. More recently, Compton scattering experiments were successfully conducted on Kondo lattices CeRu_2Si_2 [269] and YbRh_2Si_2 [270] in order to explore the Fermi surfaces related to localized versus itinerant behavior of f -electrons.

Part II

5f electrons in Uranium alloys

Chapter 8

Introduction

In continuation of our study of strongly correlated f -electron materials, in this part of this thesis, we proceed to $5f$ systems. In $5f$ systems, due to their non-integer partially filled shells, multiple energy scales compete with each other: the exchange bandwidth, the $5f$ bandwidth, the spin-orbit interaction, and intra-atomic $f - f$ Coulomb interaction. The interplay and competition between these interactions can give rise to a very complex phase diagram at low temperature with conventional phases like ferromagnetic [29], antiferromagnetic [178], or conventional superconductivity, unconventional heavy-fermion superconductivity [29, 178] or even some sometimes enigmatic states [271]. This plethora of phases with very different microscopic mechanisms makes them interesting to study.

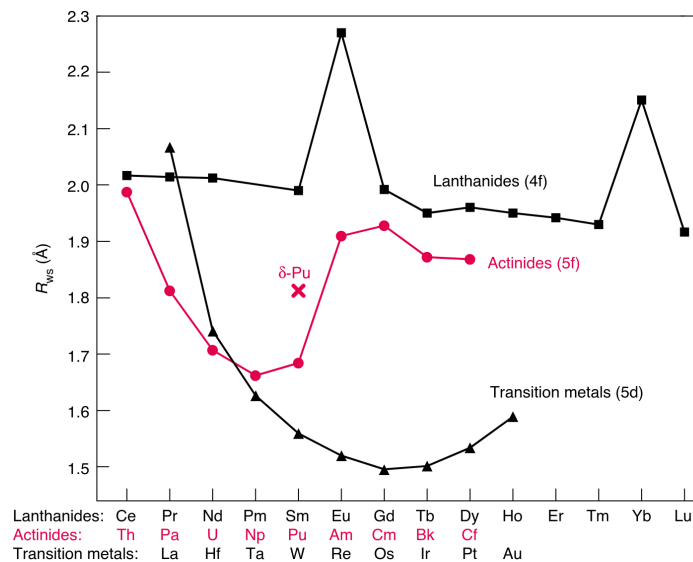


Figure 8.1: Wigner-Seitz radius (R_{WS}) of $5d$, $4f$ and $5f$ metals as a function of atomic number Z , where Wigner-Seitz radius is defined as $(4\pi/3)R_{WS}^3 = V$ while V being the equilibrium volume of the primitive unit cell. From [272]

Upon the $5f$ -shell filling, the f -electrons can be either localized, itinerant, or

sometimes ambiguously can acquire both localized and non-localized characteristics [10, 250, 273]. Let us focus, at first, only on the localized versus itinerant behavior in actinides. This can be visualized by comparing the Wigner-Seitz radius of actinides with transition metals and rare-earth metals. Figure 8.1 presents this comparison. With the increase in $5f$ -electrons count, at first, the volume of actinides decreases similarly as transition metals, and then a sharp rise is noticed around Pu. After Pu, the Wigner-Seitz radius evolves similarly to rare-earth atoms. These two different tendencies mark both the itinerant and localized behavior of $5f$ electrons, and the frontier between them lies near Pu. Additionally, clear evidence of these two different tendencies are also observed through various experiments where transuranium (primarily Np, Pu, and Am) compounds were found to have analogous features as the rare-earth compounds [274–278] and the f -electrons in light actinides have the tendency to be itinerant. Similarly, we can observe that uranium lie between these two tendencies, and thus $5f$ states can also be seen as intermediate states between $3d$ and $4f$ states.

8.1 Nature of $5f$ electrons in uranium based compounds

8.1.1 Hill criterion

In 1970, H. Hill [280] proposed a criterion based on f -atom spacing to explain the formation of ground-state phase with localized or itinerant f -electrons. Figure 8.2 shows the critical temperatures of various uranium-based compounds according to uranium-uranium atomic distance. From this figure, we can observe that phases with itinerant electrons occur at a short uranium-uranium distance, whereas the phases with localized electrons occur at a large uranium-uranium distance. Overall, this Hill limit between itinerancy and localization lies around 3.5 \AA . To understand this criterion, we can look out to the $5f$ wave function, which is more spatially extended than that of $4f$ wave function (see figure 1.2). Thus, $5f$ wave function can overlap with their neighboring sites to form coherent Bloch states within the Hill limit.

The itinerant scenario promoted by Hill criterion for UB_2 with U-U distance of 3.123 \AA smaller than Hill limit was confirmed through angle-resolved photoelectron spectroscopy [281] where $5f$ states participate in the formation of Fermi surfaces. On the other hand, the localized $5f$ states were found on UPd_3 [282, 283] with large U-U separation.

8.1.2 Heavy fermions

From the figure 8.2, we can observe that some compounds like UPt_3 , UBe_{13} do not obey the Hill criterion even with a large U-U distance. More interestingly,

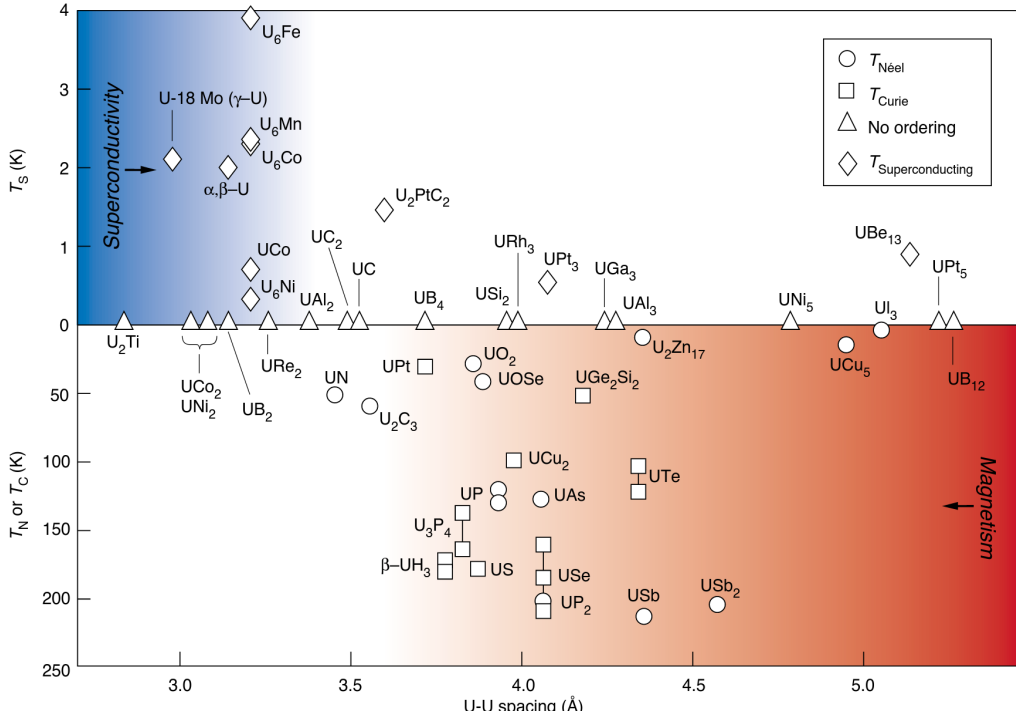


Figure 8.2: Hill plot for various uranium based compounds showing the transition temperatures of itinerant or localized f -electron phases with respect to inter-atomic uranium-uranium distance. From [279].

they can gain quasiparticle mass hundreds of times of bare electron mass [28, 284, 285]. Furthermore, the discovery of heavy-fermion with metallic low-temperature behavior [284, 286] with narrow $5f$ bands in these compounds came as a surprise. Until now, ten uranium-based heavy fermions are found: $U\text{Be}_{13}$, $U\text{Pt}_3$, $U\text{Pd}_2\text{Al}_3$, $U\text{Ni}_2\text{Al}_3$, $U\text{Ru}_2\text{Si}_2$, $U\text{Ge}_2$, $U\text{Ir}$, $U\text{CoGe}$, $U\text{RhGe}$, and $U\text{Te}_2$. One can be tempted to relate the heavy fermionic behavior of $4f$ compounds with those of $5f$ compounds. However, here we deal with intermediate valent compounds [287] with no distinct valence peaks [288], thus the Kondo mechanism treated in the first part of this thesis is excluded. Thus, this raises the question about the microscopic mechanism that leads to heavy fermions.

8.2 Microscopic mechanism: dualism of f -electron

In this section, we present the dual nature of $5f$ -electrons as a microscopic mechanism that can lead to the heavy fermionic behavior in uranium-based compounds. In our case, a part of $5f$ electrons is itinerant, whereas the remaining remains localized. The itinerant part comes from the hopping mediated through the hybridization with conduction states. Thus, the itinerant part participates in the formation of the Fermi surface. On the other hand, the localized part gets scattered off giving effective mass

enhancement, similarly as for Pr metal where heavy-mass of conduction electrons results from virtual crystal-field excitations of localized $4f^2$ electrons [289].

This dual model [290] showed some faithful results on effective masses and dHvA frequencies on UPt₃ [17] and UPd₂Al₃ [291] when compared with the experiment results [292, 293]. Furthermore, the dual model applied to UPt₂Si₂ [294] was consistent with the experimental observation of probable field-induced first-order Lifshitz-type transition.

Apart from these successful applications, a clear sign of dual nature of f electrons for UPd₂Al₃, UPt₃ was observed by identifying the high-resolution photoemission spectra [287, 295] with a localized system UPd₃ and an itinerant system UB₂. More recently, two different types of X-ray experiments were employed to UM₂Si₂ (M=Pd, Ni, Ru, Fe), which showed both localized and itinerant $5f$ states with different levels of itineracy for each compound depending upon their $5f$ band-filling. The co-existence of superconductivity along with ferromagnetism found in UCoGe and URhGe [296] is also compatible with this vision of the dual character of f -electrons. Similarly, Lifshitz transitions were observed in UCoGe [297] indicates further the dual picture of $5f$ states. Furthermore, in these heavy fermionic systems, f -electron count was found to be somewhere between 2 and 3 [287, 298–300], supports our dual picture.

8.3 Phenomenological modeling of duality

Duality was a direct or indirect subject of study on multiple studies through various approaches. We could note particularly, the case when orbital-selective localization: electrons get Mott localized in particular orbitals while other remains delocalized on other orbitals. Several mechanisms were proposed that can lead to the orbital-selective localization: crystal-field splitting of two bands of equal bandwidth [301] where orbital-selective localization can occur under doping, crystal field splitting of multi-band systems with unequal kinetic energy of electrons, band hopping anisotropies [302], the Hund's rule coupling enhances the orbital differentiation [56, 303].

The above examples concern primarily $3d$ and $4d$ systems with large crystal-field, however the crystal-field effect on $5f$ systems is rather small or irrelevant when compared to other interactions. Thus, here we propose that the competition between intra-atomic correlations and hopping leads to orbital-selective localization. More precisely, intra-atomic correlations resulting from the anisotropic part of the Coulomb repulsion may considerably enhance pre-existing hopping anisotropies where the states with sub-dominant hopping channels get localized.

8.3.1 Model Hamiltonian

In this section, we present our model Hamiltonian. Due to the large nuclear charge in uranium, the spin-orbit interaction ¹ is of the order of 1 eV. This large spin-orbit interaction makes the electrons couple with their individual angular momentum jj -coupling instead of LS -coupling. With $l = 3$ being orbital angular momentum and $s = \frac{1}{2}$ being the spin and large spin-orbit, we use total angular momentum $l \otimes s = (j = \frac{5}{2}) \oplus (j = \frac{7}{2})$ basis as single-particle states instead of $l = 3$, magnetic quantum number m and spin s , noting that both basis are equivalent and transformation between two basis are unitary. Figure 8.3 show a schematic view is of this spin-orbit coupling. Since the spin-orbit splitting between $j = 5/2$ and $j = 7/2$ is around 1 eV, we do not consider the states with $j = 7/2$ [304]. Thus, we write our Hamiltonian on jj_z basis set, with j_z being azimuthal quantum number

$$\mathcal{H} = \sum_{\langle a,b \rangle, j_z} t_{j_z} c_{aj_z}^\dagger c_{bj_z} + H_{Coul.}, \quad (8.1)$$

where $c_{aj_z}^\dagger$ (c_{aj_z}) denotes creator(annihilator) operator which creates(annihilate) a 5f-electron on site a with angular momentum $j = 5/2$ and z -components $j_z = -5/2 \dots 5/2$, t_{j_z} is the nearest site hopping in orbital index j_z . First term describes the Kinetic energy operator whereas the $H_{Coul.}$ describes the local Coulomb repulsion which is identical as in [60] will be defined more precisely in the chapter 9.

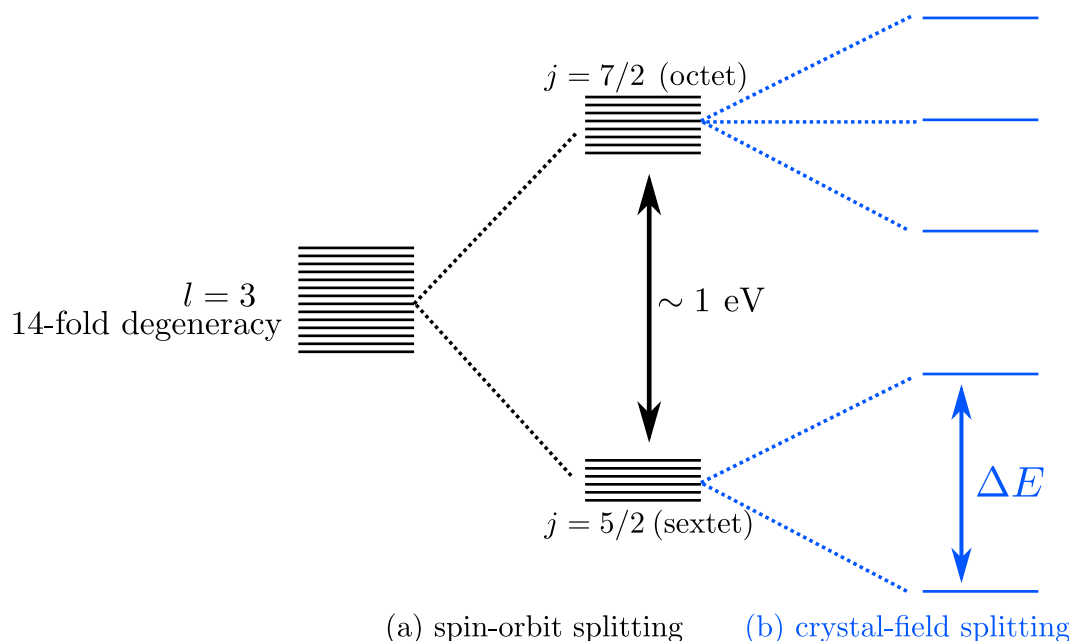


Figure 8.3: Schematic view jj -coupling scheming for an local f -electron. (a) spin-orbit splitting and (b) crystal-field splitting. Since, 5f electrons are closer to the nuclei, thus the crystal-field splitting is smaller and less relevant.

¹The spin-orbit interaction scales as Z^4 with the atomic number.

8.3.2 Approaches

We intend to solve the Hamiltonian (8.1), but full microscopic treatment becomes very tedious since the Hilbert space increases exponentially with the number of uranium sites. However, the treatment becomes possible for the small clusters like in [60], where this model Hamiltonian was solved for two, three, and four site clusters which captured the essential physics. Figure 8.4 presents a phase diagram obtained through exact diagonalization for a two-sites cluster with five electrons, characterized by z -component of the total angular momentum $\mathcal{J}_z = J_{1z} + J_{2z}$, where J_{1z} and J_{2z} are angular momentum projections on site 1 and 2 respectively. In this study, orbital-dependent partial localizations of f -electrons occurs with five partially localized phases: two ferromagnetically correlated phases with $\mathcal{J}_z = 15/2, 11/2$ and three antiferromagnetically correlated phases with $\mathcal{J}_z = 1/2, 3/2, 5/2$ were found. For $t_{3/2} > t_{1/2}$, at weak hopping, phase with $\mathcal{J}_z = 15/2$ determined by fully localized $j_z = 5/2, 1/2$ and delocalized $j_z = 3/2$ was obtained. It was seen that the increase in hopping $t_{3/2}$ partially breaks the Hund's rule with $t_{3/2} > t_{1/2}$, thus at intermediate hopping a phase with $\mathcal{J}_z = 5/2$ and at high hopping a phase $\mathcal{J}_z = 11/2, 1/2$ was observed. Furthermore, for $t_{3/2} < t_{1/2}$, a phase with $\mathcal{J}_z = 3/2$ was observed with empty $j_{-3/2}$.

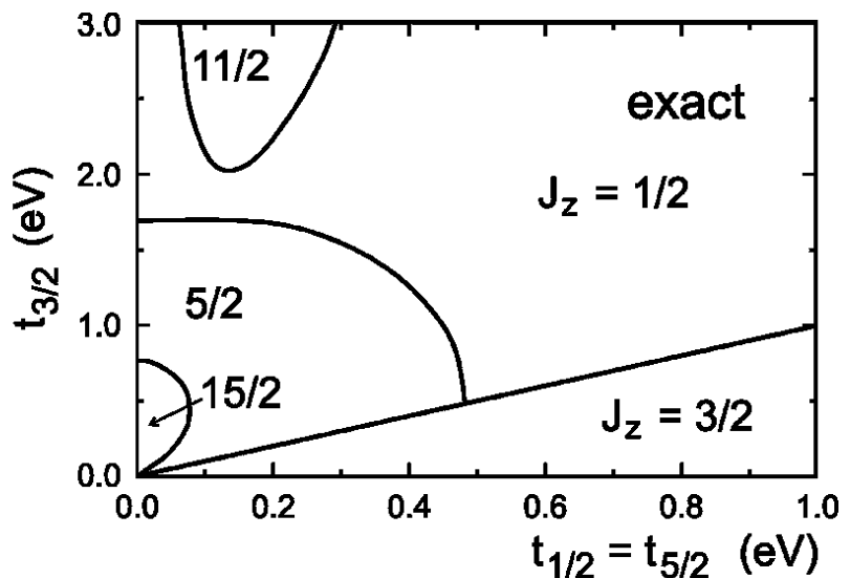


Figure 8.4: Phase diagram obtained through exact diagonalization for two-sites cluster, derived from total magnetization $\mathcal{J}_z = J_{1z} + J_{2z}$, where J_{1z} and J_{2z} are angular momentum projections on site 1 and 2 respectively. Here, only f^2 and f^3 configurations are considered. $t_{3/2}$ and $t_{1/2} = t_{5/2}$ are nearest-site hopping along orbitals $j_z = 3/2$ and $j_z = 1/2, 5/2$ respectively. Extracted from [60, 305]

Similarly, approaches with approximations and simplifications can also be applied. For example, cluster perturbation theory was employed for linear chain [250,

306] to calculate $5f$ spectral functions. In their study, both dispersive quasiparticle peaks near Fermi energy and incoherent local excitations were seen at the low-energy part of the spectra, suggesting the dual nature of $5f$ electrons. Even though small cluster calculations give essential qualitative physics related to duality, the physical properties in the thermodynamic limit remain to be explored. Thus, in this present work, we adopt a slave-boson mean-field approach to find the ground-state phase diagram.

8.4 An outline to slave-bosons approaches

In this section, we will give details on various slave-bosons approaches with their advantages and drawbacks. The slave-boson representations were first introduced by Holstein-Primakoff [307] and Schwinger [308] where spins operators may be represented by Bose operators. But, it was Barnes [71, 309] who first introduced a representation involving both auxiliary bosonic and fermionic operators for Anderson model [310]. This particular method was further generalized to cure its defaults. Thus, there is not only one possible slave boson representation, but rather multiple versions of them exist [72, 74, 309, 311] which are more or less connected to each other. Below, we present two versions of slave-bosons representations in order to present a general idea behind the slave-bosons approaches.

8.4.1 Barnes' representation

In this slave-bosons approach [71, 309], the idea is to decompose the local electronic excitations into spins and charge degree of freedom by using bosonic and fermionic operators. With this idea, Barnes mapped the four physical states of an electron by using two bosonic and one fermionic operators. The table 8.1 resumes the mapping.

<u>Initial physical states</u>	<u>Barnes's slave boson representation</u>
$ 0_i\rangle \mapsto vac\rangle$	$ 0_i\rangle \mapsto e_i^\dagger vac\rangle$
$ \uparrow_i\rangle \mapsto c_{i\uparrow}^\dagger vac\rangle$	$ \uparrow_i\rangle \mapsto f_{i\uparrow}^\dagger vac\rangle$
$ \downarrow_i\rangle \mapsto c_{i\downarrow}^\dagger vac\rangle$	$ \downarrow_i\rangle \mapsto f_{i\downarrow}^\dagger vac\rangle$
$ \uparrow\downarrow_i\rangle \mapsto c_{i\uparrow}^\dagger c_{i\downarrow}^\dagger vac\rangle$	$ \uparrow\downarrow_i\rangle \mapsto d_i^\dagger vac\rangle$

Table 8.1: Table resumming Barnes slave-boson representation

In the table 8.1, $|vac\rangle$ denotes vacuum state and e_i^\dagger, d_i^\dagger are bosonic operators corresponding to an empty and doubly-occupied site whereas $f_{i\sigma}^\dagger$ is fermionic creation operator for an electron of spin σ in a site i . Similarly, e_i^\dagger, d_i^\dagger obey Bose commutation relations and $f_{i\sigma}^\dagger$ obey Fermi anti-commutation relations. One could notice that the

empty site $|0\rangle$ is created from a vacuum state rather than assumed as a pre-existing state. The use of auxiliary operators to represent spin and charge components enlarges the Fock space than that of the original physical states. In order to eliminate the non-physical states and to ensure the physical meaning of results, the enlarged Fock space should be span back as original. This can be done by enforcing by constraint below

$$e_i^\dagger e_i + d_i^\dagger d_i + \sum_{\sigma} f_{i\sigma}^\dagger f_{i\sigma} = 1. \quad (8.2)$$

The constraint (8.2) is a completeness equation. The physical second quantized operators can be written in terms of projection operators as

$$c_{i\sigma} = |0_i\rangle\langle\sigma_i| + z_{\sigma}|\bar{\sigma}_i\rangle\langle\uparrow\downarrow_i|, \quad (8.3)$$

where $z_{\sigma} = 1$ or -1 for $\sigma = \uparrow$ or \downarrow respectively. With the help of auxiliary bosons and fermions and the equation (8.3), the physical creator (annihilator) operators can be expressed by as

$$c_{i\sigma} = e_i^\dagger f_{i\sigma} + z_{\sigma} d_i f_{i\sigma}^\dagger. \quad (8.4)$$

This representation is used in multiple cases primarily when $U \rightarrow \infty$ [312, 313] because the double occupancy operators drop out. From the above equation (8.4), we can clearly observe that this slave boson representation mixes fermionic operators with bosonic operators. Charges are expressed in terms of bosons, whereas spin degrees are represented by fermion operators. The bosonic operators do not carry spin. Unequal treatment of spin and charge components might lead to unnecessary errors in any approximations [73]. This disadvantage paves a path to a new slave boson representation where spin and charge degrees of freedom may be expressed in terms of bosons.

8.4.2 Kotliar and Ruckenstein's representation

To overcome the separate bosonic and fermionic representation of charge and spin degree of freedom, Kotliar and Ruckenstein [72] introduced a new representation with two additional bosons linked with the spin degree of freedom. Thus, both the spin and charge degree of freedom of physical electron operators are represented by slave-boson. To do so, they introduced slave bosons to each of four states per site and a spin doublet of fermion operators for singly occupied sites. The table 8.2 resumes the mapping.

Initial physical states	KR's slave boson representation
$ 0_i\rangle \mapsto vac\rangle$	$ 0_i\rangle \mapsto e_i^\dagger vac\rangle$
$ \uparrow_i\rangle \mapsto c_{i\uparrow}^\dagger vac\rangle$	$ \uparrow_i\rangle \mapsto p_{i\uparrow}^\dagger f_{i\uparrow}^\dagger vac\rangle$
$ \downarrow_i\rangle \mapsto c_{i\downarrow}^\dagger vac\rangle$	$ \downarrow_i\rangle \mapsto p_{i\downarrow}^\dagger f_{i\downarrow}^\dagger vac\rangle$
$ \uparrow\downarrow_i\rangle \mapsto c_{i\uparrow}^\dagger c_{i\downarrow}^\dagger vac\rangle$	$ \uparrow\downarrow_i\rangle \mapsto d_i^\dagger f_{i\uparrow}^\dagger f_{i\downarrow}^\dagger vac\rangle$

Table 8.2: Table resuming Kotliar and Ruckenstein's slave bosons representation

Here, e_i^\dagger , $p_{i\sigma}^\dagger$ and d_i^\dagger are bosonic operators associated with an empty site, a site with one electron with spin σ and doubly occupied site respectively, whereas $f_{i\sigma}^\dagger$ are auxiliary fermionic operators. Like in Barnes's approach (see section 8.4.1), the introduction of auxiliary operators enlarges the initial Hilbert space. In order to eliminate nonphysical states, constraints (8.5) and (8.6) should be enforced.

$$e_i^\dagger e_i + \sum_{\sigma} p_{i\sigma}^\dagger p_{i\sigma} + d_i^\dagger d_i = 1, \quad (8.5)$$

$$f_{i\sigma}^\dagger f_{i\sigma} - (p_{i\sigma}^\dagger p_{i\sigma} + d_i^\dagger d_i) = 0. \quad (8.6)$$

The constraint (8.5) is a completeness relation that translates either a site is empty ($|0_i\rangle$), singly occupied, or double occupied and the number of bosons per site is one. The constraint (8.6) translates that when a site is occupied it is either singly or double occupied. It also translates that the counting of $f_{i\sigma}^\dagger f_{i\sigma}$ or $p_{i\sigma}^\dagger p_{i\sigma} + d_i^\dagger d_i$ is equivalent. In this representation, the physical electron operators are expressed as

$$c_{i\sigma} = f_{i\sigma} (e_i^\dagger p_{i\sigma} + p_{i\bar{\sigma}}^\dagger d_i) \quad (8.7)$$

$$= \bar{z}_{i\sigma} f_{i\sigma}, \quad (8.8)$$

where $\bar{\sigma}$ is the opposite sign of σ and the relation $\bar{z}_{i\sigma} = e_i^\dagger p_{i\sigma} + p_{i\bar{\sigma}}^\dagger d_i$ is the new renormalization factor for auxiliary fermions $f_{i\sigma}$.

From the renormalization factor, one can define the quasiparticle weight as $Z_\sigma = \langle \bar{z}_{i\sigma}^\dagger \bar{z}_{i\sigma} \rangle$. Within mean-field approximation as $e_i \rightarrow e$, $p_{i\sigma} \rightarrow p_\sigma$, and $d_i \rightarrow d$, the quasiparticle weight is rewritten as $Z_\sigma = (e p_\sigma + p_{\bar{\sigma}} d)^2$. One of the example of the use of this approach is that it can capture Mott metal-insulator transition. To do so, we can consider half-filled one-band Hubbard model in paramagnetic phase. Z_σ plays the role of mass renormalization and of quasiparticle residue. In this simple case, a localization of an electron can be obtained when quasiparticle weight $Z_\sigma \rightarrow 0$ vanishes.

Different from previous approach, the mixing of fermionic and bosonic operators in the completeness relation is gone and thus faithfully describes the electrons moving on site i to j . Even though KR's representation corrects the previous representation, the spin degree of freedom is not rotationally invariant. The transverse

components of the spin operator may not be simply represented in the terms of auxiliary operators since $S^{x,y}$ is neither related to $\frac{1}{2} \sum_{\sigma\sigma'} f_{\sigma}^{\dagger} \tau_{\sigma\sigma'}^{x(y)} f_{\sigma'}$ nor to $\frac{1}{2} \sum_{\sigma\sigma'} p_{\sigma}^{\dagger} \tau_{\sigma\sigma'}^{x(y)} p_{\sigma'}$. Thus, the spin representation $|\sigma\rangle$ is not spin rotation invariant making it dependent on the choice of quantization axis in spin space. This shortcoming lead to the development of spin-rotation-invariant slave boson approach [73].

8.4.3 Li, Wölfel and Hirschfeld's representation

Li, Wölfel, and Hirschfeld's slave boson representation (LWH) [73, 311] corrects the spin non-invariance problem that was stated in previous sections. In their approach, Li, Wölfel and Hirschfeld represented the operator product $p_{i\sigma}^{\dagger} f_{i\sigma}^{\dagger}$ of KR's mapping (8.2) as a composite particle of spin $\frac{1}{2}$. The LWH mapping is resumed in the table 8.3.

Initial physical states	LWH's slave boson representation
$ 0_i\rangle \mapsto vac\rangle$	$ 0_i\rangle \mapsto e_i^{\dagger} vac\rangle$
$ \uparrow_i\rangle \mapsto c_{i\uparrow}^{\dagger} vac\rangle$	$ \uparrow_i\rangle \mapsto \frac{1}{\sqrt{2}}\{p_{i\uparrow\downarrow}^{\dagger}f_{i\downarrow}^{\dagger} + p_{i\uparrow\uparrow}^{\dagger}f_{i\uparrow}^{\dagger}\} vac\rangle$
$ \downarrow_i\rangle \mapsto c_{i\downarrow}^{\dagger} vac\rangle$	$ \downarrow_i\rangle \mapsto \frac{1}{\sqrt{2}}\{p_{i\downarrow\downarrow}^{\dagger}f_{i\downarrow}^{\dagger} + p_{i\downarrow\uparrow}^{\dagger}f_{i\uparrow}^{\dagger}\} vac\rangle$
$ \uparrow\downarrow_i\rangle \mapsto c_{i\uparrow}^{\dagger}c_{i\downarrow}^{\dagger} vac\rangle$	$ \uparrow\downarrow_i\rangle \mapsto d_i^{\dagger}f_{i\uparrow}^{\dagger}f_{i\downarrow}^{\dagger} vac\rangle$

Table 8.3: Table resuming Li, Wölfel and Hirschfeld's slave bosons representation

From the above mapping (8.3), we can observe that this method introduces altogether two auxiliary fermionic quasiparticle operators : $f_{i\uparrow}, f_{i\downarrow}$ and six bosonic operators : e_i, \mathbf{p}_i, d_i where,

$$\mathbf{p}_i = \begin{pmatrix} p_{i\uparrow\uparrow} & p_{i\uparrow\downarrow} \\ p_{i\downarrow\uparrow} & p_{i\downarrow\downarrow} \end{pmatrix} \quad (8.9)$$

e_i and d_i are associated with empty site and doubly occupied site whereas $p_{i\sigma\sigma'}$ is associated with singly occupied. The first index σ in single-particle boson is associate with local state and the second index σ' is associated with the auxiliary fermion quasi-particle degree of freedom. Also, the bosons $p_{i\sigma\sigma'}$ permits to connect the low-energy quasiparticle excitations to its identical high-energy local counterpart as well as other local configurations such as a state with opposite spin configuration. Thus, this general structure renders spin rotationally invariant. Further, $p_{i\sigma\sigma'}$ can be represented as

$$p_{i\sigma\sigma'} = \frac{1}{2} \sum_{\mu=0,x,y,z} p_{\mu} \tau_{\sigma\sigma'}^{\mu}, \quad (8.10)$$

where τ_{μ} are Pauli matrices and τ^0 it the unit matrix.

Knowing that the spin values of auxiliary pseudo-fermions $f_{i\sigma}$ should be $\frac{1}{2}$, the possible spin values for $p_{i\sigma\sigma'}$ bosons are $S = 0$ or $S = 1$. Accordingly, a scalar field spin singlet p_0 and a vector field spin triplet $\mathbf{p}_i = (p_{ix}, p_{iy}, p_{iz})$ is defined for $S = 0$ and $S = 1$ respectively. The $S = 0$ boson p_{i0} represent the charge degree of freedom of the spinor states whereas the $S = 1$ boson p_i describes spin degree of freedom. However, one should note that these fields do not automatically represent the electron charge and spin operators because the density operators involve the square of the matrix \mathbf{p}_i of the equation (8.9).

To recover the initial physical space, the auxiliary operators need to satisfy the following constraints

$$e_i^\dagger e_i + d_i^\dagger d_i + \sum_{\sigma\sigma'} p_{i\sigma\sigma'}^\dagger p_{i\sigma\sigma'} = 1, \quad (8.11)$$

$$f_{i\sigma'}^\dagger f_{i\sigma} - \sum_{\sigma_1} p_{i\sigma_1\sigma'}^\dagger p_{i\sigma\sigma_1} - \delta_{\sigma\sigma'} d_i^\dagger d_i = 0, \quad (8.12)$$

$$p_{i0}^\dagger \mathbf{p}_i + \mathbf{p}_i^\dagger p_{i0} - i \mathbf{p}_i^\dagger \times \mathbf{p}_i = \sum_{\sigma\sigma'} f_{i\sigma}^\dagger \boldsymbol{\tau}_{\sigma'\sigma} f_{i\sigma'}. \quad (8.13)$$

Enforcement of the completeness constraint (8.11) ensure that a site is either empty, singly occupied, or doubly occupied, whereas enforcement of the constraint (8.12) ensure the number of electrons matches the number of p bosons and d bosons. The constraint (8.13) ensures that the spin of the physical electrons matches the spin of the bosons. With this at hand, the electron operators may be written as

$$c_{i\sigma}^\dagger = \sum_{\sigma'} (p_{i\sigma\sigma'}^\dagger f_{i\sigma'}^\dagger e_i + \sigma\sigma' d_i^\dagger f_{i\sigma'} p_{i\bar{\sigma}\bar{\sigma}}) = \sum_{\sigma'} R_{i\sigma\sigma'}^\dagger f_{i\sigma'}^\dagger, \quad (8.14)$$

$$c_{i\sigma} = \sum_{\sigma'} (e_i^\dagger f_{i\sigma'} p_{i\sigma'\sigma} + \sigma\sigma' p_{i\bar{\sigma}\bar{\sigma}}^\dagger f_{i\sigma'} d_i) = \sum_{\sigma'} f_{i\sigma'} R_{i\sigma'\sigma}, \quad (8.15)$$

where $R_{i\sigma'\sigma} = e_i^\dagger p_{i\sigma'\sigma} + \sigma\sigma' p_{i\bar{\sigma}\bar{\sigma}}^\dagger d_i$. The operator $R_{i\sigma'\sigma}$ describes the sum of processes: from a singly occupied site to an empty site and from a doubly occupied site to a singly occupied site with time-reversed spin. Furthermore, this formalism makes the foundation for rotationally-invariant slave-boson, which can be applied to the general multi-orbital systems [74] and we will be using the latter formalism throughout this thesis.

8.4.4 Other variations of slave-bosons techniques

In this section, we present a non-exhaustive selection of other variations of slave-bosons. Each of the slave-boson variations was developed for specific purposes or as an extension of previous. We could start from the slave-boson developed by Coleman [314] for the mixed-valent impurity problem, which is inspired by Barnes'

approach [309]. In his approach, the Hubbard operators [315] were replaced by a product of boson and fermion operators in order to avoid notorious algebraic calculations. Slave-boson techniques are also generalized to study superconductivity [316–319] or even Kondo cloud [320]. Further, Li, Wölfe, and Hirschfeld’s representation in the section 8.4.3 has been generalized to multi-band models by Lechermann, Georges, Kotliar, and Parcollet [74] and also by Bünemann [321] where, e.g., the effects of multiple orbitals, orbital degeneracy, and the Hund’s rule can be studied. In the past, multi-orbital RISB method was applied to study the strongly correlated real systems like UO_2 [322], iron chalcogenides [323] or $\text{Nd}_{1-x}\text{Sr}_x\text{NiO}_2$ [324] with good agreement with experimental data.

8.5 Motivations and objectives

The dual model presented by Zwicky *et al.* [10, 325] (see section 8.3.1) gave some promising reproducing dHvA frequencies and core-level photoemission spectra [326], suggesting orbital-selective partial localization due to anisotropic bandwidths. Indeed, small cluster calculations [60] showed the partial localization (see figure 8.4) of f -electrons, but their calculations suffered problems at non-interacting limit. Moreover, a full thermodynamic calculation is still missing. Thus, in this thesis, we consider all the f -electron configurations: f^0 , f^1 , f^2 , f^3 , f^4 , f^5 and f^6 with non-integer valency, as suggested by multiple experiments. The local correlations will be treated through the rotationally-invariant slave-boson approach [74], and we will consider jj -coupling scheme while ignoring crystal field effects. This work is the continuation of the previous work conducted by Duc-Anh Le [327], where he conducted the necessary analytical calculations. Here, we do not intend to perform *ab-initio* calculation, but we plan to provide a possible microscopic description of the duality of f -electron. Thus, in this thesis, we analyze orbital-selective Mott transitions and construct a phase diagram with partially localized phases, considering paramagnetic and ferromagnetic phases. Further, we will also analyze orbital-dependant electronic filling, quasiparticle weight, magnetization, and f -electron configuration in terms of bandwidth anisotropies. Below, we present the organization of this part of the thesis.

Chapter 9 is dedicated to the theoretical details of our study. We will start by detailing the model Hamiltonian. Thereafter, we will present the rotationally-invariant slave-boson approach and the mean-field approximations within. Finally, we will present our system of equations to be solved numerically.

Chapter 10 presents the numerical aspects of our study. We will give details about our local and global minimization schemes along with different routines used.

Chapter 11 is dedicated to the presentation of our results. At first, we present the result for the isotropic case, and thereafter, the effect of anisotropies in orbital-dependent electronic bandwidth will be studied in terms of orbital-selective Mott

localization. Then, we will build and analyze our phase diagram with partially localized phases.

Chapter 12 present the conclusions of our study along with future perspectives.

Chapter 9

Model and rotationally-invariant slave bosons

In this chapter, we present the model, method, and approximations that we have used to study the duality of $5f$ electrons. At first, we start by detailing the model Hamiltonian, thereafter the method rotationally invariant slave-boson approach (RISB), and the mean-field approximations along with the self-consistent equations.

9.1 Model Hamiltonian

Our model Hamiltonian to describe $5f$ electrons is

$$\mathcal{H} = \sum_{\langle a,b \rangle, j_z} \{t_{j_z} - \mu \delta_{ab}\} c_{aj_z}^\dagger c_{bj_z} + H_{Coul.}, \quad (9.1)$$

where $c_{aj_z}^\dagger$ (c_{aj_z}) denotes creator(annihilator) operator which creates(annihilate) a $5f$ -electron on site a with angular momentum $j = 5/2$ and z -components $j_z = -5/2 \dots 5/2$ and μ is the chemical potential fixing the f -electron occupation n_f . We assume that the nearest site hopping t_{j_z} is diagonal in the orbital index j_z . The first term of the Hamiltonian describes the kinetic, whereas the second term $H_{Coul.}$ reflects the Coulomb interaction. This Coulomb interaction is further expressed as

$$H_{Coul.} = \frac{1}{2} \sum_a \sum_{j_{z_1}, j_{z_2}, j_{z_3}, j_{z_4}} \langle j_{z_1} j_{z_2} | \hat{U} | j_{z_3} j_{z_4} \rangle c_{aj_{z_1}}^\dagger c_{aj_{z_2}}^\dagger c_{aj_{z_3}} c_{aj_{z_4}}, \quad (9.2)$$

with $\langle j_{z1}j_{z2}|\hat{U}|j_{z3}j_{z4}\rangle$ are Coulomb matrix elements which are evaluated as

$$\begin{aligned}\langle j_{z1}j_{z2}|\hat{U}|j_{z3}j_{z4}\rangle &= \delta_{j_{z1}+j_{z2},j_{z3}+j_{z4}} \sum_J \langle \frac{5}{2}j_{z1} \frac{5}{2}j_{z2} | JJ_z \rangle U_J \langle JJ_z | \frac{5}{2}j_{z2} \rangle \\ &= \sum_J U_J C_{5/2,j_{z1};5/2,j_{z2}}^{JJ_z} C_{5/2,j_{z3};5/2,j_{z4}}^{JJ_z}.\end{aligned}\quad (9.3)$$

where C_{\dots} are the Clebsh-Gordon coefficients and J denotes the total angular momentum and $J_z = j_{z1} + j_{z2} = j_{z3} + j_{z4}$.

9.2 Method: rotationally-invariant slave-bosons

In order to study the model Hamiltonian (9.1) and to treat the intra-atomic correlations, we use the rotationally invariant slave bosons approach (RISB) as introduced by Lechermann *et al.* [74]. An introduction to slave-boson approaches in the section 8.4 of chapter 8, while below we present a short overview of the RISB formalism and the equations related to it. We would like to point out that this work continues the theoretical and numerical work conducted by Duc-Ahn Le [327] based on the previous work.

9.2.1 Expanded Hilbert space and basis set

By taking account of quasiparticles orbital degree of freedom within RISB formalism, we introduce the auxiliary fermionic operators $f_{aj_z}^\dagger, f_{aj_z}$ associated each orbital j_z and bosonic operators $\phi_{A,n}^\dagger, \phi_{A,n}$ where A is a basis of local Hilbert space and n label Fock states. These newly introduced operators are used to replace the operators $c_{j_z}^\dagger, c_{j_z}$ and connect the initial physical Hilbert space with the auxiliary particle Hilbert space. To do so a basis set for physical Hilbert space as well as for auxiliary Hilbert space needs to be defined.

Initial physical states for $M = 0, 1$	RISB representation
$ 0\rangle \mapsto vac\rangle$	$ 0\rangle \mapsto \phi^\dagger vac\rangle$
$ \eta_{j_z}\rangle \mapsto c_{j_z}^\dagger vac\rangle$	$ \eta_{j_z}\rangle \mapsto \sum_{j'_z} \phi_{j_z j'_z}^\dagger f_{j'_z}^\dagger vac\rangle$

Table 9.1: Table showing RISB mapping for zero and one particle sector (M) and $M = \sum_{j_z} \eta_{j_z}$.

Table 9.1 shows the RISB mapping only for zero ($M = 0$) and ($M = 1$) particle sectors, where the slave bosons $\phi_{j_z j'_z}^\dagger$ connects physical Fock states $|\eta_{j_z}\rangle$ to quasiparticle state $|\eta'_{j_z}\rangle$. In this particular case, the atomic multiplets are also Fock states.

However, for $M \geq 2$, this is not necessarily true. Thus, it would be natural to define a new basis set associating both atomic multiplets and Fock states. Even though, the basis sets can be chosen arbitrarily, we choose multiplet-Fock basis set where a multiplet state $|\Gamma\rangle$ is an eigenstate of local interaction as $\hat{U}|\Gamma\rangle = E_\Gamma|\Gamma\rangle$ and a Fock state $|n\rangle$ an eigenstate of the occupation number operator $\sum_{j_z} f_{j_z}^\dagger f_{j_z}$. More precisely, multiplet basis $|\Gamma\rangle$ is chosen for initial physical Hilbert space whereas Fock state $|n\rangle$ is chosen for auxiliary Hilbert space. Here, a multiplet state with M -particles, total angular momentum J , and its projection over z -direction J_z is labelled as $|\Gamma\rangle = |f^M; J, J_z\rangle$. Similarly, a Fock state $|n\rangle = |\eta_{-5/2}\eta_{-3/2}\eta_{-1/2}\eta_{1/2}\eta_{3/2}\eta_{5/2}\rangle$ represent M -particle states such as $M = \sum_{j_z} \eta_{j_z}$. The choice of using multiplet-Fock basis is because the local interactions are diagonal in the multiplet basis, and it also simplifies the constraints. For now, we ignore the site-index to simplify the notation and a multiplet in multiple-Fock basis is defined as

$$|\underline{\Gamma}\rangle \equiv \frac{1}{\sqrt{D_\Gamma}} \sum_n \phi_{\Gamma n}^\dagger |vac\rangle \otimes |n\rangle, \quad (9.4)$$

where D_Γ denotes the dimension of the sub-space of the Hilbert space with particle number identical to that of Γ . The relation (9.4) insures a proper normalization of a state. The underline in $|\underline{\Gamma}\rangle$ distinguishes $|\underline{\Gamma}\rangle$ from $|\Gamma\rangle$ since $|\underline{\Gamma}\rangle$ lives in Hilbert space of quasiparticle and boson states whereas $|\Gamma\rangle$ lives in Hilbert space of physical electron. From the equation (9.4), we identify the slave-bosons $\phi_{\Gamma n}$ associated to each pair of atomic multiplet $|\Gamma\rangle$ and quasiparticles Fock state $|n\rangle$.

9.2.2 Local constraints

The slave-boson mapping enlarges the Hilbert phases, which needs to be reduced in order to eliminate non-physical states. Thus, the local constraints need to be enforced. In our case, the constraints [74] are

$$\sum_{\Gamma n} \phi_{\Gamma n}^\dagger \phi_{\Gamma n} = 1, \quad (9.5)$$

$$\sum_{\Gamma n n'} \langle n | f_{j_z}^\dagger f_{j_z} | n' \rangle \phi_{\Gamma n'}^\dagger \phi_{\Gamma n} = f_{j_z}^\dagger f_{j_z}. \quad (9.6)$$

The constraint (9.5) is the completeness equation ensuring that the physical states are single boson states as Eq. (8.11). The constraint (9.6) ensures the conservation of quasiparticle number by considering the correct slave-bosons with the same total particle charge sector in the physical and quasiparticle Hilbert space.

9.2.3 Representation of physical electron operators and RISB Hamiltonian

The action of creation operator in enlarged Hilbert space should be same as in physical Hilbert space. This lead us to the equation

$$\langle \underline{\Gamma} | \underline{c}_{j_z}^\dagger | \underline{\Gamma}' \rangle = \langle \Gamma | c_{j_z}^\dagger | \Gamma' \rangle . \quad (9.7)$$

The c_{j_z} operators are expressed in term of auxiliary bosons and fermions as

$$c_{j_z} = R_{j_z}^\dagger[\Phi] f_{j_z} , \quad (9.8)$$

where Φ is slave-boson matrix and the operator $R_{j_z}^\dagger[\Phi]$ is defined as

$$R_{j_z}^\dagger[\Phi] = \frac{\hat{\gamma}_{j_z}[\Phi]}{\sqrt{\hat{n}_{j_z}[\Phi](1 - \hat{n}_{j_z}[\Phi])}} , \quad (9.9)$$

with

$$\hat{\gamma}_{j_z}[\Phi] = \sum_{\Gamma\Gamma', nn'} \langle \Gamma | c_{j_z}^\dagger | \Gamma' \rangle \langle n | f_{j_z}^\dagger | n' \rangle \phi_{\Gamma n}^\dagger \phi_{\Gamma' n'} , \quad (9.10)$$

$$\hat{n}_{j_z} = \sum_{\Gamma n} \langle n | f_{j_z}^\dagger f_{j_z} | n \rangle \phi_{\Gamma n}^\dagger \phi_{\Gamma n} . \quad (9.11)$$

By using the Eq. (9.8) and reintroducing the site-index, the Hamiltonian (9.1) is written in terms of auxiliary bosons as

$$H = - \sum_{\langle a, b \rangle, j_z} t_{j_z} [R_{j_z}[\Phi_a] R_{j_z}^\dagger[\Phi_b] f_{a j_z}^\dagger f_{b j_z} + \sum_{a, \Gamma n} E_\Gamma \phi_{a, \Gamma n}^\dagger \phi_{a, \Gamma n} , \quad (9.12)$$

where E_Γ is the eigenvalues of the local interaction \hat{U} as $\hat{U}|\Gamma\rangle = E_\Gamma|\Gamma\rangle$.

9.2.4 Basis transformations

The basis set for the physical Hilbert space can be chosen arbitrarily in the RISB formalism due to its rotational invariance. Thus, a linear transformation can be applied to change a basis set to another set. For instance, the basis transformation from multiplet-Fock basis to Fock-Fock basis can be done by applying a linear transformation as

$$\phi_{n'n}^\dagger = \sum_{\Gamma} \langle \Gamma | n' \rangle \phi_{\Gamma n}^\dagger . \quad (9.13)$$

Similarly, a linear transformation to change into multiplet-multiplet basis can be done as

$$\phi_{\Gamma'}^\dagger = \sum_n \langle n | \Gamma' \rangle \phi_{\Gamma n}^\dagger. \quad (9.14)$$

We can combine the above two linear transformation (9.13) and (9.14) in order to find the relation between the Fock-Fock bosons and the multiplet-multiplet bosons

$$\phi_{\Gamma'}^\dagger = \sum_{nn'} \langle \Gamma | n' \rangle \langle n | \Gamma' \rangle \phi_{n'n}^\dagger. \quad (9.15)$$

Whether on a Fock-Fock basis or multiplet-multiplet basis, the first index refers to a state in the initial physical Hilbert space, whereas the second index refers to a state in the auxiliary Hilbert space.

9.3 Approximations

We have rewritten the effective Hamiltonian (9.1) within RISB formalism. Now, we can further apply mean-field approximations, considering a constant density of states to obtain self-consistent equations.

9.3.1 Mean-field approximations for auxiliary fields

The mean-field approximations are

- The slave-bosonic operators are replaced by their expected values as $\phi_{a,\Gamma n}^\dagger, \phi_{a,\Gamma n} \rightarrow \varphi_{\Gamma n}$.
- The constraints (9.5-9.6) are applied through enforcing Lagrange parameters λ and λ_{j_z} respectively.

With these approximations in hand and by invoking Fourier transformation, the RISB Hamiltonian (9.12) is rewritten as

$$\begin{aligned} \mathcal{H}^{MF} = & \sum_{\mathbf{k}, j_z} \epsilon_{\mathbf{k}, j_z} Z_{j_z}[\Phi] f_{\mathbf{k}, j_z}^\dagger f_{\mathbf{k}, j_z} - \sum_{\mathbf{k}, j_z} \lambda_{j_z} f_{\mathbf{k}, j_z}^\dagger f_{\mathbf{k}, j_z} + \mathcal{N} \sum_{\Gamma n} E_\Gamma \varphi_{\Gamma n}^2 + \lambda \mathcal{N} \left(\sum_{\Gamma n} \varphi_{\Gamma n}^2 - 1 \right) \\ & + \mathcal{N} \sum_{j_z} \lambda_{j_z} n_{j_z}[\Phi] + \mu \mathcal{N} \left(\sum_{j_z} n_{j_z}[\Phi] - n_f \right), \end{aligned} \quad (9.16)$$

where, $\epsilon_{\mathbf{k}, j_z}$ are the energy levels associated with the nearest neighbor hopping integrals t_{j_z} , \mathcal{N} is the total number of sites and μ is the chemical potential fixing number of f -electrons n_f . In the above Eq. (9.16), $Z[\Phi]$ is the quasiparticle weight

which is defined as

$$Z_{j_z}[\Phi] = R^2[\Phi] = \frac{\gamma_{j_z}^2[\Phi]}{n_{j_z}[\Phi](1 - n_{j_z}[\Phi])}, \quad (9.17)$$

where γ_{j_z} and n_{j_z} are explicit functions of the slave-bosons $\varphi_{\Gamma n}$ and are defined similarly as the operators $\hat{\gamma}_{j_z}$ and \hat{n}_{j_z} as in the equations (9.10 - 9.11) but with mean-field approximations. In order to obtain the relations for mean-field parameters λ , and μ , we minimize the free energy of the system $\mathcal{F} = -\frac{1}{\beta} \ln \text{Tr}[e^{-\beta H^{MF}}]$, where $\beta = \frac{1}{k_B T}$ with k_B being Boltzmann constant and T is the temperature of the system. Thus, we write our saddle-point equations as

$$\sum_{\Gamma n} \varphi_{\Gamma n}^2 = 1, \quad (9.18)$$

$$\sum_{j_z} n_{j_z}[\Phi] = n_f, \quad (9.19)$$

$$n_{j_z}[\Phi] = \frac{1}{\mathcal{N}} \sum_{\mathbf{k}} \langle f_{\mathbf{k}j_z}^\dagger f_{\mathbf{k}j_z} \rangle, \quad (9.20)$$

$$2(E_\Gamma + \lambda)\varphi_{\Gamma n} = - \sum_{j_z} (\lambda_{j_z} + \mu) \frac{\partial n_{j_z}[\Phi]}{\partial \varphi_{\Gamma n}} - \frac{1}{\mathcal{N}} \sum_{j_z} \frac{\partial Z_{j_z}[\Phi]}{\partial \varphi_{\Gamma n}} \sum_{\mathbf{k}} \epsilon_{\mathbf{k}j_z} \langle f_{\mathbf{k}j_z}^\dagger f_{\mathbf{k}j_z} \rangle, \quad (9.21)$$

with

$$\langle f_{\mathbf{k}j_z}^\dagger f_{\mathbf{k}j_z} \rangle = n_F(\epsilon_{\mathbf{k}} Z_{j_z}[\Phi] - \lambda_{j_z}), \quad (9.22)$$

where n_F is Fermi distribution. From the expressions of $Z_{j_z}[\Phi]$, $\gamma_{j_z}[\Phi]$, and $n_{j_z}[\Phi]$, the partial derivation $\frac{\partial Z_{j_z}[\Phi]}{\partial \varphi_{\Gamma n}}$ is expressed as

$$\frac{\partial Z_{j_z}[\Phi]}{\partial \varphi_{\Gamma n}} = Z_{j_z}[\Phi] \frac{2n_{j_z}[\Phi] - 1}{n_{j_z}[\Phi](1 - n_{j_z}[\Phi])} \frac{\partial n_{j_z}[\Phi]}{\partial \varphi_{\Gamma n}} + 2 \frac{\gamma_{j_z}[\Phi]}{n_{j_z}[\Phi](1 - n_{j_z}[\Phi])} \frac{\partial \gamma_{j_z}[\Phi]}{\partial \varphi_{\Gamma n}}, \quad (9.23)$$

with,

$$\frac{\partial \gamma_{j_z}[\Phi]}{\partial \varphi_{\Gamma n}} = \sum_{\Gamma' n'} \langle \Gamma | c_{j_z}^\dagger | \Gamma' \rangle \langle n | f_{j_z}^\dagger | n' \rangle \varphi_{\Gamma' n'}, \quad (9.24)$$

$$\frac{\partial n_{j_z}[\Phi]}{\partial \varphi_{\Gamma n}} = 2\varphi_{\Gamma n} \langle n | f_{j_z}^\dagger f_{j_z} | n \rangle. \quad (9.25)$$

9.3.2 Constant density of states

For our numerical calculations, within the mean-field equations (9.18-9.21), we consider an orbital-dependent constant density of states as

$$\rho_{j_z}(\omega) = \frac{1}{W_{j_z}} \theta \left(\frac{W_{j_z}}{2} - |\omega| \right), \quad (9.26)$$

where, W_{j_z} and θ are orbital-dependent electronic bandwidth and Heaviside function respectively.

9.4 Self-consistent equations system and parameters

In this section, we present our self-consistent equations. To do so, we consider the constant density of states provided by the Eq. (9.26) along with the average occupation $\langle f_{\mathbf{k}j_z}^\dagger f_{\mathbf{k}j_z} \rangle$ from the Eq. (9.22), at zero temperature the Eq. (9.20) can be expressed as

$$n_{j_z}[\Phi] = \int \rho_{j_z}(\omega) n_F(\omega Z_{j_z}[\Phi] - \lambda_{j_z}) d\omega = \frac{\lambda_{j_z}}{W_{j_z} Z_{j_z}} + \frac{1}{2}. \quad (9.27)$$

In the similar way, one can treat the Eq. (9.21). Hence, we resume our final set of self-consistent equations as

$$\sum_{\Gamma_n} \varphi_{\Gamma_n}^2 = 1, \quad (9.28)$$

$$\sum_{j_z} n_{j_z}[\Phi] = n_f, \quad (9.29)$$

$$n_{j_z}[\Phi] = \frac{\lambda_{j_z}}{W_{j_z} Z_{j_z}} + \frac{1}{2}, \quad (9.30)$$

$$[E_\Gamma + \lambda + \mu \sum_{j_z} \langle n | c_{j_z}^\dagger c_{j_z} | n \rangle] \varphi_{\Gamma_n} = \sum_{j_z} \frac{W_{j_z}}{2} \gamma_{j_z}[\Phi] \frac{\partial \gamma_{j_z}[\Phi]}{\partial \varphi_{\Gamma_n}}. \quad (9.31)$$

Similarly, the energy of the system pre site is obtained from the Eq. (9.16) as $\frac{\langle \mathcal{H}^{MF} \rangle}{N}$, which gives the final equation as

$$\frac{\langle \mathcal{H}^{MF} \rangle}{N} = E[\Phi] = - \sum_{j_z} \frac{W_{j_z}}{2} Z_{j_z}[\Phi] n_{j_z}[\Phi] (1 - n_{j_z}[\Phi]) + \sum_{\Gamma_n} E_\Gamma \varphi_{\Gamma_n}^2. \quad (9.32)$$

The equations (9.28-9.31) makes a set of self-consistent equations to minimize the energy (9.32). Within RISB formalism, a density matrix needs to be constructed $n_{j_z} = \sum_{\Gamma n} \varphi_{\Gamma n}^2 \langle n | f_{j_z}^\dagger f_{j_z} | n \rangle$. This construction of this density matrix can lead to a large amount of auxiliary slave-bosons operators. However, the number of slave bosons could be reduced using symmetries of local interactions. For instance, the particle number conservation of the local Hamiltonian and diagonal nature of interaction \hat{U} on a multiplet basis leads to cancellation of all the slave-bosons $\varphi_{\Gamma n}$ with $\langle n | \Gamma \rangle = 0$. Thus in our case, slave-bosons numbers can be reduced considerably to 116 and can be found in the appendix E.

Chapter 10

Numerical approach: algorithm and technical challenges

Numerical resolution of RISB equations can be very tedious and challenging. The difficulties can be purely numerical or algorithmic, or even both. Thus, each step of numerical calculation should be carefully chosen in order to get the correct solution. Assuming that all the technical difficulties are fixed, the resolution of RISB equations can be very time-consuming. This makes the optimization of numerical codes very necessary whenever possible. In our case, we chose Python due to its large libraries in optimization routines. Furthermore, the python functions were compiled by using Numba [328] whenever possible for faster executions. Finally, for our study, we have used different types of optimization routines mixed together.

10.1 Reduction of Hilbert space and slave-bosons

In the previous chapter, we have seen that we are dealing with 116 slave-bosons present in six different particle charge sectors (see appendix E). Ideally, we should consider all the 116 φ_{Γ_n} spanning through the Hilbert space of all six particle sectors. But, this leads to 116 equations to be solved self-consistently. However, depending upon the W/U_4 , solving all 116 equations along with two physical constraints is not always necessary since the ground state might not be composed of all f -electron configurations. To demonstrate at first, we consider the atomic limit $W = 0$. From the previous dual model calculations and from Hund's, the ground-state at $W/U_4 = 0$ is composed of f^2 and f^3 configurations with $J = 4$ and $J = 9/2$ respectively. So, in this case, we can consider only the slave-bosons representing f^2 and f^3 configurations. This assumption will reduce the number of φ_{Γ_n} to 36 instead of 116. Now, with a slight increase in W , electrons can hop as $f^3 \leftrightarrow f^4$. Thus, the slave-bosons representing 3 or 4 electrons particle sectors can become non-zeros. Figure 10.1 schematizes this process where we do a preliminary optimization within a λ and μ grid. This preliminary grid calculation permits us to have an initial guess parameter

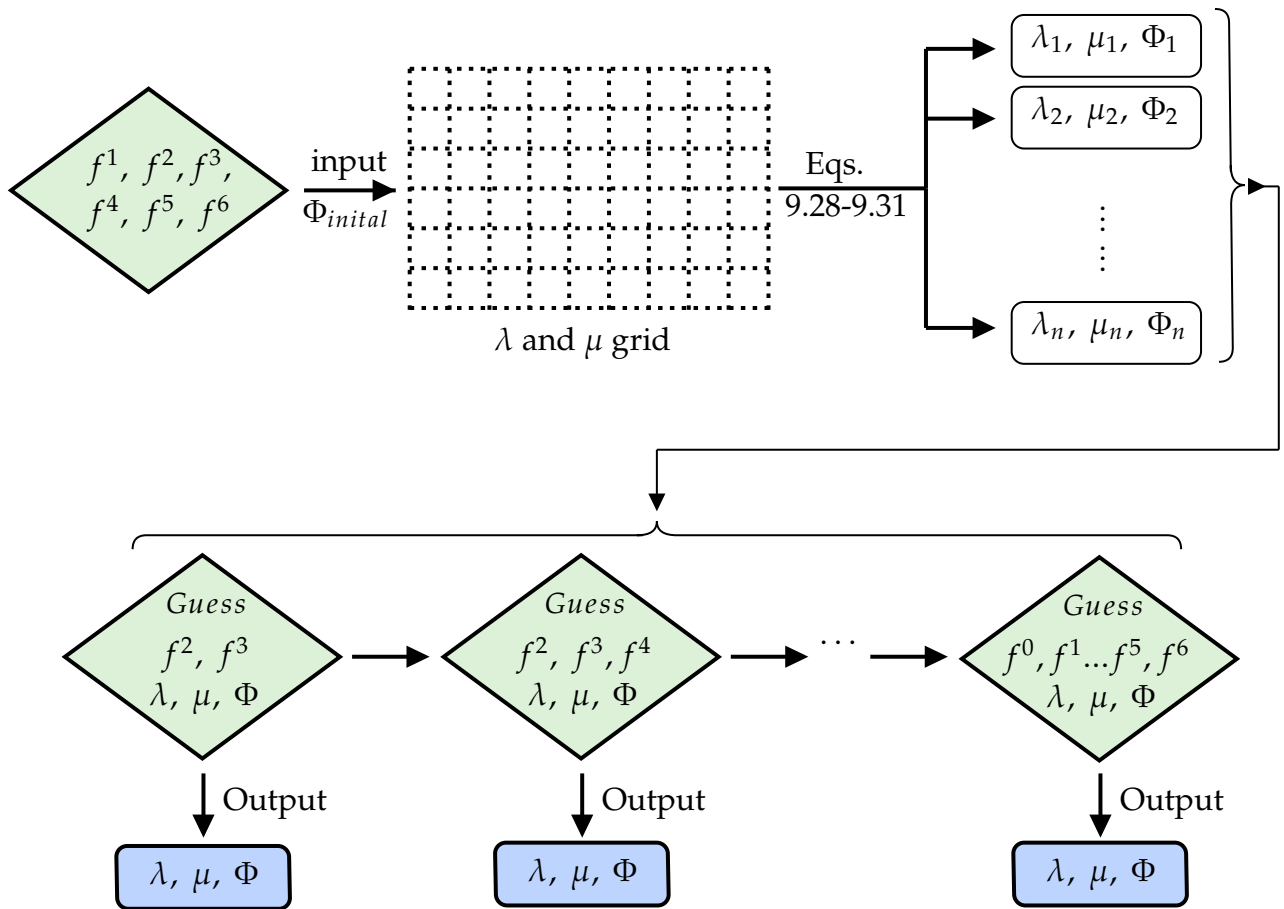


Figure 10.1: Schematic view of initial optimizing process to get guess parameters while considering various f -configurations using the Eqs. 9.28-9.31. Whenever the physical constraints are satisfied, the scheme ejects an output with λ, μ and slave-boson vector Φ .

without any phase consideration. However, one need not do initial calculation over λ and μ -grid for each value of W , but rather when there is a jump in mean-field parameters or a phase transition is suspected.

10.2 Minimization of Energy

Using a single optimization technique can lead to a local minimum or the worst-case scenario to nonphysical results. In our work, we have used various classes of optimization routines to assure the convergence of RISB mean-field equations to their global minimum. Below, we present the python routines that we have considered and their advantages and drawbacks, and how we have used them in our code.

10.2.1 Choice of optimization algorithms

During our whole numerical optimization process, the choice of algorithm and the method of iteration was a crucial step. We found that gradient-based methods were not so effective for either local minimization or global minimization of energy. So we have used gradient-free methods throughout our study. To solve the auto-consistent equations (9.28-9.31), we have used the derivative-free Powell method from NLOpt library [329] along with Scipy's [330] least-squares. For local minimization of energy was either conducted by using Pymoo's [331] heuristic pattern search and/or Scipy's trust region method was used. Furthermore, global minimization was conducted with Scipy's stochastic basin hopping or with differential evolution.

10.2.2 Global and local optimizations

The methods described in section 10.2.1 were used to find local or global minima. Figure 10.2 shows the schematic view of an overall view of local minimizations. During our calculations, we found that an iterative method where a previous solution is injected to calculate a new solution for a new set of parameters was not efficient. However, it can be used in some situations, for example, non-interacting case $U = 0$. The local optimization iteration process can be defined in the following steps.

- i) At first, a set of non-zeros $\varphi_{\Gamma n}^{Guess}$ slave-bosons are determined as guess parameters by using the method in section 10.1.
- ii) We actualize the mean-field parameters λ and μ for given hopping with $\varphi_{\Gamma n}^{Guess}$ as input. In the meantime, $\varphi_{\Gamma n}^{Guess}$ is actualized into $\varphi_{\Gamma n}$.
- iii) A local minimization is conducted with routines stated above in the section 10.2.1.

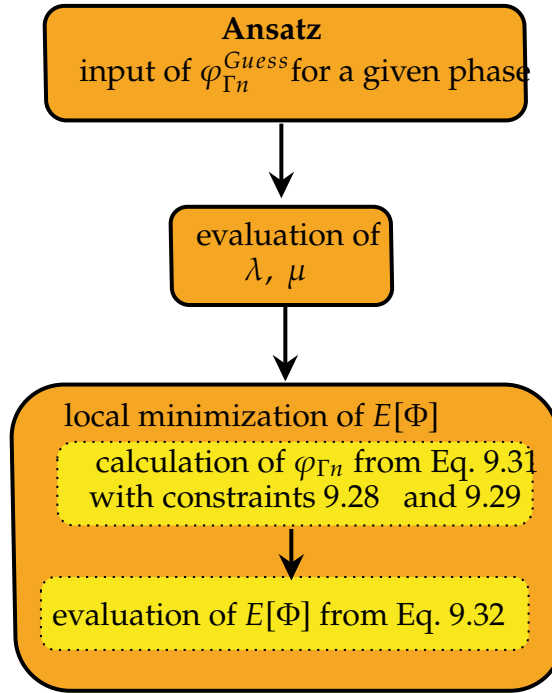


Figure 10.2: Schematic view of local minimization for a given phase with a set of $\varphi_{\Gamma n}$ non-zeros.

During our numerical calculations, we found that the slave-boson matrix Φ for a given particular solution with partially localized orbitals is not always unique. Thus, in order to assure the ground-state phase diagram, a systematic global optimization must be conducted after the local minimization. Figure 10.3 presents our complete algorithm scheme, which includes the global optimization step.

10.3 Numerical error tolerance on constraints

We have altogether two physical constraints: the completeness equation $\sum_{\Gamma n} \varphi_{\Gamma n}^2 = 1$ and the conservation of fermionic particle number $\sum_{j_z} n_{j_z}[\Phi] = n_f$. The convergence of a solution is defined upon the tolerance of these constraints. From the equation 9.32, we can also deduce that the numerical error on the energy is proportional to the number of non-zeros slave-bosons. Since, we can have up to 116 non-zeros bosons, this addition can significantly impact the differentiation between two close phases. During our minimization of energy, we found that the minimums of energies can be as close as 0.1% to each other relatively. Thus, all our solutions were calculated with a minimum tolerance of 10^{-6} .

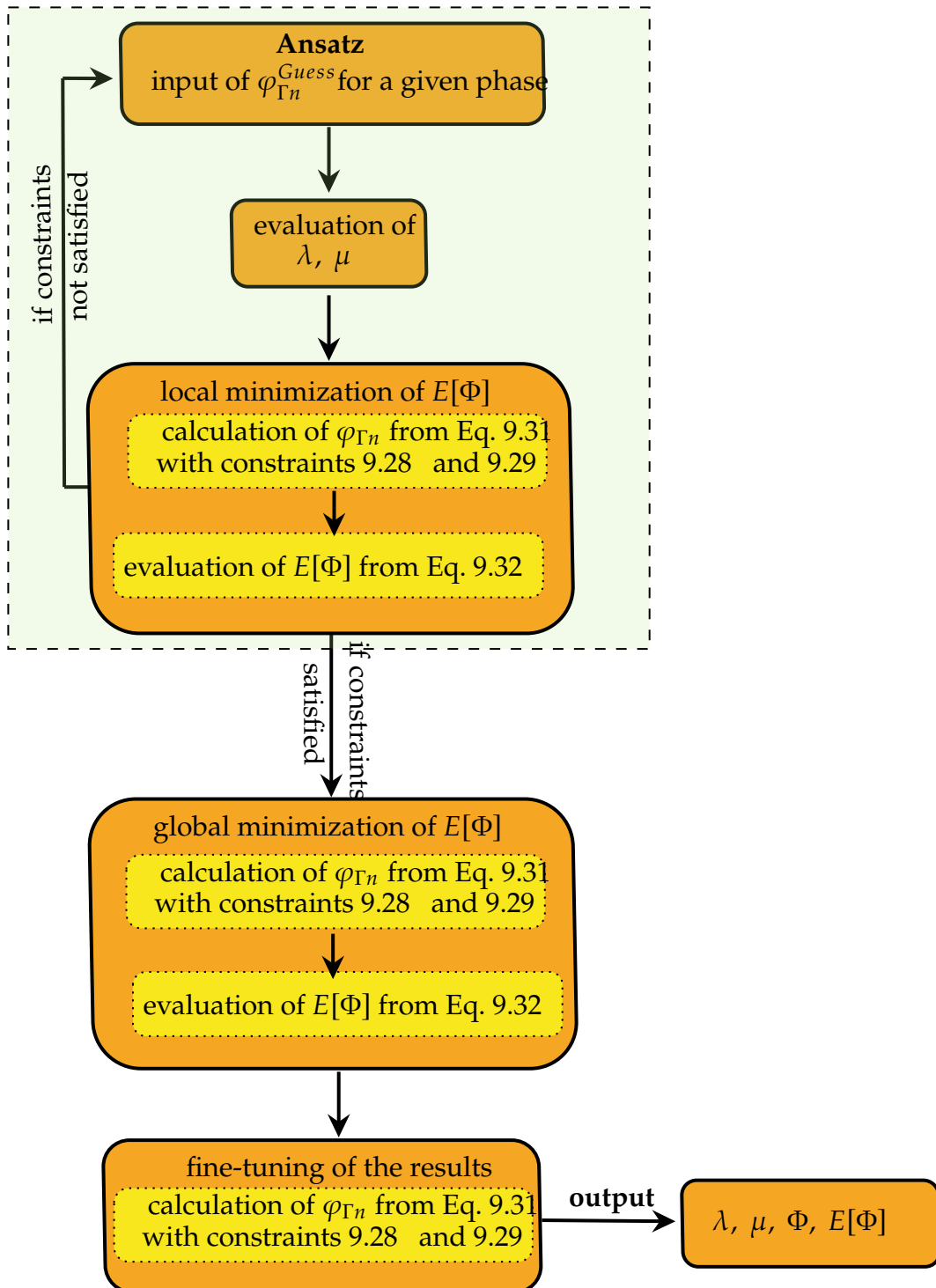


Figure 10.3: Schematic view of the complete numerical process. The light green background shows the local minimization process, and its output is injected into a global minimization routine.

Chapter 11

Results

In this chapter, we present the numerical results that we have obtained by solving the self-consistent equations (9.18 - 9.21). In our calculations, we consider two different orbital-dependent electronic bandwidths: $W_{3/2}$ and $W_{1/2} = W_{5/2}$, along with f -electron count and Coulomb interactions as parameters. Depending upon case of study, we will be varying the electronic bandwidths, Coulomb interactions, and f -electron count n_f . Table 11.1 resumes the parameters used on various cases.

	n_f	U_0	ΔU_2	ΔU_4	$W_{3/2}$	$W_{5/2} = W_{1/2}$
Non-interacting						
limit	from 3.0 to 2.5	0	0	0	W	W
Atomic limit	$(2+3)/2 = 2.5$	21.00 eV	-2.72 eV	-3.79 eV	0	0
General case	$(2+3)/2 = 2.5$	21.00 eV	-2.72 eV	-3.79 eV	W	W'

Table 11.1: Table resuming the parameters for different case of study.

After checking the limits of our model, we will perform a full calculation by varying orbital-dependent electronic bandwidths to analyze the effect of its anisotropies. For that, we also consider non-integer f -electron count $n_f = 2.5$, which is justified through the experimental observations [287, 298–300, 332] where f -electron valencies situate between 2 and 3 for uranium-based heavy-fermions. Here, we consider the Coulomb interactions $U_{J=4} = 17.21\text{eV}$, $U_{J=2} = 18.28\text{eV}$ and $U_{J=0} = 21.00\text{eV}$ which was obtained from the local density approximation $5f$ wave functions calculation [17] for UPt_3 . From these Coulomb parameters, one could notice the anisotropic as $\Delta U_4 = U_{J=4} - U_{J=0} = -3.79\text{ eV}$ and $\Delta U_2 = U_{J=2} - U_{J=0} = -2.72\text{ eV}$. This anisotropy depends weakly upon the chemical environment are usually not screened whereas U_0 get screened. The choice of UPt_3 is motivated by the previous calculations [17, 327] done within the dual model. This will permit us to make a direct comparison of our results with the previous calculations whenever possible.

11.1 Non-localized paramagnetic phase in isotropic hopping case

In this section, we present our results for non-interacting ($U = 0$) and atomic ($W_{j_z} = 0$) limits on the isotropic line ($W = W_{1/2} = W_{1/2} = W_{5/2}$). The solutions on the isotropic line are highly degenerate. Nevertheless, the analytical solutions for both limits can be determined. Thus, these limits set a benchmark for our numerical method to produce consistent results. Furthermore, the solutions at these limits provide us a solid starting point to perform global minimization for other sets of parameters $W_{3/2}$ and $W_{3/2} = W_{1/2}$.

11.1.1 Non-interacting limit

At first, we start from electronic occupation $n_f = 3.00$ in the non-interacting limit. Thereafter, we will gradually decrease n_f to obtain the intermediate occupation $n_f = 2.5$. For $n_f = 3.0$ with $U = 0$, all the slave-bosons $\varphi_{nn'}$ on the Fock-Fock basis set are equivalent and the slave-boson matrix is diagonal. From this argument, we can easily determine the amplitudes of slave-bosons as

$$\varphi_{nn'} = \frac{\delta_{nn'}}{\sqrt{64}}. \quad (11.1)$$

Instead of Fock-Fock basis set, one can freely choose multiplet-multiplet basis set to represent both physical and auxiliary states. The linear transformation (9.15) can be applied to the equation (11.1) to obtain φ_{Γ} . However, we perform our numerical work using multiplet-Fock basis, and we apply again a linear transformation to obtain $\varphi_{\Gamma n}$ as

$$\varphi_{\Gamma} = \sum_n \langle n | \Gamma \rangle \varphi_{\Gamma n}. \quad (11.2)$$

With the relations 11.1, and 11.2, we solved the RISBMF equations from $n_f = 3.00$ to 2.5. Figure 11.1 shows the numerical results with slave-boson probabilities. For $n_f = 3.00$, all the slave-boson amplitudes are equivalent with $|\varphi_{\Gamma}|^2 = (1/\sqrt{64})^2 = 0.015625$ and the orbitals are fully delocalized $Z_{j_z} = 1$. As soon as n_f is moved away from the half-filling $n_f = 3.0$, the symmetry of $|\varphi_{\Gamma}|^2$ over all charge sectors breaks. However, the symmetry over the same particle sector is still preserved.

11.1.2 Atomic limit

At the atomic limit $W = 0$, the ground-state verifies the Hund's rule, and is made up of the local atomic multiplets $|f^2; J = 4, J_z\rangle$ and $|f^3; J = 9/2, J_z\rangle$ with the conditions below

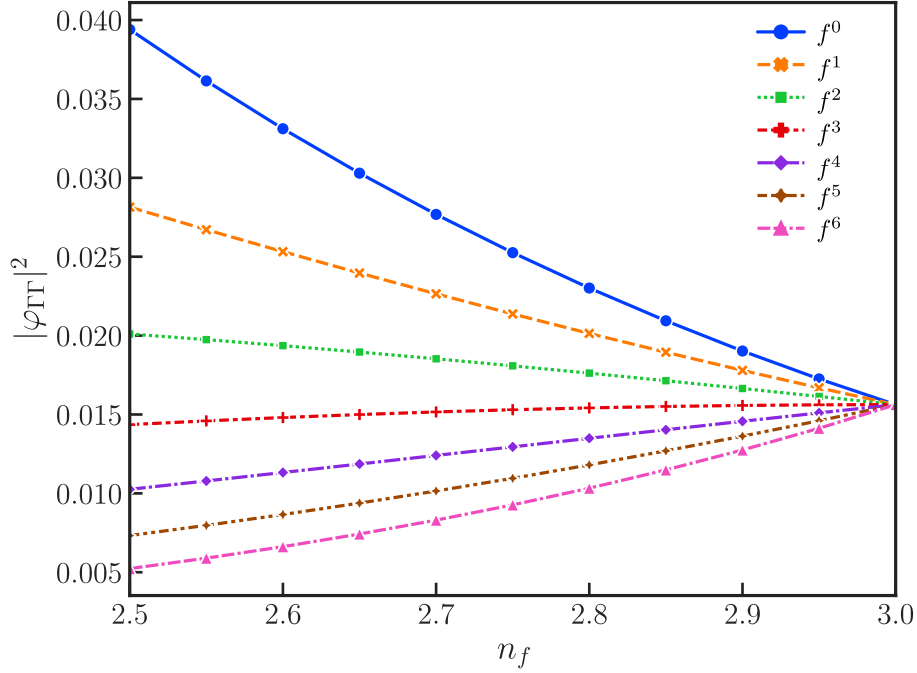


Figure 11.1: Evolution of slave boson probabilities $|\varphi_{\Gamma\Gamma}|^2$ on multiplet-multiplet basis along with f -electron occupation from $n_f = 3.0$ to $n_f = 2.5$ for charge sectors f^M configurations for non-interacting case (see table 11.1).

$$\sum_{J_z=-4}^4 |\varphi_{f^2;J=4,J_z}, |f^2;J=4,J_z}\rangle|^2 = \frac{1}{2}, \quad (11.3)$$

$$\sum_{J_z=-9/2}^{9/2} |\varphi_{f^3;J=9/2,J_z}, |f^3;J=9/2,J_z}\rangle|^2 = \frac{1}{2}. \quad (11.4)$$

Expanding the expressions 11.3 and 11.4, we can deduce that the values of each slave-boson contributing to the ground-state solution at the atomic limit is

$$|\varphi_{|M=2;J=4,J_z}, |M=2;J=4,J_z}\rangle|^2 = \frac{1}{18}, \quad (11.5)$$

$$|\varphi_{|M=3;J=9/2,J_z}, |M=3;J=9/2,J_z}\rangle|^2 = \frac{1}{20}. \quad (11.6)$$

From the equations 11.3 and 11.4, one can deduce that the ground-state energy at the atomic limit is the sum of Coulomb energy of $|f^2; J = 4, J_z\rangle$ and $|f^3; J = 9/2, J_z\rangle$

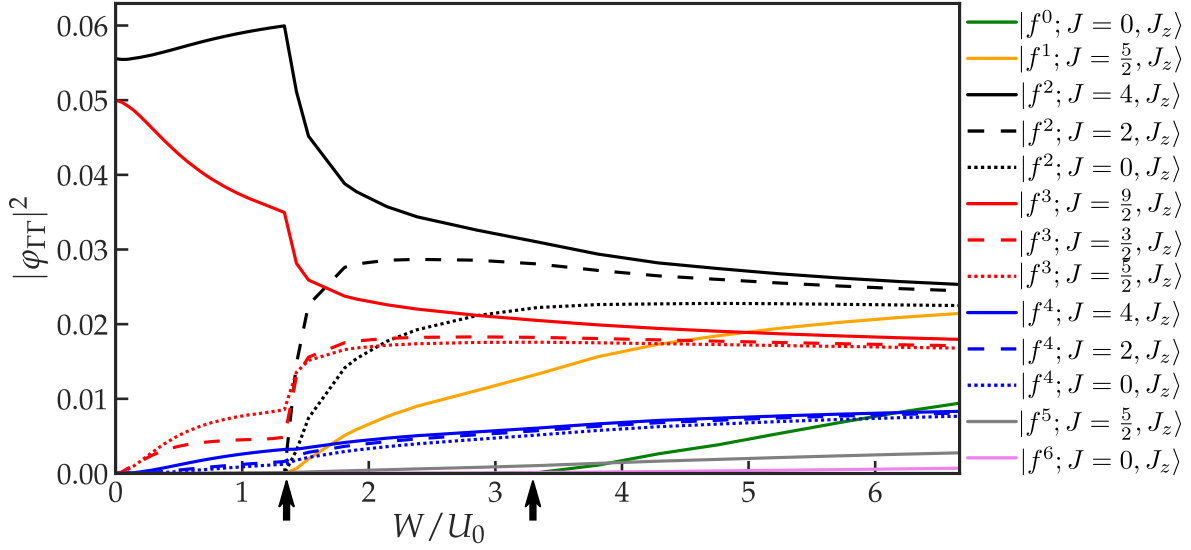


Figure 11.2: Diagonal slave bosons probabilities $|\varphi_{\Gamma\Gamma}|^2$ on the isotropic line ($W = W'$) for all six charge sectors $|f^M; J, J_z\rangle$. The black arrows on the x-axis points the towards the threshold values of W/U_0 where transition in valency configuration is observed.

configurations as

$$E_0(W = 0) = \frac{U_4 + U_{M=3, J=9/2}}{2} = 34.76 eV . \quad (11.7)$$

In order to solve the mean-field equations numerically at the atomic limit, we start from the solution obtained for $n_f = 2.5$ at $U = 0$. Thereafter, we gradually increase the Coulomb integrals U_J with $W \gg U$ until $U_0 = 21.00$ eV, $U_2 = 18.28$ eV and $U_4 = 17.21$ eV. Thereafter, we slowly decrease the isotropic electronic bandwidth until $W = 0$. We found that the ground state is highly degenerate i.e. any set of slave-boson matrix Φ fulfilling the conditions 11.3 and 11.4 with the energy E_0 can be a solution. This made the numerical resolution challenging. However, we were able to recover the analytical solutions 11.5 and 11.5 with ground-state energy E_0 . The numerical result is presented in the figure 11.2. This also shows the correctness and robustness of our numerical method to solve RISBMF equations.

11.1.3 From atomic limit to non-interacting limit: the appearance of three distinct regions

In this section, we will present our results on the isotropic line while moving from atomic limit to non-interacting limit by gradually increasing isotropic electronic bandwidth. Figure 11.2 presents the slave-boson probabilities on a multiplet-multiplet basis. By analyzing the non-zeros slave-bosons probabilities, we can distinguish two thresholds on electronic bandwidth, delimiting three regions: the first

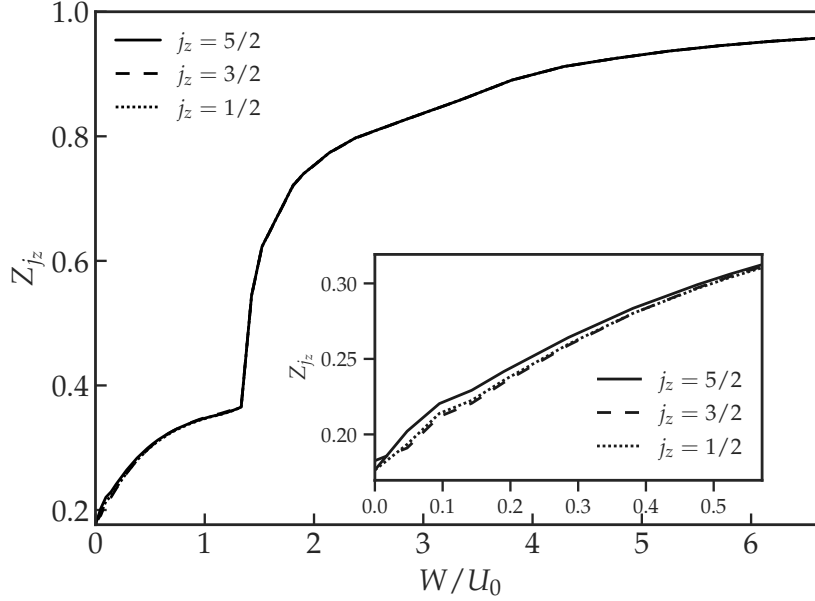


Figure 11.3: Quasiparticles weight Z_{j_z} as a function of electronic bandwidth W/U_0 on the isotropic line ($W_{5/2} = W_{3/2} = W_{1/2}$) for orbitals $j_z = 5/2, 3/2$ and $1/2$ for paramagnetic phase. The inset shows a zoom of Z_{j_z} around small W/U_0 .

region lies between $W/U_0 = 0$ to ≈ 1.32 , the second region lies between $W/U_0 \approx 1.32$ to ≈ 3.27 , and the third region lies for $W/U_0 \gtrsim 3.27$. Furthermore, the signatures of the thresholds can also be observed in the quasiparticle weight Z_{j_z} and mean-field energies E .

Let's start with the first region. As per Hund's rule, the ground state of the system at atomic-limit is made up of from f^2 and f^3 -electron configurations with total angular momentum $J = 4$ and $J = 9/2$ respectively. As soon as the isotropic electronic hopping gets a finite value $W > 0$, the slave-bosons associated with f^4 configuration become non-zeros, suggesting valency configuration transition. Here, the ground-state is made up of local configurations: $|f^2; J = 4, J_z\rangle$, $|f^3; J = 9/2, J_z\rangle$, $|f^3; J = 5/2, J_z\rangle$, $|f^3; J = 3/2, J_z\rangle$, $|f^4; J = 4, J_z\rangle$, $|f^4; J = 2, J_z\rangle$ and $|f^4; J = 0, J_z\rangle$. Due to Hund's rule, the quasiparticles weight Z_{j_z} associated with each orbital j_z is anisotropic such that $Z_{5/2} \neq Z_{3/2} \neq Z_{1/2}$. The inset in the figure 11.3 presents this anisotropic behavior.

The second region starts at $W/U_0 \approx 1.32$ and is marked by slave-boson associated with configurations $|f^1; J = 5/2\rangle$, $|f^5; J = 5/2\rangle$, $|f^2; J = 2\rangle$ and $|f^2; J = 4\rangle$ becoming non-zero. Thus, these additional local multiplets contribute to the formation of ground-state. The quasiparticle weight presents a large Z_{j_z} around $W/U_0 \approx 1.32$. Similar behavior is also observed in the energy and the mean-field parameters and is presented in the figurefigure 11.4. Similar jumps in energies were seen in the two sites model [60] resulting from the competition between Coulomb interaction and hopping.

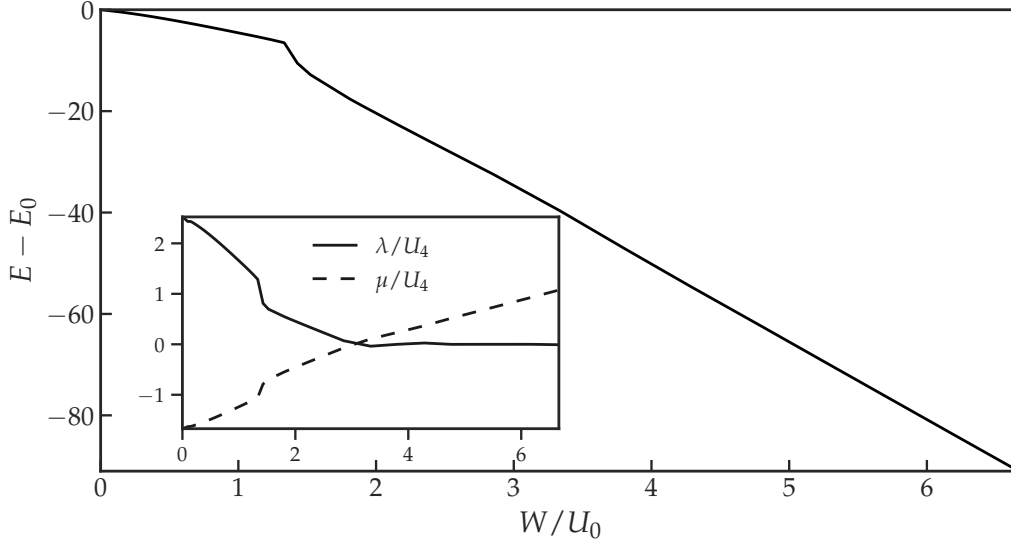


Figure 11.4: $E - E_0$ on the isotropic line from $W/U_4 = 0$ to large W/U_0 large. The inset shows the mean-field parameters λ and μ .

The third region starts approximately at $W/U_0 \approx 3.27$ where all the slave-bosons on all the charge sectors become non-zeros. Thus, the ground-state is composed of all the configurations: $f^0, f^1, f^2, f^3, f^4, f^5$, and f^6 as for non-interacting limit. From the figure 11.4, we can observe that the mean-field parameter λ cancels out, and μ changes its sign from negative to positive as in the non-interacting case. The quasiparticle weight is isotropic and recovers the value $Z_{j_z} \simeq 1$ for large W .

In this isotropic case, we were able to recover the non-interacting limit from the atomic limit. The results on both limits are similar to those obtained by Duc-Anh Le [327]. However, multiple differences were obtained. For low hopping, we obtained anisotropic Z_{j_z} , which was not observed in the previous study [327]. Furthermore, successive transitions in valency configurations were observed due to interplay between Hund's rule, Coulomb interaction, and increasing bandwidth: $(f^2, f^3) \rightarrow (f^2, f^3, f^4) \rightarrow (f^1, f^2, f^3, f^4, f^5) \rightarrow (f^0, f^1, f^2, f^3, f^4, f^5, f^6)$. However, due to the isotropic nature of electronic bandwidth, no orbital-selective Mott transition was observed in this case which is not the case when the anisotropic in electronic bandwidths are present.

11.2 Ground-state phase diagram

After the isotropic case, we solved the RISBMF equations considering paramagnetic (PM) and ferromagnetic (FM) phases in the range of $0 \leq W_{1/2} \leq 15$ and $0 \leq W_{5/2} (= W_{1/2}) \leq 15$. In order to simply, we note $W = W_{3/2}$ and $W' = W_{5/2} = W_{1/2}$. Her, a paramagnetic phase is characterized by having symmetric j_z and $-j_z$ orbitals:

$n_{j_z} = n_{-j_z}$ and $Z_{j_z} = Z_{-j_z}$. Similarly, a ferromagnetic phase is characterized by having at least one orbital j_z being fully occupied and its counterpart $-j_z$ being empty: $n_{j_z} = 1, Z_{j_z} = 0$ and $n_{j_z} = 0, Z_{j_z} = 0$. Also, a saturated ferromagnetic phase (SFM) is characterized by having all the j_z orbitals occupied and all $-j_z$ empty.

From our numerical calculations, we have found altogether twelve phases with partially localized orbitals: five PM, five FM, and two SFM phases. Furthermore, each phase can be either one-electron localized or two-electron localized. From here, if a phase is paramagnetic with $j_z = 5/2$ and $1/2$ localized, we will note it as $\text{PM}_{\frac{5}{2}, \frac{1}{2}}$. The table 11.2 regroupes the necessary information on the orbitals occupancy and the quasiparticle weight of the different partially localized phases.

Localized orbitals (j_z)	Phase	Orbital occupancy						Quasiparticle weight					
		$n_{\frac{5}{2}}$	$n_{\frac{3}{2}}$	$n_{\frac{1}{2}}$	$n_{-\frac{1}{2}}$	$n_{-\frac{3}{2}}$	$n_{-\frac{5}{2}}$	$Z_{\frac{5}{2}}$	$Z_{\frac{3}{2}}$	$Z_{\frac{1}{2}}$	$Z_{-\frac{1}{2}}$	$Z_{-\frac{3}{2}}$	$Z_{-\frac{5}{2}}$
5/2, 1/2	$\text{PM}_{\frac{5}{2}, \frac{1}{2}}$	0.50	0.25	0.50	0.50	0.25	0.50	0	...	0	0	...	0
	$\text{FM}_{\frac{5}{2}, \frac{1}{2}}$	1	...	1	0	...	0	0	...	0	0	...	0
	$\text{SFM}_{\frac{5}{2}, \frac{1}{2}}$	1	0.50	1	0	0	0	0	1	0	0	0	0
5/2, 3/2	$\text{PM}_{\frac{5}{2}, \frac{3}{2}}$	0.50	0.50	0.25	0.25	0.50	0.50	0	0	0	0
	$\text{FM}_{\frac{5}{2}, \frac{3}{2}}$	1	1	0.25	0.25	0	0	0	0	0	0
	$\text{SFM}_{\frac{5}{2}, \frac{3}{2}}$	1	1	0.50	0	0	0	0	0	1	0	0	0
5/2	$\text{PM}_{\frac{5}{2}}$	0.50	0.50	0	0
	$\text{FM}_{\frac{5}{2}}$	1	0	0	0
3/2	$\text{PM}_{\frac{3}{2}}$...	0.50	0.50	0	0	...
	$\text{FM}_{\frac{3}{2}}$...	1	0	0	0	...
1/2	$\text{PM}_{\frac{1}{2}}$	0.50	0.50	0	0
	$\text{FM}_{\frac{1}{2}}$	1	0	0	0

Table 11.2: Orbitals occupations (n_{j_z}) and quasiparticles weights (Z_{j_z}) for various partially localized phases. Here, PM signifies paramagnetic phase, FM signifies ferromagnetic phase and SFM signifies saturated ferromagnetic phase and the notation $\text{PM}_{\frac{5}{2}, \frac{1}{2}}$ means paramagnetic phase with $j_z = 5/2$ and $j_z = 1/2$ orbitals localized.

In order to construct a phase diagram, we compare the energies. The energy for each phase is obtained from the equation below

$$E[\Phi] = - \sum_{j_z} \frac{W_{j_z}}{2} Z_{j_z}[\Phi] n_{j_z}[\Phi] (1 - n_{j_z}[\Phi]) + \sum_{\Gamma n} E_{\Gamma} \varphi_{\Gamma n}^2. \quad (11.8)$$

The first term of the equation (11.8) gives the kinetic energy, and the second term is related to the energy due to local interactions. The total energy of the system for a given phase depends only on the contribution from its non-localized orbitals.

In order the effect of anisotropies, we present the energies of each partially

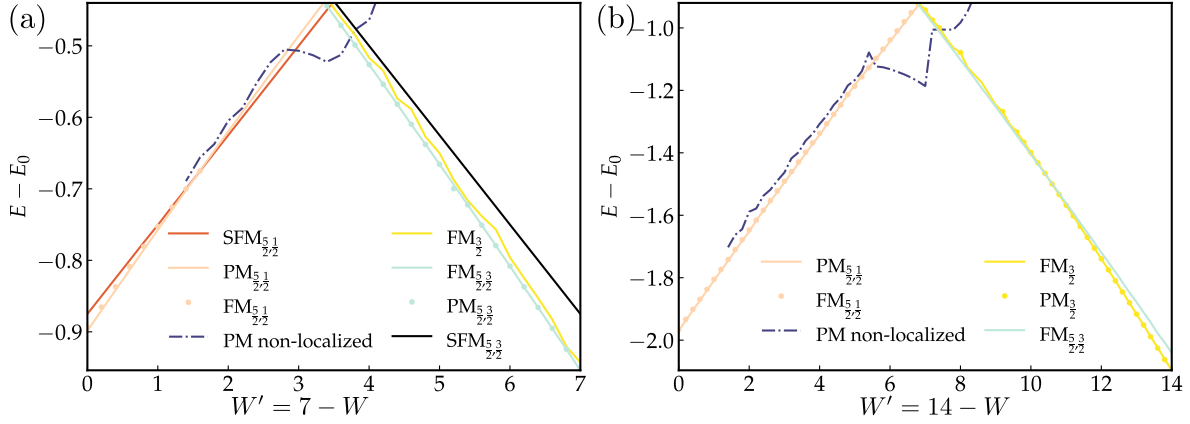


Figure 11.5: Energies of partially localized phases along the line $W + W' = \text{constant}$: (a) $W + W' = 7$ and (b) $W + W' = 14$ while $W = W_{3/2}$ and $W' = W_{5/2} = W_{1/2}$. Colors of each line correspond to the color of each phase in figure 11.6.

localized phase along the line $W + W' = 7$ and $W + W' = 14$ in the figure 11.5. The representation of the energies along these lines permits us to include all the phases in the ground state phase diagram (see figures 11.6 and 11.7). First, we can clearly remark that the energy of the partially localized phase decreases linearly with increasing W_{j_z} due to a decrease of kinetic energy. However, it is partially compensated by energy due to local interaction. Furthermore, we observe that the FM and PM phases with the same localized orbitals are degenerate. The crossing of energies curves translating phase transitions happens smoothly except near isotropic line where a jump in energy for non-localized paramagnetic phase is seen (see section 11.1.3).

For smaller electronic bandwidths with anisotropy, the two-electrons localized phases are found to be more stable than a one-electron localized phase. However, phases with one-electron localized can be stabilized for larger hopping when $W > W'$ and $W' > W$. Depending upon the anisotropy, different sets of orbitals can be localized. For $W > W'$, either $j_z = 5/2, 1/2$ or $j_z = 5/2$ or $j_z = 1/2$ orbitals can be localized. For $W' > W$, either $j_z = 5/2, 3/2$ or $j_z = 3/2$ can be localized. Figure 11.6 compiles our results and presents the ground-state phase diagram. Below, we present detailed information about the various one-electron and two-electron localized phases on the different parts of our phase diagram.

11.2.1 One-electron localized phases

Let's start from the situation $W > W'$ where we found $\text{FM}_{5/2}$, $\text{PM}_{5/2}$, $\text{FM}_{1/2}$ and $\text{PM}_{1/2}$ phases. All these phases were found for $W \geq 5.20$ eV. The local configurations $|f^2; J = 4, J_z\rangle$, $|f^3; J = 9/2, J_z\rangle$, and $|f^3; J = 5/2, J_z\rangle$ made up the phase $\text{FM}_{5/2}$. Similarly, the local configurations $|f^2; J = 4, J_z\rangle$, $|f^3; J = 9/2, J_z\rangle$, $|f^3; J = 5/2, J_z\rangle$, $|f^3; J = 3/2, J_z\rangle$ and $|f^4; J = 4, J_z\rangle$ made up the phase $\text{FM}_{1/2}$. From our calculations, the localization

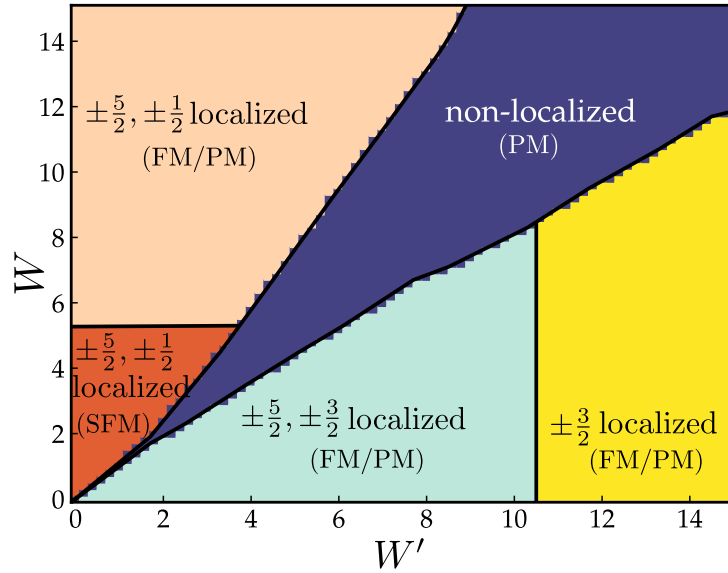


Figure 11.6: Phase diagram with partially localized phases for the electronic bandwidths $0 \leq W \leq 15$ and $0 \leq W' \leq 15$. Solid lines are guides to the eyes separating two phases. (FM/PM) indicates that ferromagnetic and paramagnetic phases are degenerate.

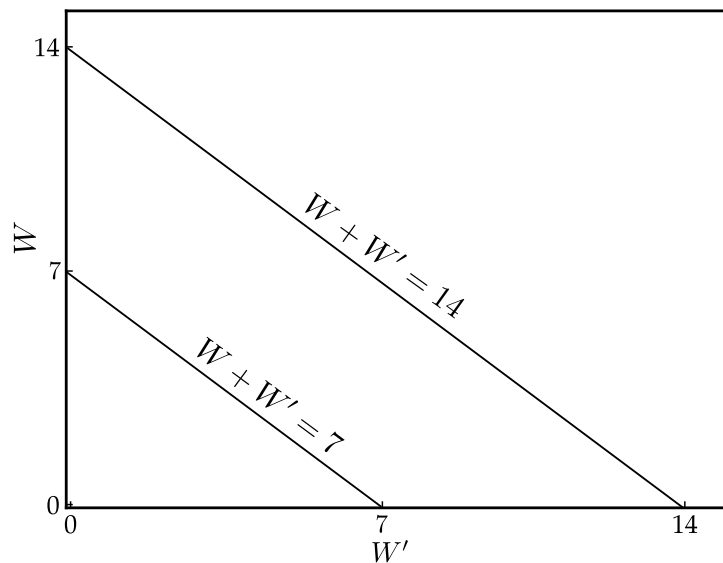


Figure 11.7: Figure showing the line $W + W' = 7$ and $W + W' = 14$ on the phase diagram.

of orbital $j_z = 5/2$ was more energetically favorable than the localization of $j_z = 1/2$. This can be understood since the Coulomb matrix element $\langle j_z j_z | \hat{U} | -j_z - j_z \rangle$ in the Hamiltonian (9.1) is 0.23 eV larger for $j_z = 5/2$ than $j_z = 1/2$. Moreover, PM phases are degenerate with FM phases, and they can be obtained by the linear combination of two FM phases with its counterpart obtained by flipping the quantization axis. Either way, none of these one-electron localized phases were found to be in the ground-state phase diagram. This result is in contrast with the previous result obtained within RISB [327] and also in the two-site model [60].

For the anisotropy $W < W'$, we were able to localize the orbital $j_z = 3/2$ both in FM or PM phases. As before, PM and FM phases are degenerate and PM phase can be obtained by the combination of two FM phases. The local configurations $|f^2; J = 4, J_z\rangle$, $|f^3; J = 9/2, J_z\rangle$, $|f^3; J = 5/2, J_z\rangle$, $|f^3; J = 3/2, J_z\rangle$, $|f^4; J = 4, J_z\rangle$, and $|f^4; J = 2, J_z\rangle$ made up both FM and PM phases. This phase is found to be stable when $W' \gtrsim 10.40$ eV. Similar result was obtained in previous calculation [327] but in our case the transition between $\text{FM}_{\frac{3}{2}}(\text{PM}_{\frac{3}{2}})$ and $\text{FM}_{\frac{5}{2}, \frac{3}{2}}(\text{PM}_{\frac{5}{2}, \frac{3}{2}})$ happens at $W' \simeq 10.30$ eV instead of $W' \simeq 2.60$ eV [327].

A possible explication of localization of one-electron can be done in an analogous manner as Mott localization. Following the same scenario, the Coulomb interaction $\langle j_z j_z | \hat{U} | -j_z - j_z \rangle$ between the electrons on j_z and $-j_z$ orbitals compete with the orbital-dependent electronic bandwidth as $\frac{\langle j_z j_z | \hat{U} | -j_z - j_z \rangle}{W_{j_z}}$. Thus, under a certain threshold in $\frac{\langle j_z j_z | \hat{U} | -j_z - j_z \rangle}{W_{j_z}}$, the localization of an electron in an orbital j_z can happen.

11.2.2 Two-electrons localized phases

Here, we analyze the phases with two localized electrons. At first, we concentrate on the region $W > W'$, where we obtained localization of electrons in the orbitals $j_z = 5/2$ and $1/2$.

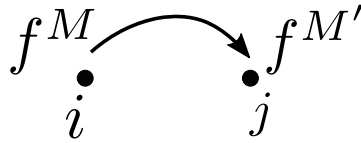


Figure 11.8: Schematic view of an electron hopping from a site- i with f^M configuration to a site- j with $f^{M'}$ configuration. For $M' < M$, this hopping becomes favorable. For instance, the hopping from $M = 3$ to $M = 2$ is more favorable than other way around since the hopping from $M = 2$ to $M = 3$ will create more energetic states with $M = 1$ and $M = 5$ particles.

Let's us consider $W \lesssim 5.20$ eV with $W' = 0$ eV, in this case $\text{SFM}_{\frac{5}{2}, \frac{1}{2}}$ was found to be stable. The formation of this phase follows the Hund's rule with the multiplets $|f^2; J = 4, J_z = 3\rangle = |000101\rangle$ and $|f^3; J = 9/2, J_z = 9/2\rangle = |000111\rangle$ forming the macroscopic phase. From these multiplets, we can easily deduce that only the

electron in $j_z = 3/2$ orbital from f^3 configuration can hop to f^2 , since hopping from f^2 to f^3 will give less favorable high energetic f^4 electron state (see figure 11.8). Similar results were also obtained in two-sites model [60] where a phase with total magnetization $\mathcal{J}_z = 15/2$ was obtained. The $\mathcal{J}_z = 15/2$ (see figure 8.4) in two-sites model corresponds to our $\text{SFM}_{\frac{5}{2}, \frac{1}{2}}$ with only positive orbitals occupied. At $W \simeq 5.20$ eV, transition from $\text{SFM}_{\frac{5}{2}, \frac{1}{2}}$ to $\text{FM}_{\frac{5}{2}, \frac{1}{2}}$ ($\text{PM}_{\frac{5}{2}, \frac{1}{2}}$) happens with additional multiplets $|f^3; J = 4, J_z = 3/2\rangle$, $|f^3; J = 3/2, J_z = 3/2\rangle$ and $|f^4; J = 4, J_z = 4\rangle$ contributing to the formation of the ground-state for $\text{FM}_{\frac{5}{2}, \frac{1}{2}}$ ($\text{PM}_{\frac{5}{2}, \frac{1}{2}}$) phase.

For $W' > W$, only the orbitals $j_z = 5/2$ and $3/2$ are localized simultaneously in either PM, FM or SFM. For low W_2 , $\text{SFM}_{\frac{5}{2}, \frac{3}{2}}$ and $\text{FM}_{\frac{5}{2}, \frac{3}{2}}$ competes with each other but $\text{FM}_{\frac{5}{2}, \frac{3}{2}}$ was found to be the ground state. Same as above, $\text{FM}_{\frac{5}{2}, \frac{3}{2}}$ and $\text{PM}_{\frac{5}{2}, \frac{3}{2}}$ are degenerate. Both phases follow the Hund's rule where $\text{SFM}_{\frac{5}{2}, \frac{3}{2}}$ is made up of local multiplets $|f^2; J = 4, J_z = 4\rangle$, and $|f^3; J = 9/2, J_z = 9/2\rangle$ whereas $\text{FM}_{\frac{5}{2}, \frac{3}{2}}$ have additional local multiplets $|f^3; J = 9/2, J_z = 7/2\rangle$ and $|f^4; J = 4, J_z = 4\rangle$ than $\text{SFM}_{\frac{5}{2}, \frac{3}{2}}$.

11.3 Physical signatures and manifestations of duality

In this section, we will treat the various aspects of partially localized phases through quasiparticle weight Z_{j_z} , electronic occupancies n_{j_z} , magnetization $m_z = \sum_{j_z} n_{j_z} j_z$ and f -electron valency configurations along $W + W' = 7$ and $W + W' = 14$ (see figure 11.7).

11.3.1 Quasiparticle weight

An orbital is localized when $Z_{j_z} = 0$ and delocalized when $Z_{j_z} \neq 0$. With these definitions on hand, we can now analyze the quasiparticle weight of our ground-state phase diagram up on anisotropy of non-interacting electronic bandwidth.

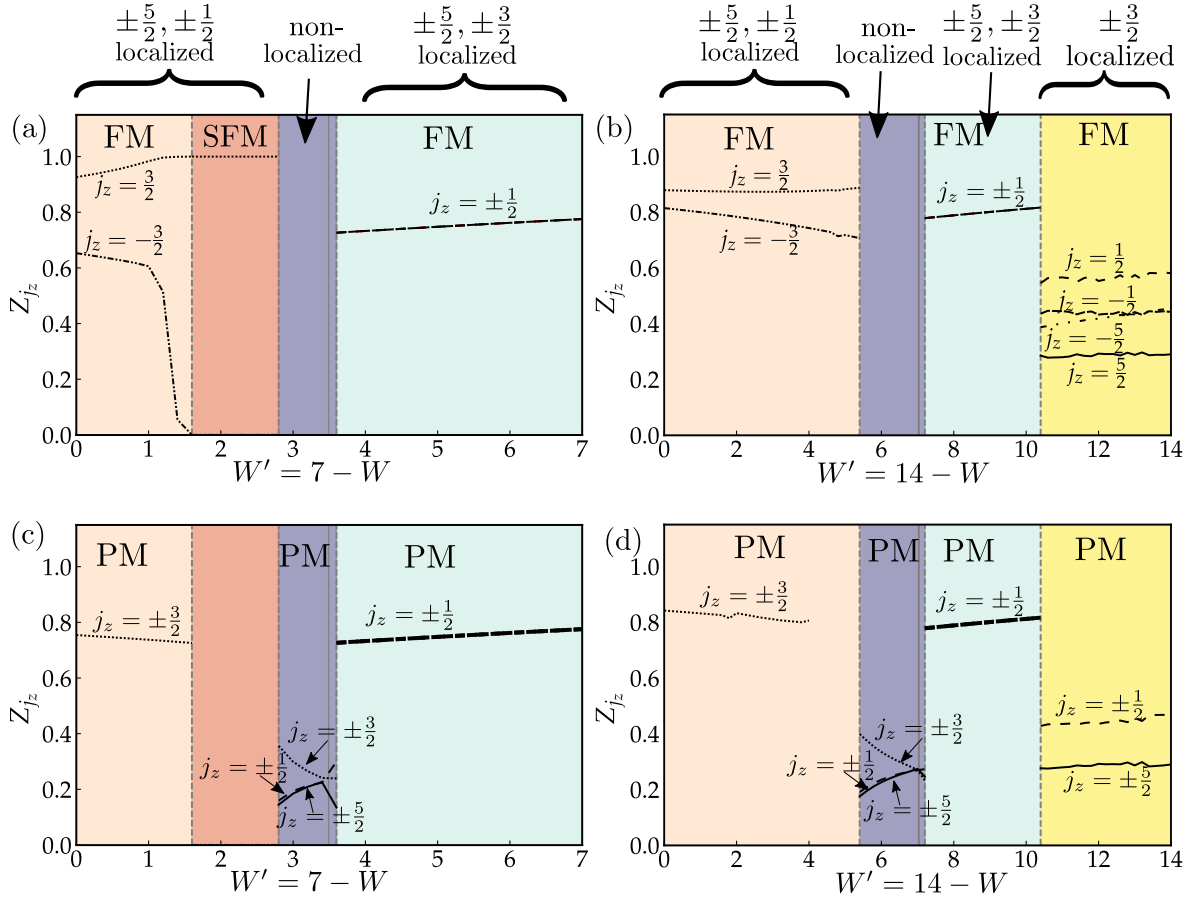


Figure 11.9: Quasiparticle weights of non-localized orbitals along the line: $W + W' = 7$ ((a) and (c)) and $W + W' = 14$ ((b) and (d)) in the phase diagram. Only delocalized orbitals are presented here for PM phases ((c) and (d)) and for FM phases ((a) and (b)). Localized orbitals per phase are indicated on the top the figure, and aside of each line for each orbital. Vertical dotted lines are guides for eyes marking frontier between phases whereas solid vertical gray line indicate isotropic point.

Figure 11.9(a) and (c) presents Z_{j_z} for non-localized orbitals on the line $W + W' = 7$ for FM and PM phases respectively. Since there is no equivalent counterpart phase of SFM in PM phase, 11.9(c) misses Z_{j_z} partially. The left side of each graph in figure 11.9 corresponds to the anisotropic region with $W > W'$ where only orbital $j_z = 3/2$ is delocalized. For $\text{FM}_{\frac{5}{2}, \frac{1}{2}}$ quasiparticle weights of delocalized orbitals are orbital dependent: $Z_{-3/2} \neq Z_{3/2}$. This orbital dependency can be explained through the hopping of an electron from one local multiplet to another. In this phase, the electrons in $j_z = 3/2$ can hop from f^3 -configuration to f^2 -configuration which produces more energetic favorable f^3 -configuration than the hopping of electrons in $j_z = -3/2$ from $f^3 \rightarrow f^3$ which produces f^4 -configuration. Thus, the orbital $j_z = 3/2$ is more delocalized than $j_z = -3/2$. Furthermore, we observe that $Z_{3/2}$ in $\text{PM}_{\frac{5}{2}, \frac{1}{2}}$ and $\text{FM}_{\frac{5}{2}, \frac{1}{2}}$ are different even though both phases are degenerate. Thus, the internal magnetic configuration can lead to the different quasiparticle weights per orbitals, even for degenerate phases.

Decreasing W gradually saturates the $\text{FM}_{\frac{5}{2},\frac{1}{2}}$ phase leading to $\text{SFM}_{\frac{5}{2},\frac{1}{2}}$ phase with delocalized $j_z = 3/2$ orbital ($Z_{3/2} = 1$) and localized $-3/2$ orbital ($Z_{-3/2} = 0$). In this case, only hopping of $j_z = 3/2$ is possible from f^3 to f^2 -configuration. Upon further decrease of anisotropy $W \simeq W'$, a sharp discontinuity in Z_{j_z} is observed which marks the onset of non-localized paramagnetic phase (PM_{nL}). With $W' > W$, orbitals $j_z = 5/2$ and $3/2$ get localized. The quasiparticle weight for delocalized $j_z = 1/2$ and $-1/2$ remains same for FM phase which was not the case when $j_z = 5/2$ and $1/2$ were localized. This can be explained since either an electron in $j_z = 1/2$ or $-1/2$ can hop from the local multiplet $|f^4; J = 4, J_z\rangle$ to another local multiplet $|f^3; J = 9/2, J_z\rangle$, to generate again $|f^4; J = 4, J_z\rangle$, forming the macroscopic $\text{FM}_{\frac{5}{2},\frac{3}{2}}$ or $\text{PM}_{\frac{5}{2},\frac{3}{2}}$ phase.

In figure 11.9(b) and (d), we present Z_{j_z} on the line $W + W' = 14$. Similar conclusions can be drawn for $\text{FM}_{\frac{5}{2},\frac{1}{2}}$ ($\text{PM}_{\frac{5}{2},\frac{1}{2}}$), PM_{nL} and $\text{FM}_{\frac{5}{2},\frac{3}{2}}$ ($\text{PM}_{\frac{5}{2},\frac{3}{2}}$) phases. However for $W > W'$, $\text{FM}_{\frac{3}{2}}$ ($\text{PM}_{\frac{3}{2}}$) with only one electron localized is present. In this phase, similar as above, the quasiparticle weights are orbital-dependent with $j_z = 1/2$ being more delocalized than $j_z = 5/2$.

11.3.2 Occupations and magnetization

In this section, we will analyze the occupancies and the magnetization of the ground-state phase diagram. Here, we define the magnetization as

$$m_z = \sum_{j_z} n_{j_z} j_z. \quad (11.9)$$

We found that the orbitals j_z and $-j_z$ will be localized when sum of their occupancies equals to 1: $n_{j_z} + n_{-j_z} = 1$. From this condition, we can deduce that in PM phase, a localized j_z -orbital will have occupancy of $n_{j_z} = 0.5$ whereas in FM phase it will be either 0 or 1. Figure 11.10 presents occupations of delocalized orbitals and the figure 11.11 presents the net magnetization in FM phase of our ground-state phase diagram for $W + W' = 7$ and $W + W' = 14$.

Starting from $\text{FM}_{\frac{5}{2},\frac{1}{2}}$ phase with increasing W_2 , $n_{3/2}$ increases gradually whereas $n_{-3/2}$ decreases gradually. Similar behavior was also obtained in quasiparticle hopping (see figure 11.9). This lead in gradual increase of net magnetization until the saturation of orbital $3/2$ and the magnetization $m_z = 3.75$ at phase transition to $\text{SFM}_{\frac{5}{2},\frac{1}{2}}$. Since, the magnetization between the phases $\text{FM}_{\frac{5}{2},\frac{1}{2}}$ and $\text{SFM}_{\frac{5}{2},\frac{1}{2}}$ does not present a discontinuity, it suggests that the transition is second-order. Meanwhile, all other phase transitions seem to be of first-order since the discontinuities in magnetization are present.

On the other hand for $W' > W$ and in $\text{FM}_{\frac{5}{2},\frac{3}{2}}$ ($\text{PM}_{\frac{5}{2},\frac{3}{2}}$), the occupation of delocalized orbital $j_z = 1/2$ remains constant $n_{\pm 1/2} = 0.25$ with constant magnetization of $m_z = 4$ for $\text{FM}_{\frac{5}{2},\frac{3}{2}}$ phase. As for one-electron localized phase $\text{FM}_{\frac{3}{2}}$, the occupancies depends

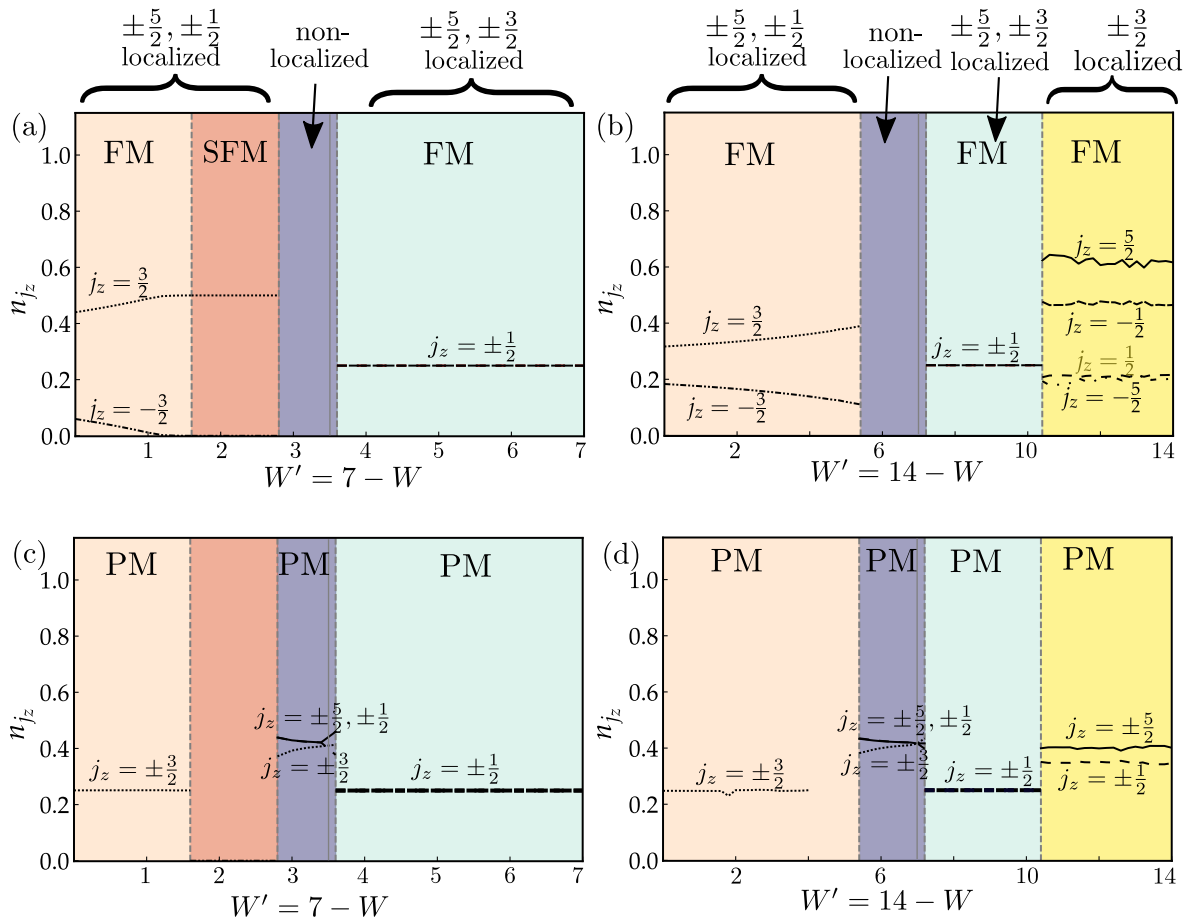


Figure 11.10: Electronic occupations for delocalized orbitals along $W + W' = 7$: (a) and (c), and along $W + W' = 14$: (b) and (d). Upper diagrams (a) and (b) are for FM phases whereas middle diagrams (c) and (d) are for PM phases. Localized orbitals are indicated on the top the figure, and aside of each line for each orbital. Vertical dotted lines are guides for eyes marking frontier between phases whereas solid vertical gray line indicate isotropic point.

up on orbitals with $n_{1/2} < n_{5/2}$. This is again consistent with our Z_{j_z} where electrons in $j_z = 1/2$ were more delocalized than $j_z = 5/2$.

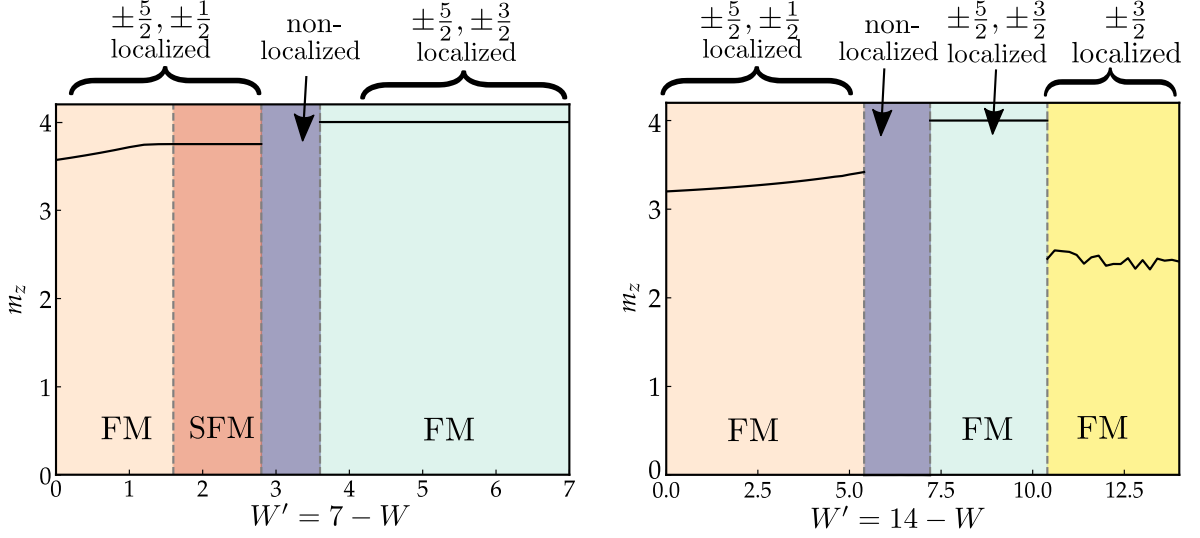


Figure 11.11: Magnetization is presented for only FM phases along $W + W' = 7$ (left), along $W + W' = 14$ (right). Localized orbitals are indicated on the top the figure. Vertical dotted lines are guides for eyes marking frontier between phases whereas solid vertical gray line indicate isotropic point.

11.3.3 Fermi surfaces

The quasiparticle weight Z_{j_z} normalizes the electronic bandwidth as $W_{j_z} \rightarrow W_{j_z} Z_{j_z}$. From the equation (9.30), we can evaluate the chemical potential λ_{j_z} fixing electronic occupation n_{j_z} per orbital. With this in hand, we present this renormalized effective bandwidths in the figures 11.12 and 11.13 for one-electron localized phases with $W = 0, W' = 14.0$ and two-electron localized phases with $W = 10.0, W' = 0.0$ respectively. Similarly, the Fermi surfaces also become orbital dependent. Furthermore, we also present a schematic view of Fermi surfaces corresponding to each delocalized orbitals on 2D square lattice with dispersion $\epsilon_{\mathbf{k}, j_z} = \frac{W_{j_z}}{4} (\cos(\mathbf{k}_x) + \cos(\mathbf{k}_y))$. The Fermi surfaces are obtained from the spectral function $\mathcal{A}(\mathbf{k}, \omega) = -\frac{1}{\Pi} \text{Im}(G_{j_z}(\mathbf{k}, \omega + i\eta^+))$ at $\omega = 0$, where η is an infinitesimal positive number and the Green function $G_{j_z}(\mathbf{k}, \omega + i\eta^+) = 1/(\omega + i\eta^+ - \epsilon_{\mathbf{k}} + \lambda_{j_z})$.

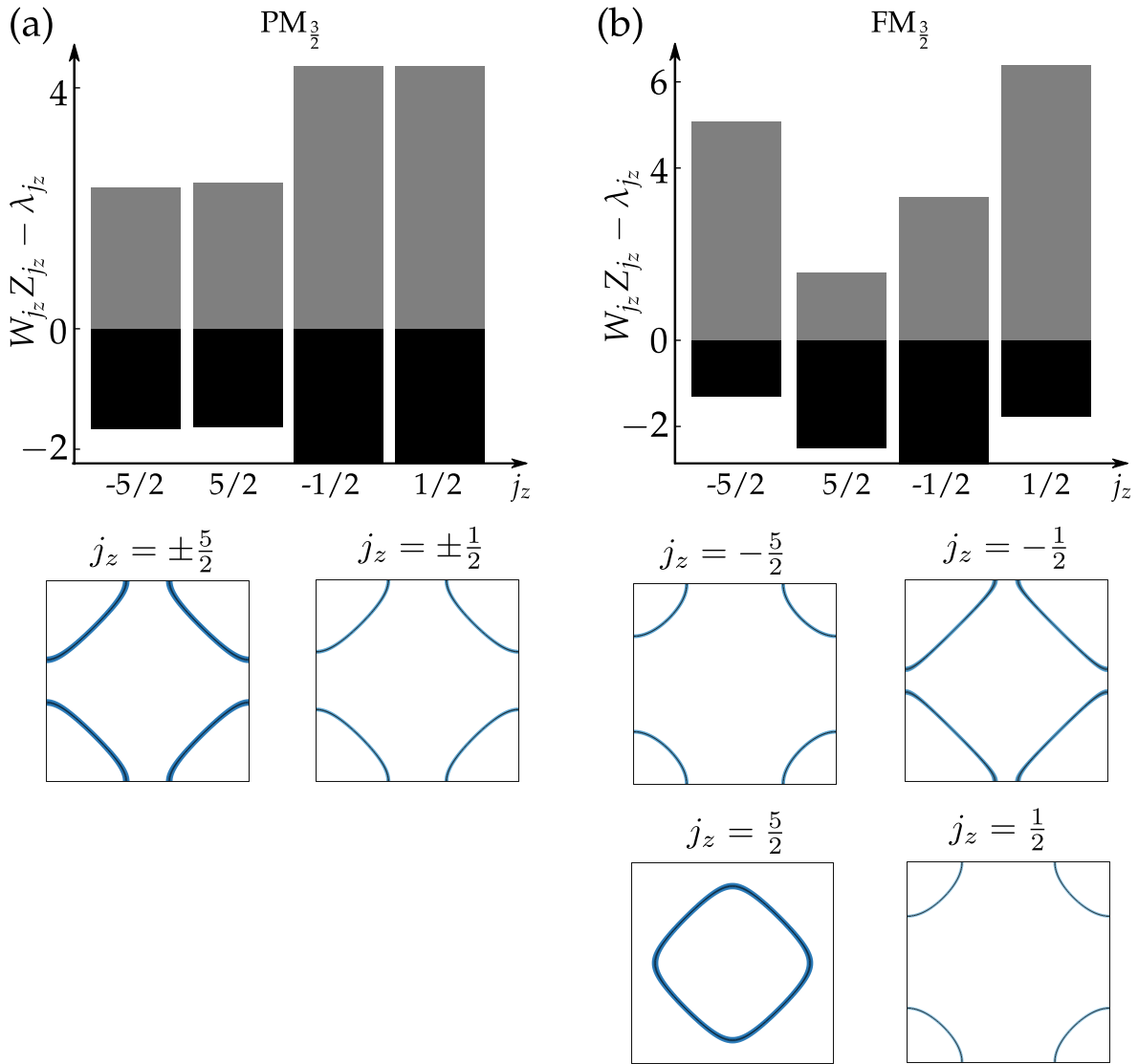


Figure 11.12: Up: renormalized electronic bandwidth ($W_{j_z} Z_{j_z}$) for $j_z = 3/2$ localized orbital, calculated at the parameters $W = 0$ and $W' = 14$ for paramagnetic phase (a) and ferromagnetic phase (b). For each bar, black color indicates the electronic bandwidth below Fermi level with occupied states and gray color indicates the electronic bandwidth with unoccupied states. Down: schematic view of Fermi surfaces on 2D square lattice. Thin black line represent the Fermi surfaces. Darker blue color shades around Fermi surfaces indicate low Fermi velocity $v_F \propto Z_{j_z} W_{j_z}$ with high effective mass m^* , whereas lighter blue color shades indicate lighter effective mass with higher Fermi velocity. The width of the shades is determined by $1/W_{j_z} Z_{j_z}$ representing schematically the density of states at Fermi level.

First, we can observe the symmetry between j_z and $-j_z$ orbitals in PM phases, since bandwidths for both orbitals are renormalized similarly. On the other hand, for its counterpart FM phase, all the W_{j_z} are renormalized differently. This difference in bandwidth normalization will reduce the number of Fermi surface sheets by twice in PM phases compared to their degenerate FM phases. For example, we can refer to the

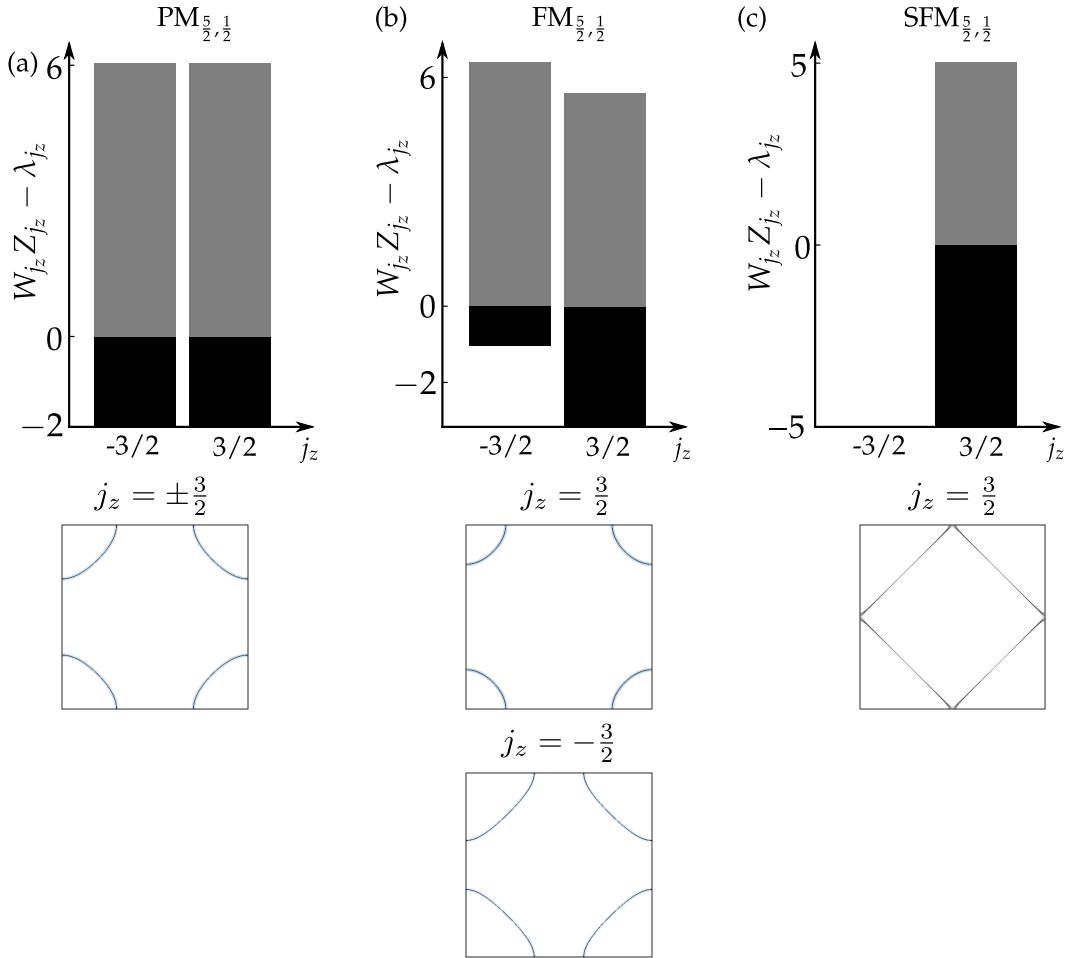


Figure 11.13: Up: renormalized electronic bandwidth ($W_{j_z} Z_{j_z}$) with $j_z = 5/2$ and $j_z = 1/2$ localized orbitals calculated at the parameters $W = 10$ and $W' = 0$ for paramagnetic phase (a), ferromagnetic phase (b) and saturated ferromagnetic phase (c). For each bar, black color indicates the electronic bandwidth below Fermi level with occupied states and gray color indicates the electronic bandwidth with unoccupied states. Down: schematic view of Fermi surfaces on 2D square lattice. Thin black line represent the Fermi surfaces. Darker blue color shades around Fermi surfaces indicate low Fermi velocity $v_F \propto Z_{j_z} W_{j_z}$ with high effective mass m^* , whereas lighter blue color shades indicate lighter effective with higher Fermi velocity. The width of the shades is determined by $1/W_{j_z} Z_{j_z}$ representing schematically the density of states at Fermi level.

figure 11.12 where $PM_{\frac{3}{2}}$ phase presents two unique sheets of Fermi surfaces whereas its counterpart degenerate $FM_{\frac{5}{2}}$ present four sheets of Fermi surfaces. Moreover, this difference between Fermi surfaces in two degenerate phases is a direct result of orbital-dependent occupancies. Similar situation can be also observed in two-electron localized phases (see figure 11.13).

Here, the quasiparticle weight Z_{j_z} is the inverse of the effective mass m^* [324]. We can also relate the quasiparticle weight as $Z_{j_z} \equiv [1 - \partial \text{Re}(\Sigma(\omega))/\partial \omega]_{|\omega=0}^{-1}$ with comparison to the previous definition of our effective mass in the chapter 5. Furthermore, as the effective mass gets larger, the electrons move slowly. This can be easily understood from free electron model where $v_F = \hbar^{-1} \partial \epsilon_{\mathbf{k}} / \partial \mathbf{k}|_{\mathbf{k}=\mathbf{k}_F} = \hbar \mathbf{k}_F / m$ with $\epsilon_{\mathbf{k}} = \hbar \mathbf{k}^2 / 2m$. In the figures 11.12 and 11.13, the darker to lighter blue color shades around Fermi surface represent schematically the lower to higher Fermi velocity. And, the width of the shades represents schematically the density of states at the Fermi level, which is determined by $1/W_{j_z} Z_{j_z}$. Here, we observe that the delocalized orbital with larger Fermi surfaces will have smaller Fermi velocity with larger effective mass. This can be understood through Coulomb repulsion that increases when occupancy increases, decreasing the degree of delocalization.

11.3.4 f -electron valency configurations

In this section, we will analyze the slave-boson probabilities described as

$$p(M) = \sum_{\alpha\beta \in M} |\varphi_{\alpha\beta}|^2, \quad (11.10)$$

where α, β can be a set of basis set representing physical Hilbert space and auxiliary Hilbert space in M particle charge sector. Here, $p(M)$ may be interpreted as the weight for finding a state characterized by α, β in f^M -electron configuration. Thus analyzing $p(M)$ per f -electron configuration permits us to have more insight over the multi-configurational nature of $5f$ orbitals [333, 334] and the effect of anisotropy on it.

Here, we rewrite the completeness Eq. (9.28) and the conservation of number of fermions from the Eq. (9.29) as

$$\sum_M p(M) = 1, \quad (11.11)$$

$$\sum_M M p(M) = 2.5. \quad (11.12)$$

From the Eqs. (11.11) and (11.12), we can show that the variations on $p(2)$ and $p(3)$ depend linearly upon $p(4)$ as $p(4) = p(2) - 0.5$ and $p(4) = \frac{1}{2}(0.5 - 2p(3))$. In the figure 11.14, we plot $\Delta p(2) = p(2) - 0.5$, $\Delta p(3) = p(3) - 0.5$ and $\Delta p = p(4)$ along the line $W + W' = 7$ and $W + W' = 14$. First, we can observe that our results are consistent

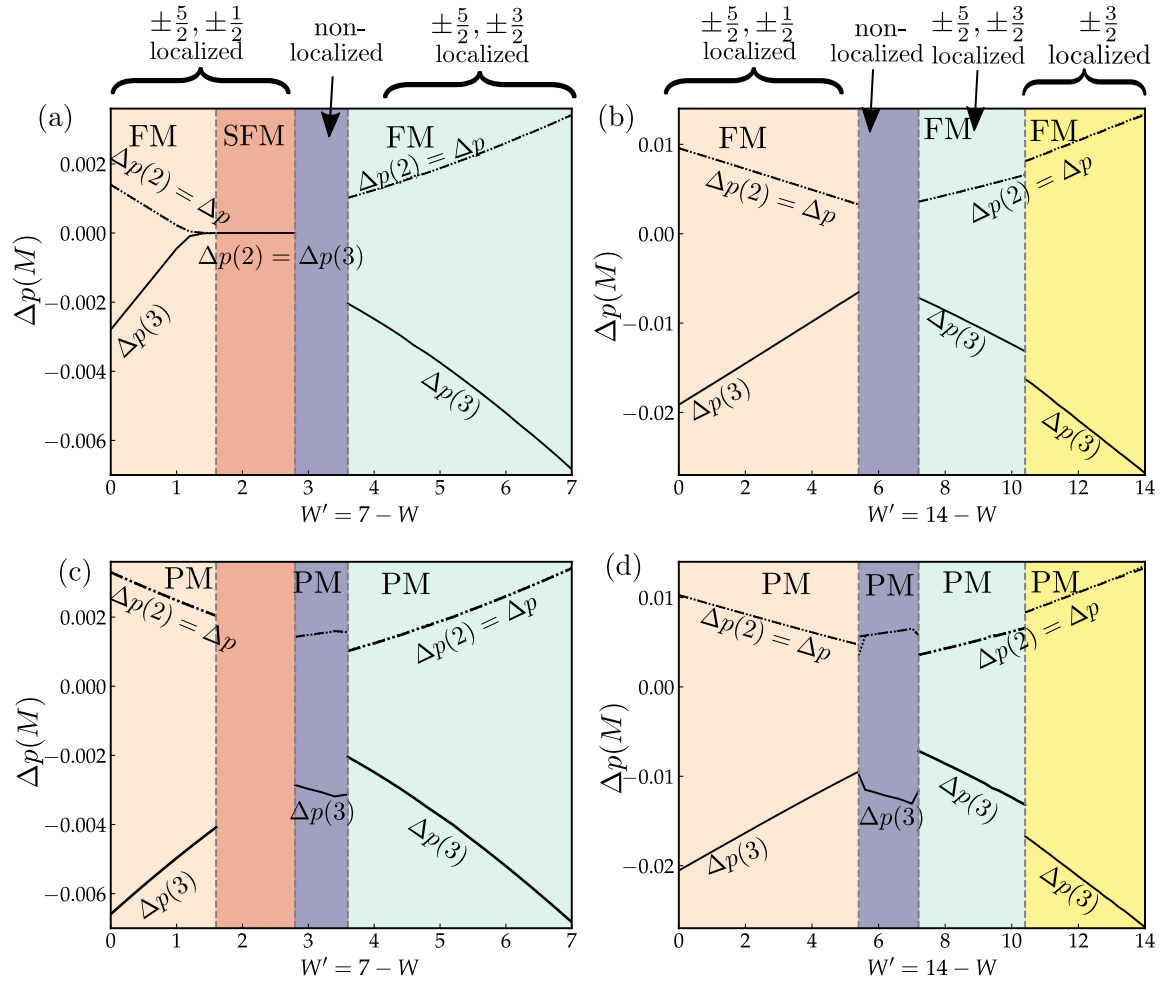


Figure 11.14: Variations of slave bosons probabilities $\Delta p(M)$ per f -electron configuration represented here for lines $W + W' = 7$ ((a) and (c)) and $W + W' = 14$ ((b) and (d)). Slave bosons probabilities for FM phases are presented in the upper panel ((a) and (b)) whereas PM phases are presented in the lower panel ((c) and (d)). Here, $\Delta p(2) = p(2) - 0.5$, $\Delta p(3) = p(3) - 0.5$ and $\Delta p = p(4)$.

with the theoretical prediction since the small variations in $p(4)$ coincide with $\Delta p(2)$. This small $p(4)$ values creates the small deviations of $p(2)$ and $p(3)$ from half-half weight. However, the differences between the two-particle sectors and three-particle sector enlarges with increasing anisotropy.

Chapter 12

Conclusions and perspectives

In this thesis, we looked at the link between duality in $5f$ electrons with orbital-selective partially localized phases and the origin of heavy-fermionic behavior in uranium-based compounds. For that, we have carried out theoretical modal calculations using rotationally-invariant slave-bosons (RISB), considering the typical Coulomb parameters for uranium-based heavy-fermion compounds. This part emphasizes two major aspects: it contains a comprehensive discussion on algorithmic and numerical aspects and on the microscopic mechanism leading to putative orbital-selective localization.

The numerical treatment of RISB presents a great challenge due to the large number of parameters to be optimized. The procedure requires 116 non-linear self-consistent equations to be solved. In this thesis, we have developed an efficient algorithm based both on the local search of minimal and on the global search of minimal to solve RISB equations. For this, we combine gradient-based methods for the local optimization and non-gradient methods like basin hopping, simulated annealing, and differential evolution for global optimization. A complete schematic view is present in the figure 10.3. Before performing the full optimization calculations, one needs a good initial input parameter. For that, we have developed a strategy (see figure 10.1) based on grid search combined with the reductions of Hilbert space defined by the charge sectors of f -electrons. This permits us to scan all the partially localized phases spanning through all the charge sectors.

Our study started with the verification of the relevance of our numerical method. This was confirmed by the faithful reproduction of the analytical results at the atomic limit, where the multiplets $|f^2; J = 4\rangle$, $|f^3; J = 9/2\rangle$ formed the ground state, and on the non-interacting limit all the orbitals were fully delocalized. From atomic limit, increasing the electronic bandwidth in isotropic case ($W_{3/2} = W_{5/2} = W$) induces transitions in f -electron valency configurations to the more energetic states. More importantly, the transition in valency configurations happens stepwise: (f^2, f^3) at $W = 0$, $(f^2, f^3) \rightarrow (f^2, f^3, f^4)$ for $0 < W/U_0 \lesssim 1.32$, $(f^2, f^3, f^4) \rightarrow (f^1, f^2, f^3, f^4, f^5)$ at $W/U_4 \simeq 1.62$, and $(f^1, f^2, f^3, f^4, f^5) \rightarrow (f^0, f^1, f^2, f^3, f^4, f^5, f^6)$ at $W/U_0 \simeq 3.27$.

For $W \gg U_0$, we recover the results of non-interacting limit with $Z_{j_z} \simeq 1.00$.

With the results in isotropic line in hand, we varied the anisotropy ($W_{3/2} \neq W_{5/2}(= W_{1/2})$) in electronic bandwidth with f -electron count $n_f = 2.5$. We found that the intra-atomic correlations enhances the anisotropies resulting in the partial localization of electrons on the sub-dominant hopping channel. Altogether we have found twelve partially localized phases: three one-electron localized PM phases, three one-electron localized FM phases, two two-electron localized PM phases, two two-electron localized FM phases, and two two-electron localized SFM. Thereafter, we constructed an orbital-selective partially localized phase diagram by comparing their energies. Figure 11.6 presents this phase diagram. At a low electronic bandwidth region with anisotropy, two electrons localization tends to be favorable. These two-electron localized phases follows the Hund's rule with the multiplets $|f^2; J = 4\rangle$, $|f^3; J = 9/2\rangle$ and $|f^4; J = 4\rangle$ forming the ground-states. More precisely, when $W_{3/2} > W_{5/2}$ with $W_{3/2} \lesssim 5.20$, SFM phase with orbitals $j_z = 5/2$ and $j_z = 1/2$ localized is found be more stable than PM or FM phases. This SFM $_{\frac{5}{2}, \frac{1}{2}}$ phase lead to FM $_{\frac{5}{2}, \frac{1}{2}}$ (PM $_{\frac{5}{2}, \frac{1}{2}}$) when $W_{3/2} \gtrsim 5.20$. For $W_{3/2} < W_{5/2}$, FM (PM) phase with orbitals $j_z = 5/2$ and $j_z = 3/2$ is found to be more stable instead of SFM $_{\frac{5}{2}, \frac{3}{2}}$. With sufficiently large $W_{5/2}$, FM $_{\frac{5}{2}, \frac{3}{2}}$ (PM $_{\frac{5}{2}, \frac{3}{2}}$) lead to FM $_{\frac{3}{2}}$ (PM $_{\frac{3}{2}}$) with only one-electron localization. The mechanism of localization of one-electron can be similar to that of Mott localization where the ratio of $\frac{U_{j_z}}{W_{j_z}}$ plays a vital role. Furthermore, our phase diagram is consistent with the previous results [60, 327].

To gain further insight into the nature of the partially localized phases, we have analyzed Fermi surfaces, orbital occupations, magnetization, and f -electron valency configurations. With FM and PM being degenerate but having different occupations per non-localized orbitals, FM phases have twice more unique Fermi surface sheets than their counterpart PM phase. As expected, we observed that the magnetization of two-electron localized phases is larger than that of one-electron localized phases. We also found that increasing electronic bandwidth changes the f -electron valency configurations, where four electrons states can form the ground-state satisfying Hund's rule for two-electron localized phases. Furthermore, we also find that the bandwidth anisotropy increases the weight of f^2 configuration.

This study has several perspectives. At first, the model calculations can be extended to the parameters $W_{3/2} > 15$ eV and $W_{5/2}(W_{1/2}) > 15$. In this case, the more energetic configurations like f^5, f^1 can participate in the formation of partially localized phases. This may stabilize one-electron localized phases like FM $_{\frac{5}{2}}$ (PM $_{\frac{5}{2}}$) as ground-state for $W_{3/2} > W_{5/2}$, which was observed in previous study [327]. One could also seek the possibility of having an antiferromagnetic phase in the further analysis of partially localized phases. Furthermore, this present study provides crucial information to perform a future model calculation with the inclusion of magnetic field and also more qualitative band-structure calculations for other uranium-based heavy-fermions. A second direction is to account for more general DOS profiles. A

final goal is certainly to combine the present ansatz with material-specific *ab-initio* calculations. Hence, this thesis puts a new brick on the understanding of the dualism of $5f$ electrons and paves a new way for more realistic band structure calculations.

Part III
Appendices

Appendices

Appendix A

Evaluation of energies and ground state phase diagrams

Total energy in each phase is determined by taking average of the Hamiltonian per site as $E/N = \langle H \rangle / N$, where N is the total number of sites in our system. Below, we present the equations to calculate energy for each considered phase.

A.1 Expressions of energies

Paramagnetic Kondo phase

$$\frac{E_K}{N} = \frac{1}{N} \sum_{\mathbf{k}\sigma} \epsilon_{\mathbf{k}} \langle c_{\mathbf{k}\sigma}^\dagger c_{\mathbf{k}\sigma} \rangle - x \frac{2r^2}{J_K} \quad (\text{A.1})$$

Ferromagnetic phase

$$\frac{E_F}{N} = \frac{1}{N} \sum_{\mathbf{k}\sigma} \epsilon_{\mathbf{k}} \langle c_{\mathbf{k}\sigma}^\dagger c_{\mathbf{k}\sigma} \rangle + x J_K m_f m_c \quad (\text{A.2})$$

Antiferromagnetic phase

$$\frac{E_{AF}}{N} = \frac{1}{N} \sum_{\mathbf{k} \in \text{RBZ}, \sigma} \{ \epsilon_{\mathbf{k}} \langle c_{\mathbf{k}\sigma}^\dagger c_{\mathbf{k}\sigma} \rangle + \epsilon_{\mathbf{k}+\mathbf{Q}} \langle c_{\mathbf{k}+\mathbf{Q}\sigma}^\dagger c_{\mathbf{k}+\mathbf{Q}\sigma} \rangle + x J_K m_f m_c \} \quad (\text{A.3})$$

A.2 Evaluation of ground state phase diagram

Since we have noticed that ground energies (without interaction, $J_K = 0$) for each method are not exactly same. So the phase diagram were constructed by evaluating the energies differences $E_K - E_K^0(J_K = 0)$, $E_F - E_F^0(J_K = 0)$ and $E_{AF} - E_{AF}^0(J_K = 0)$.

Appendix B

Matrix DMFT/CPA for Néel ordered antiferromagnetic phase

In this chapter of the appendix, we present a complete detail of our calculations and techniques that we have used to obtain DMFT equations. The first step would be the diagrammatic expansion. From now, every 2×2 matrices are represented by bold letters, and every 4×4 matrices are represented by bold letters and two bars upon it.

B.1 Diagrammatic development of Green function

In this diagrammatic expansion, we consider only direct part connecting from site i to site j . Thus, Green's function G_{ij}^σ for Kondo alloy model can be expressed as

$$G_{ij}^\sigma = \sum_{allpaths} \Pi_{ii}^\sigma \gamma_{ii_1} \mathbf{P}_i^\dagger \mathbf{W} \mathbf{P}_{i_1} \Pi_{i_1 i_1}^\sigma \gamma_{i_1 i_2} \mathbf{P}_{i_1}^\dagger \mathbf{W} \mathbf{P}_{i_2} \dots \Pi_{i_p i_p}^\sigma \gamma_{i_p j} \mathbf{P}_{i_p}^\dagger \mathbf{W} \mathbf{P}_j \Pi_{jj}^\sigma, \quad (\text{B.1})$$

multiplying above equation by the projectors \mathbf{P}_i on left side and \mathbf{P}_j^\dagger on the right side, and taking average over disorder, we get

$$\langle \mathbf{P}_i G_{ij}^\sigma \mathbf{P}_j^\dagger \rangle = \sum_{allpaths} \langle \mathbf{P}_i \Pi_{ii}^\sigma \mathbf{P}_i^\dagger \rangle \gamma_{ii_1} \mathbf{W} \langle \mathbf{P}_{i_1} \Pi_{i_1 i_1}^\sigma \mathbf{P}_{i_1}^\dagger \rangle \gamma_{i_1 i_2} \mathbf{W} \dots \langle \mathbf{P}_{i_p} \Pi_{i_p i_p}^\sigma \mathbf{P}_{i_p}^\dagger \rangle \gamma_{i_p j} \mathbf{W} \langle \mathbf{P}_j \Pi_{jj}^\sigma \mathbf{P}_j^\dagger \rangle. \quad (\text{B.2})$$

We simplify the notation as $\langle \mathbf{P}_i \Pi_{ii}^\sigma \mathbf{P}_i^\dagger \rangle = \langle \tilde{\Pi}_i^\sigma \rangle$, the equation B.2 is rewritten as

$$\langle \mathbf{G}_{ij}^\sigma \rangle = \langle \tilde{\Pi}_{ii}^\sigma \rangle \delta_{ij} + \sum_{\text{allpaths}} \langle \tilde{\Pi}_{ii}^\sigma \rangle \gamma_{ii_1} \mathbf{W} \langle \tilde{\Pi}_{i_1 i_1}^\sigma \rangle \gamma_{i_1 i_2} \mathbf{W} \langle \tilde{\Pi}_{i_2 i_2}^\sigma \rangle \dots \gamma_{i_p j} \mathbf{W} \langle \tilde{\Pi}_{jj}^\sigma \rangle \quad (\text{B.3})$$

$$= \langle \tilde{\Pi}_{ii}^\sigma \rangle \delta_{ij} + \langle \tilde{\Pi}_{ii}^\sigma \rangle \sum_{\text{allpaths}} \gamma_{ii_1} \mathbf{W} \langle \tilde{\Pi}_{i_1 i_1}^\sigma \rangle \gamma_{i_1 i_2} \mathbf{W} \langle \tilde{\Pi}_{i_2 i_2}^\sigma \rangle \dots \gamma_{i_p j} \mathbf{W} \langle \tilde{\Pi}_{jj}^\sigma \rangle \quad (\text{B.4})$$

$$= \langle \tilde{\Pi}_{ii}^\sigma \rangle \delta_{ij} + \langle \tilde{\Pi}_{ii}^\sigma \rangle \sum_l \gamma_{il} \mathbf{W} \sum_{\text{allpaths}} \langle \tilde{\Pi}_{ll}^\sigma \rangle \gamma_{l_1 l_2} \mathbf{W} \langle \tilde{\Pi}_{l_2 l_2}^\sigma \rangle \dots \gamma_{l_p j} \mathbf{W} \langle \tilde{\Pi}_{jj}^\sigma \rangle \quad (\text{B.5})$$

$$= \langle \tilde{\Pi}_{ii}^\sigma \rangle \delta_{ij} + \langle \tilde{\Pi}_{ii}^\sigma \rangle \sum_l \gamma_{il} \mathbf{W} \langle \mathbf{G}_{lj}^\sigma \rangle. \quad (\text{B.6})$$

Finally,

$$\langle \mathbf{G}_{ij}^\sigma \rangle = \Pi_i^\sigma (\delta_{ij} + \sum_l \gamma_{il} \mathbf{W} \langle \mathbf{G}_{lj}^\sigma \rangle), \quad (\text{B.7})$$

where $\Pi_i^\sigma = \langle \tilde{\Pi}_{ii}^\sigma \rangle = \left\langle \left(\begin{array}{cc} \hat{x}_i \hat{x}_i \Pi_{ii}^\sigma & \hat{x}_i \hat{y}_i \Pi_{ii}^\sigma \\ \hat{y}_i \hat{x}_i \Pi_{ii}^\sigma & \hat{y}_i \hat{y}_i \Pi_{ii}^\sigma \end{array} \right) \right\rangle$. We would like take Fourier transform of above equation so multiplying both sides by $\frac{1}{N} \sum_{ij} e^{i\mathbf{k}'\mathbf{R}_j - i\mathbf{k}\mathbf{R}_i}$, so we get

$$\mathbf{G}_{\mathbf{k}\mathbf{k}'}^\sigma = \frac{1}{N} \sum_{ij} e^{i(\mathbf{k}' - \mathbf{k})\mathbf{R}_i} \Pi_i^\sigma + \frac{1}{N} \sum_{ij} e^{i\mathbf{k}'\mathbf{R}_j - i\mathbf{k}\mathbf{R}_i} \Pi_i^\sigma \gamma_{il} \mathbf{W} \mathbf{G}_{lj}^\sigma, \quad (\text{B.8})$$

with few lines of algebraic calculations, we obtain

$$\mathbf{G}_{\mathbf{k}\mathbf{k}'}^\sigma = \Pi_{\mathbf{k}' - \mathbf{k}}^\sigma + \sum_{\mathbf{k}''} \Pi_{\mathbf{k}'' - \mathbf{k}}^\sigma \gamma_{\mathbf{k}''} \mathbf{G}_{\mathbf{k}''\mathbf{k}'}^\sigma. \quad (\text{B.9})$$

B.2 Green's function matrix in reduced Brillouin zone

Here, we are treating Néel ordered antiferromagnetic (AF) phase with wave ordering vector $\mathbf{Q} = (\pi, \pi)$ considering two lattice sites in a unit antiferromagnetic cell. To do so, we have to rewrite the equations on the reduced Brillouin zone (RBZ) considering the bipartite organization in AF lattice with two sub-lattices A and B and δ_0 between the distance between the first neighboring sites. In this way, the local propagator

terms are written in RBZ i.e. $\mathbf{k}', \mathbf{k} \in \text{RBZ}$ as:

$$\begin{aligned}
 \Pi_{(\mathbf{k}'-\mathbf{k})}^\sigma &= \frac{1}{N} \sum_i \Pi_i^\sigma e^{i(\mathbf{k}'-\mathbf{k})\mathbf{R}_i} \\
 &= \frac{1}{N} \sum_{i \in L_A} \Pi_i^\sigma e^{i(\mathbf{k}'-\mathbf{k})\mathbf{R}_i} + \frac{1}{N} \sum_{i \in L_B} \Pi_i^\sigma e^{i(\mathbf{k}'-\mathbf{k})\mathbf{R}_i} \\
 &= \frac{1}{N} \left\{ \Pi_A^\sigma \sum_{i \in L_A} e^{i(\mathbf{k}'-\mathbf{k})\mathbf{R}_i} + \Pi_B^\sigma \sum_{i \in L_A} e^{i(\mathbf{k}'-\mathbf{k})(\mathbf{R}_i+\delta_0)} \right\} \\
 &= \frac{1}{N} \left\{ \Pi_A^\sigma \frac{N}{2} \delta_{\mathbf{k}\mathbf{k}'} + \Pi_B^\sigma \frac{N}{2} \delta_{\mathbf{k}\mathbf{k}'} \right\} \\
 &= \frac{\Pi_A^\sigma + \Pi_B^\sigma}{2} \delta_{\mathbf{k}\mathbf{k}'}, \tag{B.10}
 \end{aligned}$$

where Π_A^σ and Π_B^σ are local propagators for a site in a sublattice A or B respectively. Similarly, the other three local propagators are expressed as

$$\Pi_{(\mathbf{k}'+\mathbf{Q}-\mathbf{k})}^\sigma = \frac{\Pi_A^\sigma - \Pi_B^\sigma}{2} \delta_{\mathbf{k}\mathbf{k}'}, \tag{B.11}$$

$$\Pi_{(\mathbf{k}'-\mathbf{k}+\mathbf{Q})}^\sigma = \frac{\Pi_A^\sigma - \Pi_B^\sigma}{2} \delta_{\mathbf{k}\mathbf{k}'}, \tag{B.12}$$

$$\Pi_{(\mathbf{k}'+\mathbf{Q}-\mathbf{k}+\mathbf{Q})}^\sigma = \frac{\Pi_A^\sigma + \Pi_B^\sigma}{2} \delta_{\mathbf{k}\mathbf{k}'}. \tag{B.13}$$

To be more clear and concise, we define $\Pi_\sigma^+ = \frac{\Pi_A^\sigma + \Pi_B^\sigma}{2}$ and $\Pi_\sigma^- = \frac{\Pi_A^\sigma - \Pi_B^\sigma}{2}$. $\mathbf{G}_{\mathbf{k}\mathbf{k}'}^\sigma$ is expanded in RBZ as

$$\begin{aligned}
 \mathbf{G}_{\mathbf{k}\mathbf{k}'}^\sigma &= \Pi_{\mathbf{k}'-\mathbf{k}}^\sigma + \sum_{\mathbf{k}''} \Pi_{\mathbf{k}''-\mathbf{k}}^\sigma \gamma_{\mathbf{k}''} \mathbf{W} \mathbf{G}_{\mathbf{k}''\mathbf{k}'}^\sigma \\
 &= \Pi_{\mathbf{k}'-\mathbf{k}}^\sigma + \sum_{\mathbf{k}''} \left\{ \gamma_{\mathbf{k}''} \Pi_{\mathbf{k}''-\mathbf{k}}^\sigma \mathbf{W} \mathbf{G}_{\mathbf{k}''\mathbf{k}'}^\sigma + \gamma_{(\mathbf{k}''+\mathbf{Q})} \Pi_{(\mathbf{k}''+\mathbf{Q})-\mathbf{k}}^\sigma \mathbf{W} \mathbf{G}_{(\mathbf{k}''+\mathbf{Q}),\mathbf{k}'}^\sigma \right\} \\
 &= \Pi_\sigma^+ \delta_{\mathbf{k}\mathbf{k}'} + \sum_{\mathbf{k}''} \left\{ \gamma_{\mathbf{k}''} \Pi_\sigma^+ \mathbf{W} \mathbf{G}_{\mathbf{k}''\mathbf{k}'}^\sigma \delta_{\mathbf{k}\mathbf{k}''} + \gamma_{(\mathbf{k}''+\mathbf{Q})} \Pi_\sigma^- \mathbf{W} \mathbf{G}_{(\mathbf{k}''+\mathbf{Q}),\mathbf{k}'}^\sigma \delta_{\mathbf{k}\mathbf{k}''} \right\} \\
 &= \Pi_\sigma^+ \delta_{\mathbf{k}\mathbf{k}'} + \Pi_\sigma^+ \mathbf{E}_{\mathbf{k}} \mathbf{G}_{\mathbf{k}\mathbf{k}'}^\sigma + \Pi_\sigma^- \mathbf{E}_{\mathbf{k}+\mathbf{Q}} \mathbf{G}_{\mathbf{k}+\mathbf{Q},\mathbf{k}'}^\sigma, \tag{B.14}
 \end{aligned}$$

with $\mathbf{E}_{\mathbf{k}} = \gamma_{\mathbf{k}} \mathbf{W}$ and $\mathbf{E}_{\mathbf{k}+\mathbf{Q}} = \gamma_{\mathbf{k}+\mathbf{Q}} \mathbf{W}$ are dispersion matrices.

similarly,

$$\mathbf{G}_{\mathbf{k},\mathbf{k}'+\mathbf{Q}}^\sigma = \Pi_\sigma^- \delta_{\mathbf{k}\mathbf{k}'} + \Pi_\sigma^+ \mathbf{E}_{\mathbf{k}} \mathbf{G}_{\mathbf{k},\mathbf{k}'+\mathbf{Q}}^\sigma + \Pi_\sigma^- \mathbf{E}_{\mathbf{k}+\mathbf{Q}} \mathbf{G}_{\mathbf{k}+\mathbf{Q},\mathbf{k}'+\mathbf{Q}}^\sigma, \quad (\text{B.15})$$

$$\mathbf{G}_{\mathbf{k}+\mathbf{Q},\mathbf{k}'}^\sigma = \Pi_\sigma^- \delta_{\mathbf{k}\mathbf{k}'} + \Pi_\sigma^- \mathbf{E}_{\mathbf{k}} \mathbf{G}_{\mathbf{k},\mathbf{k}'}^\sigma + \Pi_\sigma^+ \mathbf{E}_{\mathbf{k}+\mathbf{Q}} \mathbf{G}_{\mathbf{k}+\mathbf{Q},\mathbf{k}'}^\sigma, \quad (\text{B.16})$$

$$\mathbf{G}_{\mathbf{k}+\mathbf{Q},\mathbf{k}'+\mathbf{Q}}^\sigma = \Pi_\sigma^+ \delta_{\mathbf{k}\mathbf{k}'} + \Pi_\sigma^- \mathbf{E}_{\mathbf{k}} \mathbf{G}_{\mathbf{k},\mathbf{k}'+\mathbf{Q}}^\sigma + \Pi_\sigma^+ \mathbf{E}_{\mathbf{k}+\mathbf{Q}} \mathbf{G}_{\mathbf{k}+\mathbf{Q},\mathbf{k}'+\mathbf{Q}}^\sigma. \quad (\text{B.17})$$

We would like to express the matrix $\bar{\bar{\mathbf{G}}}_{\mathbf{k}\mathbf{k}'}^\sigma$, which is a tensor whose components are $\mathbf{G}_{\mathbf{k}\mathbf{k}'}^\sigma$, $\mathbf{G}_{\mathbf{k}+\mathbf{Q},\mathbf{k}'}^\sigma$, $\mathbf{G}_{\mathbf{k},\mathbf{k}'+\mathbf{Q}}^\sigma$ and $\mathbf{G}_{\mathbf{k}+\mathbf{Q},\mathbf{k}'+\mathbf{Q}}^\sigma$. We define a 4×4 matrix as $\bar{\bar{\mathbf{G}}}_{\mathbf{k}\mathbf{k}'}^\sigma = \begin{pmatrix} \mathbf{G}_{\mathbf{k}\mathbf{k}'}^\sigma & \mathbf{G}_{\mathbf{k}\mathbf{k}'+\mathbf{Q}}^\sigma \\ \mathbf{G}_{\mathbf{k}+\mathbf{Q},\mathbf{k}'}^\sigma & \mathbf{G}_{\mathbf{k}+\mathbf{Q},\mathbf{k}'+\mathbf{Q}}^\sigma \end{pmatrix}$. Inserting relations B.14, B.15, B.16 and B.17 along with few calculations, we get

$$\bar{\bar{\mathbf{G}}}_{\mathbf{k}\mathbf{k}'}^\sigma = \left\{ \begin{pmatrix} \Pi_\sigma^+ & \Pi_\sigma^- \\ \Pi_\sigma^- & \Pi_\sigma^+ \end{pmatrix}^{-1} - \begin{pmatrix} \mathbf{E}_{\mathbf{k}} & 0 \\ 0 & \mathbf{E}_{\mathbf{k}+\mathbf{Q}} \end{pmatrix} \right\}^{-1} \delta_{\mathbf{k}\mathbf{k}'} \quad (\text{B.18})$$

B.3 Some relations using Pauli matrices

Here, we define a 4×4 matrix \mathbf{K} such as $\mathbf{K} = \begin{pmatrix} \mathbf{a} & \mathbf{b} \\ \mathbf{c} & \mathbf{d} \end{pmatrix}$ where each \mathbf{a} , \mathbf{b} , \mathbf{c} and \mathbf{d} are the blocks of 2×2 matrices and \mathbf{K} . With the help of three Pauli matrices σ_x , σ_y and σ_z as 2×2 , we can write the expressions below which will be useful to map 4×4 Green's function matrices to 2×2 Green's functions matrices.

- $\begin{pmatrix} \mathbf{a} & 0 \\ 0 & 0 \end{pmatrix} = \frac{1}{2}(\mathbb{1} \otimes \mathbb{1} + \sigma_z \otimes \mathbb{1}) \mathbf{K} \frac{1}{2}(\mathbb{1} \otimes \mathbb{1} - i\sigma_y \otimes \mathbb{1})$
- $\begin{pmatrix} \mathbf{b} & 0 \\ 0 & 0 \end{pmatrix} = \frac{1}{2}(\mathbb{1} \otimes \mathbb{1} + \sigma_z \otimes \mathbb{1}) \mathbf{K} \frac{1}{2}(\sigma_x \otimes \mathbb{1} - i\sigma_y \otimes \mathbb{1})$
- $\begin{pmatrix} \mathbf{c} & 0 \\ 0 & 0 \end{pmatrix} = \frac{1}{2}(\sigma_x \otimes \mathbb{1} + i\sigma_y \otimes \mathbb{1}) \mathbf{K} \frac{1}{2}(\mathbb{1} \otimes \mathbb{1} + \sigma_z \otimes \mathbb{1})$
- $\begin{pmatrix} \mathbf{d} & 0 \\ 0 & 0 \end{pmatrix} = \frac{1}{2}(\sigma_x \otimes \mathbb{1} + i\sigma_y \otimes \mathbb{1}) \mathbf{K} \frac{1}{2}(\sigma_x \otimes \mathbb{1} - i\sigma_y \otimes \mathbb{1})$

$$\begin{aligned}
 \bullet \begin{pmatrix} 0 & 0 \\ 0 & \mathbf{a} \end{pmatrix} &= \frac{1}{2}(\sigma_x \otimes \mathbb{1} - i\sigma_y \otimes \mathbb{1})\mathbf{K}\frac{1}{2}(\sigma_x \otimes \mathbb{1} + i\sigma_y \otimes \mathbb{1}) & \bullet \begin{pmatrix} 0 & 0 \\ 0 & \mathbf{c} \end{pmatrix} &= \frac{1}{2}(\mathbb{1} \otimes \mathbb{1} - \sigma_z \otimes \mathbb{1})\mathbf{K}\frac{1}{2}(\sigma_x \otimes \mathbb{1} + i\sigma_y \otimes \mathbb{1}) \\
 \bullet \begin{pmatrix} 0 & 0 \\ 0 & \mathbf{b} \end{pmatrix} &= \frac{1}{2}(\sigma_x \otimes \mathbb{1} - i\sigma_y \otimes \mathbb{1})\mathbf{K}\frac{1}{2}(\mathbb{1} \otimes \mathbb{1} - \sigma_z \otimes \mathbb{1}) & \bullet \begin{pmatrix} 0 & 0 \\ 0 & \mathbf{d} \end{pmatrix} &= \frac{1}{2}(\mathbb{1} \otimes \mathbb{1} - \sigma_z \otimes \mathbb{1})\mathbf{K}\frac{1}{2}(\mathbb{1} \otimes \mathbb{1} - \sigma_z \otimes \mathbb{1})
 \end{aligned}$$

B.4 Local Green's function matrix

We define a local Green's function matrix as

$$\mathbf{G}_{loc,\alpha}^\sigma = \begin{pmatrix} xG_{\mathcal{K}}^\sigma & 0 \\ 0 & (1-x)G_N^\sigma \end{pmatrix}, \quad (\text{B.19})$$

where α denotes sublattice type: A or B. Now, we would like to express $\mathbf{G}_{loc,\alpha}^\sigma$ in reciprocal \mathbf{k} -space. To do so, we use the Fourier transform as $\mathbf{G}_{loc,\alpha}^\sigma = \frac{1}{N} \sum_{\mathbf{k}\mathbf{k}' \in BZ} \mathbf{G}_{\mathbf{k}\mathbf{k}'}^\sigma e^{i(\mathbf{k}-\mathbf{k}')\mathbf{R}_\alpha}$. Here, \mathbf{k}, \mathbf{k}' are in normal first Brillouin zone. Since, here we are considering anti-ferromagnetic phase with ordering vector ($\mathbf{Q} = (\pi, \pi)$) with two lattice sites per unit cell. We have the Brillouin zone reduced by half. We have to rewrite above equation on reduced Brillouin zone (RBZ).

$$\begin{aligned}
 \mathbf{G}_{loc,\alpha}^\sigma &= \frac{1}{N} \sum_{\mathbf{k}\mathbf{k}' \in BZ} \mathbf{G}_{\mathbf{k}\mathbf{k}'}^\sigma e^{i(\mathbf{k}-\mathbf{k}')\mathbf{R}_\alpha} & (\text{B.20}) \\
 &= \frac{1}{N} \sum_{\mathbf{k}\mathbf{k}' \in RBZ} \{ \underbrace{\mathbf{G}_{\mathbf{k}\mathbf{k}'}^\sigma e^{i(\mathbf{k}-\mathbf{k}')\mathbf{R}_\alpha}}_{\delta_{\mathbf{k}\mathbf{k}'}} + \mathbf{G}_{\mathbf{k}+\mathbf{Q}\mathbf{k}'}^\sigma e^{i(\mathbf{k}-\mathbf{k}')\mathbf{R}_\alpha} e^{i\mathbf{Q}\mathbf{R}_\alpha} \\
 &\quad + \mathbf{G}_{\mathbf{k}\mathbf{k}'+\mathbf{Q}}^\sigma e^{i(\mathbf{k}-\mathbf{k}')\mathbf{R}_\alpha} e^{-i\mathbf{Q}\mathbf{R}_\alpha} + \mathbf{G}_{\mathbf{k}+\mathbf{Q}\mathbf{k}'+\mathbf{Q}}^\sigma e^{i(\mathbf{k}-\mathbf{k}')\mathbf{R}_\alpha} \}, & (\text{B.21})
 \end{aligned}$$

the factor $e^{\pm i\mathbf{Q}\mathbf{R}_\alpha}$ is whether +1 or -1 depending upon sublattice type 'A' or 'B'. Rewriting $e^{\pm i\mathbf{Q}\mathbf{R}_\alpha}$ as α , finally our equation becomes :

$$\mathbf{G}_{loc,A}^\sigma = \frac{1}{N} \sum_{\mathbf{k} \in RBZ} \{ \mathbf{G}_{\mathbf{k}\mathbf{k}}^\sigma + \mathbf{G}_{\mathbf{k}+\mathbf{Q}\mathbf{k}}^\sigma + \mathbf{G}_{\mathbf{k}\mathbf{k}+\mathbf{Q}}^\sigma + \mathbf{G}_{\mathbf{k}+\mathbf{Q}\mathbf{k}+\mathbf{Q}}^\sigma \}, \quad (\text{B.22})$$

$$\mathbf{G}_{loc,B}^\sigma = \frac{1}{N} \sum_{\mathbf{k} \in RBZ} \{ \mathbf{G}_{\mathbf{k}\mathbf{k}}^\sigma - \mathbf{G}_{\mathbf{k}+\mathbf{Q}\mathbf{k}}^\sigma - \mathbf{G}_{\mathbf{k}\mathbf{k}+\mathbf{Q}}^\sigma + \mathbf{G}_{\mathbf{k}+\mathbf{Q}\mathbf{k}+\mathbf{Q}}^\sigma \}. \quad (\text{B.23})$$

We define a new 4×4 local Green's function matrix $\bar{\mathbf{G}}_{loc}^\sigma$ composed of $\mathbf{G}_{loc,\alpha}^\sigma$ and $\mathbf{G}_{loc,\alpha \in B}^\sigma$ as below

$$\bar{\bar{\mathbf{G}}}_{loc}^{\sigma} = \begin{pmatrix} \mathbf{G}_{loc,A}^{\sigma} & 0 \\ 0 & \mathbf{G}_{loc,B}^{\sigma} \end{pmatrix}. \quad (\text{B.24})$$

Putting the equations (B.22, B.23) in (B.24) we get

$$\bar{\bar{\mathbf{G}}}_{loc}^{\sigma} = \frac{1}{N} \sum_{\mathbf{k} \in \text{RBZ}} \begin{pmatrix} \mathbf{G}_{\mathbf{k}\mathbf{k}}^{\sigma} + \mathbf{G}_{\mathbf{k}+\mathbf{Q}\mathbf{k}}^{\sigma} + \mathbf{G}_{\mathbf{k}\mathbf{k}+\mathbf{Q}}^{\sigma} + \mathbf{G}_{\mathbf{k}+\mathbf{Q}\mathbf{k}+\mathbf{Q}}^{\sigma} & 0 \\ 0 & \mathbf{G}_{\mathbf{k}\mathbf{k}}^{\sigma} - \mathbf{G}_{\mathbf{k}+\mathbf{Q}\mathbf{k}}^{\sigma} - \mathbf{G}_{\mathbf{k}\mathbf{k}+\mathbf{Q}}^{\sigma} + \mathbf{G}_{\mathbf{k}+\mathbf{Q}\mathbf{k}+\mathbf{Q}}^{\sigma} \end{pmatrix}. \quad (\text{B.25})$$

Using relations in B.3, we can express the equation (B.25) as

$$\begin{aligned} \bar{\bar{\mathbf{G}}}_{loc}^{\sigma} = \frac{1}{N} \sum_{\mathbf{k} \in \text{RBZ}} & \left\{ \frac{1}{2}((\mathbb{1} + \sigma_z) \otimes \mathbb{1}) \bar{\bar{\mathbf{G}}}_{\mathbf{k}\mathbf{k}}^{\sigma} \frac{1}{2}((\mathbb{1} + \sigma_z) \otimes \mathbb{1}) + \frac{1}{2}((\mathbb{1} + \sigma_z) \otimes \mathbb{1}) \bar{\bar{\mathbf{G}}}_{\mathbf{k}\mathbf{k}}^{\sigma} \frac{1}{2}((\sigma_x - i\sigma_y) \otimes \mathbb{1}) \right. \\ & + \frac{1}{2}((\sigma_x + i\sigma_y) \otimes \mathbb{1}) \bar{\bar{\mathbf{G}}}_{\mathbf{k}\mathbf{k}}^{\sigma} \frac{1}{2}((\mathbb{1} + \sigma_z) \otimes \mathbb{1}) + \frac{1}{2}((\sigma_x + i\sigma_y) \otimes \mathbb{1}) \bar{\bar{\mathbf{G}}}_{\mathbf{k}\mathbf{k}}^{\sigma} \frac{1}{2}((\sigma_x - i\sigma_y) \otimes \mathbb{1}) \\ & + \frac{1}{2}((\sigma_x - i\sigma_y) \otimes \mathbb{1}) \bar{\bar{\mathbf{G}}}_{\mathbf{k}\mathbf{k}}^{\sigma} \frac{1}{2}((\sigma_x + i\sigma_y) \otimes \mathbb{1}) + \frac{1}{2}((\sigma_x - i\sigma_y) \otimes \mathbb{1}) \bar{\bar{\mathbf{G}}}_{\mathbf{k}\mathbf{k}}^{\sigma} \frac{1}{2}((\mathbb{1} - \sigma_z) \otimes \mathbb{1}) \\ & \left. + \frac{1}{2}((\mathbb{1} - \sigma_z) \otimes \mathbb{1}) \bar{\bar{\mathbf{G}}}_{\mathbf{k}\mathbf{k}}^{\sigma} \frac{1}{2}((\sigma_x + i\sigma_y) \otimes \mathbb{1}) + \frac{1}{2}((\mathbb{1} - \sigma_z) \otimes \mathbb{1}) \bar{\bar{\mathbf{G}}}_{\mathbf{k}\mathbf{k}}^{\sigma} \frac{1}{2}((\mathbb{1} - \sigma_z) \otimes \mathbb{1}) \right\} \end{aligned} \quad (\text{B.26})$$

where $\bar{\bar{\mathbf{G}}}_{\mathbf{k}\mathbf{k}}^{\sigma}$ is defined in the section B.2. With some simple algebraic calculations we obtain a simplified equation as

$$\bar{\bar{\mathbf{G}}}_{loc}^{\sigma} = \frac{1}{2N} \sum_{\mathbf{k} \in \text{RBZ}} \left\{ ((\sigma_z + \sigma_x) \otimes \mathbb{1}) \bar{\bar{\mathbf{G}}}_{\mathbf{k}\mathbf{k}}^{\sigma} ((\sigma_z + \sigma_x) \otimes \mathbb{1}) + ((\mathbb{1} + i\sigma_y) \otimes \mathbb{1}) \bar{\bar{\mathbf{G}}}_{\mathbf{k}\mathbf{k}}^{\sigma} ((\mathbb{1} - i\sigma_y) \otimes \mathbb{1}) \right\}. \quad (\text{B.27})$$

Inserting the expression B.18 in the above Eq. B.27 and knowing that,

$$\bullet \{(\sigma_z + \sigma_x) \otimes \mathbb{1}\}^{-1} = ((\sigma_z + \sigma_x)^{-1} \otimes \mathbb{1}) = \frac{1}{2}((\sigma_z + \sigma_x)^{-1} \otimes \mathbb{1}) \quad (\text{B.28})$$

$$\bullet \{(\mathbb{1} - i\sigma_y) \otimes \mathbb{1}\}^{-1} = ((\mathbb{1} - i\sigma_y)^{-1} \otimes \mathbb{1}) = \frac{1}{2}((\mathbb{1} + i\sigma_y) \otimes \mathbb{1}) \quad (\text{B.29})$$

$$\bullet \{(\mathbb{1} + i\sigma_y) \otimes \mathbb{1}\}^{-1} = ((\mathbb{1} + i\sigma_y)^{-1} \otimes \mathbb{1}) = \frac{1}{2}((\mathbb{1} - i\sigma_y) \otimes \mathbb{1}) \quad (\text{B.30})$$

We get

$$\begin{aligned} \bar{\bar{\mathbf{G}}}_{loc}^{\sigma} = \frac{1}{2N} \sum_{\mathbf{k} \in \text{RBZ}} & \left\{ \frac{1}{4}((\sigma_z + \sigma_x) \otimes \mathbb{1}) (\bar{\bar{\mathbf{M}}}^{\sigma-1} - \bar{\bar{\mathbf{E}}}_{\mathbf{k}}) ((\sigma_z + \sigma_x) \otimes \mathbb{1})^{-1} \right. \\ & \left. + \frac{1}{4}((\mathbb{1} + i\sigma_y) \otimes \mathbb{1}) (\bar{\bar{\mathbf{M}}}^{\sigma-1} - \bar{\bar{\mathbf{E}}}_{\mathbf{k}}) ((\mathbb{1} - i\sigma_y) \otimes \mathbb{1})^{-1} \right\}, \end{aligned}$$

where $\bar{\mathbf{M}} = \begin{pmatrix} \Pi_{\sigma}^{+} & \Pi_{\sigma}^{-} \\ \Pi_{\sigma}^{-} & \Pi_{\sigma}^{+} \end{pmatrix}$ and $\bar{\mathbf{E}}_{\mathbf{k}} = \begin{pmatrix} \mathbf{E}_{\mathbf{k}} & 0 \\ 0 & \mathbf{E}_{\mathbf{k}+\mathbf{Q}} \end{pmatrix}$. with the help of usual matrix relations: $\{\mathbf{A}^{-1}\mathbf{B}^{-1}\mathbf{C}^{-1}\} = \{\mathbf{CBA}\}^{-1}$ and $\mathbf{A}^{-1} + \mathbf{B}^{-1} = \mathbf{A}^{-1}(\mathbf{B} + \mathbf{A})\mathbf{B}^{-1}$, and with few lines of straight forward algebraic calculations, we arrive to the expression

$$\bar{\mathbf{G}}_{loc}^{\sigma} = \frac{2}{N} \sum_{\mathbf{k} \in \text{RBZ}} (\sigma_x \otimes \mathbb{1}) \left\{ (\sigma_x \otimes \mathbb{1}) \bar{\mathbf{M}}_D^{\sigma-1} (\sigma_x \otimes \mathbb{1}) - (\mathbb{1} \otimes \mathbf{E}_{\mathbf{k}}) \bar{\mathbf{M}}_D^{\sigma} (\mathbb{1} \otimes \mathbf{E}_{\mathbf{k}}) \right\}^{-1} (\sigma_x \otimes \mathbb{1}), \quad (\text{B.31})$$

with $\mathbf{M}_D^{\sigma-1} = (\mathbb{1} \otimes \Pi_{\sigma}^{+} + \sigma_z \otimes \Pi_{\sigma}^{-})^{-1}$. Again, with few lines of few lines matrix calculations, we arrive our final expression

$$\mathbf{G}_{loc,\alpha}^{\sigma} = \frac{2}{N} \sum_{\mathbf{k} \in \text{RBZ}} (\Pi_{\alpha\sigma}^{-1} - \mathbf{E}_{\mathbf{k}} \Pi_{\bar{\alpha}\sigma} \mathbf{E}_{\mathbf{k}})^{-1}. \quad (\text{B.32})$$

where $\alpha = A, B$ and $\bar{\alpha} = B, A$.

B.5 Dynamical local bath

In this section of this appendix, we will be deriving the equation of dynamical local bath. At first, we write the expression of the dynamical local bath as

$$\Delta^{\sigma} = \sum_{ij} \gamma_{i\alpha} \gamma_{\alpha j} \mathbf{W} \langle \mathbf{G}_{ij}^{(\alpha)} \rangle_{dis} \mathbf{W}, \quad (\text{B.33})$$

with α is a cavity site either belongs to sublattice A or B. Inserting $\langle \mathbf{G}_{ij}^{(\alpha)} \rangle_{dis} = \langle \mathbf{G}_{ij} \rangle_{dis} - \langle \mathbf{G}_{i\alpha} \rangle \mathbf{G}_{loc}^{-1} \langle \mathbf{G}_{\alpha j} \rangle_{dis}$ in the equation B.33, we get

$$\Delta_{\alpha}^{\sigma} = \sum_{ij} \gamma_{i\alpha} \gamma_{\alpha j} \mathbf{W} \langle \mathbf{G}_{ij}^{\sigma} \rangle_{dis} \mathbf{W} - \left(\sum_i \gamma_{i\alpha} \mathbf{W} \langle \mathbf{G}_{i\alpha}^{\sigma} \rangle_{dis} \right) \left[\langle \mathbf{G}_{\alpha\alpha}^{\sigma} \rangle_{dis} \right]^{-1} \left(\sum_j \gamma_{\alpha j} \langle \mathbf{G}_{\alpha j}^{\sigma} \rangle_{dis} \mathbf{W} \right). \quad (\text{B.34})$$

In order to express the Eq. B.34 in reciprocal \mathbf{k} -space is reduced Brillouin zone, we perform the same type of method as in B.21. Thus, we can easily express each term of the Eq. B.34 in RBZ as

APPENDIX B. MATRIX DMFT/CPA FOR NÉEL ORDERED
ANTIFERROMAGNETIC PHASE

$$\begin{aligned} \sum_i \gamma_{i\alpha} \mathbf{W} \langle \mathbf{G}_{i\alpha}^\sigma \rangle_{dis} &= \frac{1}{N} \sum_{\mathbf{k} \in RBZ} \{ \gamma_{\mathbf{k}} \mathbf{W} \mathbf{G}_{\mathbf{k}\mathbf{k}}^\sigma + \alpha \gamma_{\mathbf{k}} \mathbf{W} \mathbf{G}_{\mathbf{k}\mathbf{k}+\mathbf{Q}}^\sigma \\ &\quad + \alpha \gamma_{\mathbf{k}+\mathbf{Q}} \mathbf{W} \mathbf{G}_{\mathbf{k}+\mathbf{Q}\mathbf{k}}^\sigma + \gamma_{\mathbf{k}+\mathbf{Q}} \mathbf{W} \mathbf{G}_{\mathbf{k}+\mathbf{Q}\mathbf{k}+\mathbf{Q}}^\sigma \}, \end{aligned} \quad (\text{B.35})$$

$$\begin{aligned} \sum_j \gamma_{\alpha j} \langle \mathbf{G}_{\alpha j}^\sigma \rangle_{dis} \mathbf{W} &= \frac{1}{N} \sum_{\mathbf{k} \in RBZ} \{ \gamma_{\mathbf{k}} \mathbf{G}_{\mathbf{k}\mathbf{k}}^\sigma \mathbf{W} + \alpha \gamma_{\mathbf{k}} \mathbf{G}_{\mathbf{k}\mathbf{k}+\mathbf{Q}}^\sigma \mathbf{W} \\ &\quad + \alpha \gamma_{\mathbf{k}+\mathbf{Q}} \mathbf{G}_{\mathbf{k}+\mathbf{Q}\mathbf{k}}^\sigma \mathbf{W} + \gamma_{\mathbf{k}+\mathbf{Q}} \mathbf{G}_{\mathbf{k}+\mathbf{Q}\mathbf{k}+\mathbf{Q}}^\sigma \mathbf{W} \}, \end{aligned} \quad (\text{B.36})$$

$$\begin{aligned} \sum_{ij} \gamma_{i\alpha} \gamma_{\alpha j} \mathbf{W} \langle \mathbf{G}_{ij}^\sigma \rangle_{dis} \mathbf{W} &= \frac{1}{N} \sum_{\mathbf{k} \in RBZ} \{ \gamma_{\mathbf{k}} \gamma_{\mathbf{k}} \mathbf{W} \mathbf{G}_{\mathbf{k}\mathbf{k}}^\sigma \mathbf{W} + \alpha \gamma_{\mathbf{k}} \gamma_{\mathbf{k}+\mathbf{Q}} \mathbf{W} \mathbf{G}_{\mathbf{k}\mathbf{k}+\mathbf{Q}}^\sigma \mathbf{W} \\ &\quad + \alpha \gamma_{\mathbf{k}+\mathbf{Q}} \gamma_{\mathbf{k}} \mathbf{W} \mathbf{G}_{\mathbf{k}+\mathbf{Q}\mathbf{k}}^\sigma \mathbf{W} + \gamma_{\mathbf{k}+\mathbf{Q}} \gamma_{\mathbf{k}+\mathbf{Q}} \mathbf{W} \mathbf{G}_{\mathbf{k}+\mathbf{Q}\mathbf{k}+\mathbf{Q}}^\sigma \mathbf{W} \}, \end{aligned} \quad (\text{B.37})$$

where $\alpha = 1$ if a site belongs to sublattice A or -1 if a site belongs to sublattice B. In order to find the expression of Δ_α^σ , we describe a tensor Δ^σ composed of $\Delta_{\alpha \in A}^\sigma$ and $\Delta_{\alpha \in B}^\sigma$ as :

$$\Delta^\sigma = \begin{pmatrix} \Delta_A^\sigma & 0 \\ 0 & \Delta_B^\sigma \end{pmatrix}. \quad (\text{B.38})$$

The next step would be rewriting B.38 using δ_0 between A and B sites, and we obtain

$$\begin{aligned} \Delta^\sigma &= \sum_{ij} \begin{pmatrix} \gamma_{i\alpha} \gamma_{\alpha j} \mathbf{W} \mathbf{G}_{ij}^\sigma \mathbf{W} & 0 \\ 0 & \gamma_{i+\delta_0} \gamma_{\alpha+\delta_0 j+\delta_0} \mathbf{W} \mathbf{G}_{i+\delta_0 j+\delta_0}^\sigma \mathbf{W} \end{pmatrix} \\ &\quad - \sum_i \begin{pmatrix} \gamma_{i\alpha} \mathbf{W} \mathbf{G}_{i\alpha}^\sigma & 0 \\ 0 & \gamma_{i+\delta_0 \alpha+\delta_0} \mathbf{W} \mathbf{G}_{i+\delta_0 \alpha+\delta_0}^\sigma \end{pmatrix} \begin{pmatrix} \mathbf{G}_{loc,A}^\sigma & 0 \\ 0 & \mathbf{G}_{loc,B}^\sigma \end{pmatrix}^{-1} \sum_j \begin{pmatrix} \gamma_{\alpha j} \mathbf{G}_{\alpha j}^\sigma \mathbf{W} & 0 \\ 0 & \gamma_{\alpha+\delta_0 j+\delta_0} \mathbf{G}_{\alpha+\delta_0 j+\delta_0}^\sigma \mathbf{W} \end{pmatrix}. \end{aligned} \quad (\text{B.39})$$

We insert Eqs. B.35, B.36 and B.37 in each of the terms of B.39 and treating with Pauli

matrices, we obtain

$$\sum_i \begin{pmatrix} \gamma_{i\alpha} \mathbf{W} \mathbf{G}_{i\alpha}^\sigma & 0 \\ 0 & \gamma_{i+\delta_0\alpha+\delta_0} \mathbf{W} \mathbf{G}_{i+\delta_0\alpha+\delta_0}^\sigma \end{pmatrix} = -(\mathbf{1} \otimes \mathbf{1}) + (\mathbf{1} \otimes \mathbf{\Pi}_\sigma^+ + \sigma_z \otimes \mathbf{\Pi}_\sigma^-)^{-1} \bar{\mathbf{G}}_{loc}^\sigma \quad (\text{B.40})$$

$$\sum_j \begin{pmatrix} \gamma_{\alpha j} \mathbf{G}_{\alpha j}^\sigma \mathbf{W} & 0 \\ 0 & \gamma_{\alpha+\delta_0 j+\delta_0} \mathbf{G}_{\alpha+\delta_0 j+\delta_0}^\sigma \mathbf{W} \end{pmatrix} = -(\mathbf{1} \otimes \mathbf{1}) + \mathbf{G}_{loc}^\sigma (\mathbf{1} \otimes \mathbf{\Pi}_\sigma^+ + \sigma_z \otimes \mathbf{\Pi}_\sigma^-)^{-1} \quad (\text{B.41})$$

$$\sum_{ij} \begin{pmatrix} \gamma_{i\alpha} \gamma_{\alpha j} \mathbf{W} \mathbf{G}_{ij}^\sigma \mathbf{W} & 0 \\ 0 & \gamma_{i+\delta_0} \gamma_{\alpha+\delta_0 j+\delta_0} \mathbf{W} \mathbf{G}_{i+\delta_0 j+\delta_0}^\sigma \mathbf{W} \end{pmatrix} = -(\mathbf{1} \otimes \mathbf{\Pi}_\sigma^+ + \sigma_z \otimes \mathbf{\Pi}_\sigma^-)^{-1} + (\mathbf{1} \otimes \mathbf{\Pi}_\sigma^+ + \sigma_z \otimes \mathbf{\Pi}_\sigma^-)^{-1} \mathbf{G}_{loc}^\sigma (\mathbf{1} \otimes \mathbf{\Pi}_\sigma^+ + \sigma_z \otimes \mathbf{\Pi}_\sigma^-)^{-1} \quad (\text{B.42})$$

Putting all three equations obtained above into the equation B.39, and we get an equation

$$\Delta^\sigma = (\mathbf{1} \otimes \mathbf{\Pi}_\sigma^+ + \sigma_z \otimes \mathbf{\Pi}_\sigma^-)^{-1} - [\bar{\mathbf{G}}_{loc}^\sigma]^{-1}. \quad (\text{B.43})$$

From the above equation, one can also derive the equation for dynamical local bath for sub-lattices $\alpha = \text{A}$ or B :

$$\Delta_\alpha^\sigma = [\mathbf{\Pi}_\alpha^\sigma]^{-1} - [\mathbf{G}_{loc,\alpha}^\sigma]^{-1}. \quad (\text{B.44})$$

APPENDIX B. MATRIX DMFT/CPA FOR NÉEL ORDERED
ANTIFERROMAGNETIC PHASE

Appendix C

Results on Bethe lattice

Parallely, with 2D lattice, we have equally evaluated DMFT equations for Bethe lattice with infinite coordination. In this appendix, we present the phase diagram, some results on local potential scattering, and static magnetic susceptibility that we have obtained for Bethe lattice. However, for the calculations on Bethe lattice, we have considered only the paramagnetic Kondo case. The aim of these extra calculations is to verify the pertinence of our DMFT study of the 2D lattice.

C.1 Equations for local Green's functions

Here, we present the equations for dynamical local bath and the local Green's functions for Bethe lattice. Since we consider Bethe lattice with infinite coordination, the Green's functions can be replaced by local Green's functions in the equations for the dynamical local bath in the Eq 3.21. This lead us to a much simpler equation as

$$\Delta(i\omega) = xt^2 G_{\mathcal{K}}(i\omega) + (1-x)t^2 G_{\mathcal{N}}(i\omega), \quad (\text{C.1})$$

Furthermore, the equation C.1 can be inserted in the expressions of local Green's functions $G_{\mathcal{N}}(i\omega) = 1/(i\omega + \mu - \Delta(i\omega))$ and $G_{\mathcal{K}}(i\omega) = 1/(i\omega + \mu - \Delta(i\omega) - \Sigma_{\mathcal{K}}(i\omega))$. With few lines of algebraic calculations, we can obtain the equations as

$$G_{\mathcal{K}}(i\omega) = \frac{a}{2xt^2} \left[1 - \sqrt{1 - \frac{4xt^2}{a^2}} \right], \quad (\text{C.2})$$

$$G_{\mathcal{N}}(i\omega) = \frac{b}{2(1-x)t^2} \left[1 - \sqrt{1 - \frac{4(1-x)t^2}{b^2}} \right], \quad (\text{C.3})$$

with $a = i\omega + \mu - (1-x)t^2 G_{\mathcal{N}}(i\omega) - \Sigma_{\mathcal{K}}(i\omega)$ and $b = i\omega + \mu - xt^2 G_{\mathcal{K}}(i\omega)$. Now, we have all the equations necessary to perform the DMFT loop as for 2D lattice. Numerically, We solve DMFT equations 3.19 and 3.22 along with self-consistent equations 3.25, 3.26 and 3.27 for paramagnetic phase.

C.2 Phase diagram

Au contrary to the 2D lattice, here we don't consider magnetically ordered phase. The aim is to compare the dilute-dense paramagnetic Kondo phase diagram with a 2D lattice.

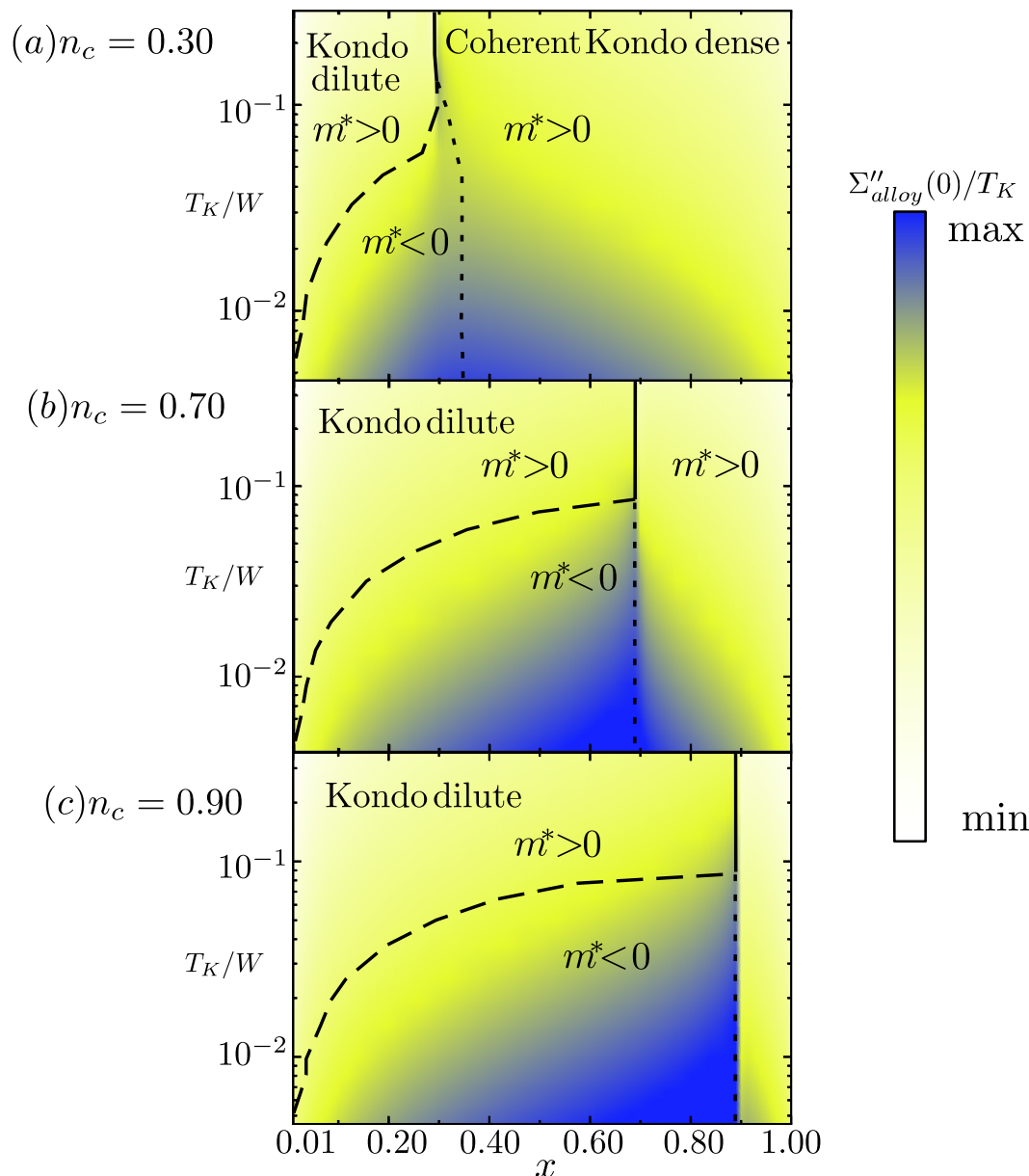


Figure C.1: Dense-dilute phase diagram for paramagnetic Kondo phase for Bethe lattice for $n_c = 0.30, 0.70$ and 0.90 . Yellow-blue background represent imaginary part of self-energy representing decoherence.

As we can remark that the paramagnetic phase diagram for Bethe lattice in figure C.1 is similar to that of 2D lattice in figure 5.9.

C.3 Local potential scattering

The local potential is described in section 6.1.1. We use the same definition, and we analyze local potential scattering for Bethe lattice in paramagnetic phase as for 2D lattice. It will permit us to compare our result with previously published results on local potential scattering in [138].

C.3.1 Large Kondo coupling

Figure C.2 present the results for large Kondo coupling at $T_K/W = 0.169$ for $n_c = 0.70$. In this figure, we can clearly observe that the discontinuity seen in 2D lattice at $x = n_c$ is present here along with other characteristics. Here, the only difference that we observe is that the imaginary part of local potential scattering can take negative values. The negative values for local potential scattering were also observed in [138].

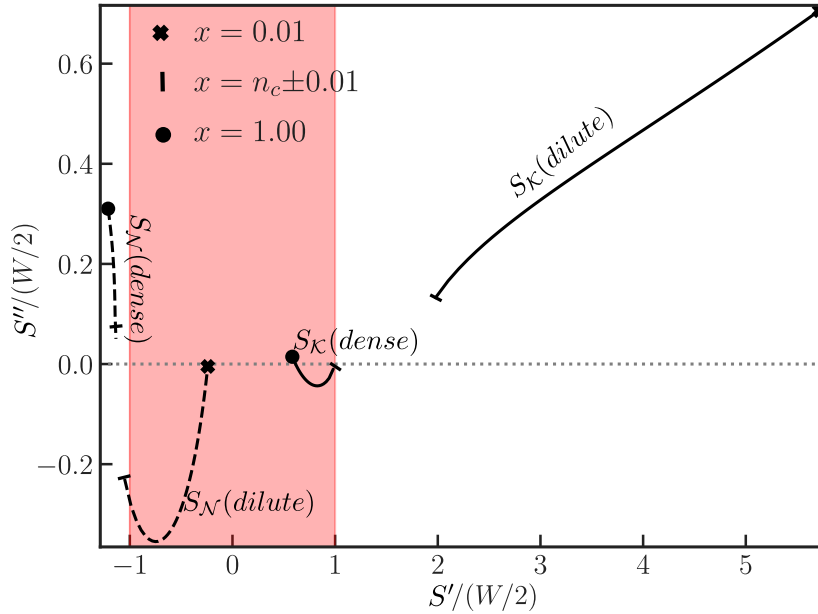


Figure C.2: Local potential scattering for Bethe lattice in paramagnetic Kondo phase for Kondo coupling $T_K/W = 0.169$ and for $n_c = 0.70$. Solid line represent LPS for \mathcal{K} -site whereas dashed line represent LPS for \mathcal{N} -site. (\bullet) indicates Kondo lattice ($x = 1.00$), and (\star) the most diluted case ($x = 0.01$). Light red background highlights the electronic bandwidth W .

C.3.2 Low Kondo coupling

Figure C.3 present the results for large Kondo coupling at $T_K/W = 0.009$ for $n_c = 0.70$. In this figure, we can clearly observe that the discontinuity seen in 2D lattice at $x = n_c$

disappears, and it is translated by a jump near $x = n_c$. $S_{\mathcal{N}}(0)$ remains inside the non-interacting electronic bandwidth and the $S_{\mathcal{K}}(0)$ slowly crosses the bandwidth at the upper edge of the electronic bandwidth. Again, we observe that the imaginary part can take negative values.

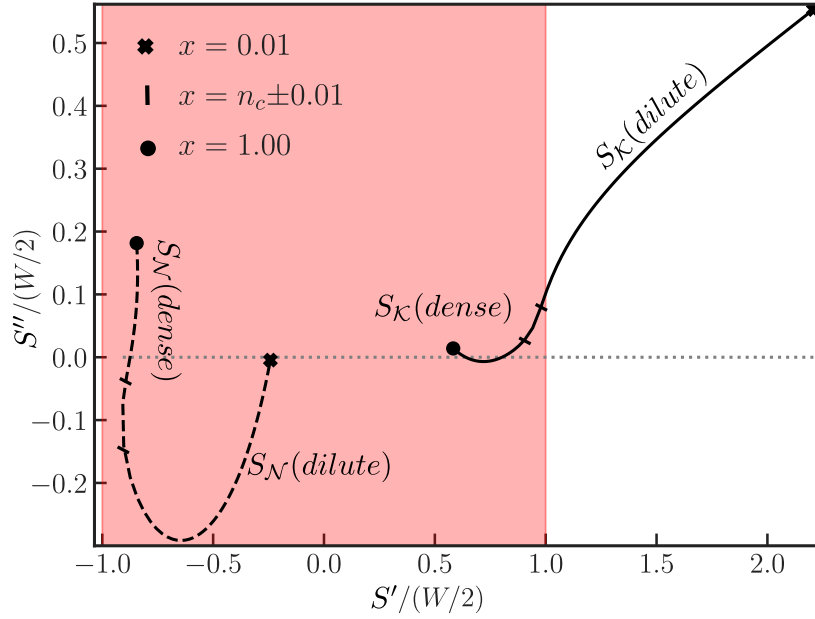


Figure C.3: Local potential scattering for Bethe lattice in paramagnetic Kondo phase for Kondo coupling $T_K/W = 0.009$ and for $n_c = 0.70$. Solid line represent LPS for \mathcal{K} -site whereas dashed line represent LPS for \mathcal{N} -site. (•) indicates Kondo lattice ($x = 1.00$), and (•) the most diluted case ($x = 0.01$). Light red background highlights the electronic bandwidth W .

Appendix D

Toy model for negative mass

In this part of the appendix, we present a simple toy model to explain the possible origin of the cancellation of the effective mass corresponding to the exceptional point.

D.1 Two reservoirs model

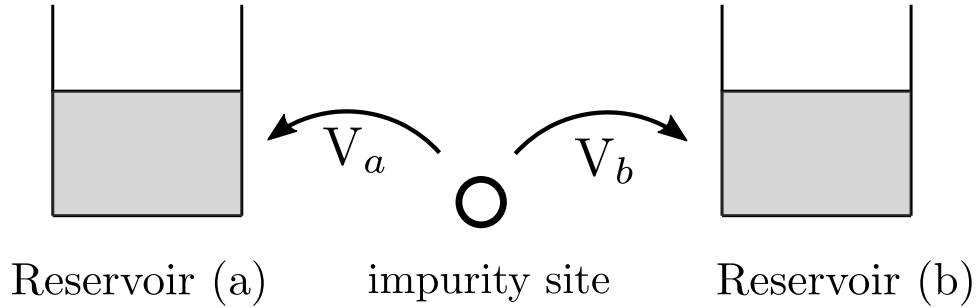


Figure D.1: Schematic view of two reservoirs (a) and (b) to which an impurity site interacts.

We consider an impurity site that is coupled with the two reservoirs (a) and (b) via the hybridizations V_a and V_b respectively. In this case, the local Green function at the impurity can be written as

$$G_0^{imp}(\omega) = \frac{1}{\omega - \lambda + i \text{sign}(\omega)\Delta_b}, \quad (\text{D.1})$$

where $\Delta_b = \pi\rho_b(0)V_b^2$, $\rho_b(0)$ being density of states of reservoir (b) at Fermi level. We rewrite $\tilde{\lambda} = -\lambda + i\Delta_b$. Furthermore, the local self-energy describing the reservoir (a) can be written as

$$\Sigma_a(\omega) = V_a^2 G_0^{imp}(\omega). \quad (\text{D.2})$$

Henceforth, the effective mass can be expressed as

$$m_a^* = 1 - \frac{\partial \Re(\Sigma_a(\omega))}{\partial \omega} \Big|_{\omega=0} = 1 + \frac{(\lambda^2 - \Delta_b^2)V_a^2}{(\lambda^2 + \Delta_b^2)^2}. \quad (\text{D.3})$$

If the imaginary part Δ_b is zero, the effective mass is always larger or equal to 1. Otherwise, m^* can be decreased or even negative if the $\arg(\tilde{\lambda}) > \pi/4$.

D.2 Application to $\Sigma_{\text{alloy}}(\omega)$

We rewrite the expression of self-energy alloy (see Eq. 5.5 in the section 5.2.1) as

$$\Sigma_{\text{alloy}}(\omega) = \frac{xr^2}{\omega + \lambda - (1-x)r^2G_{\mathcal{N}}(\omega)}. \quad (\text{D.4})$$

At $\omega = 0$ and with $G_{\mathcal{N}}(0) = G'_{\mathcal{N}}(0) + iG''_{\mathcal{N}}(0)$, we can identify from the equation (D.4) and (D.1) where the reservoir (a) acts as Kondo sites and reservoir (b) acts as non-Kondo sites. Thus, the hybridization V_a^2 will get dressed by a factor x , the probability of having a Kondo site and similarly, $(1-x)$ will dress the quantities related to non-Kondo sites. Thus, we get

$$\Re(\tilde{\lambda}) = -\lambda + (1-x)r^2G'_{\mathcal{N}}(0), \quad (\text{D.5})$$

$$\Im(\tilde{\lambda}) = -(1-x)r^2G''_{\mathcal{N}}(0). \quad (\text{D.6})$$

Thus, dependent upon the value of $\Re(\tilde{\lambda})$ and $\Im(\tilde{\lambda})$, m^* can be either negative or positive. Hence, we can obtain both nature: particle or hole.

Appendix E

Slave-bosons mappings

In this section, we present the mapping of slave-bosons on multiplet-Fock basis set. Altogether there are 64 multiplets with 116 slave-bosons. The table below resumes the multiplets and slave bosons according to different changer sectors.

f^n	J	J_z	$ \Gamma_n\rangle$	E_Γ	ϕ_{Γ_n}
0	0	0	$ \Gamma_1\rangle = 000000\rangle$	0	$\phi_{1, 000000\rangle}$
1	5/2	5/2	$ \Gamma_2\rangle = 000001\rangle$	0	$\phi_{2, 000001\rangle}$
		3/2	$ \Gamma_3\rangle = 000010\rangle$		$\phi_{3, 000010\rangle}$
		1/2	$ \Gamma_4\rangle = 000100\rangle$		$\phi_{4, 000100\rangle}$
		-1/2	$ \Gamma_5\rangle = 001000\rangle$		$\phi_{5, 001000\rangle}$
		-3/2	$ \Gamma_6\rangle = 010000\rangle$		$\phi_{6, 010000\rangle}$
		-3/2	$ \Gamma_7\rangle = 100000\rangle$		$\phi_{7, 100000\rangle}$
2	4	4	$ \Gamma_8\rangle = 000011\rangle$	U_4	$\phi_{8, 000011\rangle}$
		3	$ \Gamma_9\rangle = 000101\rangle$		$\phi_{9, 000101\rangle}$
		2	$ \Gamma_{10}\rangle = \sqrt{5} 000110\rangle + 3 001001\rangle$		$\phi_{10, 001100\rangle},$ $\phi_{10, 001001\rangle}$
		1	$ \Gamma_{11}\rangle = \sqrt{5} 001010\rangle + \sqrt{2} 010001\rangle$		$\phi_{11, 001010\rangle},$ $\phi_{11, 010001\rangle}$
		0	$ \Gamma_{12}\rangle = 2 001100\rangle + 3 010010\rangle + 100001\rangle$		$\phi_{12, 001100\rangle},$ $\phi_{12, 010010\rangle},$ $\phi_{12, 100001\rangle}$
		-1	$ \Gamma_{13}\rangle = \sqrt{5} 010100\rangle + \sqrt{2} 100010\rangle$		$\phi_{13, 010100\rangle},$ $\phi_{13, 100010\rangle}$
		-2	$ \Gamma_{14}\rangle = \sqrt{5} 011000\rangle + 3 100100\rangle$		$\phi_{14, 011000\rangle},$ $\phi_{14, 100100\rangle}$

APPENDIX E. SLAVE-BOSONS MAPPINGS

	-3		$ \Gamma_{15}\rangle = 101000\rangle$		$\phi_{15, 101000\rangle}$
	-4		$ \Gamma_{16}\rangle = 110000\rangle$		$\phi_{16, 110000\rangle}$
2	2		$ \Gamma_{17}\rangle = 3 001100\rangle - \sqrt{5} 001001\rangle$	U_2	$\phi_{17, 001100\rangle},$ $\phi_{17, 001001\rangle}$
	1		$ \Gamma_{18}\rangle = \sqrt{2} 001010\rangle - \sqrt{5} 010001\rangle$		$\phi_{18, 001010\rangle},$ $\phi_{18, 010001\rangle}$
	0		$ \Gamma_{19}\rangle = 4 001100\rangle - 010010\rangle - 5 100001\rangle$		$\phi_{19, 001100\rangle},$ $\phi_{19, 010010\rangle},$ $\phi_{19, 100001\rangle}$
	-1		$ \Gamma_{20}\rangle = \sqrt{2} 010100\rangle - \sqrt{5} 100010\rangle$		$\phi_{20, 010100\rangle},$ $\phi_{20, 100010\rangle}$
	-2		$ \Gamma_{21}\rangle = 3 011000\rangle - \sqrt{5} 100100\rangle$		$\phi_{21, 011000\rangle},$ $\phi_{21, 100100\rangle}$
0	0	0	$ \Gamma_{22}\rangle = 001100\rangle - 010010\rangle + 100001\rangle$	U_0	$\phi_{22, 001100\rangle},$ $\phi_{22, 010010\rangle},$ $\phi_{22, 100001\rangle}$
3	9/2	9/2	$ \Gamma_{23}\rangle = 000111\rangle$	$U_{3, \frac{9}{2}}$	$\phi_{22, 000111\rangle}$
	7/2		$ \Gamma_{24}\rangle = 001011\rangle$		$\phi_{22, 001011\rangle}$
	5/2		$ \Gamma_{25}\rangle = 010011\rangle + 001101\rangle$		$\phi_{25, 010011\rangle},$ $\phi_{25, 001101\rangle}$
	3/2		$ \Gamma_{26}\rangle = 001110\rangle + \sqrt{\frac{32}{5}} 010101\rangle + 100011\rangle$		$\phi_{26, 001110\rangle},$ $\phi_{26, 010101\rangle},$ $\phi_{26, 100011\rangle}$
	1/2		$ \Gamma_{27}\rangle = 010110\rangle + \sqrt{\frac{4}{5}} 011001\rangle + 100101\rangle$		$\phi_{27, 010110\rangle},$ $\phi_{27, 011001\rangle},$ $\phi_{27, 100101\rangle}$
	-1/2		$ \Gamma_{28}\rangle = 011010\rangle + \sqrt{\frac{4}{5}} 100110\rangle + 101001\rangle$		$\phi_{28, 011010\rangle},$ $\phi_{28, 100110\rangle},$ $\phi_{28, 101001\rangle}$
	-3/2		$ \Gamma_{29}\rangle = 011100\rangle + \sqrt{\frac{32}{5}} 101010\rangle + 110001\rangle$		$\phi_{29, 011100\rangle},$ $\phi_{29, 101010\rangle},$ $\phi_{29, 110001\rangle}$
	-5/2		$ \Gamma_{30}\rangle = 110010\rangle + 101100\rangle$		$\phi_{30, 110010\rangle},$ $\phi_{30, 101100\rangle}$
	-7/2		$ \Gamma_{31}\rangle = 110100\rangle$		$\phi_{31, 110100\rangle}$

APPENDIX E. SLAVE-BOSONS MAPPINGS

	-9/2		$ \Gamma_{32}\rangle = 111000\rangle$		$\phi_{32, 111000\rangle}$
	3/2	3/2	$ \Gamma_{33}\rangle = 001110\rangle - \sqrt{\frac{5}{8}} 010101\rangle + 100011\rangle$	$U_{3,\frac{3}{2}}$	$\phi_{33, 001110\rangle},$ $\phi_{33, 010101\rangle},$ $\phi_{33, 100011\rangle}$
	1/2		$ \Gamma_{34}\rangle = 010110\rangle - \sqrt{5} 011001\rangle + 100101\rangle$		$\phi_{34, 010110\rangle},$ $\phi_{34, 011001\rangle},$ $\phi_{34, 100101\rangle}$
	-1/2		$ \Gamma_{35}\rangle = 011010\rangle - \sqrt{5} 100110\rangle + 101001\rangle$		$\phi_{35, 011010\rangle},$ $\phi_{35, 100110\rangle},$ $\phi_{35, 101001\rangle}$
	-3/2		$ \Gamma_{36}\rangle = 011100\rangle - \sqrt{\frac{5}{8}} 101010\rangle + 110001\rangle$		$\phi_{36, 011100\rangle},$ $\phi_{36, 101010\rangle},$ $\phi_{36, 110001\rangle}$
	5/2	5/2	$ \Gamma_{37}\rangle = 010011\rangle - 001101\rangle$	$U_{3,\frac{5}{2}}$	$\phi_{37, 010011\rangle},$ $\phi_{37, 001101\rangle}$
	3/2		$ \Gamma_{38}\rangle = 001110\rangle - 100011\rangle$		$\phi_{38, 001110\rangle},$ $\phi_{38, 100011\rangle}$
	1/2		$ \Gamma_{39}\rangle = 010110\rangle - 100101\rangle$		$\phi_{39, 010110\rangle},$ $\phi_{39, 100101\rangle}$
	-1/2		$ \Gamma_{40}\rangle = 011010\rangle - 101001\rangle$		$\phi_{40, 011010\rangle},$ $\phi_{40, 101001\rangle}$
	-3/2		$ \Gamma_{41}\rangle = 011100\rangle - 110001\rangle$		$\phi_{41, 011100\rangle},$ $\phi_{41, 110001\rangle}$
	-5/2		$ \Gamma_{42}\rangle = 110010\rangle - 101100\rangle$		$\phi_{42, 110010\rangle},$ $\phi_{42, 101100\rangle}$
4	4	4	$ \Gamma_{43}\rangle = 001111\rangle$	$U_{4,4}$	$\phi_{43, 010011\rangle}$
	3		$ \Gamma_{44}\rangle = 010111\rangle$		$\phi_{44, 010111\rangle}$
	2		$ \Gamma_{45}\rangle = \sqrt{5} 100111\rangle + 3 011011\rangle$		$\phi_{45, 100111\rangle},$ $\phi_{45, 011011\rangle}$
	1		$ \Gamma_{46}\rangle = \sqrt{5} 101011\rangle + \sqrt{2} 011101\rangle$		$\phi_{46, 101011\rangle},$ $\phi_{46, 011101\rangle}$
	0		$ \Gamma_{47}\rangle = 2 110011\rangle + 3 101101\rangle + 011110\rangle$		$\phi_{47, 110011\rangle},$ $\phi_{47, 101101\rangle},$ $\phi_{47, 011110\rangle}$
	-1		$ \Gamma_{48}\rangle = \sqrt{5} 110101\rangle + \sqrt{2} 101110\rangle$		$\phi_{48, 110101\rangle},$ $\phi_{48, 101110\rangle}$

APPENDIX E. SLAVE-BOSONS MAPPINGS

	-2		$ \Gamma_{49}\rangle = \sqrt{5} 111001\rangle + 3 110110\rangle$		$\phi_{49, 111001\rangle},$ $\phi_{49, 110110\rangle}$
	-3		$ \Gamma_{50}\rangle = 111010\rangle$		$\phi_{50, 111010\rangle}$
	-4		$ \Gamma_{51}\rangle = 111100\rangle$		$\phi_{51, 111100\rangle}$
2	2		$ \Gamma_{52}\rangle = 3 100111\rangle - \sqrt{5} 011011\rangle$	$U_{4,2}$	$\phi_{52, 100111\rangle},$ $\phi_{52, 011011\rangle}$
	1		$ \Gamma_{53}\rangle = \sqrt{2} 101011\rangle - \sqrt{5} 011101\rangle$		$\phi_{53, 101011\rangle},$ $\phi_{53, 011101\rangle}$
	0		$ \Gamma_{54}\rangle = 4 110011\rangle - 101101\rangle - 5 011110\rangle$		$\phi_{54, 110011\rangle},$ $\phi_{54, 101101\rangle},$ $\phi_{54, 011110\rangle}$
	-1		$ \Gamma_{55}\rangle = \sqrt{2} 110101\rangle - \sqrt{5} 101110\rangle$		$\phi_{55, 110101\rangle},$ $\phi_{55, 101110\rangle}$
	-2		$ \Gamma_{56}\rangle = 3 111001\rangle - \sqrt{5} 110110\rangle$		$\phi_{56, 111001\rangle},$ $\phi_{56, 110110\rangle}$
0	0		$ \Gamma_{57}\rangle = 110011\rangle - 101101\rangle + 011110\rangle$	$U_{4,0}$	$\phi_{57, 110011\rangle},$ $\phi_{57, 101101\rangle},$ $\phi_{57, 011110\rangle}$
5	5/2	5/2	$ \Gamma_{58}\rangle = 011111\rangle$	$U_{5,5/2}$	$\phi_{58, 011111\rangle}$
	3/2		$ \Gamma_{59}\rangle = 101111\rangle$		$\phi_{59, 101111\rangle}$
	1/2		$ \Gamma_{60}\rangle = 110111\rangle$		$\phi_{60, 110111\rangle}$
	-1/2		$ \Gamma_{61}\rangle = 111011\rangle$		$\phi_{61, 111011\rangle}$
	-3/2		$ \Gamma_{62}\rangle = 111101\rangle$		$\phi_{62, 111101\rangle}$
	-5/2		$ \Gamma_{63}\rangle = 111110\rangle$		$\phi_{63, 111110\rangle}$
6	0	0	$ \Gamma_{64}\rangle = 111111\rangle$	$U_{6,0}$	$\phi_{64, 111111\rangle}$

with

$$\begin{aligned}
 U_{3,3/2} &= \frac{9U_2 + 33U_4}{14}, & U_{4,4} &= \frac{U_0 + 5U_2 + 12U_4}{3}, & U_{5,5/2} &= \frac{2U_0 + 10U_2 + 18U_4}{3}, \\
 U_{3,3/2} &= \frac{15U_2 + 6U_4}{7}, & U_{4,2} &= \frac{U_0 + 8U_2 + 9U_4}{3}, & U_{6,0} &= \frac{U_0 + 5U_2 + 9U_4}{3}. \\
 U_{3,5/2} &= \frac{4U_0 + 5U_2 + 9U_4}{6}, & U_{4,0} &= \frac{4U_0 + 5U_2 + 9U_4}{3}, & &
 \end{aligned}$$

List of Figures

1.1	Kadowaki–Woods ratio for a wide range of $4f$ and $5f$ -electron heavy-fermion materials with normalized $\tilde{A} = A/(N(N-1))$ and $\tilde{\gamma} = \gamma/(N(N-1))$ with ground-state degeneracy N . From [52]	4
1.2	Radial extend of $4f$ electrons in Sm^{3+} and Pu^{3+} respectively with both relativistic and nonrelativistic effects. x -axis in radial distance from the nucleus whereas $P(R)$ radial probability to find an electron at a distance r from the nucleus. From [86]	6
2.1	Schematic view of spin-flip process during electron scatter in Kondo model.	11
2.2	Two historical example showing Kondo effect. (a) Resistivity of impure gold from 1 K to 5 K where we observe a minimum resistivity around 4 K, extracted from [19]. (b) Resistivity of $\text{Ce}_x\text{La}_{1-x}\text{Cu}_6$ series with Ce-La substitution. Single-impurity Kondo effect can be seen at $x = 0.094$ and multi-impurity at $x = 1.0$, extracted from [89].	13
2.3	Schematic view of Doniach’s phase diagram. Blue line indicate Kondo temperature T_K and red line indicate magnetic order temperature scale T_{RKKY}	15
2.4	Schematic representation of Kondo lattice with impurity concentration x greater than electronic filling n_c in large Kondo coupling scenario. Impurity spins are represented by blue double arrows and conduction electrons are represented by green arrows. Red glow represent the formation of spin-singlet formation between impurity spins and conduction spins screening the local moments.	16
2.5	Left: large Fermi surface of YbRh_2Si_2 seen through (a) band renormalization calculation and (b) ARPES, where f -electron enter the description of Fermi surface at the temperature $T < T_K$. Right: small Fermi surface of YbCo_2Si_2 (a) LDA calculation and (b) ARPES, at the temperature $T > T_K$. From [135]	17

LIST OF FIGURES

2.6	Schematic representation of dilution of magnetic impurities. In both case, impurity spin (in blue arrow) forms a spin-singlet with conduction spin, represented by red glow. Right: the conduction electrons hop from singlet site to bachelor site, left: the conduction electrons hops from non-magnetic site to non-magnetic site.	18
3.1	Schematic view of matrix-DMFT approach of mapping a lattice problem (a) into a two local site local problem (b).	24
3.2	Figure illustrating the bipartite nature of the lattice for a Néel ordered antiferromagnetic phase. Dotted rectangle in the figure represent a unit cell composed two lattice sites belonging to each sublattices A and B	29
3.3	Schematic view of the generalized matrix-DMFT approach of mapping a lattice problem (a) onto four effective sites (b) in a bipartite system interacting with dynamical effective local bath in each case, where \bullet denotes sub-lattice A and \circ denotes sub-lattice B , red arrows are Kondo impurity spins, and the black arrows denotes the dynamical local baths.	30
3.4	(3.4a) DMFT loop for paramagnetic Kondo phase and (3.4b) for magnetically ordered phases	36
4.1	Magnetic phase diagram of $\text{CeRu}_2(\text{Si}_x\text{Ge}_{1-x})$. Substitution of Si by Ge increases the unit cell volume. A cascade of magnetic to non-magnetic phase transition is observed for increase Si concentration. From [119]	41
4.2	phase diagrams (a) 1D 'chain', (b) 2D 'square', 3D 'cubic' lattices at $T = 0$. K = paramagnetic Kondo phase, F = ferromagnetic phase, sat. F = saturated ferromagnetic phase and AF = antiferromagnetic phase	45
4.3	from left to right: ground state phase diagrams of the Kondo alloys for $n_c=0.30, 0.70$ and 0.30 . AFII = Néel ordered anti-ferromagnetic phase, and F = ferromagnetic phase	47
4.4	Schematic description of the Kondo alloys phase diagrams depicted on figure 4.3, with Kondo (K) and magnetically ordered (MO) phases. In order to fix the energy scale, the K - MO transition is arbitrarily chosen to be realized here at $T_K \approx 10$ Kelvin for the Kondo lattice ($x = 1$) and at around 1 Kelvin in the dilute limit $x \ll 1$. Dashed lines describe four examples of Kondo alloys: $\text{Ce}_x\text{La}_{1-x}\text{Pt}_2\text{Si}_2$ (circle), $\text{Ce}_x\text{La}_{1-x}\text{Ni}_2\text{Ge}_2$ (star), $\text{Ce}_x\text{La}_{1-x}\text{Ru}_2\text{Si}_2$ (square) and $\text{Ce}_x\text{La}_{1-x}\text{Pd}_2\text{Si}_2$ (triangle).	48

5.1	Left figures: Electronic density curve showing Kondo resonance peak (below) at on-resonance ARPES spectra. Right figure: Comparison of ARPES derived hybridized band and PAM hybridized band. From [231].	53
5.2	First Brillouin zone of the square lattice, with indications of the points $\Gamma = (0, 0)$, $X = (0, \pi)$, and $M = (\pi, \pi)$	55
5.3	Spectral function evaluated for $n_c = 0.70$ at relatively strong coupling $T_K/W = 0.169$ for Kondo impurity concentrations $x = 0.01, 0.30, 0.70$, and 1.00 . The wavevector \mathbf{k} axis corresponds to the high symmetry lines $\Gamma - X - M - \Gamma$ in the square lattice first Brillouin zone (see figure 5.2). The corresponding electronic density of states $\rho(\omega)$ is plotted on the right side. Each individual cases of this figure are indicated in the phase diagram depicted in the figure 5.9.	57
5.4	Spectral function evaluated for $n_c = 0.70$ at relatively small coupling $T_K/W = 0.019$ for Kondo impurity concentrations $x = 0.01, 0.08, 0.50$, and 1.00 with $x^* = 0.08$. The wavevector \mathbf{k} axis corresponds to the high symmetry lines $\Gamma - X - M - \Gamma$ in the square lattice first Brillouin zone (see figure 5.2). The corresponding electronic density of states $\rho(\omega)$ is plotted on the right side. Each individual case of this f are indicated in the phase diagram depicted in the figure 5.9.	58
5.6	Fermi surface structure for $T_K/W = 0.175$ for $n_c = 0.70$ at $x = n_c - 0.1$, $x = n_c$ and $x = n_c + 0.1$ from left to right. A clear evidence of Lifshitz-like transition is marked by the discontinuity of Fermi surface at $x = n_c$	59
5.5	FS spectra assuming a Kondo paramagnetic ground state for $x = 0.01, 0.20, 0.30, 0.40, 0.50, 0.60, 0.70, 0.80, 0.90, 1.00$ (from left to right) and $n_c = 0.20, 0.30, 0.40, 0.50, 0.60, 0.70, 0.80, 0.90, 1.00$ (from bottom to top). Each square corresponds to the first Brillouin zone of the square lattice (see figure 5.2). From top to bottom, $T_K/W = 0.175, 0.082$, and 0.0058 : the Lifshitz-like transition around $x = n_c$ is observed for a sufficiently strong Kondo interaction, and it becomes a gradual crossover for smaller values of the interaction. The red lines for $T_K/W = 0.082$ and 0.0058 separates the regimes $x < x^*$ and $x > x^*$. In both cases, x^* increases with increasing n_c . However, for $T_K/W = 0.0058$, this is not visible because x^* lies between $x = 0.01$ and $x = 0.20$ for all values of n_c considered.	60
5.7	Fermi surface spectra for $n_c = 0.30$ and $x = 0.05, 0.35, 0.65$ and 0.95 . (a) $T_K/W = 0.012$ with Kondo ground states: we observe signatures of a breakdown of coherence associated with a change of topology in the Fermi-surface. (b) $T_K/W = 0.0031$ with ferromagnetic ground states: we observe Zeeman splitting effect only.	61

5.8	Fermi surface spectra for $n_c = 0.90$, and $x = 0.05, 0.35, 0.65$ and 0.95 . (a) $T_K/W = 0.0143$ with Kondo ground states: we observe signatures of a breakdown of coherence associated with a change of topology in the Fermi-surface. (b) $T_K/W = 0.0045$ with antiferromagnetic ground states: we observe only the folding of the Fermi-surface which results from the staggered Néel ordering.	61
5.9	Ground state phase diagram of the KAM as functions of x and T_K/W for (a) $n_c = 0.30$, (b) $n_c = 0.70$ and (c) $n_c = 0.90$. (\blacktriangle) indicates the individual cases presented in the figure 5.3 and figure 5.4 for $n_c = 0.70$. In the Kondo phases the solid line indicates the discontinuity of the self-energy observed at $x = n_c$ for sufficiently strong T_K . This transition from the dense coherent Kondo phase becomes a crossover marked by an inflection in the self energy at smaller T_K (doted line), and a significant increase in the intensity of imaginary part of the self-energy (color or black and white gradient). A continuous vanishing of the effective mass m^* is obtained at concentration x^* (dashed line), and we find $m^* < 0$ in the intermediate region $x^* < x < n_c$. We also solved the DMFT equations obtained for a Bethe lattice, considering the Kondo paramagnetic solution only and the same values of model parameters as depicted here. Results for Bethe lattice can be found in the appendix C.2. We were not able to distinguish the figures corresponding to the Bethe lattice from the ones depicted here for the 2D square lattice. This strong similarity excludes several interpretations that might invoke specificities of the lattice structure.	63
5.10	(a) Real part of the self-energy $\Sigma'_{Alloy}(0)/W$, (b) Effective mass m^*/m_0 as functions of x , for $n_c = 0.70$. Different Kondo temperatures have been used for the numerics, illustrating the transition (at strong T_K) and crossover (at smaller T_K) obtained around $x = n_c$. The inset in (b) is a focus around the critical concentration x^* which is characterized by a vanishing of m^* when T_K relatively small. At intermediate concentrations $x^* < x < n_c$ we find $m^* < 0$	64
5.11	Imaginary part of self-energy $\Sigma''(0)/T_K$ for $T_K/W = 0.169, 0.019$ and 0.006 . $\Sigma''(0)/T_K$ is negative and increases with increasing T_K with a maximum at $x = n_c$	65
5.12	Evolution of the critical concentration x^* with respect to the Kondo coupling T_K/W presented here on $\log - \log$ scale. Solid line represent $n_c = 0.90$, dashed line represent $n_c = 0.70$ and dotted line represent $n_c = 0.30$ with a slope γ of $0.83 \pm 0.013, 0.78 \pm 0.006$, and 0.71 ± 0.016 respectively.	66

- 5.13 Frequency dependence of the real part of the self-energy, $\omega - \Sigma'_{Alloy}(\omega) + \Sigma'_{Alloy}(0)$ for $n_c = 0.70$ and $T_K = 0.019$. Top: for x in the vicinity of the critical point $x^* = 0.08$ which is characterized by $m^* = 0$, we observe the emergence of a non-monotonicity at low energy. This leads to the gradual formation of a multiple-branches dispersion for $x > x^*$. Center: for x in the vicinity of n_c , the maximum is realized at $\omega < 0$ for $x < n_c$ and at $\omega > 0$ for $x > n_c$ resulting in a second change of sign of m^* . Bottom: for x close to 1, we observe signatures of the singularity $\Sigma_K(\omega) = \frac{r^2}{\omega + \lambda}$ which is obtained in the mean-field approximation for the Kondo lattice. The non-monotonicity obtained at lower concentrations is reminiscent of this singularity, and we expect this feature to survive qualitatively beyond the mean-field approximation. . . . 67
- 6.1 Evolution of local potential scattering $S_a(0)$ for $n_c = 0.70$ relatively large Kondo coupling $T_K/W = 0.169$ represented on Argand diagram. Solid line represent LPS for \mathcal{K} -site whereas dashed line represent LPS for \mathcal{N} -site. (●) indicates Kondo lattice ($x = 1.00$), short vertical solid line indicates the concentrations $x = n_c \pm 0.01$ and (★) the most diluted case ($x = 0.01$). Light red background highlights the electronic bandwidth W 72
- 6.2 Evolution of local potential scattering $S_a(0)$ for $n_c = 0.70$ relatively low coupling $T_K/W = 0.019$ represented on Argand diagram. Solid line represent LPS for \mathcal{K} -site whereas dashed line represent LPS for \mathcal{N} -site. (●) indicates Kondo lattice ($x = 1.00$), short vertical solid line indicates the concentrations $x = n_c \pm 0.01$ and (★) the most diluted case ($x = 0.01$). Light red background highlights the electronic bandwidth W 73
- 6.3 Charge occupation on \mathcal{K} and \mathcal{N} -sites with the dilution of magnetic impurities x for different Kondo temperature T_K . Left: occupation for Kondo site, Right: occupation for non-Kondo site. The solid lines represent theoretical values expected for $T_K/W \rightarrow \infty$. $n_{\mathcal{K}}$ and $n_{\mathcal{N}}$ verifies the sum rule as: $x n_{\mathcal{K}} + (1 - x) n_{\mathcal{N}} = n_c$ 74
- 8.1 Wigner-Seitz radius (R_{WS}) of $5d$, $4f$ and $5f$ metals as a function of atomic number Z , where Wigner-Seitz radius is defined as $(4\pi/3)R_{WS}^3 = V$ while V being the equilibrium volume of the primitive unit cell. From [272] 83
- 8.2 Hill plot for various uranium based compounds showing the transition temperatures of itinerant or localized f -electron phases with respect to inter-atomic uranium-uranium distance. From [279]. . . . 85

LIST OF FIGURES

8.3	Schematic view jj -coupling scheming for an local f -electron. (a) spin-orbit splitting and (b) crystal-field splitting. Since, $5f$ electrons are closer to the nuclei, thus the crystal-field splitting is smaller and less relevant.	87
8.4	Phase diagram obtained through exact diagonalization for two-sites cluster, derived from total magnetization $\mathcal{J}_z = J_{1z} + J_{2z}$, where J_{1z} and J_{2z} are angular momentum projections on site 1 and 2 respectively. Here, only f^2 and f^3 configurations are considered. $t_{3/2}$ and $t_{1/2} = t_{5/2}$ are nearest-site hopping along orbitals $j_z = 3/2$ and $j_z = 1/2, 5/2$ respectively. Extracted from [60, 305]	88
10.1	Schematic view of intial optimizing process to get guess parameters while considering various f -configurations using the Eqs. 9.28-9.31. Whenever the physical constraints are satisfied, the scheme ejects an output with λ , μ and slave-boson vector Φ	106
10.2	Schematic view of local minimization for a given phase with a set of $\varphi_{\Gamma n}$ non-zeros.	108
10.3	Schematic view of the complete numerical process. The light green background shows the local minimization process, and its output is injected into a global minimization routine.	109
11.1	Evolution of slave boson probabilities $ \varphi_{\Gamma\Gamma} ^2$ on multiplet-multiplet basis along with f -electron occupation from $n_f = 3.0$ to $n_f = 2.5$ for charge sectors f^M configurations for non-interacting case (see table 11.1).	113
11.2	Diagonal slave bosons probabilities $ \varphi_{\Gamma\Gamma} ^2$ on the isotropic line ($W = W'$) for all six charge sectors $ f^M; J, J_z\rangle$. The black arrows on the x-axis points the towards the threshold values of W/U_0 where transition in valency configuration is observed.	114
11.3	Quasiparticules weight Z_{j_z} as a function of electronic bandwidth W/U_0 on the isotropic line ($W_{5/2} = W_{3/2} = W_{1/2}$) for orbitals $j_z = 5/2, 3/2$ and $1/2$ for paramagnetic phase. The inset shows a zoom of Z_{j_z} around small W/U_0	115
11.4	$E - E_0$ on the isotropic line from $W/U_4 = 0$ to large W/U_0 large. The inset shows the mean-field parameters λ and μ	116
11.5	Energies of partially localized phases along the line $W + W' = \text{constant}$: (a) $W + W' = 7$ and (b) $W + W' = 14$ while $W = W_{3/2}$ and $W' = W_{5/2} = W_{1/2}$. Colors of each line correspond to the color of each phase in figure 11.6.	118

11.6 Phase diagram with partially localized phases for the electronic bandwidths $0 \leq W \leq 15$ and $0 \leq W' \leq 15$. Solid lines are guides to the eyes separating two phases. (FM/PM) indicates that ferromagnetic and paramagnetic phases are degenerate. 119

11.7 Figure showing the line $W + W' = 7$ and $W + W' = 14$ on the phase diagram. 119

11.8 Schematic view of an electron hopping from a site- i with f^M configuration to a site- j with $f^{M'}$ configuration. For $M' < M$, this hopping becomes favorable. For instance, the hopping from $M = 3$ to $M = 2$ is more favorable than other way around since the hopping from $M = 2$ to $M = 3$ will create more energetic states with $M = 1$ and $M = 5$ particles. 120

11.9 Quasiparticle weights of non-localized orbitals along the line: $W + W' = 7$ ((a) and (c)) and $W + W' = 14$ ((b) and (d)) in the phase diagram. Only delocalized orbitals are presented here for PM phases ((c) and (d)) and for FM phases ((a) and (b)). Localized orbitals per phase are indicated on the top the figure, and aside of each line for each orbital. Vertical dotted lines are guides for eyes marking frontier between phases whereas solid vertical gray line indicate isotropic point. . . . 122

11.10 Electronic occupations for delocalized orbitals along $W + W' = 7$: (a) and (c), and along $W + W' = 14$: (b) and (d). Upper digrams (a) and (b) are for FM phases whereas middle diagrams (c) and (d) are for PM phases. Localized orbitals are indicated on the top the figure, and aside of each line for each orbital. Vertical dotted lines are guides for eyes marking frontier between phases whereas solid vertical gray line indicate isotropic point. 124

11.11 Magnetization is presented for only FM phases along $W + W' = 7$ (left), along $W + W' = 14$ (right). Localized orbitals are indicated on the top the figure. Vertical dotted lines are guides for eyes marking frontier between phases whereas solid vertical gray line indicate isotropic point. 125

- 11.12 Up: renormalized electronic bandwidth ($W_{j_z} Z_{j_z}$) for $j_z = 3/2$ localized orbital, calculated at the parameters $W = 0$ and $W' = 14$ for paramagnetic phase (a) and ferromagnetic phase (b). For each bar, black color indicates the electronic bandwidth below Fermi level with occupied states and gray color indicates the electronic bandwidth with unoccupied states. Down: schematic view of Fermi surfaces on 2D square lattice. Thin black line represent the Fermi surfaces. Darker blue color shades around Fermi surfaces indicate low Fermi velocity $v_F \propto Z_{j_z} W_{j_z}$ with high effective mass m^* , whereas lighter blue color shades indicate lighter effective with higher Fermi velocity. The width of the shades is determined by $1/W_{j_z} Z_{j_z}$ representing schematically the density of states at Fermi level. 126
- 11.13 Up: renormalized electronic bandwidth ($W_{j_z} Z_{j_z}$) with $j_z = 5/2$ and $j_z = 1/2$ localized orbitals calculated at the parameters $W = 10$ and $W' = 0$ for paramagnetic phase (a), ferromagnetic phase (b) and saturated ferromagnetic phase (c). For each bar, black color indicates the electronic bandwidth below Fermi level with occupied states and gray color indicates the electronic bandwidth with unoccupied states. Down: schematic view of Fermi surfaces on 2D square lattice. Thin black line represent the Fermi surfaces. Darker blue color shades around Fermi surfaces indicate low Fermi velocity $v_F \propto Z_{j_z} W_{j_z}$ with high effective mass m^* , whereas lighter blue color shades indicate lighter effective with higher Fermi velocity. The width of the shades is determined by $1/W_{j_z} Z_{j_z}$ representing schematically the density of states at Fermi level. 127
- 11.14 Variations of slave bosons probabilities $\Delta p(M)$ per f -electron configuration represented here for lines $W + W' = 7$ ((a) and (c)) and $W + W' = 14$ ((b) and (d)). Slave bosons probabilities for FM phases are presented in the upper panel ((a) and (b)) whereas PM phases are presented in the lower panel ((c) and (d)). Here, $\Delta p(2) = p(2) - 0.5$, $\Delta p(3) = p(3) - 0.5$ and $\Delta p = p(4)$ 129
- C.1 Dense-dilute phase diagram for paramagnetic Kondo phase for Bethe lattice for $n_c = 0.30, 0.70$ and 0.90 . Yellow-blue background represent imaginary part of self-energy representing decoherence. 152
- C.2 Local potential scattering for Bethe lattice in paramagnetic Kondo phase for Kondo coupling $T_K/W = 0.169$ and for $n_c = 0.70$. Solid line represent LPS for \mathcal{K} -site whereas dashed line represent LPS for \mathcal{N} -site. (\bullet) indicates Kondo lattice ($x = 1.00$), and (\star) the most diluted case ($x = 0.01$). Light red background highlights the electronic bandwidth W 153

C.3	Local potential scattering for Bethe lattice in paramagnetic Kondo phase for Kondo coupling $T_K/W = 0.009$ and for $n_c = 0.70$. Solid line represent LPS for \mathcal{K} -site whereas dashed line represent LPS for \mathcal{N} -site. (●) indicates Kondo lattice ($x = 1.00$), and (✱) the most diluted case ($x = 0.01$). Light red background highlights the electronic bandwidth W	154
D.1	Schematic view of two reservoirs (a) and (b) to which an impurity site interacts.	155

LIST OF FIGURES

List of Tables

4.1	Table that resumes local Green's function invariance according to the transformations for K, F and AFII phases	43
4.2	commensurate AF phases with and their respective wave ordering vectors.	44
8.1	Table resuming Barnes slave-boson representation	89
8.2	Table resuming Kotliar and Ruckenstein's slave bosons representation	91
8.3	Table resuming Li, Wölfle and Hirschfeld's slave bosons representation	92
9.1	Table showing RISB mapping for zero and one particle sector (M) and $M = \sum_{j_z} \eta_{j_z}$	98
11.1	Table resuming the parameters for different case of study.	111
11.2	Orbitals occupations (n_{j_z}) and quasiparticles weights (Z_{j_z}) for various partially localized phases. Here, PM signifies paramagnetic phase, FM signifies ferromagnetic phase and SFM signifies saturated ferromagnetic phase and the notation $\text{PM}_{\frac{5}{2}, \frac{1}{2}}$ means paramagnetic phase with $j_z = 5/2$ and $j_z = 1/2$ orbitals localized.	117

LIST OF TABLES

Bibliography

1. Landau, L. D. The theory of a Fermi liquid. *Soviet Physics JETP-USSR* **3**, 920–925 (1957).
2. Stewart, G. R. Non-Fermi-liquid behavior in *d*- and *f*-electron metals. *Rev. Mod. Phys.* **73**, 797–855 (4 Oct. 2001).
3. Hohenberg, P. & Kohn, W. Inhomogeneous Electron Gas. *Phys. Rev.* **136**, B864–B871 (3B Nov. 1964).
4. Kohn, W. & Sham, L. J. Self-Consistent Equations Including Exchange and Correlation Effects. *Phys. Rev.* **140**, A1133–A1138 (4A Nov. 1965).
5. Georges, A., Kotliar, G., Krauth, W. & Rozenberg, M. J. Dynamical mean-field theory of strongly correlated fermion systems and the limit of infinite dimensions. *Rev. Mod. Phys.* **68**, 13–125 (1 Jan. 1996).
6. Pavarini, E., Vollhardt, D., Koch, E. & Lichtenstein, A. *DMFT: From Infinite Dimensions to Real Materials* tech. rep. (Theoretische Nanoelektronik, 2018).
7. Avella, A. & Mancini, F. *Strongly correlated systems: experimental techniques* (Springer, 2014).
8. Avella, A. & Mancini, F. *Strongly correlated systems: theoretical methods* (Springer Science & Business Media, 2011).
9. Avella, A. & Mancini, F. *Strongly Correlated Systems* (Springer, 2013).
10. Zwicknagl, G. & Fulde, P. The dual nature of 5f electrons and the origin of heavy fermions in U compounds. *Journal of Physics: Condensed Matter* **15**, S1911 (2003).
11. Ashcroft, N. W., Mermin, N. D., *et al.* *Solid state physics* 1976.
12. Slater, J. C. The Electronic Structure of Metals. *Rev. Mod. Phys.* **6**, 209–280 (4 Oct. 1934).
13. Imada, M., Fujimori, A. & Tokura, Y. Metal-insulator transitions. *Rev. Mod. Phys.* **70**, 1039–1263 (4 Oct. 1998).
14. Moore, K. T. & van der Laan, G. Nature of the 5f states in actinide metals. *Rev. Mod. Phys.* **81**, 235–298 (1 Feb. 2009).

BIBLIOGRAPHY

15. Fujimori, S.-i. Band structures of 4f and 5f materials studied by angle-resolved photoelectron spectroscopy. *J. Phys.: Condens. Matter* **28**, 153002 (Mar. 2016).
16. Knöpfle, K., Mavromaras, A., Sandratskii, L. & Kübler, J. The Fermi surface of UPd₂Al₃. *Journal of Physics: Condensed Matter* **8**, 901 (1996).
17. Zwicknagl, G., Yaresko, A. N. & Fulde, P. Microscopic description of origin of heavy quasiparticles in UPt₃. *Phys. Rev. B* **65**, 081103 (8 Feb. 2002).
18. De Boer, J. H. & Verwey, E. J. Semi-conductors with partially and with completely filled 3d-lattice bands. *Proceedings of the Physical Society (1926-1948)* **49**, 59 (1937).
19. de Haas, W., de Boer, J. & van den Berg, G. The electrical resistance of gold, copper and lead at low temperatures. *Physica* **1**, 1115–1124 (1934).
20. Mott, N. & Peierls, R. Discussion of the paper by de Boer and Verwey. *Proceedings of the Physical Society (1926-1948)* **49**, 72 (1937).
21. Mott, N. F. The basis of the electron theory of metals, with special reference to the transition metals. *Proceedings of the Physical Society. Section A* **62**, 416 (1949).
22. Kondo, J. Resistance minimum in dilute magnetic alloys. *Progress of theoretical physics* **32**, 37–49 (1964).
23. Andres, K., Graebner, J. E. & Ott, H. R. 4f-Virtual-Bound-State Formation in CeAl₃ at Low Temperatures. *Phys. Rev. Lett.* **35**, 1779–1782 (26 Dec. 1975).
24. Steglich, F. *et al.* Superconductivity in the Presence of Strong Pauli Paramagnetism: CeCu₂Si₂. *Phys. Rev. Lett.* **43**, 1892–1896 (25 Dec. 1979).
25. Bednorz, J. G. & Müller, K. A. Possible high T_c superconductivity in the Ba-La-Cu-O system. *Zeitschrift für Physik B Condensed Matter* **64**, 189–193 (1986).
26. Vojta, M. Quantum phase transitions. *Reports on Progress in Physics* **66**, 2069–2110 (2003).
27. Saxena, S. *et al.* Superconductivity on the border of itinerant-electron ferromagnetism in UGe₂. *Nature* **406**, 587–592 (2000).
28. Ott, H. R., Rudigier, H., Fisk, Z. & Smith, J. L. UBe₁₃: An Unconventional Actinide Superconductor. *Phys. Rev. Lett.* **50**, 1595–1598 (20 May 1983).
29. Aoki, D., Ishida, K. & Flouquet, J. Review of U-based ferromagnetic superconductors: Comparison between UGe₂, URhGe, and UCoGe. *Journal of the Physical Society of Japan* **88**, 022001 (2019).
30. Schilling, A., Cantoni, M., Guo, J. & Ott, H. Superconductivity above 130 K in the Hg-Ba-Ca-Cu-O system. *Nature* **363**, 56–58 (1993).
31. Monteverde, M. *et al.* High-pressure effects in fluorinated HgBa₂Ca-2Cu₃O₈ + δ. *EPL (Europhysics Letters)* **72**, 458 (2005).

32. Zhi-An, R. *et al.* Superconductivity at 55 K in iron-based F-doped layered quaternary compound Sm [O_{1-x}F_x] FeAs. *Chinese Physics Letters* **25**, 2215 (2008).
33. Gardner, J. S., Gingras, M. J. P. & Greedan, J. E. Magnetic pyrochlore oxides. *Rev. Mod. Phys.* **82**, 53–107 (1 Jan. 2010).
34. Bramwell, S. T. & Gingras, M. J. Spin ice state in frustrated magnetic pyrochlore materials. *Science* **294**, 1495–1501 (2001).
35. Vuletić, T. *et al.* The spin-ladder and spin-chain system (La, Y, Sr, Ca) 14Cu₂₄O₄₁: Electronic phases, charge and spin dynamics. *Physics reports* **428**, 169–258 (2006).
36. Kondo, S. *et al.* LiV₂O₄: A Heavy Fermion Transition Metal Oxide. *Phys. Rev. Lett.* **78**, 3729–3732 (19 May 1997).
37. Maeno, Y., Kittaka, S., Nomura, T., Yonezawa, S. & Ishida, K. Evaluation of spin-triplet superconductivity in Sr₂RuO₄. *Journal of the Physical Society of Japan* **81**, 011009 (2011).
38. Kanoda, K. Recent progress in NMR studies on organic conductors. *Hyperfine Interactions* **104**, 235–249 (1997).
39. McKenzie, R. H. A strongly correlated electron model for the layered organic superconductors κ-(BEDT-TTF)₂X. *arXiv preprint cond-mat/9802198* (1998).
40. Zwerger, W. Mott–Hubbard transition of cold atoms in optical lattices. *Journal of Optics B: Quantum and Semiclassical Optics* **5**, S9 (2003).
41. Juzeliūnas, G., Ruseckas, J. & Dalibard, J. Generalized Rashba-Dresselhaus spin-orbit coupling for cold atoms. *Physical Review A* **81**, 053403 (2010).
42. Rozenberg, M. J., Inoue, I. H. & Sanchez, M. J. Strong electron correlation effects in nonvolatile electronic memory devices. *Applied Physics Letters* **88**, 033510 (2006).
43. Tokura, Y., Kawasaki, M. & Nagaosa, N. Emergent functions of quantum materials. *Nature Physics* **13**, 1056–1068 (2017).
44. Ramirez, A. Colossal magnetoresistance. *Journal of Physics: Condensed Matter* **9**, 8171 (1997).
45. Phan, M.-H. & Yu, S.-C. Review of the magnetocaloric effect in manganite materials. *Journal of Magnetism and Magnetic Materials* **308**, 325–340 (2007).
46. Rozenberg, M. J., Inoue, I. H. & Sánchez, M. J. Nonvolatile Memory with Multilevel Switching: A Basic Model. *Phys. Rev. Lett.* **92**, 178302 (17 Apr. 2004).
47. Haghiri-Gosnet, A. & Renard, J. CMR manganites: physics, thin films and devices. *Journal of Physics D: Applied Physics* **36**, R127 (2003).
48. Yu-Kuai, L., Yue-Wei, Y. & Xiao-Guang, L. Colossal magnetoresistance in manganites and related prototype devices. *Chinese Physics B* **22**, 087502 (2013).

BIBLIOGRAPHY

49. Fiebig, M. Revival of the magnetoelectric effect. *Journal of physics D: applied physics* **38**, R123 (2005).
50. Fusil, S., Garcia, V., Barthélémy, A. & Bibes, M. Magnetoelectric devices for spintronics. *Annual Review of Materials Research* **44**, 91–116 (2014).
51. Ramesh, R. & Spaldin, N. A. Multiferroics: progress and prospects in thin films. *Nanoscience And Technology: A Collection of Reviews from Nature Journals*, 20–28 (2010).
52. Tsujii, N., Kontani, H. & Yoshimura, K. Universality in Heavy Fermion Systems with General Degeneracy. *Phys. Rev. Lett.* **94**, 057201 (5 Feb. 2005).
53. Zhao, L. *et al.* Evidence of an odd-parity hidden order in a spin–orbit coupled correlated iridate. *Nature Physics* **12**, 32–36 (2016).
54. Kim, B. J. *et al.* Novel $J_{\text{eff}} = 1/2$ Mott State Induced by Relativistic Spin-Orbit Coupling in Sr_2IrO_4 . *Phys. Rev. Lett.* **101**, 076402 (7 Aug. 2008).
55. Mravlje, J. *et al.* Coherence-incoherence crossover and the mass-renormalization puzzles in Sr_2RuO_4 . *Physical review letters* **106**, 096401 (2011).
56. Georges, A., Medici, L. d. & Mravlje, J. Strong correlations from Hund’s coupling. *Annu. Rev. Condens. Matter Phys.* **4**, 137–178 (2013).
57. Dang, H. T., Mravlje, J., Georges, A. & Millis, A. J. Electronic correlations, magnetism, and Hund’s rule coupling in the ruthenium perovskites SrRuO_3 and CaRuO_3 . *Phys. Rev. B* **91**, 195149 (19 May 2015).
58. Chen, W.-Q., Yang, K.-Y., Zhou, Y. & Zhang, F.-C. Strong Coupling Theory for Superconducting Iron Pnictides. *Phys. Rev. Lett.* **102**, 047006 (4 Jan. 2009).
59. Yin, Z., Haule, K. & Kotliar, G. Magnetism and charge dynamics in iron pnictides. *Nature physics* **7**, 294–297 (2011).
60. Efremov, D. V., Hasselmann, N., Runge, E., Fulde, P. & Zwicknagl, G. Dual nature of $5f$ electrons: Effect of intra-atomic correlations on hopping anisotropies. *Phys. Rev. B* **69**, 115114 (11 Mar. 2004).
61. Engel, E. & Dreizler, R. M. *Density functional theory* (Springer, 2013).
62. Anisimov, V. I., Zaanen, J. & Andersen, O. K. Band theory and Mott insulators: Hubbard U instead of Stoner I. *Phys. Rev. B* **44**, 943–954 (3 July 1991).
63. Anisimov, V. I., Aryasetiawan, F. & Lichtenstein, A. First-principles calculations of the electronic structure and spectra of strongly correlated systems: the LDA+U method. *Journal of Physics: Condensed Matter* **9**, 767 (1997).
64. Perdew, J. P., McMullen, E. R. & Zunger, A. Density-functional theory of the correlation energy in atoms and ions: A simple analytic model and a challenge. *Phys. Rev. A* **23**, 2785–2789 (6 June 1981).

65. Skriver, H. L. *The LMTO method: muffin-tin orbitals and electronic structure* (Springer Science & Business Media, 2012).
66. Zwicknagl, G. Quasi-particles in Heavy Fermion systems. *Advances in Physics* **41**, 203–302 (1992).
67. Perdew, J. P., Ernzerhof, M. & Burke, K. Rationale for mixing exact exchange with density functional approximations. *The Journal of chemical physics* **105**, 9982–9985 (1996).
68. Heyd, J., Scuseria, G. E. & Ernzerhof, M. Hybrid functionals based on a screened Coulomb potential. *The Journal of chemical physics* **118**, 8207–8215 (2003).
69. Bylander, D. M. & Kleinman, L. Good semiconductor band gaps with a modified local-density approximation. *Phys. Rev. B* **41**, 7868–7871 (11 Apr. 1990).
70. Perdew, J. P., Burke, K. & Ernzerhof, M. Generalized Gradient Approximation Made Simple. *Phys. Rev. Lett.* **77**, 3865–3868 (18 Oct. 1996).
71. Barnes, S. E. New method for the Anderson model. II. The $U=0$ limit. *Journal of Physics F: Metal Physics* **7**, 2637–2647 (Dec. 1977).
72. Kotliar, G. & Ruckenstein, A. E. New Functional Integral Approach to Strongly Correlated Fermi Systems: The Gutzwiller Approximation as a Saddle Point. *Phys. Rev. Lett.* **57**, 1362–1365 (11 Sept. 1986).
73. Frésard, R. & Wölfle, P. Unified slave boson representation of spin and charge degrees of freedom for strongly correlated Fermi systems. *International Journal of Modern Physics B* **6**, 685–704 (1992).
74. Lechermann, F., Georges, A., Kotliar, G. & Parcollet, O. Rotationally invariant slave-boson formalism and momentum dependence of the quasiparticle weight. *Phys. Rev. B* **76**, 155102 (15 Oct. 2007).
75. Metzner, W. & Vollhardt, D. Analytic calculation of ground-state properties of correlated fermions with the Gutzwiller wave function. *Phys. Rev. B* **37**, 7382–7399 (13 May 1988).
76. Caffarel, M. & Krauth, W. Exact diagonalization approach to correlated fermions in infinite dimensions: Mott transition and superconductivity. *Phys. Rev. Lett.* **72**, 1545–1548 (10 Mar. 1994).
77. White, S. R. Density matrix formulation for quantum renormalization groups. *Phys. Rev. Lett.* **69**, 2863–2866 (19 Nov. 1992).
78. Becca, F. & Sorella, S. *Quantum Monte Carlo approaches for correlated systems* (Cambridge University Press, 2017).
79. Sénéchal, D., Perez, D. & Pioro-Ladrière, M. Spectral Weight of the Hubbard Model through Cluster Perturbation Theory. *Phys. Rev. Lett.* **84**, 522–525 (3 Jan. 2000).

BIBLIOGRAPHY

80. Sénéchal, D., Perez, D. & Plouffe, D. Cluster perturbation theory for Hubbard models. *Phys. Rev. B* **66**, 075129 (7 Aug. 2002).
81. Kotliar, G. *et al.* Electronic structure calculations with dynamical mean-field theory. *Rev. Mod. Phys.* **78**, 865–951 (3 Aug. 2006).
82. Kent, P. R. & Kotliar, G. Toward a predictive theory of correlated materials. *Science* **361**, 348–354 (2018).
83. Paul, A. & Birol, T. Applications of DFT+ DMFT in materials science. *Annual Review of Materials Research* **49**, 31–52 (2019).
84. Brooks, M. Electronic structure of NaCl-type compounds of the light actinides. I. UN, UC, and UO. *Journal of Physics F: Metal Physics* **14**, 639 (1984).
85. Keller, O. Chemistry of the heavy actinides and light transactinides. *Radiochimica Acta* **37**, 169–180 (1984).
86. Clark, D. L. The chemical complexities of plutonium. *Los Alamos Science* **26**, 364–381 (2000).
87. Hewson, A. C. *The Kondo problem to heavy fermions* (Cambridge University Press, 1997).
88. Fulde, P., Thalmeier, P. & Zwicknagl, G. Strongly correlated electrons. *arXiv preprint cond-mat/0607165* (2006).
89. Sumiyama, A. *et al.* Coherent Kondo State in a Dense Kondo Substance: $\text{Ce}_x\text{La}_{1-x}\text{Cu}_6$. *Journal of the Physical Society of Japan* **55**, 1294–1304 (1986).
90. Michishita, Y., Yoshida, T. & Peters, R. Relationship between exceptional points and the Kondo effect in *f*-electron materials. *Phys. Rev. B* **101**, 085122 (8 Feb. 2020).
91. Meissner, W. & Voigt, B. Messungen mit Hilfe von flüssigem Helium XI Widerstand der reinen Metalle in tiefen Temperaturen. *Annalen der Physik* **399**, 892–936 (1930).
92. Yamada, K. *Electron correlation in metals* (Cambridge University Press, 2010).
93. Anderson, P. W. & Yuval, G. Exact Results in the Kondo Problem: Equivalence to a Classical One-Dimensional Coulomb Gas. *Phys. Rev. Lett.* **23**, 89–92 (2 July 1969).
94. Anderson, P. A poor man's derivation of scaling laws for the Kondo problem. *Journal of Physics C: Solid State Physics* **3**, 2436 (1970).
95. Anderson, P. W., Yuval, G. & Hamann, D. R. Exact Results in the Kondo Problem. II. Scaling Theory, Qualitatively Correct Solution, and Some New Results on One-Dimensional Classical Statistical Models. *Phys. Rev. B* **1**, 4464–4473 (11 June 1970).

96. Wilson, K. G. The renormalization group: Critical phenomena and the Kondo problem. *Rev. Mod. Phys.* **47**, 773–840 (4 Oct. 1975).
97. Nozieres, P. A “Fermi-liquid” description of the Kondo problem at low temperatures. *Journal of low temperature physics* **17**, 31–42 (1974).
98. Nozières, P. *Impuretés magnétiques et effet Kondo* in *Annales de physique* **10** (1985), 19–35.
99. Ragel, F., du Plessis, P. d. V. & Strydom, A. Effects of La dilution on the CePt₂Si₂ Kondo lattice. *J. Phys.: Condens. Matter* **20**, 055218 (2008).
100. Hodovanets, H. *et al.* Remarkably Robust and Correlated Coherence and Antiferromagnetism in (Ce_{1-x}La_x)Cu₂Ge₂. *Phys. Rev. Lett.* **114**, 236601 (23 June 2015).
101. Pikul, A. P. *et al.* Single-Ion Kondo Scaling of the Coherent Fermi Liquid Regime in Ce_{1-x}La_xNi₂Ge₂. *Phys. Rev. Lett.* **108**, 066405 (6 Feb. 2012).
102. Andrei, N. Diagonalization of the Kondo Hamiltonian. *Phys. Rev. Lett.* **45**, 379–382 (5 Aug. 1980).
103. Filyov, V. & Wiegmann, P. A method for solving the kondo problem. *Physics Letters A* **76**, 283–286 (1980).
104. Doniach, S. The Kondo lattice and weak antiferromagnetism. *physica B+C* **91**, 231–234 (1977).
105. Lacroix, C. & Cyrot, M. Phase diagram of the Kondo lattice. *Phys. Rev. B* **20**, 1969 (1979).
106. Fazekas, P. & Müller-Hartmann, E. Magnetic and non-magnetic ground states of the Kondo lattice. *Z. Phys. B Condens. Matter* **85**, 285–300 (1991).
107. Tsunetsugu, H., Sigrist, M. & Ueda, K. Phase diagram of the one-dimensional Kondo-lattice model. *Phys. Rev. B* **47**, 8345–8348 (13 Apr. 1993).
108. Tsunetsugu, H., Sigrist, M. & Ueda, K. The ground-state phase diagram of the one-dimensional Kondo lattice model. *Rev. Mod. Phys.* **69**, 809–864 (3 July 1997).
109. Bernhard, B. & Lacroix, C. Coexistence of magnetic order and Kondo effect in the Kondo-Heisenberg model. *Phys. Rev. B* **92**, 094401 (2015).
110. Asadzadeh, M. Z., Becca, F. & Fabrizio, M. Variational Monte Carlo approach to the two-dimensional Kondo lattice model. *Phys. Rev. B* **87**, 205144 (20 May 2013).
111. Peters, R. & Kawakami, N. Competition of striped magnetic order and partial Kondo screened state in the Kondo lattice model. *Phys. Rev. B* **96**, 115158 (11 Sept. 2017).

BIBLIOGRAPHY

112. Si, Q., Rabello, S., Ingersent, K. & Smith, J. L. Locally critical quantum phase transitions in strongly correlated metals. *Nature* **413**, 804–808 (2001).
113. Burdin, S., Grepel, D. R. & Georges, A. Heavy-fermion and spin-liquid behavior in a Kondo lattice with magnetic frustration. *Phys. Rev. B* **66**, 045111 (4 July 2002).
114. Burdin, S., Grilli, M. & Grepel, D. Large-N analysis of the local quantum critical point and the spin-liquid phase. *Phys. Rev. B* **67**, 121104 (12 Mar. 2003).
115. Paul, I., Pépin, C. & Norman, M. R. Kondo Breakdown and Hybridization Fluctuations in the Kondo-Heisenberg Lattice. *Phys. Rev. Lett.* **98**, 026402 (2 Jan. 2007).
116. Pépin, C. Selective Mott transition and heavy fermions. *Phys. Rev. B* **77**, 245129 (24 June 2008).
117. Pépin, C. Kondo Breakdown as a Selective Mott Transition in the Anderson Lattice. *Phys. Rev. Lett.* **98**, 206401 (20 May 2007).
118. Süllo, S., Aronson, M., Rainford, B. & Haen, P. Doniach phase diagram, revisited: From ferromagnet to Fermi liquid in pressurized CeRu₂Ge₂. *Phys. Rev. Lett.* **82**, 2963–2966 (14 Apr. 1999).
119. Aoki, H., Kimura, N. & Terashima, T. Fermi surface properties, metamagnetic transition and quantum phase transition of CeRu₂Si₂ and its alloys probed by the dHvA effect. *J. Phys. Soc. Jpn.* **83**, 072001 (2014).
120. Custers, J. *et al.* The break-up of heavy electrons at a quantum critical point. *Nature* **424**, 524–527 (2003).
121. Schröder, A. *et al.* Onset of antiferromagnetism in heavy-fermion metals. *Nature* **407**, 351–355 (2000).
122. Löhneysen, H. v. *et al.* Non-Fermi-liquid behavior in a heavy-fermion alloy at a magnetic instability. *Phys. Rev. Lett.* **72**, 3262 (1994).
123. Nozières, P. Some comments on Kondo lattices and the Mott transition. *The European Physical Journal B-Condensed Matter and Complex Systems* **6**, 447–457 (1998).
124. Joyce, J. J. *et al.* Temperature-invariant photoelectron spectra in cerium heavy-fermion compounds: Inconsistencies with the Kondo model. *Phys. Rev. Lett.* **68**, 236–239 (2 Jan. 1992).
125. Lacroix, C. Coherence effects in the Kondo lattice. *J. Magn. Magn. Mater.* **60**, 145–152 (1986).
126. Burdin, S., Georges, A. & Grepel, D. R. Coherence Scale of the Kondo Lattice. *Phys. Rev. Lett.* **85**, 1048–1051 (5 July 2000).

127. Coqblin, B., Lacroix, C., Gusmão, M. A. & Iglesias, J. R. Band-filling effects on Kondo-lattice properties. *Phys. Rev. B* **67**, 064417 (6 Feb. 2003).
128. Pruschke, T., Bulla, R. & Jarrell, M. Low-energy scale of the periodic Anderson model. *Phys. Rev. B* **61**, 12799–12809 (19 May 2000).
129. Tahvildar-Zadeh, A. N., Jarrell, M., Pruschke, T. & Freericks, J. K. Evidence for exhaustion in the conductivity of the infinite-dimensional periodic Anderson model. *Phys. Rev. B* **60**, 10782–10787 (15 Oct. 1999).
130. Madhavan, V., Chen, W., Jamneala, T., Crommie, M. & Wingreen, N. Tunneling into a single magnetic atom: spectroscopic evidence of the Kondo resonance. *Science* **280**, 567–569 (1998).
131. Liang, W., Shores, M. P., Bockrath, M., Long, J. R. & Park, H. Kondo resonance in a single-molecule transistor. *Nature* **417**, 725–729 (2002).
132. Kouwenhoven, L. & Glazman, L. Revival of the Kondo effect. *Physics world* **14**, 33 (2001).
133. Lacroix, C. Some exact results for the Kondo lattice with infinite exchange interaction. *Solid State Communications* **54**, 991–994 (1985).
134. Luttinger, J. M. Fermi Surface and Some Simple Equilibrium Properties of a System of Interacting Fermions. *Phys. Rev.* **119**, 1153–1163 (4 Aug. 1960).
135. Kummer, K. *et al.* Temperature-Independent Fermi Surface in the Kondo Lattice YbRh₂Si₂. *Phys. Rev. X* **5**, 011028 (1 Mar. 2015).
136. Burdin, S. & Lacroix, C. Lifshitz transition in Kondo alloys. *Phys. Rev. Lett.* **110**, 226403 (22 May 2013).
137. Da Silva Jr, J. L. F. *Theory of lanthanide systems: valence transitions and interplay of Kondo effect and disorder* PhD thesis (Université Grenoble Alpes, 2016).
138. Burdin, S. & Lacroix, C. Breakdown of coherence in Kondo alloys: crucial role of concentration vs band filling. *J. Phys.: Condens. Matter* **31**, 395601 (July 2019).
139. Dobrosavljević, V. & Kotliar, G. Hubbard models with random hopping in $d=\infty$. *Phys. Rev. Lett.* **71**, 3218–3221 (19 Nov. 1993).
140. Dobrosavljević, V. & Kotliar, G. Mean Field Theory of the Mott-Anderson Transition. *Phys. Rev. Lett.* **78**, 3943–3946 (20 May 1997).
141. Burdin, S. & Fulde, P. Random Kondo alloys investigated with the coherent potential approximation. *Phys. Rev. B* **76**, 104425 (10 Sept. 2007).
142. Shannon, R. D. Revised effective ionic radii and systematic studies of interatomic distances in halides and chalcogenides. *Acta crystallographica section A: crystal physics, diffraction, theoretical and general crystallography* **32**, 751–767 (1976).

BIBLIOGRAPHY

143. De Andrade, M. C. *et al.* Evidence for a Common Physical Description of Non-Fermi-Liquid Behavior in Chemically Substituted f -Electron Systems. *Phys. Rev. Lett.* **81**, 5620–5623 (25 Dec. 1998).
144. Knopp, G. *et al.* Magnetic order in a Kondo lattice: a neutron scattering study of CeCu_2Ge_2 . *Z. Phys. B Condens. Matter* **77**, 95–104 (1989).
145. Kaul, R. K. & Vojta, M. Strongly inhomogeneous phases and non-Fermi-liquid behavior in randomly depleted Kondo lattices. *Phys. Rev. B* **75**, 132407 (13 Apr. 2007).
146. Watanabe, H. & Ogata, M. *Ground state properties of randomly-doped Kondo lattice model* in *Journal of Physics: Conference Series* **200** (Jan. 2010), 012221.
147. Watanabe, H. & Ogata, M. Crossover from dilute-Kondo system to heavy-fermion system. *Phys. Rev. B* **81**, 113111 (11 Mar. 2010).
148. Otsuki, J., Kusunose, H. & Kuramoto, Y. Effect of disorder on Fermi surface in heavy electron systems. *Journal of the Physical Society of Japan* **79**, 114709 (2010).
149. Grenzebach, C., Anders, F. B., Czycholl, G. & Pruschke, T. Influence of disorder on the transport properties of heavy-fermion systems. *Phys. Rev. B* **77**, 115125 (11 Mar. 2008).
150. Vidhyadhiraja, N. S. & Kumar, P. Non-Fermi-liquid behavior from dynamical effects of impurity scattering in correlated Fermi liquids. *Phys. Rev. B* **88**, 195120 (19 Nov. 2013).
151. Kumar, P. & Vidhyadhiraja, N. S. Kondo-hole substitution in heavy fermions: Dynamics and transport. *Phys. Rev. B* **90**, 235133 (23 Dec. 2014).
152. Dagotto, E. Correlated electrons in high-temperature superconductors. *Rev. Mod. Phys.* **66**, 763–840 (3 July 1994).
153. Vojta, T., Vojta, T., Epperlein, F. & Schreiber, M. Quantum Coulomb Glass: Anderson localization in an interacting system. *physica status solidi (b)* **205**, 53–59 (1998).
154. White, S. R. Strongly correlated electron systems and the density matrix renormalization group. *Physics Reports* **301**, 187–204 (1998).
155. Farhoodfar, A., Chen, X., Gooding, R. J. & Atkinson, W. A. Real-space variational Gutzwiller wave functions for the Anderson-Hubbard model. *Phys. Rev. B* **80**, 045108 (4 July 2009).
156. Von der Linden, W. A quantum Monte Carlo approach to many-body physics. *Physics Reports* **220**, 53–162 (1992).
157. Schreiber, M. & Vojta, T. The Hartree-Fock based diagonalization—an efficient algorithm for the treatment of interacting electrons in disordered solids. *Mathematics and Computers in Simulation* **62**, 243–254 (2003).

158. Coleman, P. Heavy fermions: Electrons at the edge of magnetism. *arXiv preprint cond-mat/0612006* (2006).
159. Metzner, W. & Vollhardt, D. Correlated lattice fermions in $d=\infty$ dimensions. *Phys. Rev. Lett.* **62**, 324 (1989).
160. Georges, A. & Kotliar, G. Hubbard model in infinite dimensions. *Phys. Rev. B* **45**, 6479–6483 (12 Mar. 1992).
161. Park, H., Haule, K. & Kotliar, G. Cluster Dynamical Mean Field Theory of the Mott Transition. *Phys. Rev. Lett.* **101**, 186403 (18 Oct. 2008).
162. Krien, F., van Loon, E. G. C. P., Katsnelson, M. I., Lichtenstein, A. I. & Capone, M. Two-particle Fermi liquid parameters at the Mott transition: Vertex divergences, Landau parameters, and incoherent response in dynamical mean-field theory. *Phys. Rev. B* **99**, 245128 (24 June 2019).
163. Byczuk, K., Hofstetter, W. & Vollhardt, D. Mott-Hubbard Transition versus Anderson Localization in Correlated Electron Systems with Disorder. *Phys. Rev. Lett.* **94**, 056404 (5 Feb. 2005).
164. Dobrosavljević, V. & Miranda, E. Absence of Conventional Quantum Phase Transitions in Itinerant Systems with Disorder. *Phys. Rev. Lett.* **94**, 187203 (18 May 2005).
165. Miranda, E. & Dobrosavljević, V. Localization-Induced Griffiths Phase of Disordered Anderson Lattices. *Phys. Rev. Lett.* **86**, 264–267 (2 Jan. 2001).
166. Aguiar, M. C. O., Miranda, E. & Dobrosavljević, V. Localization effects and inelastic scattering in disordered heavy electrons. *Phys. Rev. B* **68**, 125104 (12 Sept. 2003).
167. Poudel, B., Lacroix, C., Zwicky, G. & Burdin, S. Photo-emission signatures of coherence breakdown in Kondo alloys: dynamical mean-field theory approach. *New Journal of Physics* (2021).
168. Metzner, W. & Vollhardt, D. Correlated Lattice Fermions in $d = \infty$ Dimensions. *Phys. Rev. Lett.* **62**, 324–327 (3 Jan. 1989).
169. Rubtsov, A. N., Savkin, V. V. & Lichtenstein, A. I. Continuous-time quantum Monte Carlo method for fermions. *Phys. Rev. B* **72**, 035122 (3 July 2005).
170. Garcia, D. J., Hallberg, K. & Rozenberg, M. J. Dynamical Mean Field Theory with the Density Matrix Renormalization Group. *Phys. Rev. Lett.* **93**, 246403 (24 Dec. 2004).
171. Schollwöck, U. The density-matrix renormalization group. *Reviews of modern physics* **77**, 259 (2005).
172. Hettler, M. H., Mukherjee, M., Jarrell, M. & Krishnamurthy, H. R. Dynamical cluster approximation: Nonlocal dynamics of correlated electron systems. *Phys. Rev. B* **61**, 12739–12756 (19 May 2000).

BIBLIOGRAPHY

173. Bulla, R., Costi, T. A. & Pruschke, T. Numerical renormalization group method for quantum impurity systems. *Rev. Mod. Phys.* **80**, 395–450 (2 Apr. 2008).
174. Maier, T., Jarrell, M., Pruschke, T. & Keller, J. A non-crossing approximation for the study of intersite correlations. *The European Physical Journal B-Condensed Matter and Complex Systems* **13**, 613–624 (2000).
175. Coleman, P. $\frac{1}{N}$ expansion for the Kondo lattice. *Phys. Rev. B* **28**, 5255–5262 (9 Nov. 1983).
176. Read, N., Newns, D. & Doniach, S. Stability of the Kondo lattice in the large- N limit. *Phys. Rev. B* **30**, 3841 (1984).
177. Pavarini, E., Coleman, P. & Koch, E. *Many-Body Physics: From Kondo to Hubbard* tech. rep. (Theoretische Nanoelektronik, 2015).
178. Pfleiderer, C. Superconducting phases of f -electron compounds. *Rev. Mod. Phys.* **81**, 1551–1624 (4 Nov. 2009).
179. Thalmeier, P. & Zwicknagl, G. Unconventional superconductivity and magnetism in lanthanide and actinide intermetallic compounds. *Handbook on the physics and chemistry of rare earths* **34**, 135 (2004).
180. Wu, Z. *et al.* Revealing the Heavy Quasiparticles in the Heavy-Fermion Superconductor CeCu_2Si_2 . *Phys. Rev. Lett.* **127**, 067002 (6 Aug. 2021).
181. Nakatsuji, S. *et al.* Metallic Spin-Liquid Behavior of the Geometrically Frustrated Kondo Lattice $\text{Pr}_2\text{Ir}_2\text{O}_7$. *Phys. Rev. Lett.* **96**, 087204 (8 Mar. 2006).
182. Felten, R., Weber, G. & Rietschel, H. Specific heats and crystal-field splittings of CeCu_2Ge_2 , CeRu_2Ge_2 and UBe_{13} . *Journal of magnetism and magnetic materials* **63**, 383–385 (1987).
183. de Boer, F. *et al.* CeCu_2Ge_2 : Magnetic order in a Kondo lattice. *Journal of Magnetism and Magnetic Materials* **63-64**, 91–94 (1987).
184. Link, P. & Jaccard, D. Pressure induced heavy-fermion behaviour of CeAu_2Si_2 near 17 GPa. *Physica B: Condensed Matter* **230**, 31–34 (1997).
185. Chevalier, B. *et al.* Hydrogenation inducing antiferromagnetism in the heavy-fermion ternary silicide CeRuSi . *Phys. Rev. B* **77**, 014414 (1 Jan. 2008).
186. Araki, S., Nakashima, M., Settai, R., Kobayashi, T. C. & Onuki, Y. Pressure-induced superconductivity in an antiferromagnet CeRh_2Si_2 . *Journal of Physics: Condensed Matter* **14**, L377 (2002).
187. Nakano, T., Ohashi, M., Oomi, G., Matsubayashi, K. & Uwatoko, Y. Pressure-induced superconductivity in the orthorhombic Kondo compound CePtSi_2 . *Phys. Rev. B* **79**, 172507 (17 May 2009).
188. Hegger, H. *et al.* Pressure-Induced Superconductivity in Quasi-2D CeRhIn_5 . *Phys. Rev. Lett.* **84**, 4986–4989 (21 May 2000).

189. Nakashima, M. *et al.* High-pressure effect on the electronic state in CeNiGe₃: Pressure-induced superconductivity. *Journal of Physics: Condensed Matter* **16**, L255 (2004).
190. Manago, M., Kotegawa, H., Tou, H., Harima, H. & Tanida, H. Unusual Non-magnetic Ordered State in CeCoSi Revealed by ⁵⁹Co-NMR and NQR Measurements. *Journal of the Physical Society of Japan* **90**, 023702 (2021).
191. Hong, S., Mun, E., Takeda, N., Ishikawa, M. & Kwon, Y. Non-Fermi-liquid behavior in CeNiGe_{2-x}Si_x single crystals. *Physica B: Condensed Matter* **329**, 518–519 (2003).
192. Hong, S., Mun, E. & Kwon, Y. Transport and magnetic properties of CeNiGe_{2-x}Si_x single crystals. *Physica B: Condensed Matter* **329**, 514–515 (2003).
193. Pandey, S., Siruguri, V. & Rawat, R. Quantum critical point and intermediate valence fluctuations in CeRu_{2-x}Co_xGe₂. *Phys. Rev. B* **98**, 155129 (15 Oct. 2018).
194. Ikeda, Y., Ito, Y., Araki, S., Kobayashi, T. C. & Yoshizawa, H. Resistance Anomalies Accompanying Crossover from Heavy-Fermion Regime to Intermediate-Valence Regime: A Study of Cu–Ni Substitution and Pressure Effects on CeCu₂Si₂. *Journal of the Physical Society of Japan* **84**, 024702 (2015).
195. Ōnuki, Y. & Komatsubara, T. in *Anomalous Rare Earths and Actinides* 281–288 (Elsevier, 1987).
196. Chen, Q. *et al.* Spin glass, single-ion and dense effects in La_{1-x}Ce_xFePO. *EPL (Europhysics Letters)* **123**, 57002 (2018).
197. Polyakov, A. *et al.* Fermi-surface evolution in Yb-substituted CeCoIn₅. *Phys. Rev. B* **85**, 245119 (24 June 2012).
198. Helm, T. *et al.* Magnetic Breakdown in the Electron-Doped Cuprate Superconductor Nd_{2-x}Ce_xCuO₄: The Reconstructed Fermi Surface Survives in the Strongly Overdoped Regime. *Phys. Rev. Lett.* **105**, 247002 (24 Dec. 2010).
199. Ragel, F. C., du Plessis, P. d. V. & Strydom, A. Dilution and non-Fermi-liquid effects in the CePtIn Kondo lattice. *Journal of Physics: Condensed Matter* **21**, 046008 (2009).
200. Killer, U. *et al.* Unusual Single-Ion Non-Fermi-Liquid Behavior in Ce_{1-x}La_xNi₉Ge₄. *Phys. Rev. Lett.* **93**, 216404 (21 Nov. 2004).
201. Scheidt, E.-W. *et al.* Crossover from single ion to coherent non-Fermi liquid behavior in Ce_{1-x}La_xNi₉Ge₄. *Physica B: Condensed Matter* **359**, 254–256 (2005).
202. Assaad, F. Quantum Monte Carlo simulations of the half-filled two-dimensional Kondo lattice model. *Phys. Rev. Lett.* **83**, 796 (1999).
203. Peters, R. & Pruschke, T. Magnetic phases in the correlated Kondo-lattice model. *Phys. Rev. B* **76**, 245101 (2007).

BIBLIOGRAPHY

204. Shibata, N. & Ueda, K. The one-dimensional Kondo lattice model studied by the density matrix renormalization group method. *J. Phys.: Condens. Matter* **11**, R1 (1999).
205. McCulloch, I. P., Juozapavicius, A., Rosengren, A. & Gulacsi, M. Localized spin ordering in Kondo lattice models. *Phys. Rev. B* **65**, 052410 (5 Jan. 2002).
206. Peters, R. & Kawakami, N. Ferromagnetic state in the one-dimensional Kondo lattice model. *Phys. Rev. B* **86**, 165107 (2012).
207. Honner, G. & Gulácsi, M. One-Dimensional Kondo Lattice at Partial Band Filling. *Phys. Rev. Lett.* **78**, 2180–2183 (11 Mar. 1997).
208. Peters, R., Hoshino, S., Kawakami, N., Otsuki, J. & Kuramoto, Y. Charge order in Kondo lattice systems. *Phys. Rev. B* **87**, 165133 (16 Apr. 2013).
209. Peters, R., Kawakami, N. & Pruschke, T. *Dynamical Mean Field Study of the Kondo Lattice Model with Frustration* in *Journal of Physics: Conference Series* **320** (2011), 012057.
210. Misawa, T., Yoshitake, J. & Motome, Y. Charge Order in a Two-Dimensional Kondo Lattice Model. *Phys. Rev. Lett.* **110**, 246401 (24 June 2013).
211. Martin, L. C. & Assaad, F. F. Evolution of the Fermi Surface across a Magnetic Order-Disorder Transition in the Two-Dimensional Kondo Lattice Model: A Dynamical Cluster Approach. *Phys. Rev. Lett.* **101**, 066404 (6 Aug. 2008).
212. Liu, Y., Zhang, G.-M. & Yu, L. Weak ferromagnetism with the Kondo screening effect in the Kondo lattice systems. *Phys. Rev. B* **87**, 134409 (13 Apr. 2013).
213. Costa, N. d. C., Lima, J. & dos Santos, R. R. Spiral magnetic phases on the Kondo Lattice Model: A Hartree–Fock approach. *Journal of Magnetism and Magnetic Materials* **423**, 74–83 (2017).
214. Coqblin, B. *et al.* Effect of conduction band filling on the competition Kondo-magnetism in the Kondo lattice. *Physica B: Condensed Matter* **281-282**, 50–52 (2000).
215. Jarrell, M. Symmetric periodic Anderson model in infinite dimensions. *Phys. Rev. B* **51**, 7429–7440 (12 Mar. 1995).
216. Tahvildar-Zadeh, A. N., Jarrell, M. & Freericks, J. K. Protracted screening in the periodic Anderson model. *Phys. Rev. B* **55**, R3332–R3335 (6 Feb. 1997).
217. Tahvildar-Zadeh, A. N., Jarrell, M. & Freericks, J. K. Low-Temperature Coherence in the Periodic Anderson Model: Predictions for Photoemission of Heavy Fermions. *Phys. Rev. Lett.* **80**, 5168–5171 (23 June 1998).
218. Zhang, G.-M. & Yu, L. Kondo singlet state coexisting with antiferromagnetic long-range order: A possible ground state for Kondo insulators. *Phys. Rev. B* **62**, 76–79 (1 July 2000).

219. Jurecka, C. & Brenig, W. Bond-operator mean-field theory of the half-filled Kondo lattice model. *Phys. Rev. B* **64**, 092406 (9 Aug. 2001).
220. Besnus, M., Braghta, A. & Meyer, A. Kondo behaviour in magnetic (Ce-La)Pd₂Si₂. *Z. Phys. B Condens. Matter* **83**, 207–211 (1991).
221. Parks, R. D., Reihl, B., Mårtensson, N. & Steglich, F. Resonant photoemission studies of the Kondo-lattice systems CeCu₂Si₂, CeAg₂Si₂, CeAu₂Si₂, and CePd₂Si₂. *Phys. Rev. B* **27**, 6052–6057 (10 May 1983).
222. Kirchner, Stefan and Paschen, Silke and Chen, Qiuyun and Wirth, Steffen and Feng, Donglai and Thompson, Joe D. and Si, Qimiao. Colloquium: Heavy-electron quantum criticality and single-particle spectroscopy. *Rev. Mod. Phys.* **92**, 011002 (1 Mar. 2020).
223. Denlinger, J. D. *et al.* Comparative study of the electronic structure of XRu₂Si₂: probing the Anderson lattice. *J. Electron Spectros. Relat. Phenomena* **117**, 347–369 (2001).
224. Okane, T. *et al.* 4*f*-Derived Fermi Surfaces of CeRu₂(Si_{1-x}Ge_x)₂ near the Quantum Critical Point: Resonant Soft-X-Ray ARPES Study. *Phys. Rev. Lett.* **102**, 216401 (21 May 2009).
225. Yano, M. *et al.* Electronic structure of CeRu₂X₂ (X = Si, Ge) in the paramagnetic phase studied by soft x-ray ARPES and hard x-ray photoelectron spectroscopy. *Phys. Rev. B* **77**, 035118 (3 Jan. 2008).
226. Yano, M. *et al.* Three-Dimensional Bulk Fermiology of CeRu₂Ge₂ in the Paramagnetic Phase by Soft X-Ray *hν*-Dependent (700–860 eV) ARPES. *Phys. Rev. Lett.* **98**, 036405 (3 Jan. 2007).
227. Li, P. *et al.* Large Fermi surface expansion through anisotropic mixing of conduction and *f* electrons in the semimetallic Kondo lattice CeBi. *Phys. Rev. B* **100**, 155110 (15 Oct. 2019).
228. Bareille, C. *et al.* Strongly anisotropic high-temperature Fermi surface of the Kondo semimetal CeNiSn revealed by angle-resolved photoemission spectroscopy. *Phys. Rev. B* **100**, 045133 (4 July 2019).
229. Danzenbächer, S. *et al.* Insight into the *f*-Derived Fermi Surface of the Heavy-Fermion Compound YbRh₂Si₂. *Phys. Rev. Lett.* **107**, 267601 (26 Dec. 2011).
230. Güttler, M. *et al.* Divalent EuRh₂Si₂ as a reference for the Luttinger theorem and antiferromagnetism in trivalent heavy-fermion YbRh₂Si₂. *Nature communications* **10**, 1–7 (2019).
231. Nakatani, Y. *et al.* Evidence for momentum-dependent heavy-fermionic electronic structures: Soft x-ray ARPES for the superconductor CeNi₂Ge₂ in the normal state. *Phys. Rev. B* **97**, 115160 (11 Mar. 2018).

BIBLIOGRAPHY

232. Malterre, D., Grioni, M. & Baer, Y. Recent developments in high-energy spectroscopies of Kondo systems. *Advances in Physics* **45**, 299–348 (1996).
233. Joyce, J. *et al.* Photoemission from YbInCu₄: testing the single impurity model. *Philos. Mag. B* **79**, 1–8 (1999).
234. Im, H. J. *et al.* Direct Observation of Dispersive Kondo Resonance Peaks in a Heavy-Fermion System. *Phys. Rev. Lett.* **100**, 176402 (17 Apr. 2008).
235. Okane, T. *et al.* Resonant Angle-Resolved Photoelectron Spectroscopy of Substitutional Solid Solutions of CeRu₂Si₂. *Journal of the Physical Society of Japan* **80**, SA060 (2011).
236. Patil, S. *et al.* ARPES view on surface and bulk hybridization phenomena in the antiferromagnetic Kondo lattice CeRh₂Si₂. *Nature communications* **7**, 1–8 (2016).
237. Zwicknagl, G. Kondo effect and antiferromagnetism in CeCu₂Ge₂: An electronic structure study. *Journal of Low Temperature Physics* **147**, 123–134 (2007).
238. Zwicknagl, G., Yaresko, A. & Fulde, P. Fermi surface and heavy masses for UPd₂Al₃. *Physical Review B* **68**, 052508 (2003).
239. Shim, J., Haule, K. & Kotliar, G. Modeling the localized-to-itinerant electronic transition in the heavy fermion system CeIrIn₅. *Science* **318**, 1615–1617 (2007).
240. Choi, H. C., Min, B. I., Shim, J. H., Haule, K. & Kotliar, G. Temperature-Dependent Fermi Surface Evolution in Heavy Fermion CeIrIn₅. *Phys. Rev. Lett.* **108**, 016402 (1 Jan. 2012).
241. Klein, M. *et al.* Coherent Heavy Quasiparticles in a CePt₅ Surface Alloy. *Phys. Rev. Lett.* **106**, 186407 (18 May 2011).
242. Choi, H. C., Haule, K., Kotliar, G., Min, B. I. & Shim, J. H. Observation of a kink during the formation of the Kondo resonance band in a heavy-fermion system. *Phys. Rev. B* **88**, 125111 (12 Sept. 2013).
243. Hirsch, J. E. Strong-coupling expansion for a Kondo-lattice model. *Phys. Rev. B* **30**, 5383–5385 (9 Nov. 1984).
244. Bastide, C. & Lacroix, C. d-Wave superconductivity in the strong-coupling Kondo lattice model. *EPL (Europhysics Letters)* **4**, 935 (1987).
245. Sigrist, M., Tsunetsugu, H., Ueda, K. & Rice, T. M. Ferromagnetism in the strong-coupling regime of the one-dimensional Kondo-lattice model. *Phys. Rev. B* **46**, 13838–13846 (21 Dec. 1992).
246. Montiel, X., Burdin, S., Pépin, C. & Ferraz, A. Modulated spin-liquid and magnetic order from a Kondo-Heisenberg model applied to URu₂Si₂. *Phys. Rev. B* **90**, 045125 (4 July 2014).

247. Poudel, B., Zwicky, G., Lacroix, C. & Burdin, S. Phase diagrams of Kondo alloys. *J. Magn. Magn. Mater.* **520**, Magnetic materials and their applications: in Memory of Dominique Givord, 167405 (2021).
248. Miranda, E. & Dobrosavljević, V. Disorder-driven non-Fermi liquid behaviour of correlated electrons. *Reports on Progress in Physics* **68**, 2337–2408 (Aug. 2005).
249. Wigner, E. On the Interaction of Electrons in Metals. *Phys. Rev.* **46**, 1002–1011 (11 Dec. 1934).
250. Zwicky, G. Strongly correlated 5 f electrons: spectral functions and mean-field ground states. *Journal of the Physical Society of Japan* **75**, 226–231 (2006).
251. Rao, C., Arulraj, A., Santosh, P. & Cheetham, A. Charge-ordering in manganates. *Chemistry of materials* **10**, 2714–2722 (1998).
252. Rao, C., Arulraj, A., Cheetham, A. & Raveau, B. Charge ordering in the rare earth manganates: the experimental situation. *Journal of Physics: Condensed Matter* **12**, R83 (2000).
253. Van Den Brink, J. & Khomskii, D. I. Multiferroicity due to charge ordering. *Journal of Physics: Condensed Matter* **20**, 434217 (2008).
254. Kohgi, M. *et al.* Charge order and one-dimensional properties of Yb₄As₃. *Physica B: Condensed Matter* **230**, 638–640 (1997).
255. Schmidt, B. *et al.* Low-energy excitations of the semimetallic one-dimensional S = 1/2 antiferromagnet Yb₄As₃. *Physica B: Condensed Matter* **300**, 121–138 (2001).
256. Kotliar, G., Savrasov, S. Y., Pálsson, G. & Biroli, G. Cellular Dynamical Mean Field Approach to Strongly Correlated Systems. *Phys. Rev. Lett.* **87**, 186401 (18 Oct. 2001).
257. Butler, W. H. Theory of electronic transport in random alloys: Korringa-Kohn-Rostoker coherent-potential approximation. *Phys. Rev. B* **31**, 3260–3277 (6 Mar. 1985).
258. Niizeki, K. & Endo, M. CPA conductivity of a binary alloy with off-diagonal disorder. *Solid State Communications* **14**, 687–690 (1974).
259. Banhart, J. Optical Conductivity of Disordered Alloys Calculated from First Principles. *Phys. Rev. Lett.* **82**, 2139–2142 (10 Mar. 1999).
260. Taranko, E., Taranko, R., Wysokiński, K. & Piłat, M. Optical conductivity of substitutionally disordered alloys: Intraband transitions. *Zeitschrift für Physik B Condensed Matter* **39**, 187–192 (1980).
261. Saha, K. K. & Mookerjee, A. Optical properties of random alloys: application to CuAu and NiPt. *Journal of Physics: Condensed Matter* **17**, 4559 (2005).

BIBLIOGRAPHY

262. Wysokiński, K. I. Spectral and transport properties of strongly correlated disordered systems. *Phys. Rev. B* **60**, 16376–16381 (24 Dec. 1999).
263. Hwang, M., Gonis, A. & Freeman, A. J. Transport properties of random and nonrandom substitutionally disordered alloys. I. Exact numerical calculation of the ac conductivity. *Phys. Rev. B* **35**, 8974–8984 (17 June 1987).
264. Hwang, M., Gonis, A. & Freeman, A. J. Transport properties of random and nonrandom substitutionally disordered alloys. II. New cluster formulation of the ac conductivity and numerical applications. *Phys. Rev. B* **35**, 8985–9003 (17 June 1987).
265. Mena, F. P., van der Marel, D. & Sarrao, J. L. Optical conductivity of CeMIn_5 ($M = \text{Co, Rh, Ir}$). *Phys. Rev. B* **72**, 045119 (4 July 2005).
266. Kimura, S. *et al.* Optical observation of non-Fermi-liquid behavior in the heavy fermion state of YbRh_2Si_2 . *Phys. Rev. B* **74**, 132408 (13 Oct. 2006).
267. Yoshida, T., Peters, R. & Kawakami, N. Non-Hermitian perspective of the band structure in heavy-fermion systems. *Phys. Rev. B* **98**, 035141 (3 July 2018).
268. Costa, N. *et al.* Coherence temperature in the diluted periodic Anderson model. *Physical Review B* **99**, 195116 (2019).
269. Koizumi, A. *et al.* *f* Electron Contribution to the Change of Electronic Structure in CeRu_2Si_2 with Temperature: A Compton Scattering Study. *Phys. Rev. Lett.* **106**, 136401 (13 Mar. 2011).
270. Güttler, M. *et al.* Visualizing the Kondo lattice crossover in YbRh_2Si_2 with Compton scattering. *Physical Review B* **103**, 115126 (2021).
271. Mydosh, J., Oppeneer, P. M. & Riseborough, P. Hidden order and beyond: An experimental—theoretical overview of the multifaceted behavior of URu_2Si_2 . *Journal of Physics: Condensed Matter* **32**, 143002 (2020).
272. Wills, J. M. & Eriksson, O. Actinide ground-state properties, theoretical predictions. *Los Alamos Science* **26**, 128 (2000).
273. Zwicknagl, G. & Reese, M. Dual nature of strongly correlated 5f electrons. *Journal of magnetism and magnetic materials* **310**, 201–206 (2007).
274. Curro, N. *et al.* Unconventional superconductivity in PuCoGa_5 . *Nature* **434**, 622–625 (2005).
275. Gofryk, K. *et al.* Kondo behavior in superconducting NpPd_5Al_2 . *Phys. Rev. B* **79**, 134525 (13 Apr. 2009).
276. Matsuda, T. D. *et al.* Anisotropic transport properties of NpPd_5Al_2 in *Journal of Physics: Conference Series* **200** (2010), 012113.
277. Bauer, E. D. *et al.* Structural Tuning of Unconventional Superconductivity in PuMGa_5 ($M = \text{Co, Rh}$). *Phys. Rev. Lett.* **93**, 147005 (14 Sept. 2004).

278. Griveau, J.-C., Rebizant, J., Haire, R., Kotliar, G. & Lander, G. Americium under pressure. *Journal of alloys and compounds* **444**, 84–87 (2007).
279. Boring, A. M. & Smith, J. L. Plutonium condensed-matter Physics. *Los Alamos Science* **26**, 90 (2000).
280. Hill, H. H. in *Nuclear Metallurgy 2* (Metallurgical Society AIME New York, 1970).
281. Ohkochi, T. *et al.* Observation of 5f electrons in the itinerant limit: Three-dimensional electronic structure of UB_2 . *Phys. Rev. B* **78**, 165110 (16 Oct. 2008).
282. Baer, Y., Ott, H. & Andres, K. 5f electron localization in metallic UPd_3 . *Solid State Communications* **36**, 387–391 (1980).
283. Andres, K. *et al.* Anomalous behavior in the low temperature properties of UPd_3 . *Solid State Communications* **28**, 405–408 (1978).
284. Taillefer, L. & Lonzarich, G. G. Heavy-fermion quasiparticles in UPt_3 . *Phys. Rev. Lett.* **60**, 1570–1573 (15 Apr. 1988).
285. Stewart, G., Fisk, Z., Willis, J. & Smith, J. in *Ten Years of Superconductivity: 1980–1990* 85–88 (Springer, 1984).
286. Taillefer, L., Flouquet, J. & Lonzarich, G. Normal and superconducting phases of heavy fermions. *Physica B: Condensed Matter* **169**, 257–270 (1991).
287. Fujimori, S.-i. *et al.* Electronic structure of heavy fermion uranium compounds studied by core-level photoelectron spectroscopy. *Journal of the Physical Society of Japan* **81**, 014703 (2011).
288. JW, A. The Kondo resonance in electron spectroscopy. *Journal of the Physical Society of Japan* **74**, 34–48 (2005).
289. White, R. M. & Fulde, P. Excitonic Mass Enhancement in Praseodymium. *Phys. Rev. Lett.* **47**, 1540–1542 (21 Nov. 1981).
290. Zwicknagl, G. The utility of band theory in strongly correlated electron systems. *Reports on Progress in Physics* **79**, 124501 (2016).
291. Zwicknagl, G., Yaresko, A. & Fulde, P. Fermi surface and heavy masses for UPd_2Al_3 . *Phys. Rev. B* **68**, 052508 (5 Aug. 2003).
292. Kimura, N. *et al.* Observation of a Main Fermi Surface in UPt_3 . *Journal of the Physical Society of Japan* **67**, 2185–2188 (1998).
293. Inada, Y. *et al.* Fermi surface and de Haas-van Alphen oscillation in both the normal and superconducting mixed states of UPd_2Al_3 . *Journal of the Physical Society of Japan* **68**, 3643–3654 (1999).
294. Grachtrup, D. S. *et al.* Magnetic phase diagram and electronic structure of UPt_2Si_2 at high magnetic fields: A possible field-induced Lifshitz transition. *Phys. Rev. B* **95**, 134422 (13 Apr. 2017).

BIBLIOGRAPHY

295. Takahashi, T. *et al.* Dual character of 5f electrons in UPd₂Al₃ observed by high-resolution photoemission spectroscopy. *Journal of the physical society of japan* **65**, 156–159 (1996).
296. Aoki, D. & Flouquet, J. Ferromagnetism and superconductivity in uranium compounds. *Journal of the Physical Society of Japan* **81**, 011003 (2011).
297. Bastien, G. *et al.* Lifshitz Transitions in the Ferromagnetic Superconductor UCoGe. *Phys. Rev. Lett.* **117**, 206401 (20 Nov. 2016).
298. Jeffries, J. R., Moore, K. T., Butch, N. P. & Maple, M. B. Degree of 5f electron localization in URu₂Si₂: Electron energy-loss spectroscopy and spin-orbit sum rule analysis. *Phys. Rev. B* **82**, 033103 (3 July 2010).
299. Kvashnina, K. O., Walker, H. C., Magnani, N., Lander, G. H. & Caciuffo, R. Resonant x-ray spectroscopy of uranium intermetallics at the M_{4,5} edges of uranium. *Phys. Rev. B* **95**, 245103 (24 June 2017).
300. Fujimori, S.-i. *et al.* Core-Level Photoelectron Spectroscopy Study of UTe₂. *Journal of the Physical Society of Japan* **90**, 015002 (2021).
301. Werner, P. & Millis, A. J. High-Spin to Low-Spin and Orbital Polarization Transitions in Multiorbital Mott Systems. *Phys. Rev. Lett.* **99**, 126405 (12 Sept. 2007).
302. Anisimov, V., Nekrasov, I., Kondakov, D., Rice, T. & Sigrist, M. Orbital-selective Mott-insulator transition in Ca_{2-x}Sr_xRuO₄. *The European Physical Journal B-Condensed Matter and Complex Systems* **25**, 191–201 (2002).
303. De’Medici, L. & Capone, M. in *The Iron Pnictide Superconductors: An Introduction and Overview* (eds Mancini, F. & Citro, R.) 115–185 (Springer International Publishing, Cham, 2017).
304. Baer, Y. & Schoenes, J. Electronic structure and Coulomb correlation energy in UO₂ single crystal. *Solid State Communications* **33**, 885–888 (1980).
305. Runge, E., Fulde, P., Efremov, D. V., Hasselmann, N. & Zwicknagl, G. Approximative treatment of 5f-systems with partial localization due to intra-atomic correlations. *Phys. Rev. B* **69**, 155110 (15 Apr. 2004).
306. Pollmann, F. & Zwicknagl, G. Spectral functions for strongly correlated 5f electrons. *Phys. Rev. B* **73**, 035121 (3 Jan. 2006).
307. Holstein, T. & Primakoff, H. Field Dependence of the Intrinsic Domain Magnetization of a Ferromagnet. *Phys. Rev.* **58**, 1098–1113 (12 Dec. 1940).
308. Schwinger, J., Biedenharn, L. & Van Dam, H. *Quantum theory of angular momentum* 1965.
309. Barnes, S. E. New method for the Anderson model. *J. Phys. F: Met. Phys.* **6**, 1375–1383 (July 1976).

310. Anderson, P. W. Localized Magnetic States in Metals. *Phys. Rev.* **124**, 41–53 (1 Oct. 1961).
311. Li, T., Wölfle, P. & Hirschfeld, P. J. Spin-rotation-invariant slave-boson approach to the Hubbard model. *Phys. Rev. B* **40**, 6817–6821 (10 Oct. 1989).
312. Barnes, S. E. All-electronic Peierls instability in the infinite-U mean-field theory for the Hubbard model. *Phys. Rev. B* **41**, 11701–11704 (16 June 1990).
313. Barnes, S. E. Spin-disordered ground state for a nearly half-filled Hubbard model. *Phys. Rev. B* **41**, 8991–9002 (13 May 1990).
314. Coleman, P. New approach to the mixed-valence problem. *Phys. Rev. B* **29**, 3035–3044 (6 Mar. 1984).
315. Ovchinnikov, S. G. & Val'kov, V. V. *Hubbard operators in the theory of strongly correlated electrons* (World Scientific, 2004).
316. Anderson, P. W., Baskaran, G., Zou, Z. & Hsu, T. Resonating–valence-bond theory of phase transitions and superconductivity in La_2CuO_4 -based compounds. *Phys. Rev. Lett.* **58**, 2790–2793 (26 June 1987).
317. Baskaran, G., Zou, Z. & Anderson, P. W. The resonating valence bond state and high- T_c superconductivity—a mean field theory. *Solid state communications* **63**, 973–976 (1987).
318. Affleck, I. & Marston, J. B. Large- n limit of the Heisenberg-Hubbard model: Implications for high- T_c superconductors. *Phys. Rev. B* **37**, 3774–3777 (7 Mar. 1988).
319. Kotliar, G. & Liu, J. Superexchange mechanism and d-wave superconductivity. *Phys. Rev. B* **38**, 5142–5145 (7 Sept. 1988).
320. Simon, P. & Affleck, I. Kondo screening cloud effects in mesoscopic devices. *Phys. Rev. B* **68**, 115304 (11 Sept. 2003).
321. Bünemann, J. A slave-boson mean-field theory for general multi-band Hubbard models. *physica status solidi (b)* **248**, 203–211 (2011).
322. Lanatà, N., Yao, Y., Deng, X., Dobrosavljević, V. & Kotliar, G. Slave Boson Theory of Orbital Differentiation with Crystal Field Effects: Application to UO_2 . *Phys. Rev. Lett.* **118**, 126401 (12 Mar. 2017).
323. Piefke, C. & Lechermann, F. Rigorous symmetry adaptation of multiorbital rotationally invariant slave-boson theory with application to Hund's rules physics. *Phys. Rev. B* **97**, 125154 (12 Mar. 2018).
324. Lechermann, F. Multiorbital Processes Rule the $\text{Nd}_{1-x}\text{Sr}_x\text{NiO}_2$ Normal State. *Phys. Rev. X* **10**, 041002 (4 Oct. 2020).
325. Zwicknagl, G., Yaresko, A. & Fulde, P. Heavy fermions in UPt_3 . *Physica B: Condensed Matter* **312**, 304–306 (2002).

BIBLIOGRAPHY

326. Zwicknagl, G. 5f Electron correlations and core level photoelectron spectra of Uranium compounds. *physica status solidi (b)* **250**, 634–637 (2013).
327. Le, M. S. D.-A. *Electrons in 5f Systems* (2010).
328. Lam, S. K., Pitrou, A. & Seibert, S. *Numba: A llvm-based python jit compiler in Proceedings of the Second Workshop on the LLVM Compiler Infrastructure in HPC* (2015), 1–6.
329. Johnson, S. G. *The NLOpt nonlinear-optimization package* (2011).
330. Virtanen, P. *et al.* SciPy 1.0: Fundamental Algorithms for Scientific Computing in Python. *Nature Methods* **17**, 261–272 (2020).
331. Blank, J. & Deb, K. pymoo: Multi-Objective Optimization in Python. *IEEE Access* **8**, 89497–89509 (2020).
332. Booth, C. H. *et al.* Probing 5f-state configurations in URu₂Si₂ with U L_{III}-edge resonant x-ray emission spectroscopy. *Phys. Rev. B* **94**, 045121 (4 July 2016).
333. Booth, C. *et al.* Multiconfigurational nature of 5f orbitals in uranium and plutonium intermetallics. *Proceedings of the National Academy of Sciences* **109**, 10205–10209 (2012).
334. Kerridge, A. f-Orbital covalency in the actinocenes (An= Th–Cm): Multiconfigurational studies and topological analysis. *RSC Advances* **4**, 12078–12086 (2014).